# Exploring the sub-keV energy region with the CRESST and NUCLEUS experiments

**Margarita Kaznacheeva**

**Technische Universität München**
TUM School of Natural Sciences

# Exploring the sub-keV energy region with the CRESST and NUCLEUS experiments

Margarita Kaznacheeva

Vollständiger Abdruck der von der TUM School of Natural Sciences der Technischen Universität München zur Erlangung einer

**Doktorin der Naturwissenschaften (Dr. rer. nat.)**

genehmigten Dissertation.

| | |
|---|---|
| Vorsitz: | Prof. Dr. Alejandro Ibarra |
| Prüfende der Dissertation: | 1. TUM Junior Fellow Dr. Raimund Strauß |
| | 2. Prof. Dr. Laura Fabbietti |
| | 3. Prof. Dr. Jules Gascon |

Die Dissertation wurde am 22.10.2024 bei der Technischen Universität München eingereicht und durch die TUM School of Natural Sciences am 28.11.2024 angenommen.

# Abstract

Cryogenic particle detectors with superconducting phonon sensors, operated at mK temperatures, have achieved excellent performance with energy thresholds as low as a few eV. This high sensitivity is essential for a variety of astroparticle physics applications, including the direct detection of sub-GeV dark matter (DM) with the CRESST experiment and the measurement of coherent elastic neutrino-nucleus scattering (CE$\nu$NS) with the NUCLEUS experiment. Both experiments search for low-energy nuclear recoils in target crystals equipped with transition-edge sensors (TESs). This thesis focuses on three topics within the framework of CRESST and NUCLEUS: the low-energy excess (LEE), nuclear recoil calibration at the 100 eV-scale, and new results on sub-GeV DM.

The LEE, steeply rising from several hundred eV toward the threshold, is currently the primary background in the region of interest for sub-GeV DM and CE$\nu$NS searches based on cryogenic detectors. In this thesis, data from two silicon detectors were analyzed and compared with results from other detectors using various target materials, all operated in the recent CRESST-III campaign in a deep-underground facility of the Laboratori Nazionali del Gran Sasso. In all detectors, the LEE rate decreases exponentially with time. Two time constants were identified: the slow one of (149±40) days and the fast one of (18±7) days, which appear after thermal cycling of the cryostat to $\mathcal{O}(10\,\mathrm{K})$. These observations rule out particle-induced backgrounds and point to solid-state effects as the dominant LEE source.

To investigate these effects, a series of measurements was conducted with a NUCLEUS detector equipped with two TESs. In this configuration, the signals generated by energy depositions within the crystal bulk are shared between the two channels. However, the analysis in this thesis revealed that, in addition to shared events, the LEE also includes a fraction of events occurring in anti-coincidence between the two TESs. By removing them, the background in the region of interest was significantly reduced, e.g., by 50% at 40 eV. The remaining shared LEE was further reduced by two orders of magnitude after a dozen thermal cycles from room to mK temperatures over the course of nine months, reaching 10 counts per day at 100 eV. However, after reassembling the detector, the LEE rate increased to its original level, indicating that stress from the holding structures plays a dominant role in the shared LEE. While the double-TES setup is essential for distinguishing between shared and single-TES LEE populations, combining it with instrumented veto holders offers the potential to identify and mitigate events caused by external stress. Additionally, controlled thermal cycling emerges as a promising strategy for reducing LEE.

This thesis presents the analysis of the successful demonstration of a novel low-energy calibration technique developed by the CRAB collaboration. Irradiating a NUCLEUS $CaWO_4$ crystal with moderated neutrons from a dedicated $^{252}$Cf neutron source enabled the first observation of a monoenergetic peak at 112.5 eV from $^{182}$W recoils after neutron capture. This establishes a new, non-intrusive, direct calibration method for sub-keV nuclear recoils, which are detection signatures for sub-GeV DM and CE$\nu$NS. Future use of a thermal neutron beam at the CRAB facility in Vienna will improve the signal-to-background ratio, enhancing the method's precision and test fundamental models in solid-state physics at low energies.

Analysis of the data from the CRESST-III 0.35 g silicon wafer detector showed a reduction of the threshold to 10 eV, which is among the best in the field. This led to exploring a new parameter space region by improving the limits on the spin-independent DM-nucleus interaction cross-section for DM masses between 130 and 165 $\mathrm{MeV/c^2}$ by up to a factor of 20. Further sensitivity improvements require the implementation of the LEE mitigation techniques proposed in this thesis.

The results of this work play a crucial role in adjusting the detector designs for the NUCLEUS and CRESST experiments. Additionally, by co-initiating the international EXCESS workshop series, I participated in launching a global discussion on the LEE within the cryogenic detectors community. Reducing the LEE and a precise understanding of the detector response to low-energy nuclear recoils are key steps for advancing the potential for reliable discoveries with cryogenic DM and CE$\nu$NS experiments.

# ZUSAMMENFASSUNG

Kryogene Teilchendetektoren mit supraleitenden Phononsensoren, die bei mK-Temperaturen betrieben werden, haben eine hervorragende Leistung mit Energie-Schwellenwerten von nur wenigen eV erreicht. Diese hohe Empfindlichkeit ist essenziell für eine Vielzahl von Anwendungen in der Astroteilchenphysik, einschließlich der direkten Detektion von sub-GeV Dunkler Materie (DM) im CRESST-Experiment sowie der Messung der kohärenten elastischen Neutrino-Kernstreuung (CE$\nu$NS) im NUCLEUS-Experiment. Beide Experimente suchen nach niederenergetischen Kernrückstößen in den Detektorkristallen, die mit Übergangskanten-Sensoren (TESs) ausgestattet sind. Diese Dissertation konzentriert sich auf drei Themen im Rahmen von CRESST und NUCLEUS: den Low-Energy Excess (LEE), die Kalibrierung von Kernrückstößen im 100 eV-Bereich und neue Ergebnisse zur sub-GeV DM.

Der LEE, der steil von mehreren hundert eV bis hin zur Schwelle ansteigt, stellt derzeit den primären Untergrund in der Zielregion für sub-GeV DM und CE$\nu$NS-Suchen dar, die auf kryogenen Detektoren basieren. In dieser Dissertation wurden Daten von zwei Siliziumdetektoren analysiert und mit Ergebnissen anderer Detektoren verglichen, die verschiedene Kristallmaterialien verwendeten und alle im Rahmen der jüngsten CRESST-III-Kampagne in einer tief unterirdischen Anlage der Laboratori Nazionali del Gran Sasso betrieben wurden. In allen Detektoren nimmt die LEE-Rate exponentiell mit der Zeit ab. Zwei Zeitkonstanten wurden identifiziert: eine langsame von (149±40) Tagen und eine schnelle von (18±7) Tagen, die auftreten, nachdem der Kryostat auf $\mathcal{O}(10\,\mathrm{K})$ aufgewärmt und dann wieder abgekühlt wurde.. Diese Beobachtungen schließen teilcheninduzierte Untergründe aus und weisen auf Festkörpereffekte als dominierende Quelle des LEE hin.

Um diese Effekte zu untersuchen, wurde eine Reihe von Messungen mit einem NUCLEUS-Detektor durchgeführt, der mit zwei TESs ausgestattet war. In dieser Konfiguration werden die Signale, die durch Energieeinträge im Kristallvolumen entstehen, auf die beiden Kanäle aufgeteilt. Die Analyse in dieser Dissertation zeigte jedoch, dass der LEE neben den geteilten Ereignissen auch eine Klasse von Ereignissen enthält, die in Anti-Koinzidenz zwischen den beiden TESs auftreten. Durch deren Entfernung konnte der Untergrund in der Zielregion signifikant reduziert werden, z.B. um 50% bei 40 eV. Der verbleibende geteilte LEE wurde nach einem Dutzend thermischer Zyklen von Raum- zu mK-Temperaturen im Verlauf von neun Monaten um zwei Größenordnungen weiter reduziert und erreichte 10 Zählungen pro Tag bei 100 eV. Nach dem Wiederzusammenbau des Detektors stieg jedoch die LEE-Rate wieder auf das ursprüngliche Niveau, was darauf hindeutet, dass Spannungen von den Haltestrukturen eine dominierende Rolle beim geteilten LEE spielen. Während die Doppel-TES-Konfiguration entscheidend ist, um zwischen geteilten und einzelnen TES-LEE-Populationen zu unterscheiden, bietet die Kombination mit instrumentierten Veto-Halterungen das Potenzial, Ereignisse durch äußeren Stress zu identifizieren und zu mindern. Zusätzlich versprechen kontrollierte thermische Zyklen eine vielversprechende Strategie zur Reduzierung des LEE zu sein.

Diese Dissertation präsentiert die Analyse der erfolgreichen Demonstration einer neuartigen Niedrigenergie-Kalibrationstechnik, die von der CRAB-Kollaboration entwickelt wurde. Die Bestrahlung eines NUCLEUS $\mathrm{CaWO_4}$-Kristalls mit moderierten Neutronen aus einer dedizierten $^{252}$Cf-Neutronenquelle ermöglichte die erste Beobachtung eines monoenergetischen Peaks bei 112,5 eV von $^{182}$W-Rückstößen nach Neutroneneinfang. Dies etabliert eine neue, nicht-invasive, direkte Kalibriermethode für sub-keV Kernrückstöße, die Signaturen für sub-GeV DM und CE$\nu$NS sind. Der zukünftige Einsatz eines thermischen Neutronenstrahls an der CRAB-Anlage in Wien wird das Signal-zu-Hintergrund-Verhältnis verbessern und somit die Genauigkeit der Methode erhöhen sowie grundlegende Modelle in der Festkörperphysik bei niedrigen Energien testen.

Die Analyse der Daten des CRESST-III 0,35 g-Silizium-Wafer-Detektors zeigte eine Reduzierung der Schwelle auf 10 eV, was zu den besten Ergebnissen in diesem Bereich gehört. Dies ermöglichte die Erforschung eines neuen Parameterraums durch die Verbesserung der Grenzen für den Spin-unabhängigen DM-Nukleus-Wechselwirkungsquerschnitt für DM-Massen zwischen 130 und 165 MeV/c$^2$ um bis zu den Faktor 20. Weitere Verbesserungen der Empfindlichkeit erfordern die Implementierung der in dieser Dissertation vorgeschlagenen LEE-Minderungsverfahren.

Die Ergebnisse dieser Arbeit spielen eine entscheidende Rolle bei der Anpassung der Detektordesigns für die NUCLEUS- und CRESST-Experimente. Darüber hinaus habe ich durch die Mitinitiierung der internationalen EXCESS-Workshop-Reihe entscheidend zu der weltweiten Diskussion über den LEE innerhalb der kryogenen Detektoren-Gemeinschaft beigetragen. Die Reduzierung des LEE und ein präzises Verständnis der des Detektorverhaltens auf niederenergetische Kernrückstöße sind entscheidende Schritte zur Weiterentwicklung des Potenzials für zuverlässige Entdeckungen mit kryogenen DM- und CE$\nu$NS-Experimenten.

# Contents

# Preface

This thesis addresses several significant topics in the field of low-threshold cryogenic particle detectors for astroparticle physics, focusing particularly on the search for sub-GeV dark matter with the CRESST experiments and the detection of Coherent Elastic Neutrino-Nucleus Scattering (CE$\nu$NS) with the NUCLEUS experiments. Several of the results presented here have led to publications in peer-reviewed journals. This preface outlines the structure of the thesis and highlights my contributions to these publications and to the broader scientific community.

Chapter 1 introduces the fundamental principles of cryogenic particle detectors and provides an overview of the current landscape of phonon sensors. It also explores the potential of these detectors in astroparticle physics. Leveraging low-threshold cryogenic detectors based on transition edge sensors (TES) allows CRESST to be one of the leading experiments for sub-GeV dark matter search. I co-authored a recent comprehensive review on cryogenic dark matter searches using scintillating low-temperature detectors [1].

Another application of low-threshold cryogenic particle detectors discussed in this chapter is the detection of CE$\nu$NS. Building on the TES technology developed for CRESST, the NUCLEUS experiment is currently under construction, aiming to measure CE$\nu$NS from reactor antineutrinos to study fundamental properties of neutrinos. The chapter concludes with a discussion of the challenges faced by modern low-threshold cryogenic detectors, including reliable energy calibration for sub-keV nuclear recoils and the steeply rising excess of events observed at low energies that populate the region of interest. This excess currently represents the most significant background, reducing the sensitivity of the detectors. It has been observed in all experiments sensitive to energy depositions of several hundred eV and below. These observations were summarized in a community-wide report published following the EXCESS workshop [2], which was specifically dedicated to investigating this phenomenon. I was one of the initiators and main organizers of this workshop, and I contributed significantly to the publication by writing a substantial portion of the shared content and co-editing the document.

Chapter 2 outlines the main analysis principles and methodologies used to process data collected by the CRESST and NUCLEUS cryogenic detectors to obtain the results presented in the subsequent chapters.

Chapter 3 reviews the observations of the low-energy excess in CRESST-III detectors and presents new insights derived from the analysis of detectors in the recent data-taking campaign. A significant portion of these findings was published in a paper by the CRESST collaboration [3], where I was one of the lead authors, created the majority of the figures, and significantly contributed to writing.

Chapter 4 presents the results from a series of measurements conducted at TUM with a novel NUCLEUS detector equipped with two TES sensors, which revealed the multi-component nature of the low-energy excess. It also provides a summary of the observations and contextualizes them with respect to earlier results, concluding with the most promising strategies for mitigating different excess populations. I presented these results at the EXCESS24 Workshop [4], and a related publication is currently under preparation.

Chapter 5 presents the analysis of a measurement campaign conducted at TUM, where a NUCLEUS $CaWO_4$ detector was irradiated with a strong neutron source. This led to the first observation of a nuclear recoil peak at the 100 eV scale, induced by thermal neutron captures, thereby demonstrating the proof of principle for the novel calibration method proposed by the CRAB collaboration. This observation was published by the CRAB and NUCLEUS collaborations in [5], in which I conducted one of the two independent analyses that lead to the presented results.

Chapter 6 presents the analysis of two silicon detectors operated during a recent CRESST-III data-taking campaign. This analysis demonstrated an energy threshold as low as 10 eV in one of the detectors, enabling the exploration of new parameter space for spin-independent dark matter interactions. The resulting work was published in a CRESST collaboration paper [6], for which I was the lead author, conducted the analysis, and wrote the entire manuscript.

Finally, Chapter 7 summarizes the key results presented throughout this thesis and provides an outlook on future developments in the field.

# 1. Low-energy frontier with cryogenic particle detectors

Cryogenic particle detectors have a rich history dating back to the mid-20th century, developed in response to the growing need for highly sensitive instruments capable of detecting small energy deposits. Low-temperature calorimetry was first proposed as a means to measure energy deposited by radioactivity in 1935 [7]. In 1949, the first detection of individual $\alpha$ particles using a superconducting bolometer was reported [8]. This detection method relied on the temporary transition of a superconducting film to its normal state after energy deposition. Over the subsequent decades, a variety of superconducting sensors were developed to increase the sensitivity and precision of cryogenic detectors. In parallel, the development of cooling technologies enabled the operation of detectors at millikelvin temperatures, further boosting their performance.

Due to their appealing sensitivities, in the 1980-s cryogenic detectors gained prominence and were proposed for the study of rare events, such as double-$\beta$ decay, neutrino interactions [9–11], and dark matter search [12]. In 1987, a dedicated meeting at Ringberg Castle near Munich brought together experts to discuss developments in low-temperature detectors for astroparticle physics applications [13]. Since then, many of the concepts discussed have been successfully implemented in experiments, yielding valuable results in these fields.

In addition to their use in particle physics and cosmology, cryogenic detectors have found applications in astronomy, both in ground-based and space-based observations across various wavelength ranges [14]. Beyond fundamental physics applications, they are used in a variety of industrial fields, including materials science, high-resolution X-ray spectroscopy, and medical research. Furthermore, cryogenic technologies are increasingly being applied in quantum computing, particularly in the development of quantum bits (qubits). The unprecedented sensitivity of cryogenic detectors, combined with a wide range of target materials, make them indispensable tools in both fundamental science and various industrial sectors.

In this chapter, particle detectors operating at $\mathcal{O}(10\,\mathrm{mK})$ temperatures achieving sub-keV energy thresholds used for astroparticle physics applications are considered. The general principles of cryogenic detectors and the various sensor technologies employed are described in Sec. 1.1. Following that, Sec. 1.2 presents the physics potential of these detectors in dark matter searches, with a focus on the CRESST experiment, and in the detection of coherent elastic neutrino-nucleus scattering (CE$\nu$NS), with emphasis on the NUCLEUS experiment. Lastly, two major challenges faced by modern low-threshold cryogenic detectors – namely, the steeply rising event rates at low energies, often referred to as the low-energy excess, and the challenges of low-energy nuclear recoil calibration – are discussed in Sec. 1.3.

## 1.1. Cryogenic particle detectors

When a particle enters a detector's target volume, its energy can be transferred through interactions with either the target nuclei, the target electrons, or both. These interactions result in different excitation processes, such as the generation of heat, charge, or scintillation light, depending on the properties of the detector material. In crystalline detectors, the majority of the deposited energy is converted into vibrations of the crystal lattice – phonon excitations – largely independent of the type of interaction.

Measuring phonons compares favorably to classical semiconductor ionization detectors, where only the portion of energy converted into ionization is accessible. This typically amounts to about 30% of the total energy for electron recoils, with significantly lower values for nuclear recoils due to quenching. Additionally, only a small fraction – on the order of a few percent – of the deposited energy is emitted as scintillation light in scintillating crystals.

At cryogenic temperatures, the excitation energy of phonons (on the order of meV) is at least three orders of magnitude lower than that required for electron-hole pair production (on the order of eV) in semiconductor detectors. As a result, phonon detection is not fundamentally limited by statistical fluctuations, allowing for the detection of much smaller energy depositions: eV-scale energy thresholds have already been achieved, and ongoing technological advancements continue to push the sensitivity further. This also broadens the range of potential target materials beyond silicon and germanium, allowing the target composition to be tailored to specific experimental goals.

In this section, the general principles of the cryogenic particle detectors are discussed in Sec. 1.1.1, while Sec. 1.1.2 presents types of phonon sensors used in currently operating sub-keV threshold solid-state cryogenic detectors for dark matter and neutrino physics applications.

### 1.1.1. General principles

A basic cryogenic detector consists of three main components: an absorber, a perfectly coupled thermometer to measure temperature increases, and a thermal link to a heat bath that returns the absorber to its desired operating temperature. Such a detector is illustrated in Fig. 1.1. The absorber is characterized by its heat capacity $C$, and the thermal link by its conductivity $G$. In thermal equilibrium, the absorber's temperature $T(t)$ is equal to the heat bath temperature $T_{bath}$.

When a particle deposits energy $\Delta E$ in the absorber's volume, it generates phonon excitations, leading to a temperature increase $\Delta T$ in the absorber, measured by the thermometer. The overall power transfer in the detector can be described as:

$$P = C\frac{dT(t)}{dt} + P_{link}, \tag{1.1}$$

where the incoming power $P$, resulting from the particle interaction, raises the temperature and drives a power flow through the thermal link, denoted as $P_{link}$. In the simplified scenario where the particle deposits its energy instantaneously, $P = \Delta E \delta(t)$, the power dissipated from the absorber through the weak thermal link to the heat bath is given by $P_{link} = G(T(t) - T_{bath})$. Thus, the thermal equation becomes:

$$\Delta E \delta(t) = C \frac{dT(t)}{dt} + G(T(t) - T_{bath}). \tag{1.2}$$

And the evolution of the absorber's temperature over time can then be described by:

$$T(t) = \frac{\Delta E}{C} e^{-\frac{t}{\tau}} + T_{bath}, \tag{1.3}$$

where the initial temperature increase $\Delta T \propto \frac{\Delta E}{C}$ diminishes exponentially back to the bath temperature, with a time constant $\tau = {}^{C}/_{G}$.

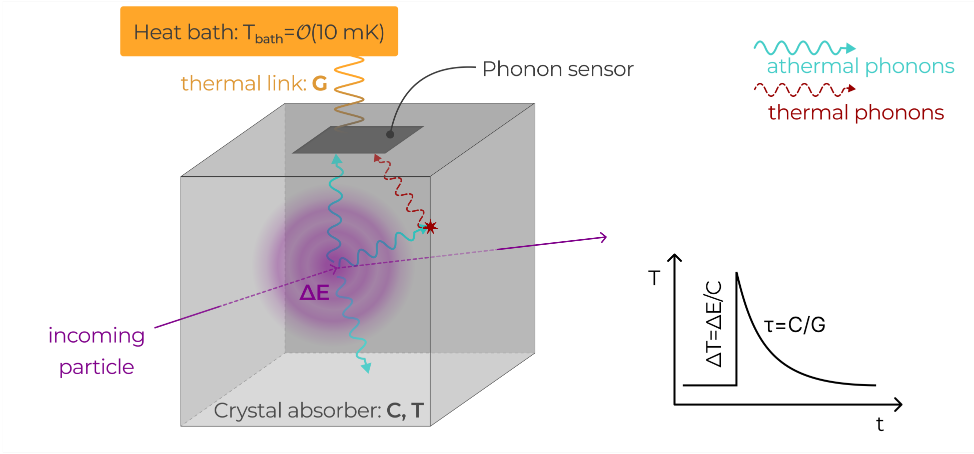

Figure 1.1.: Illustration of the general working principle of cryogenic detectors. The system consists of an absorber crystal with temperature $T$ and heat capacity $C$, a strongly coupled phonon sensor, and a weak thermal link with conductivity $G$ connecting the absorber to a thermal bath stabilized at a constant temperature $T_{bath}$. When a particle interaction happens within the absorber's volume, energy deposition of $\Delta E$ causes optical and acoustic phonon excitation. These phonons rapidly decay into athermal phonons (cyan), which propagate through the crystal and eventually downconvert into thermal excitations (red), resulting in an increase in the absorber's temperature by $\Delta T$. The temperature then decreases via the thermal link exponentially over a time scale of ${}^{C}/_{G}$. Depending on the phonon sensor technology, both athermal and thermal phonons can be measured.

The heat capacity of the absorber decreases with temperature, following a linear relationship for metals and a cubic relationship for dielectrics and semiconductors. Therefore, lower operating temperatures are advantageous for achieving larger, measurable temperature rises. To enhance sensitivity, cryogenic calorimeters are typically operated at temperatures of $\mathcal{O}(10\,\mathrm{mK})$ using $^4$He/$^3$He dilution refrigerators. The most commonly used targets are monocrystals of various materials, where $C \propto (T/\Theta_D)^3$, where $T \ll \Theta_D$ (the Debye temperature of the material). However, there are also new projects aiming to use superfluid $^4$He as a target for particle detection [15–17].

As illustrated in Fig. 1.1, when a particle interaction occurs within the crystal absorber, the energy deposition first generates optical and acoustic phonons with an average energy comparable to the Debye energy ($\sim$ 50 meV for solids). These phonons rapidly (within femtoseconds to picoseconds) decay into less energetic athermal phonons, which then propagate ballistically through the crystal. Over the course of milliseconds, these athermal phonons downconvert to thermal excitations at the $k_B T$ energy scale through inelastic scattering off crystal surfaces and impurities. The detector eventually returns to equilibrium through its weak thermal coupling to the bath. Depending on the sensor technology, the attached sensor can measure athermal phonons, thermal phonons, or both, as discussed in Sec. 1.1.2.

The theoretical energy resolution limit of cryogenic detectors is primarily determined by thermodynamic fluctuations in the energy content of the detector, due to the random exchange of phonons with the heat bath through the thermal link. These temperature fluctuations can be quantified by the root mean square (RMS) energy resolution:

$$\Delta E_{\text{rms}} \propto \sqrt{C_{\text{det}} k_B T^2}, \tag{1.4}$$

where $k_B$ is the Boltzmann constant, and $C_{\text{det}}$ is the heat capacity of the detector. This indicates that lower operating temperatures improve energy sensitivity. However, additional noise sources – such as electrical Johnson noise in the sensor and noise in the readout amplifiers – can degrade this sensitivity. A detailed discussion of these noise contributions can be found, e.g., in [18].

### 1.1.2. Phonon sensors for low-threshold cryogenic detectors

The sensor plays a fundamental role in cryogenic detectors, responsible for converting a phonon signal into a measurable quantity. Low-temperature calorimetric measurements can operate in two distinct phonon collection modes, depending on the type of thermometer used. Phonon detectors can be constructed for purely thermal detection to measure the temperature rise after phonons have reached thermal equilibrium. Alternatively, sensors can be designed to enhance the detection of athermal phonons resulting in faster response signals. This section presents various types of phonon sensors currently used in macroscopic cryogenic detectors for dark matter searches and CE$\nu$NS experiments.

**Neutron-transmutation-doped (NTD)** sensors sensitive to thermal phonons constructed from semiconducting crystals that are irradiated with neutrons to achieve a uniform doping concentration [19]. The resulting resistance of the sensor is highly sensitive to temperature ($\propto e^{\sqrt{T_0/T}}$), making it possible to detect heat through a decrease in the NTD sensor voltage bias [20]. The EDELWEISS experiment [21–23] utilizes high-purity germanium crystals equipped with germanium NTD sensors to search for DM. Based on this technology, the RICOCHET experiment aims to measure CE$\nu$NS from reactor antineutrinos [24]. Baseline energy resolutions of several tens of eV were achieved with NTDs [22, 25]. These detectors also measure ionization signals alongside thermal signals by applying an electric field to the crystal. Depending on the strength of the applied voltage, this configuration allows for either particle identification or amplification of the phonon signal via the Neganov-Trofimov-Luke (NTL) effect [26, 27].

**Kinetic Inductance Detector (KID)** [28] is an example of sensors only sensitive to athermal phonons. A KID operates as a resonator whose frequency depends on the Cooper pair density within the superconducting material. When athermal phonons from a particle interaction in the absorber reach the KID, they break Cooper pairs, thereby altering the kinetic inductance and shifting the resonance frequency. A typical KID is composed of a thin-film superconducting inductor (such as aluminum) paired with an interdigitated capacitor. The resonance frequency can be tuned, allowing multiple KIDs to be linked to a single feedline. This provides the key advantage of KIDs in astroparticle experiments – their ability to multiplex numerous sensors. The application of KIDs as phonon sensors for particle detectors in rare-event searches was suggested in [29, 30]. Ongoing development of KID arrays for DM and CE$\nu$NS experiments can be found in works like [31, 32], and they are a central component of the BULLKID project, which aims to build a kg-scale low-threshold DM detector [33].

**Metallic Magnetic Calorimeters (MMC)** use change in magnetization of a paramagnetic material in a weak magnetic field at low temperatures as a measure of the energy deposition in the absorber [34, 35]. Recently, an unprecedented energy resolution of $\Delta E_{\mathrm{FWHM}} = 1.25\,\mathrm{eV}$ at 5.9 keV has been demonstrated for a tiny gold absorber with a mass of $\sim 1\,\mu\mathrm{g}$ [36] demonstrating a large dynamic range of high sensitivity. The AMORE [37] experiment uses MMCs coupled to massive absorbers via thin gold films acting as phonon absorbers to search for neutrinoless double-beta decay. An upcoming initiative for light DM searches based on a superfluid helium target, the DELight experiment [17], aims to collect signals using a crystal wafer equipped with MMC arrays.

**Transition Edge Sensors (TES)** are among the most sensitive devices currently employed in cryogenic particle detection. A TES typically consists of a thin metal film, operated at a temperature near the midpoint of its transition between superconducting and normal-conducting phases. Due to the steep nature of this transition, examplarily shown in Fig. 1.3, small temperature fluctuations cause significant variations in TES resistance. Tungsten (W), particularly in its $\alpha$ crystalline phase, is a widely used material for TES, offering a transition temperature $T_c$ around 15 mK.

To enhance signal strength, it is advantageous to maximize the surface coverage of the absorber crystal. However, increasing the surface area of the TES also raises its heat capacity, which in turn degrades sensitivity. This issue can be mitigated by fabricating the TES with a small overlap with another superconducting material that has a higher transition temperature ($T_c$) than the TES, such as aluminum, which has $T_c \approx 1.2\,\mathrm{K}$, as illustrated in Fig. 1.2.

When athermal phonons with energies greater than twice the superconducting gap of aluminum $\Delta_{Al}$ are absorbed in the aluminum films covering absorber's surface, they

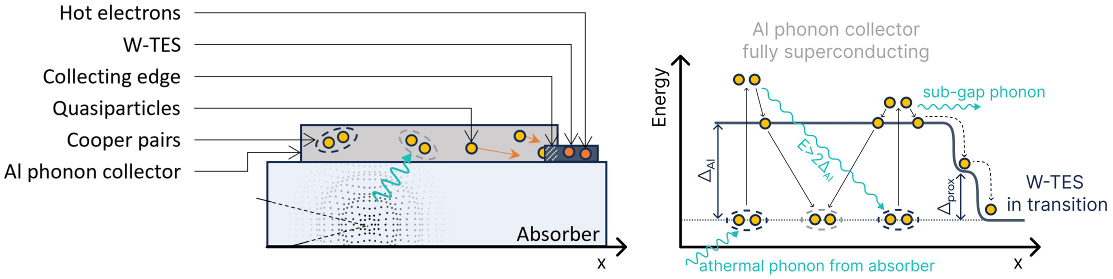

Figure 1.2.: Schematic representation of the signal formation process in a TES with phonon collectors (PCs) or a Quasiparticle-trap-assisted Electrothermal-feedback TES (QET). The left panel depicts a side view of an absorber with a W-TES and overlapping Al PC. The right panel illustrates the spatial gradient of the superconducting bandgap. When an athermal phonon with energy $> 2\Delta_{Al}$ is absorbed by the Al PC, it breaks a Cooper pair, creating excited quasiparticles. Such quasiparticles diffuse through the aluminum medium and can recombine with another quasiparticle by emitting phonons. This cycle of recombination and relaxation continues until the emitted phonon energy drops below $2\Delta_{Al}$, at which point the phonon is re-emitted into the absorber. Quasiparticles that reach the overlapping region with the tungsten film, where the bandgap is reduced to $\Delta_{prox}$ due to the proximity effect, transfer their energy to the W electron system.

break Cooper pairs, producing quasiparticles. These quasiparticles, initially well above the gap energy, diffuse through the aluminum, thermalizing through phonon emission or recombination, which releases additional phonons. As long as the phonon energies remain above $2\Delta_{Al}$, further Cooper pairs can be broken, generating more quasiparticles. Once the phonon energies drop below $2\Delta_{Al}$, they no longer have sufficient energy to break Cooper pairs and are re-emitted into the absorber contributing to the thermal component of the measured signal. Approximately half of the energy from the athermal phonons is re-emitted as sub-gap phonons. If a quasiparticle reaches an overlap region with zero band gap, it transfers its energy to the electron system of the TES, causing a rapid temperature increase. This mechanism forms the fast and dominant part of the signal. A schematic of this process is shown in Fig. 1.2. This technique, referred to as Quasiparticle-trap-assisted Electrothermal-feedback TES (QET) [38] or Phonon Collectors (PCs) [39], significantly enhances the athermal phonon signal.

Low-impedance TES devices, such as W-TES, are typically read out using Superconducting Quantum Interference Devices (SQUIDs) [41, 42]. A basic SQUID readout circuit is illustrated in Fig. 1.3. In this setup, the bias current $I_B$ is divided between the TES and a shunt resistor $R_S$. The current through one of the branches, in this case the shunt branch (as shown in Fig. 1.3), is coupled to the SQUID via an input coil $L$. Variations in TES resistance cause changes in the current, which in turn alters the magnetic field in the input coil. The SQUID detects these changes, allowing the current, and therefore the energy deposited in the absorber, to be measured through the input coil. Model describing the pulse shape of the expected signal from W-TES with Al PC is described in 2.1.

The W-TES, coupled with aluminum PCs, is used in the CRESST DM search experi-

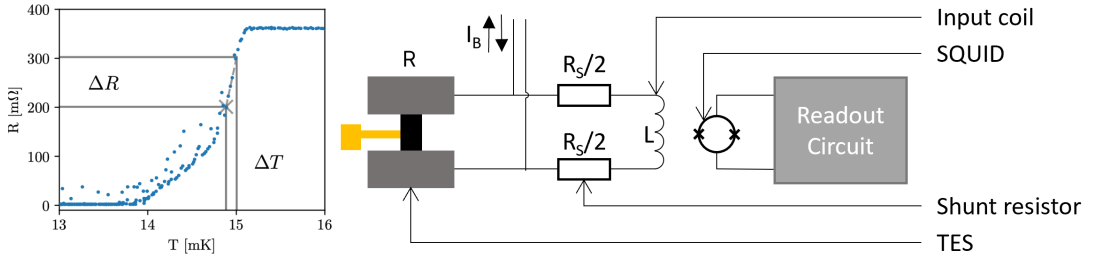

Figure 1.3.: Left: Transition curve from the superconducting to the normalconducting state. A small temperature increase of the sensor $\Delta T$ causes a change in TES resistance $\Delta R$. Figure taken from [40]. Right: Readout circuit of a TES relying on a SQUID-based amplification.

ment [43] and the NUCLEUS experiment aiming to detect CE$\nu$NS [44, 45], where it is typically evaporated to crystal targets like $CaWO_4$ and $Al_2O_3$. Ge or Si targets with W-QET arrays are used by the SuperCDMS collaboration [46–51], along with low-threshold projects such as SuperCDMS-HVeV [52–54] and SuperCDMS-CPD [55, 56].

Under the TESSERACT initiative [15, 16], several TES-based experiments are being currently developed to extend the dark matter search by pushing energy resolution to sub-eV scale. These efforts focus on both DM-nucleus scattering and DM-electron interactions, using solid absorbers such as $Al_2O_3$, $SiO_2$, and GaAs in the SPICE experiment, as well as superfluid $^4$He targets in the HeRALD experiment [57].

## 1.2. Physics potential of low-threshold cryogenic particle detectors

Cryogenic detectors employing the sensors discussed in Sec. 1.1.2 enable unprecedentedly low energy thresholds, allowing the detection of eV-scale energy depositions resulting from particle interactions. Optimizing a cryogenic detector is a complex, multi-parameter process. However, improving sensitivity is generally more feasible with smaller absorber crystals due to reduced heat capacity [58, 59]. This, of course, comes at the cost of exposure but opens up the possibility of detecting interactions with tiny energy deposits. Consequently, many recent cryogenic rare-event searches have reduced their target masses to $\mathcal{O}(10\,\mathrm{g})$ and below.

Although the detection threshold determines the sensitivity to the processes of interest, it remains largely a matter of choice, as no universally accepted convention for setting this threshold currently exists. Nevertheless, the threshold is intrinsically linked to the baseline energy resolution, which represents the resolution at zero energy deposition, constrained by finite baseline noise. Thus, the baseline energy resolution can be considered as a more fundamental metric for comparing the performance of different detectors across experiments.

Fig. 1.4 provides an overview of the achieved baseline energy resolutions, $\sigma_{BL}$, for nuclear recoils[1] with respect to their absorber crystal masses. The figure includes data from macroscopic cryogenic detectors with varying phonon sensor technologies and target materials, published in recent years, with a particular focus on experiments that rely on lowering energy threshold. Detectors with smaller absorber masses, as expected, achieve higher sensitivity due to reduced heat capacity. Additionally, a higher heat capacity of a particular material for the same absorber mass degrades performance. It is important to note that sensor adaptation is also essential for achieving consistent and predictable improvements in performance. Since in recent detector designs, special care was usually taken in sensor adaptation, implementing smaller target masses led to better baseline resolution within the same sensor technology. Furthermore, measurements conducted on the surface can suffer from environmental instabilities and high particle rates, which reduce sensitivities compared to experiments performed in low-background environments.

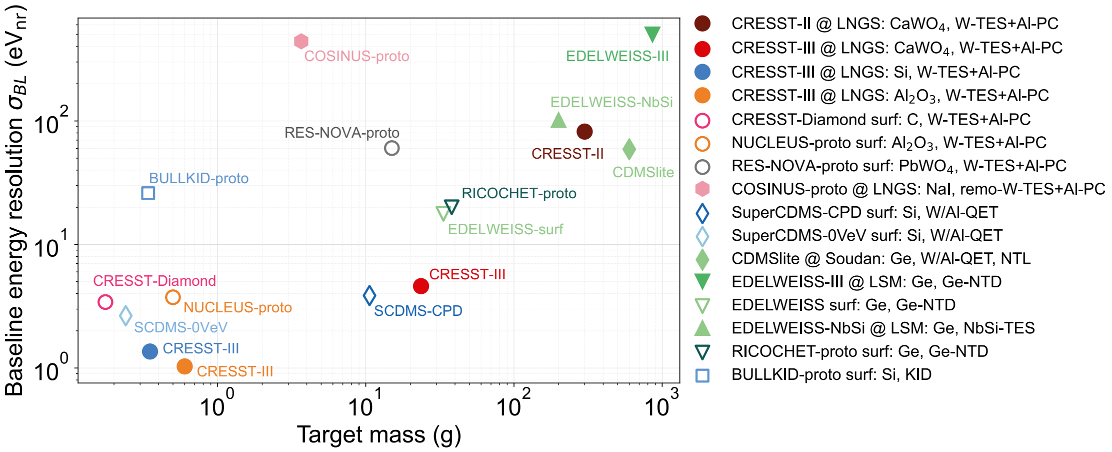

Figure 1.4.: Overview of the performance for a selection of recent macroscopic cryogenic detectors, utilizing various target materials and phonon sensor technologies: CRESST-II [60], CRESST-III CaWO$_4$ [43], CRESST-III Si [6], CRESST-III Al$_2$O$_3$ [61], CRESST-Diamond [62, 63], NUCLEUS prototype [59, 64], RES-NOVA prototype [65], COSINUS [66], SuperCDMS-CPD [55, 56], SuperCDMS-0VeV [52], CDMSlite [67], EDELWEISS-III [21, 68], EDELWEISS-surf [22], EDELWEISS-NbSi [69], RICOCHET prototype [25], and BULLKID prototype [33]. Similar colors indicate the use of common target materials, while distinct marker shapes correspond to different phonon sensor technologies. Measurements conducted in above-ground facilities are labeled with 'surf'. Detectors with smaller target masses within a given sensor technology exhibit lower baseline resolution values, indicating enhanced sensitivity.

---

[1] In experiments that exploit the NTL effect the phonon signal is enhanced by a term proportional to the number of generated electron-hole pairs. However, for nuclear recoils, this number is significantly reduced compared to electronic recoils. As a result, sensitivity to these two interaction types varies significantly. Since the applications considered in this thesis rely on scattering of particles with target nuclei, performance relevant to nuclear recoils is used for this illustration.

Such high resolutions are a key advantage of cryogenic detectors for applications requiring sensitivity to small nuclear recoils, such as the search for light dark matter discussed in Sec. 1.2.1 and CE$\nu$NS described in Sec. 1.2.2. Initially proposed in 1984 for neutrino physics [10], the technology for detecting CE$\nu$NS was soon recognized as also being sensitive to dark matter from the galactic halo [12]. Since then, advancements in detector technologies for CE$\nu$NS and dark matter searches have been closely related, as both types of experiments share key requirements such as low energy thresholds, low intrinsic background rates and, for some applications, heavy target nuclei.

### 1.2.1. Sub-GeV dark matter search

According to the standard cosmological ($\Lambda$CDM) model, dark matter (DM) constitutes approximately 84% of the universe's total matter content and 27% of the total energy budget [70]. Despite extensive indirect evidence through its gravitational effects, such as galactic rotation curves, galaxy cluster dynamics, and the cosmic microwave background (CMB), DM's nature remains elusive and poses one of the greatest mysteries in modern physics. Its non-luminous and weakly interacting nature has driven physicists to explore various theoretical models that propose new particles outside the Standard Model (SM) of particle physics.

The first indication of DM came from the observation of galaxy cluster dynamics [71]. With the systematic measurement of galaxy rotation curves which showed that stars orbiting at the outer edges moved faster than expected based solely on visible matter [72], the DM paradigm was established [73, 74]. According to it, galaxies are enveloped in a DM halo, which provides the necessary mass to explain the discrepancy between the observed and the expected acceleration due to luminous matter. Further evidence arose from galaxy cluster collisions [75] and gravitational lensing, where light bends more than can be explained by visible mass alone [76]. On cosmological scales, the CMB power spectrum and large-scale structure formation studies have also supported the existence of DM as a dominant gravitational component shaping the universe's evolution [70].

A broad range of theoretical models has been proposed to explain DM. The most prominent candidates are weakly interacting massive particles (WIMPs), which are hypothesized to interact through the weak nuclear force. WIMPs are naturally predicted by supersymmetry (SUSY), where the lightest supersymmetric particle is stable and does not decay further. This scenario was compelling due to the so-called "WIMP miracle" (i.e. mass of 10 to $10^5$ GeV/$c^2$ with weak-scale interaction cross-sections), which posits that WIMPs could account for the observed DM abundance due to thermal production in the early universe [77]. However, the parameter space predicted by the "WIMP miracle" has been majorly excluded by extensive experimental efforts. Other possibilities include axions, originally proposed to solve the strong CP problem, which could also serve as DM candidates [78].

Recently, there has been increasing interest in exploring DM models with masses smaller than the classical WIMP, particularly in the sub-GeV/$c^2$ range [79–83]. These lighter candidates are compatible with cosmological observations [84, 85] and could evade detection in traditional WIMP searches. Direct detection experiments have thus begun focusing on achieving lower energy thresholds to probe these sub-GeV DM candidates. These experiments aim to measure nuclear or electron recoils caused by DM scattering events, making them sensitive to both WIMPs and lighter DM particles.

#### 1.2.1.1. Direct dark matter detection principle

Under the assumption of a non-gravitational interaction between DM and SM particles,there are three approaches to DM detection.

At high-energy particle colliders like the Large Hadron Collider (LHC), dark matter (DM) particles may be produced if their mass is within the accessible energy range, though they remain undetectable directly, only inferred through missing transverse momentum (missing energy) in association with SM particles [86]. In indirect detection, researchers look for SM particles resulting from the annihilation or decay of DM in regions of high DM density, such as the Galactic center [87]. The direct detection approach searches for energy depositions in a target caused by interactions of DM particles propagating through it.

At present, there is a large field of experimental direct dark matter (DM) searches aiming to detect DM particles using earth-based detectors. Since the mass of the DM particle, $m_\chi$, is unknown, it is essential to conduct searches over a wide range of possible masses. One of the most common approaches in direct detection is measuring the nuclear recoil energy $E_R$ resulting from the elastic scattering of DM particles off the nuclei in the detector's target material. The expected differential recoil rate, ${}^{dR}\!/_{dE_R}$, of DM particles in a detector target of mass $M$, with nucleus mass $m_N$, can be expressed as:

$$\frac{dR}{dE_R} = \frac{M}{m_N}\frac{\rho_\chi}{m_\chi}\int_{v_{min}(E_R)}^{v_{esc}} dv f(v) v \frac{d\sigma}{dE_R}(v), \tag{1.5}$$

where $\rho_\chi$ is the local DM mass density, typically $\rho_\chi = 0.3\,(\mathrm{GeV/c^2})/\mathrm{cm^3}$ [88], and $\sigma$ is the interaction cross-section. Assuming the standard DM halo model [89], the velocity distribution $f(\vec{v})$ of DM particles in the galactic rest frame follows a Maxwell-Boltzmann distribution. In Eq. 1.5, the integration is performed from the minimum velocity $v_{min}$, which can induce a recoil energy $E_R$, up to the galactic escape velocity, $v_{esc}$, typically $v_{esc} = 544\,\mathrm{km/s}$ [90, 91]. The differential cross-section depends on the specific DM model and can vary in form. For spin-independent (SI) interactions, the DM particle interacts coherently with both protons and neutrons, enhancing the cross-section relative to the DM-nucleon cross-section, $\sigma_n$, by a factor proportional to the square of the mass number $A$ of the target nucleus:

$$\frac{d\sigma_{SI}}{dE_R} = \frac{m_N}{2v^2}\frac{\sigma_n}{\mu_n^2}A^2F^2(E_R), \tag{1.6}$$

where $\mu_n$ is the DM-nucleon reduced mass, and $F(E_R)$ is the form factor, which accounts for the finite size of the nucleus and distribution of nucleons inside the nucleus. The

Helm form factor parametrisation [92, 93] is commonly used to model this effect for large momentum transfers, while $F(E_R) = 1$ for small momentum transfers.

If the target nucleus has a non-zero spin, the experiment can also be sensitive to spin-dependent (SD) DM-nucleon interactions.

Since neither the DM mass $m_\chi$ nor the interaction cross-section $\sigma$ is known, experimental results are typically presented in a parameter space defined by these two variables. By comparing the predicted energy spectrum for different $m_\chi$ and $\sigma$ values to the measured energy spectrum, one can either identify allowed regions in the case of a signal discovery or exclude regions in the absence of a signal.

The expected differential nuclear recoil spectrum for SI DM-nucleus interactions, for several DM particle masses in an ideal $CaWO_4$ detector, is shown in Fig. 1.5. The rate is normalized to the detector mass $M$ and DM-nucleon cross-section $\sigma_n$. The contributions from tungsten, calcium, and oxygen nuclei are examplarily shown for comparison. The kinematics of the scattering process, and hence the shape of the energy spectrum, are determined by the masses of both the DM particle and the target nuclei. The maximum recoil energy is given by $E_R^{max} = {}^{2\mu_N^2 v^2}/_{m_N}$, where $\mu_N$ is the DM-nucleus reduced mass. For lower DM masses, the maximum recoil energy is smaller, imposing strict requirements on the detection threshold in DM search experiments. Heavy tungsten nuclei, with their $A^2$ enhancement, yield higher event rates, while lighter nuclei, such as oxygen, extend the energy spectrum to more accessible values.

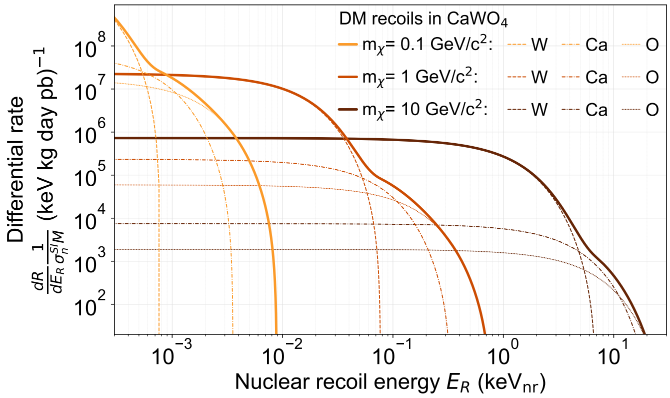

Figure 1.5.: Expected nuclear recoil energy spectra for spin-independent interactions of DM particles with masses of 0.1, 1, and 10 GeV/c$^2$ in a $CaWO_4$ target (solid lines). Individual contributions from scattering with tungsten, calcium, and oxygen nuclei are shown with dashed, dash-dotted, and dotted lines respectively.

The current experimental landscape of exclusion limits for SI DM-nucleus scattering is shown in Fig. 1.6. For WIMPs with $m_\chi \gtrsim 10\,\mathrm{GeV/c^2}$, current technologies can easily achieve the necessary detection thresholds, with the main challenge being the construction of large detectors to achieve sufficient exposure. Liquid noble gas detectors with multi-tonne-year exposures marked with blue-ish colors, as XENON [94], LUX-ZEPLIN [95], PandaX [96], DEAP [97], DarkSide [98], are leading the field in this mass range due to their low backgrounds and scalability. Meanwhile, cryogenic detectors, as CRESST [43], EDELWEISS [21], SuperCDMS [56], shown with red-ish colors, have established a leading role in the low-mass regime $(100\,\mathrm{MeV}/c^2 \lesssim m_\chi \lesssim 1\,\mathrm{GeV}/c^2)$ due to their high sensitivity. In fact, due to the higher expected event rate of lighter DM particles, gram-scale detectors like cryogenic calorimeters, which achieve ultra-low energy thresholds $\mathcal{O}(1\,\mathrm{eV})$, are sufficient to explore new DM parameter space regions. For these detectors, further reducing the detection threshold remains a primary goal.

The DAMA/LIBRA experiment has observed a modulating event rate over 25 years, with a statistical significance of $13.7\sigma$, consistent with the expected phase and period for a galactic dark matter halo. However, this result is in significant tension with other dark matter searches, prompting ongoing and upcoming experimental efforts to independently verify the DAMA/LIBRA findings [99–103].

As was discussed in Sec. 1.1.1, phonon-based detectors measure the full energy deposition, nearly independent of the interacting type. However, for DM searches of a particular interaction, it is beneficial to distinguish nuclear or electronic recoils to reduce the background and select only potential DM events. If the target crystal is a scintillator or semiconductor, particle identification can be achieved by simultaneously measuring phonons and light or charge signals [1, 47, 68].

For DM particles with $m_\chi \ll 1\,\mathrm{GeV/c^2}$, inelastic scattering processes, such as DM interacting with bound electrons [117–119] or via the Migdal effect [120, 121], offer promising detection mechanisms. These interactions allow for a significant fraction of the DM kinetic energy to be transferred to the detector target. While the term "sub-GeV" or "light DM" can refer to a wide range of DM masses, this thesis focuses on masses between approximately $100\,\mathrm{MeV/c^2}$ and $1\,\mathrm{GeV/c^2}$ accessible for nuclear recoils. The lower bound depends heavily on the detector's threshold and is expected to be extended in the coming years.

As shown in Fig. 1.6, low-temperature detectors are well-suited to detecting nuclear recoil signals from sub-GeV DM particles due to unprecedented energy thresholds provided by advanced phonon sensor technologies. One of those experiments currently providing the most stringent limits on the SI elastic DM-nucleus scattering for DM masses below $1\,\mathrm{GeV/c^2}$ is the CRESST experiment presented in the next section.

#### 1.2.1.2. The CRESST experiment

The CRESST (Cryogenic Rare Event Search with Superconducting Thermometers) experiment combines the high sensitivity of cryogenic TES-based detectors with particle identification via scintillation light. CRESST-I (1996-2001), one of the early pioneers in direct DM searches, utilized a single-channel readout of phonon signals from $\sim 250\,\mathrm{g}$ sapphire target crystals [122]. In its second phase, CRESST-II (2002-2015), the experiment reduced backgrounds in the keV energy range by employing scintillating $\mathrm{CaWO_4}$ crystals as targets, coupled with a two-channel readout system to simultaneously register phonon and light signals from particle interactions within the $\sim 300\,\mathrm{g}$ absorber [123].

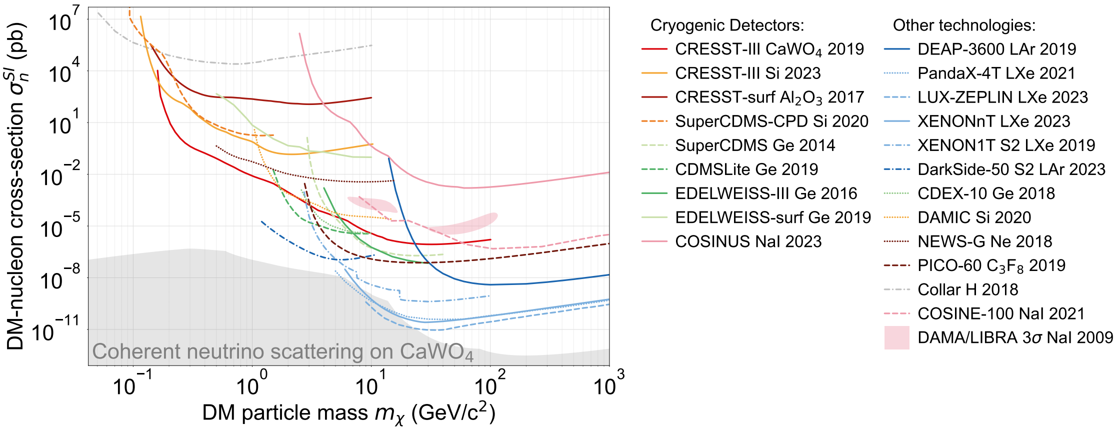

Figure 1.6.: Results of DM searches via spin-independent elastic DM-nucleus scattering obtained with various detection principles and target materials indicated in the legend. The regions above the lines are excluded. The following results are shown. With cryogenic detectors in deep-underground setups: CRESST-III $CaWO_4$ [43], CRESST-III Si [6], SuperCDMS [104], CDMSLite [49], EDELWEISS-III [21], COSINUS [66]; and in the surface facilities: CRESST-surf [64], SuperCDMS-CPD [56], and EDELWEISS-surf [22]. With liquid noble gas experiments: DEAP-3600 [97], PandaX-4T [96], LUX-ZEPLIN [95], XENONnT [94]; with ionization signal only (S2): XENON1T S2 [105], DarkSide-50 S2 [98]. With $p$-type point contact Ge detectors CDEX-10 [106], with CCD sensors DAMIC [107]; with spherical gaseous proportional counter NEWS-G [108]; with the bubble chamber PICO-60 [109]; with hydrogenated organic scintillators by J. I. Collar [110]; with NaI: COSINE-100 [111] and contours compatible with DAMA/LIBRA results [112] calculated in [113]. The gray area shows the parameter space wherein the background, induced by coherent scattering of solar and atmospheric neutrinos off the target nuclei, appears in a DM search experiment using $CaWO_4$ absorbers calculated in [114, 115]. It is commonly referred to as the neutrino floor or, more recently, neutrino fog [116].

The heavy tungsten nucleus in $CaWO_4$ also provided an advantage in WIMP searches in the $\mathcal{O}(10\,\mathrm{GeV/c^2})$ mass range due to the $A^2$ enhancement of the scattering cross-section (Eq. 1.6).

The current, third phase, CRESST-III (2016-present), focuses on sub-GeV DM searches, requiring energy thresholds as low as $\mathcal{O}(10\,\mathrm{eV})$. To achieve these thresholds, CRESST-III reduced the size of the target crystals, with standard modules now using 24 g $CaWO_4$ crystals. This design change resulted in improvement in baseline energy resolution by a factor of $\sim 20$ compared to CRESST-II (see Fig. 1.4). In the sub-GeV regime, the light oxygen nucleus becomes a more effective probe due to its higher expected recoil energy (see Fig. 1.5). While scintillation-based particle discrimination becomes ineffective below $\sim 1\,\mathrm{keV}$, the light channel remains crucial for in-situ background measurement and identification of background components at higher energies, providing essential input for background simulations. Additionally, wafer-like light absorbers, considered as primary targets, offer the potential for even lower energy thresholds.

The CRESST-III experiment is located at the Laboratori Nazionali del Gran Sasso

(LNGS), shielded by a 3600 m.w.e. rock overburden, which significantly reduces cosmic ray-induced backgrounds, suppressing the muon flux by six orders of magnitude compared to sea level [124]. The detectors are further shielded by multiple layers, including polyethylene for neutron moderation, plastic scintillators for active muon vetoing, and low-radioactivity lead and copper for $\gamma$ shielding. A nitrogen-purged box inside the muon veto prevents the buildup of radon gas. The cryogenic detectors are operated in a $^3$He/$^4$He dilution refrigerator and are shielded from neutron emissions by an additional inner polyethylene layer (see Fig. 1.7). More details on the experimental setup are available in Ref. [123].

The standard CRESST-III module (Fig. 1.8) consists of a $(20 \times 20 \times 10)\,\mathrm{mm}^3$ $CaWO_4$ crystal target, with a maximum of the emitted scintillation light spectra at $\sim 420\,\mathrm{nm}$ [126] measured by a separate $(20 \times 20 \times 0.4)\,\mathrm{mm}^3$ silicon-on-sapphire light detector facing the crystal. Both the target crystal and light detector are enclosed in a high-purity copper housing, with reflective and scintillating Vikuiti™ foil enhancing light collection. The target and light detector are mounted using scintillating $CaWO_4$ sticks, creating a fully scintillating inner housing.

The target crystal and the light detector crystal are equipped with a W-TES featuring aluminum phonon collectors for signal readout, as shown schematically in Fig. 1.2 and discussed in Sec. 1.1.2. The TES and aluminum structures are deposited on the crystal surfaces by electron-beam evaporation. The detectors operate at approximately $15\,\mathrm{mK}$, the transition temperature of tungsten in its $\alpha$ phase. A gold stripe weakly couples the W-TES to the heat bath. TES resistance changes due to energy depositions in the crystal are measured with a SQUID-based readout circuit (see Fig. 1.3) [127]. Additionally, each detector includes a gold ohmic heater for injecting artificial pulses of fixed energies, used for in real-time stabilization and detector response mapping across the detector's dynamic range. The procedure is described in 6.4 and [123]. An absolute energy calibration is obtained by a low activity $^{55}$Fe source attached to one of the walls of the module or by a more energetic external $^{57}$Co source.

A Geant4-based physics simulation code, ImpCRESST, has been developed to model expected electromagnetic backgrounds [128, 129]. Recent improvements in normalization methods increased background model accuracy by 18.6%, now explaining 82.7% of backgrounds in the 1-40 keV range [130]. Although publicly available simulation packages lack validation for materials at the 10 eV scale, the ELOISE project is working to improve electromagnetic interaction simulations for $CaWO_4$ and $Al_2O_3$ [131].

Background descriptions from these simulations can be integrated into the framework for obtaining DM results based on a profile likelihood ratio test [132]. However, since not all backgrounds are understood (see Sec. 1.3.1), CRESST's reported DM exclusion limits to date are conservatively calculated using the Yellin method [133, 134], treating all events in the acceptance region as potential signals.

The intrinsic radiopurity of the crystals plays a significant role in determining background levels [130], and the optical properties of the target influence the available scintillating light for particle identification [135]. The $CaWO_4$ crystals used in CRESST are

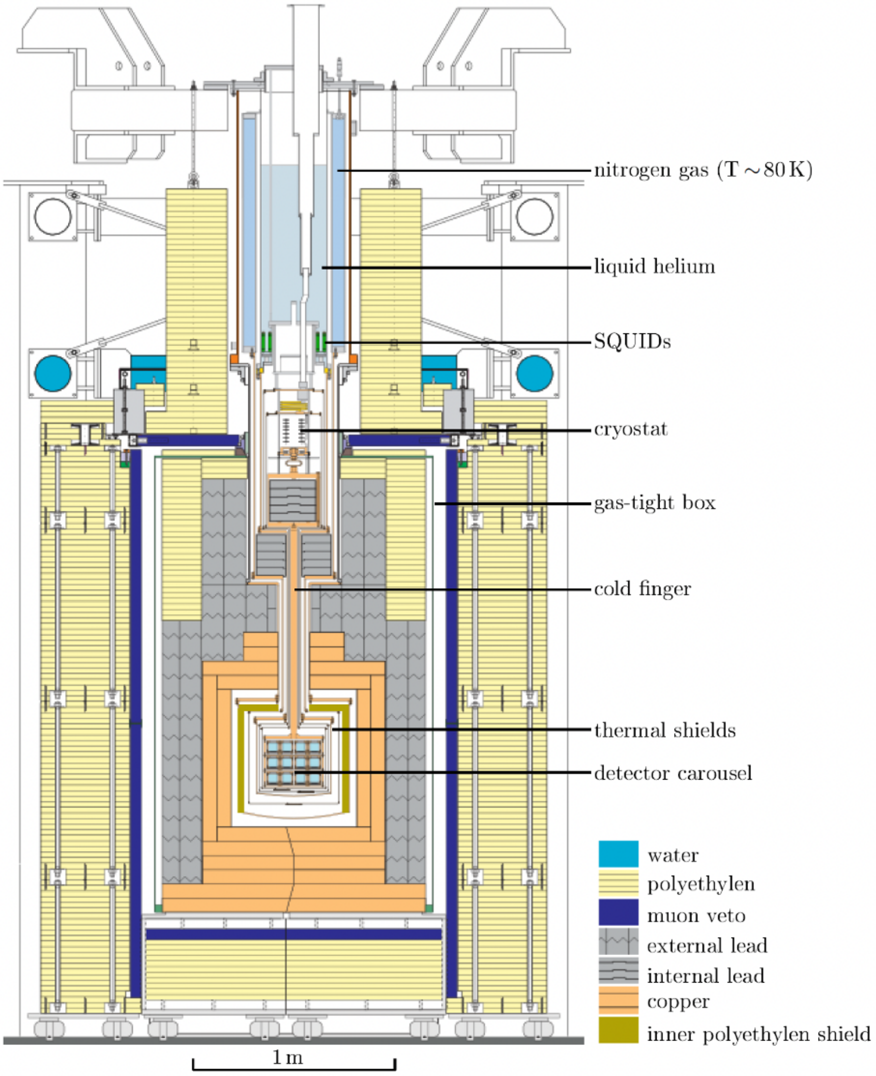

Figure 1.7.: Scheme of the setup of the CRESST experiment at LNGS. The detectors are mounted in a so-called carousel and operated inside a dilution cryostat providing temperatures below 10 mK coupled to the courusel via the copper cold finger. Several layers of passiv shielding and active plastic scintillator muon veto are surrounding the detectors to shield them from the remaining backgrounds. Figure is taken from [125].

grown in-house at the Technical University of Munich [136], where strict control over production ensures high radiopurity, optical quality, and minimal lattice stress [137, 138]. In the most recent data-taking campaign, extensive chemical purification of raw materials further reduced $\alpha$-decay backgrounds by a factor of 6 compared to previous crystals [125, 139], making intrinsic radioactive contamination a subdominant component of the total background.

In the first CRESST-III data-taking campaign (2016-2018), a groundbreaking energy

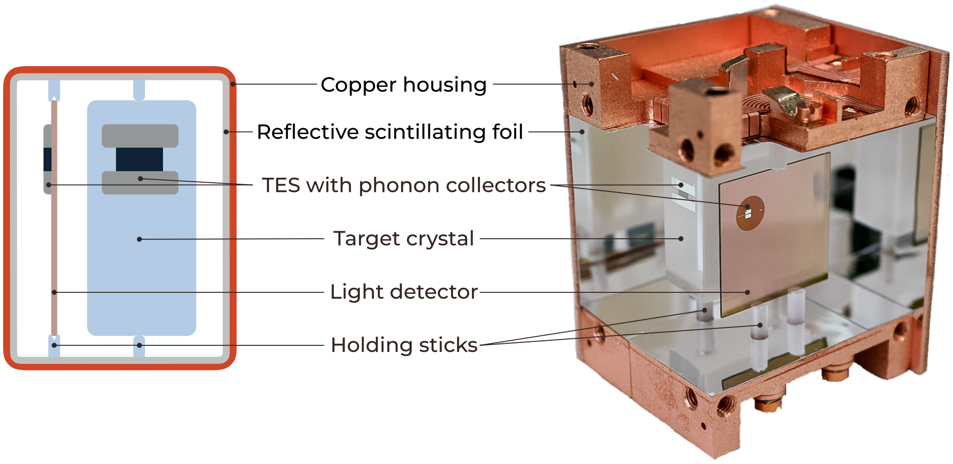

Figure 1.8.: Standard CRESST-III detector module featuring labeled main components. Left: schematic drawing, not to scale. Right: photograph of the module with two housing walls removed for better visibility, provided by the CRESST collaboration. The target crystal and wafer-shaped light detector are both equipped with a separate W-TES and mounted in a high-radiopurity copper housing. Reflective scintillating foil covers the housing walls to maximize light collection efficiency.

threshold of 30.1 eV was achieved with one of the operated 24 g $CaWO_4$ detectors [43]. This enabled CRESST-III to explore previously inaccessible DM parameter space for masses down to $0.16\,\mathrm{GeV/c^2}$, as illustrated by the solid red line in Fig. 1.6 [43]. To date, these results represent the most stringent limits on SI elastic scattering of DM particles with nuclei for sub-GeV masses as low as $0.165\,\mathrm{GeV/c^2}$.

During this first CRESST-III data-taking campaign, while achieving detection thresholds of $\mathcal{O}(10\,\mathrm{eV})$, an unexpected rise in the energy spectrum was observed below 200 eV, referred to as the Low-Energy Excess (LEE), discussed in Sec. 1.3.1. This LEE significantly affects the region of interest for DM particles with $m_\chi < 10\,\mathrm{GeV/c^2}$. Therefore, identifying the source of the LEE and mitigating its impact are key objectives of the ongoing CRESST experiment.

The subsequent CRESST-III data-taking campaign, which began in mid-2020 and concluded in early 2024, focused specifically on investigating the LEE. The flexibility of the CRESST technology allows for the use of different crystal materials as targets. In addition to $CaWO_4$, the experiment deployed detectors using $Al_2O_3$, $LiAlO_2$, and Si to examine the material dependence of the LEE. Modifications to the holding structures and module housing were also implemented. Investigating the LEE was a primary focus of this thesis, and the results are presented in Ch. 3.

Despite the LEE, CRESST-III achieved several new results on DM during this campaign using different target materials. The $LiAlO_2$ target includes three isotopes ($^{6}$Li, $^{7}$Li, and $^{27}$Al) that are sensitive to SD DM interactions. Using this crystal as an absorber, CRESST-III set the strongest limits to date on SD interactions of DM particles with protons and neutrons for masses between 0.25 and 1.5 GeV/c$^2$ [140].

In addition to their role as ancillary light collectors, the wafer detectors can also serve as primary targets. Due to their smaller size, they achieve lower detection thresholds, thereby extending sensitivity to lighter DM masses. A silicon wafer detector reached an energy threshold of 10.0 eV, and with data from this detector, CRESST-III significantly improved the limits for DM masses between 130 and 160 MeV/c$^2$, by up to a factor of 20 compared to previous results [6]. These limits are shown as the solid orange line in Fig. 1.6. The analysis of this detector was carried out as part of this thesis and is presented in Ch. 6. Additionally, a silicon-on-sapphire wafer detector achieved an even lower energy threshold, below 10 eV, enabling the exploration of DM masses below 100 MeV/c$^2$ [61].

Building on the insights gained from studying the LEE, CRESST has developed several new detector module designs for future data-taking campaigns [141], some of which have already been implemented in the run that began in 2024. In parallel, the collaboration is exploring new target materials. To enhance sensitivity to SD DM interactions with $CaWO_4$ targets, CRESST is currently investigating the feasibility of enriching the crystals with $^{17}O$ [142]. Another promising candidate material is diamond, which, due to its high Debye temperature, offers superior phonon propagation properties. A diamond crystal used as a cryogenic detector in a surface facility achieved an energy threshold of 16.8 eV, demonstrating significant potential for sub-GeV dark matter searches [62, 63].

Simultaneously, a major upgrade to the CRESST experimental setup at LNGS is underway, aiming to expand the number of available readout channels. New SQUIDs and wiring have already been acquired, while the development of the new data acquisition system and electronics is in the pre-production phase. This upgrade is expected to result in a total of 288 readout channels, significantly increasing the number of detectors that can be operated simultaneously and thereby boosting the achievable exposure.

### 1.2.2. Coherent elastic neutrino-nucleus scattering

Neutrinos remain a subject of interest in nuclear physics, particle physics, and cosmology, with many unanswered questions such as the nature of neutrino masses, whether neutrinos are their own antiparticles, and the potential existence of more than three types of neutrinos. These unresolved issues have profound implications for the Standard Model (SM) of particle physics and could pave the way for new physics paradigms. While major progress has been made in understanding neutrinos, particularly through the discovery of their mass and mixing [143, 144], further experimental exploration is required to extend the SM accordingly. One of the most promising processes for advancing this understanding is Coherent Elastic Neutrino-Nucleus Scattering (CE$\nu$NS), predicted 40 years ago [145]. In this process a neutrino scatters off an entire nucleus via the weak neutral current. CE$\nu$NS occurs when the momentum transfer during the interaction is small enough that the neutrino interacts with the entire nucleus as a whole, enhancing the cross-section by a factor proportional to the square of the neutron number, $N^2$, allowing even small-scale experiments to detect significant neutrino signals.

The theoretical prediction of CE$\nu$NS is firmly grounded in the SM of particle physics. The differential cross-section $\sigma$ of a neutrino with the energy $E_\nu$ scattering coherently and elastically off a target nucleus of the mass $m_N$ can be expressed as a function of nuclear recoil energy $E_R$ as:

$$\frac{d\sigma}{dE_R} = \frac{G_F^2}{4\pi} Q_W^2 m_N (1 - \frac{m_N E_R}{2E_\nu^2}) F^2(E_R), \tag{1.7}$$

where $Q_W$ is the weak charge of the target nucleus, $G_F$ is the Fermi coupling constant, and $F(E_R)$ is the nuclear form factor, which, like for DM-nucleus scattering, can be parametrized with the Helm approach [92, 93]. The weak charge $Q_W = N - Z(1 - 4sin^2\theta_W) \approx N$, where Z and N is the number of protons and neutrons respectively, and $sin^2\theta_W \approx 0.223$ [146] is the weak mixing angle. Thus $\sigma \propto N^2$.

The importance of CE$\nu$NS lies in both its relevance to understanding fundamental neutrino interactions and its potential as a probe for physics beyond the Standard Model (BSM). Measuring CE$\nu$NS provides a unique tool for studying several important parameters, including:

- **Weak mixing angle**: Due to the significant suppression of the proton contribution, the neutrons predominantly contribute to the CE$\nu$NS cross-section. However, precise measurement of this suppression enables constraints on the weak mixing angle.
- **Physics Beyond the Standard Model (BSM)**: Deviations from the predicted CE$\nu$NS cross-section can indicate new physics. For instance, non-standard neutrino interactions would modify the cross-section and recoil spectrum, providing constraints on potential BSM scenarios [147].
- **Neutrino Magnetic Moment and Charge Radius**: Precise CE$\nu$NS measurements provide insights into the neutrino's charge radius and can constrain the neutrino magnetic moment, which would introduce a new scattering channel beyond the weak interaction [148–150].
- **Light Mediators**: CE$\nu$NS experiments can also be sensitive to new light mediators, which would alter the momentum transfer behavior. For instance, light scalar or vector mediators coupling neutrinos to quarks would impact the interaction at low recoil energies [151–153].
- **Backround for direct DM searches**: CE$\nu$NS from solar and atmospheric neutrinos poses the ultimate background for WIMP direct detection experiments, as they cannot be shielded and generate recoil signals with the same detection signature, similar rates and energy spectra [154–157]. Large-scale noble-liquid gases detectors are already starting entering the neutrino floor region, while the cryogenic detectors are expected to be there in several years. Precise measurements of CE$\nu$NS process can serve as an input to the DM experiments in mitigating this background [115].

#### 1.2.2.1. CE$\nu$NS detection

Artificial neutrino sources provide experimental control for studying coherent elastic neutrino-nucleus scattering (CE$\nu$NS), offering advantages over naturally occurring neutrino sources, such as solar, amospheric or supernova neutrinos.

**Stopped-pion sources** at accelerators facilities produce neutrinos as their by-products through pion decay at rest ($\pi^+ \to \mu^+ \nu_\mu$), followed by the muon decays ($\mu^+ \to e^+ \nu_e \bar{\nu}_\mu$) with well-predicted energy distributions. This, together with the high energies of produced neutrinos (up to 53 MeV) and timing information, makes them convenient for CE$\nu$NS detection due to high induced recoil energies ($\mathcal{O}(1\,\text{keV})$ and higher) [158, 159]. However, in this regime a loss of full coherence is starting and a special care has to be taken for the neutron background mitigation [160].

The first observation of CE$\nu$NS was made by the COHERENT collaboration in 2017 using a CsI[Na] scintillation detector exposed to neutrino emissions produced at the Spallation Neutron Source (SNS) at Oak Ridge National Laboratory [160]. Fig. 1.9 displays the observed excess of counts during the "Beam ON" period and their arrival times. With an expanded dataset, the precision of CE$\nu$NS cross-section measurements has recently been improved [161]. Additionally, COHERENT has recently observed CE$\nu$NS with argon [162] and germanium [163] nuclei. A variety of target materials used allows demonstrating the expected $N^2$-dependence of the CE$\nu$NS cross-section.

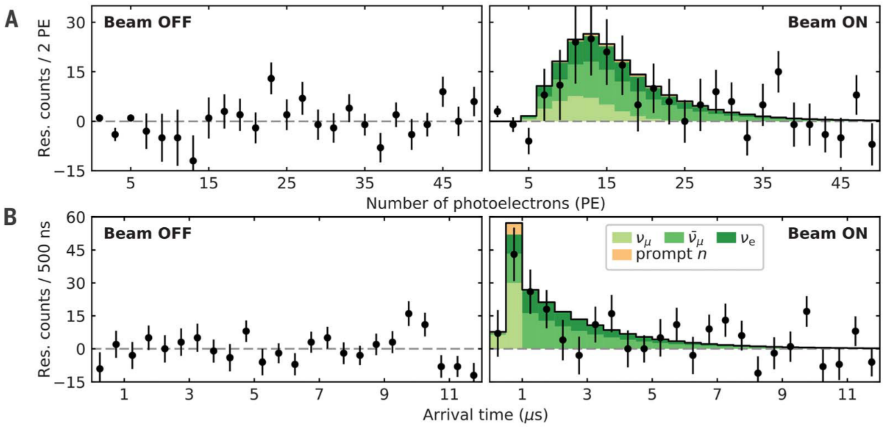

Figure 1.9.: First observation of CE$\nu$NS made by the COHERENT collaboration [160]. Residual differences (data points) between CsI[Na] signals recorded in the 12 ms following a beam trigger and those from a 12 ms window prior, as a function of (A) their energy (number of detected photoelectrons) and (B) event arrival time. Steady-state environmental backgrounds contribute equally to both groups of signals, canceling out in the subtraction. These residuals are shown for 153.5 live days of SNS inactivity ("Beam OFF") and 308.1 live days of neutrino production ("Beam ON"), during which 7.48 GWh of energy (~$1.76 \cdot 10^{23}$ protons) was delivered to the mercury target. An excess matching the SM prediction (shown as colored histograms in the right panels) is observed at a significance of $6.7\sigma$. The figure is taken from [160].

**Radiogenic sources**, such as beta-decaying isotopes (e.g., $^{51}$Cr [164, 165] or $^{144}$Ce [166]) producing antineutrinos, offer the ability to place the source near the detector underground to achieve low-background level. However, the low neutrino energies (<3 MeV) and relatively low produced fluxes require both ultra-low detection thresholds and large target masses, which are hard to relize at the current state of experimental techniques.

**Nuclear reactors**, on the other hand, provide a continuous strong neutrino flux by emitting electron antineutrinos during the fission process with an average of 6.7 $\bar{\nu}_e$ per fission [167]. An expected neutrino flux $\Phi_\nu$ at 40 m from a nuclear reactor of 4 GW power calculated according to [167] is exemplarily shown as a function of neutrino energy $E_\nu$ in Fig. 1.10a. As can be seen, a majority of the produced antineutrinos have an energy of a few MeV, with a high energy tail extending to higher energies.

An expected differential recoil rate ${}^{dR}/_{dE_R}$ from the given neutrino flux can be calculated using the differential cross-section from Eq. 1.7 as:

$$\frac{dR}{dE_R} = \int_{E_\nu^{min}}^{\infty} dE_\nu \Phi_\nu(E_{nu}) \frac{d\sigma}{dE_R}(E_\nu), \tag{1.8}$$

where $E_\nu^{min} = \sqrt{E_R M c^2/2}$ is the minimal neutrino energy required to produce a recoil energy $E_R$. Fig. 1.10b shows the expected differential recoil rate in a CaWO$_4$ target normalized to the detector mass if it experiences the flux shown in Fig. 1.10a. A $N^2$ boost of the cross-section results in up to two orders of magnitude higher rate for heavier tungsten nuclei in comparison to calcium. However, from Fig. 1.10a also shows that to benefit from this boost, low energy thresholds below 100 eV are required. Additionally, the neutrino flux scales linearly with the reactor power and as ${}^{1}/_{R^2}$ with the distance from it, therefore there is a trade-off between sufficient distance from the reactor to avoid reactor-correlated neutrons [168] and enough proximity to still get a high neutrino flux.

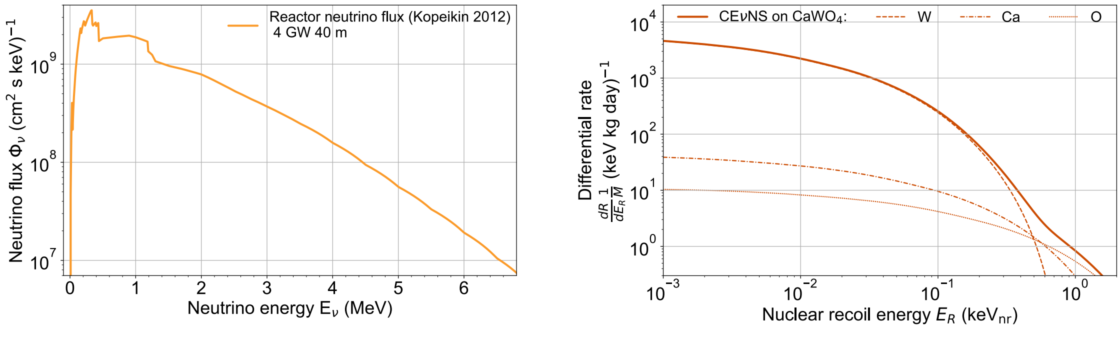

(a)

(b)

Figure 1.10.: (a) Reactor antineutrino flux predicted at 40 m distance from a reactor of 4 GW thermal power calculated according to [167]. (b) Expected differential rates of nuclear recoils induced by CE$\nu$NS from neutrino flux shown in panel (a) in a CaWO$_4$ target (solid line). Individual contributions from scattering with tungsten, calcium, and oxygen nuclei are shown with dashed, dash-dotted, and dotted lines respectively.

Nowadays plenty of experiments are operating or in preparation to measure CE$\nu$NS from reactor neutrinos.

**The TEXONO experiment** operates at the Kuo-Sheng Nuclear Power Plant in Taiwan, located about 28 meters from the 2.9 GW reactor core. The experiment uses $p$-type point-contact high-purity germanium detectors with an active mass of 1.06 kg to search for CE$\nu$NS interactions. Recent data sets of 65 kg-d, have enabled new limits on the CE$\nu$NS cross-section [169]. Future plans include extending the sensitivity to lower energy thresholds and expanding the detector mass.

**The CONUS experiment** operates four $p$-type point contact high-purity germanium detectors, previously located 17.1 m from the 3.9 GW commercial nuclear power plant in Brokdorf, Germany. A data set of 248.7 kg-d enabled the setting of constraints on the CE$\nu$NS cross-section [170]. Following the shutdown of nuclear power plants in Germany, the next phase of the experiment, CONUS+, is taking place at the 3.6 GW Leibstadt Nuclear Power Plant in Switzerland, situated about 20 m from the reactor core [171].

**The $\nu$GeN experiment** is conducted at the Kalinin Nuclear Power Plant in Russia, positioned about 12 meters from the 3.1 GW reactor core. The experiment uses a high-purity germanium (HPGe) detector with a mass of 1.4 kg. In recent measurements of above 1200 kg-d of exposure, no CE$\nu$NS signal was observed, thus providing constraints on CE$\nu$NS interactions. The experiment continues to accumulate data to explore CE$\nu$NS and study neutrino electromagnetic properties [172].

**The CONNIE experiment**, located approximately 30 m from the 3.95 GW Angra 2 reactor at the Almirante Álvaro Alberto Nuclear Power Plant in Brazil, uses CCDs with an active mass of 47.6 g to search for CE$\nu$NS interactions. The first data set, amounting to 2.1 kg-d, was used to set limits on CE$\nu$NS interactions [173]. The experiment is continuing its search for neutrino interactions and physics beyond SM with more sensitive Skipper CCDs [174].

**The RICOCHET experiment** is aiming to measure CE$\nu$NS at 8.8 meters away from the 58 MW research reactor at Institut Laue-Langevin (ILL) facility in Grenoble, France [24]. The experiment is developing two different types of detector arrays in parallel: the CryoCube and the Q-Array, each employing advanced cryogenic detection technologies.

The CryoCube consists of an array of 27 (3×3×3) NTD-based high-purity germanium detectors, with each detector of 38 grams, providing a total target mass of around one kilogram. Discrimination between electron and nuclear recoils is achieved through the ionization-to-heat ratio, with an anticipated particle identification threshold of about 100 eV. This is made possible by the combination of 10 eV heat baseline resolution and 20 $\mathrm{eV_{ee}}$ (electron-equivalent) ionization baseline resolution. Prototype measurements have already achieved an average baseline resolution of 22 eV in the heat channel [175] and 30 $\mathrm{eV_{ee}}$ in the ionization channel [25].

In parallel, the Q-Array detectors are being developed within the RICOCHET experiment. These detectors utilize novel TES technology thermally coupled to the absorber via gold wire bonds. Initial characterization of a Q-Array-style detector using a 1-gram silicon absorber achieved a baseline resolution of less than 40 eV [176]. Additionally, ongoing research is focused on employing superconducting absorbers to further improve electron/nuclear recoil discrimination through pulse shape analysis.

In 2024, the Ricochet experiment began its commissioning phase at ILL, marking a significant milestone in the development of CE$\nu$NS detection technologies.

**The MINER experiment** employs gram-to-kilogram scale cryogenic detectors with germanium, silicon, and $Al_2O_3$ absorber crystals developed from TES-based SuperCDMS technology [50] capable of reading both phonon and ionization signals, benefiting from the NTL phonon amplification. With this technology, detection thresholds of 100 eV and below are anticipated [177, 178]. The MINER experiment is located a few meters from the core of the 1 MW nuclear reactor at the Nuclear Science Center (NSC) at Texas A&M University [179].

Due to the broad scientific potential, the search for CE$\nu$NS has seen rapid development in recent years, with many new experiments joining the effort. Consequently, the list above is not exhaustive; a recent review of experimental efforts can be found in [180].

Another CE$\nu$NS experiment located at nuclear reactor is NUCLEUS which is described in more details in the next section.

#### 1.2.2.2. The NUCLEUS experiment

The NUCLEUS experiment, proposed in 2017 [181], aims to observe CE$\nu$NS from reactor antineutrinos at the Chooz B Nuclear Power Plant in France [44]. The experiment is designed to detect sub-keV nuclear recoils with TES-based ultra-low threshold cryogenic detectors with sapphire ($Al_2O_3$) and calcium tungstate ($CaWO_4$) absorbers.

The experimental setup, located in the "Very Near Site" (VNS) laboratory, is positioned 102 and 72 meters from two 4.25 GW reactor cores, ensuring a high neutrino flux of $1.7 \cdot 10^{12}\ \nu/(\mathrm{s\ cm}^2)$ [45]. Due to the shallow overburden of approximately 3 m.w.e., sophisticated shielding strategies are required to mitigate cosmic-ray-induced backgrounds. Multiple layers of active and passive shielding shown in Fig. 1.11 are installed, starting with plastic scintillator muon veto (MV) panels read out by optical fibers and Silicon Photomultipliers (SiPMs) [182]. To achieve nearly 100% geometrical efficiency, an additional cryogenic muon veto is installed at the 800 mK stage inside the cryostat, ensuring full $4\pi$ coverage [183].

Next passive shielding layers include a 5 cm thick lead layer to shield against gamma radiation and a 20 cm thick borated polyethylene layer to moderate and attenuate neutrons. Furthermore, an up-to-4 cm thick boron carbide ($B_4C$) layer inside the cryostat captures slow and thermal neutrons resulting from atmospheric neutron interactions with the outer shielding. The shielding system can be opened easily to access the cryostat, thanks to a mechanical system integrated into the design.

Inside the cryostat, active cryogenic veto systems surround the target detectors. The Cryogenic Outer Veto (COV) consists of six high-purity germanium crystals, read out in ionization mode with a threshold of about 10 keV. This system provides full $4\pi$ coverage, shielding against external backgrounds, such as ambient radioactivity and atmospheric muons. Prototype testing confirmed the feasibility of operating the COV in

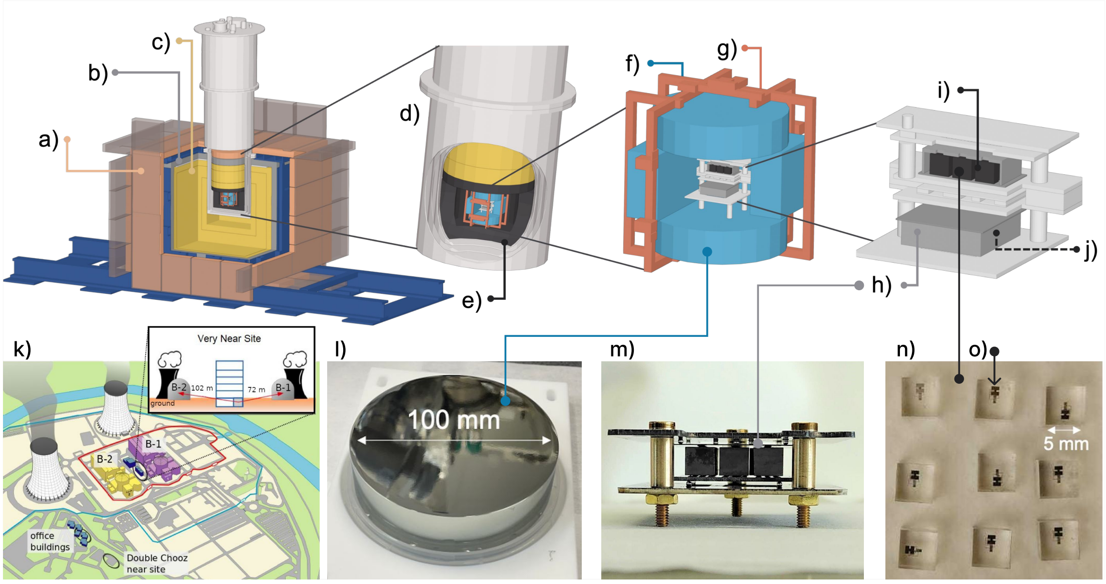

Figure 1.11.: **Top panel:** CAD drawing of the NUCLEUS experiment components. From left to right, the full NUCLEUS setup is shown with the shielding on rails (dark blue), allowing it to be opened for access to the inner part. The external multi-layer shielding includes: 28 5 cm thick plastic scintillator muon veto panels (a) read out by optical fibers and Silicon PhotoMultipliers (SiPMs), a 5 cm thick lead layer (b), and a 20 cm thick borated polyethylene layer (c). Inside, the dry dilution refrigerator (d) contains a 4 cm thick boron carbide layer (e) and the cryogenic outer veto (f), consisting of six 2.5 cm thick high-purity germanium ionization detectors housed in a copper cage (g), surrounding the cryogenic target detectors. The target detectors are arranged in two levels of nine cubes each made from $CaWO_4$ (i) and $Al_2O_3$ (j). These cubes are fully enclosed by the silicon inner veto (h) equipped with a TES. **Lower panel:** The position of the “Very Near Site”, where the NUCLEUS experiment will be located, in relation to the Chooz reactor cores (k); a photograph of one of the germanium cryogenic outer veto crystals (l); the silicon inner veto prototype with nine silicon detector dummies (m); nine $CaWO_4$ target cubes (n) cut from a larger crystal after TES production (o). See Fig. 4.2a for the picture of the crystal before cutting. The figures are adapted from [44, 45].

anti-coincidence mode with the target detectors [184]. The final cylindrical crystals have been prepared, tested, and validated [185], while the rectangular crystals are still under preparation [45]. The COV and cryogenic detectors are housed in a copper cage suspended on a spring system to isolate them from cryostat vibrations [185, 186].

Within the COV, the silicon-based inner veto (IV) provides another active layer surrounding the cryogenic detectors. The IV consists of a silicon beaker and wafer, each equipped with TES, aiming for sub-keV thresholds. The $4\pi$ coverage ensures effective discrimination of surface backgrounds by running in anti-coincidence mode. As the IV also serves as the mechanical support for the crystals, it can identify holder-related events. A prototype IV (Fig. 1.11m), consisting of two silicon wafers, operated with a $CaWO_4$

cube, achieved baseline energy resolutions of 13.4 eV and 9.1 eV [40, 187]. A dedicated veto cut successfully removed low-energy events, as will be discussed in Sec. 4.1.

The target detectors are gram-scale cryogenic calorimeters with $CaWO_4$ and $Al_2O_3$ absorbers. The readout is based on tungsten TES with phonon collectors (Fig. 1.2), adopted from the CRESST experiment (Sec. 1.2.1.2), using a SQUID-based system as shown in Fig. 1.3. NUCLEUS leverages the $N^2$-dependence of the CE$\nu$NS cross section by employing a multi-target approach, with 9 $CaWO_4$ cubes (6 g in total) for CE$\nu$NS detection on heavy tungsten nuclei and 9 $Al_2O_3$ cubes (4 g in total) for in-situ background measurement [45]. A 0.5 g prototype $Al_2O_3$ detector achieved a threshold of 19.7 $eV_{nr}$ [59]. Such low energy threshold allows accessing high rates of nuclear recoils at $\mathcal{O}(10\,\mathrm{eV})$-scale (Fig. 1.10b). In the region of interest, between 20 and 100 eV, a total counting rate of 30 $\nu$/(kg day) above particle background of 100 counts/(kg day kev) predicted by the GEANT4 simulations of the full NUCLEUS setup is expected[2].

The NUCLEUS experiment plans to use an LED-based calibration and nuclear recoil calibration method based on thermal neutron capture described in Sec. 1.3.2.

Several key milestones have already been achieved on the path of NUCLEUS to detecting CE$\nu$NS at Chooz.

At the Technical University of Munich (TUM), the full NUCLEUS setup has been successfully commissioned and tested. In summer 2024, the first long background run was performed with target detectors operated simultaneously with the COV and MC systems. All the systems have reached the expected performance and analysis is currently ongoing. Meanwhile, the VNS laboratory at Chooz is now fully prepared for the experiment, with relocation and the first technical run scheduled for 2025. Simulations and the background budget for NUCLEUS at Chooz have been finalized [188], with a publication forthcoming.

Meanwhile, to study the low energy excess (Sec. 1.3.1), a novel double-TES detector design, where one target is equipped with two sensors, has been adopted for the NUCLEUS target detectors. The first measurements revealed the multi-component nature of the observed excess and are presented in Ch. 4 of this thesis. This study shows the benefits of adjusting the final target detector design to double-TES readout for the NUCLEUS physics runs at Chooz.

In a dedicated measurement by the CRAB and NUCLEUS collaborations, a NUCLEUS $CaWO_4$ detector was irradiated with a neutron source, resulting in the first observation of a 100 eV nuclear recoil peak induced by thermal neutron capture [5]. Such monoenergetic nuclear recoil peaks offer a promising method for direct nuclear recoil calibration in the region of interest of CE$\nu$NS detectors [189], discussed in detail in Ch. 5.

---

[2] As will be discussed in Sec. 1.3.1 solid-state cryogenic experiments are currently observing an excess of events in the sub-keV region above the predicted particle backgrounds.

## 1.3. Challenges of low-threshold cryogenic detectors

Despite the excellent sensitivity of low-threshold cryogenic detectors and their broad range of scientific applications, these detectors still face significant challenges, which are the focus of this thesis. The excess of events observed at low energies, discussed in Sec. 1.3.1, currently represents the primary factor limiting sensitivity. Additionally, precise calibration of low-energy nuclear recoils, as outlined in Sec. 1.3.2, remains crucial for advancing the understanding of detector response in this range.

### 1.3.1. Low-energy excess

The rapid advancements in low-threshold detector technology over the past decade have opened up new energy ranges, unveiling previously unobservable backgrounds. These effects, while varying across detectors, commonly manifest as a steep rise in signal at energies below a few hundred eV, often referred to as the low-energy excess (LEE) [2]. Such LEEs have been observed using different target materials and sensor technologies in both underground and surface facilities [2]. These spectral features, which significantly exceed expected background contributions in the region of interest of low-threshold experiments, now represent one of the key challenges in improving sensitivity for light DM and CE$\nu$NS detection.

The widespread importance of LEEs has led to the establishment of a series of international EXCESS workshops by the DM and CE$\nu$NS communities, aimed at fostering in-depth discussions and collaboration across the communities to better understand and address the observed phenomena [190]. The first iteration took place in 2021 and resulted in the first joint white paper from the community to present the current state of the LEE observations [2]. By now, four more iterations have taken place, encouraging a continuous discussion among the collaborations [191–194].

Fig. 1.12 presents selected recoil energy spectra from various experiments observing the LEEs shared by the collaborations with the EXCESS initiative [195]. The datasets are categorized by their energy units: total energy deposition measured by phonon-based detectors are used in Fig. 1.12a for the CRESST-III [43], EDELWEISS RED20 [22], MINER [196], NUCLEUS [197], and SuperCDMS-CPD [56] experiments; and electron-equivalent energy for the DAMIC [198], EDELWEISS RED30 [23], SENSEI [199], Skipper-CCD [173], and SuperCDMS-HVeV [53, 54] experiments measuring ionization. Although conversion between these units is well understood for most detector materials, comparing results from experiments sensitive to both electron and nuclear recoils depends on the validity of the assumed interaction model since the amount of produced signal depends on the interaction type, unknown for the LEEs. Moreover, since the detected events are often indistinguishable from genuine particle recoil signatures but may not always originate from particle recoils, the energy scales must be rather interpreted in terms of "particle recoil equivalent" energy deposition.

All spectra are standardized to daily rate units, i.e. counts/(keV kg day), a typical scaling for DM and CE$\nu$NS searches since the expected signal scales with exposure. How-

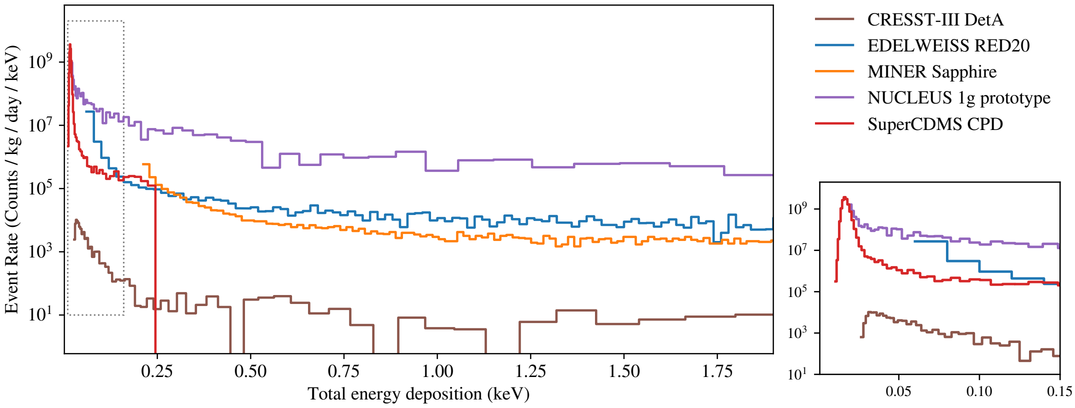

(a) Energy spectra of measurements with units of total energy deposition. The apparent peaks in the CRESST/SuperCDMS CPD data at 30 eV/20 eV are caused by the trigger threshold.

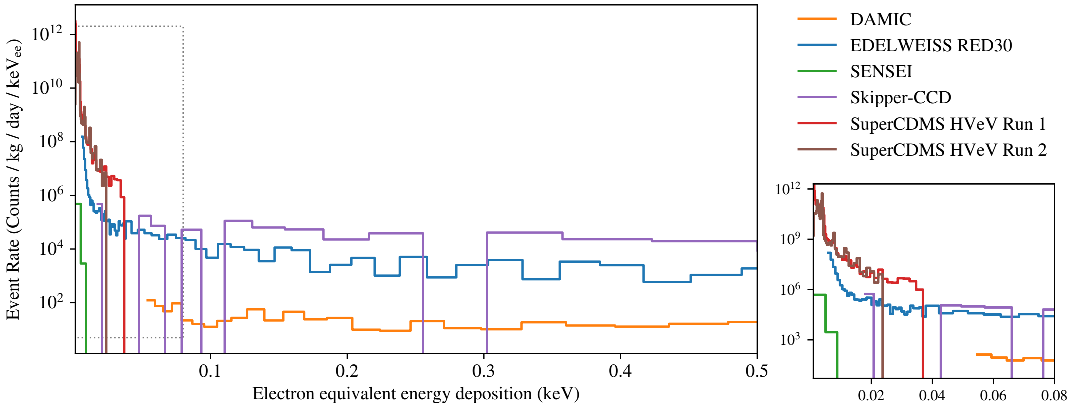

(b) Energy spectra of measurements with units of electron equivalent energy deposition.

Figure 1.12.: (a,b) Energy spectra of excess observations from the individual experiments. In all energy spectra, the rise at low energies is visible. Right: Zoom into the excess region of the spectra. The details of each data set are provided in Tab. 1.1. Figures taken from [2, 195].

ever, it is not given that this scaling is optimal for identifying the origin of the LEEs, as it may scale with factors such as surface area or measurement time rather than exposure alone. Tab. 1.1 provides a summary of key properties of the measurements displayed in Fig. 1.12, including target mass, material, sensor type, exposure, operating temperature, and overburden.

Due to the variations in signal shape, rate, and time dependency across different experiments, detectors, and measurements, a common particle-based explanation, such as DM scattering, appears unlikely, even under non-standard scenarios. A similar conclusion was reached in [200], where data from the EDELWEISS and SuperCDMS experiments

| Measurement | Target | Sensor | Exposure (kg days) | Operation Temperature | Depth (m.w.e.) |
|---|---|---|---|---|---|
| CRESST III DetA | 23.6 g $CaWO_4$ | Tungsten TES | 5.594 | 15 mK | 3600 (LNGS) |
| EDELWEISS RED20 | 33.4 g Ge | NTD | 0.033 | 17 mK | above ground |
| MINER Sapphire | 100 g $Al_2O_3$ | QET | 2.72 | 7 mK | above ground |
| NUCLEUS 1g prototype | 0.49 g $Al_2O_3$ | Tungsten TES | 0.0001 | 15-20 mK | above ground |
| SuperCDMS CPD | 10.6 Si | QET | 0.0099 | 41.5 mK | above ground |
| DAMIC | 40 g Si | CCDs | 10.927 | 140 K | 6000 (SNOLAB) |
| EDELWEISS RED30 | 33.4 g Ge | NTD, NTL amplification | 0.081 | 20.7 mK | 4800 (LSM) |
| SENSEI | 1.926 g Si | Skipper CCD | 0.0955 | 135 K | 225 (Fermilab) |
| Skipper CCD | 0.675 g Si | Skipper CCD | 0.0022 | 140 K | above ground |
| SuperCDMS HVeV Run 1 | 0.93 g Si | QET, NTL amplification | 0.00049 | 33-36 mK | above ground |
| SuperCDMS HVeV Run 2 | 0.93 g Si | QET, NTL amplification | 0.0012 | 50-52 mK | above ground |

Table 1.1.: Key properties of the measurements presented in Fig. 1.12. The first part contains the experiments shown in Fig. 1.12a, and the second part corresponds to Fig. 1.12b. Table taken from [2].

were compared using a nuclear recoil form factor fitted to the observations. In [201], the possibility of a dark matter origin via plasmon scattering was explored, but this hypothesis was later ruled out by studies in [202, 203]. Meanwhile, [204] proposed testing the recoil origin through material-dependent energy loss due to crystal defects.

Notably, the origins of the LEE appear to differ between phonon-sensitive and charge-sensitive detectors. This thesis focuses specifically on phonon-based LEE observations.

Some unique, detector-specific sources have been identified as contributing to the observed LEEs. For instance, a significant contribution to the LEE in SuperCDMS-HVeV detectors was recently traced back to luminescence from the printed circuit boards used in the detector holders [205].

However, certain common characteristics are evident across LEEs measured by cryogenic phonon detectors. One shared feature is the time-dependent decay of the LEE event rate [3, 206, 207], with a notable increase following thermal cycles to temperatures around tens of Kelvin [3, 206]. Such thermal cycles involve a controlled or accidental warm up of the detectors followed by cooling them back to their operational temperatures near $\mathcal{O}(10\,\mathrm{mK})$, before resuming data collection. The CRESST collaboration performed dedicated temperature tests to study the rate behaviour partially done in the framework of this thesis and the results are shown and discussed in Sec. 3.2.4.

To date, no radiogenic origin has been found for the LEEs, and such sources are largely ruled out as major contributors given the strong dependence of event rates on thermal manipulations. Additionally, EDELWEISS collaboration findings suggest that the LEE probably has a non-ionizing origin [21, 69]. In response, the CRYOSEL project has proposed a novel method to tag athermal phonons produced via the NTL process to effectively reject non-ionizing events [208].

The cryogenic detectors community is thus currently focused on investigating solid-state phenomena, such as stress relaxation processes induced by detector elements, thermal expansion, or intrinsic crystal properties, as potential explanations for the LEEs and their observed behavior. It is generally thought that a non-equilibrium atomic or electronic configuration within the detector or its surrounding materials undergoes spontaneous rearrangement, relaxing into a lower energy state and transferring energy to the detector's phonon system. Mechanical stress can occur at various interfaces, including between the absorber and sensor, bonded or glued components, or supporting structures, however, the precise mechanism behind this process remains a topic of ongoing investigations.

Observations of the LEE rate increase after a warm up strongly supports the hypothesis of the differential thermal contraction is responsible for creating the non-equilibrium states that give rise to the LEE. When the detector materials cool back down to base temperature after being warmed up, they contract at different rates, potentially inducing stress and leaving the system in a non-equilibrium configuration. The relaxation of atomic structures is then thought to produce the phonons responsible for the LEE.

Recent work by the SPICE/HeRALD collaboration has shown that a crystal held under higher stress, due to a glue-based mounting system, exhibits a substantially higher LEE rate below 40 eV compared to a crystal suspended with bond wires, which minimizes stress from the holders [207]. Early work by the CRESST collaboration has shown that tight detector-holding configurations could create microfracture events in the crystal, releasing energies up to hundreds of keV and resembling the particle-like pulse shape. The resulting spectrum was increasing towards the low energies following a power law, however in much higher energy region accesseble back then [209].

Therefore, minimizing mechanical stress on the crystal is a key strategy for mitigating LEEs. Another approach to reduce LEE effects is to distinguish stress-induced events from actual particle recoils in the absorber. Both CRESST [141] and NUCLEUS [187] experiments have proposed active holding structures equipped with TES sensors. These allow simultaneous readout from both the holder and absorber, aiding in the identification of interface-originating events. Meanwhile, the segmented design of BULLKID monolithic detector arrays offers the ability to reject events originating outside individual crystal segments [210].

To further distinguish particle interactions occurring within the absorber, such as expected DM and CE$\nu$NS events, from sensor-related phenomena – like stresses introduced during thin-film fabrication or thermal expansion mismatches between the sensor and the crystal – multi-sensor phonon readout is currently under active investigation. First results from several independent measurements have revealed non-coincident LEE-like events associated with a single TES channel [4, 211, 212].

These observations may suggest that this stress could be caused by the materials used in TES, such as tungsten and aluminum, or their interfaces. Thin films can be considered a potential source of the LEE, due to the possibility of high stress induced during film deposition [213] or due to thermal expansion coefficient mismatch at the interfaces [214]. These stress sources can vary greatly between detectors and deposited films [215, 216]. Additionally, aluminum films, are proposed to contribute to LEE through the sudden relaxation of lattice dislocation defects [217]. However, further experimental evidence is needed to conclusively link sensor stress to the generation of the LEE. Although the exact physical mechanism behind these events remains unclear, excluding such non-coinciding events from the recorded energy spectra allows for partial suppression of the LEE. NUCLEUS double-TES measurements are discussed in Ch. 4.

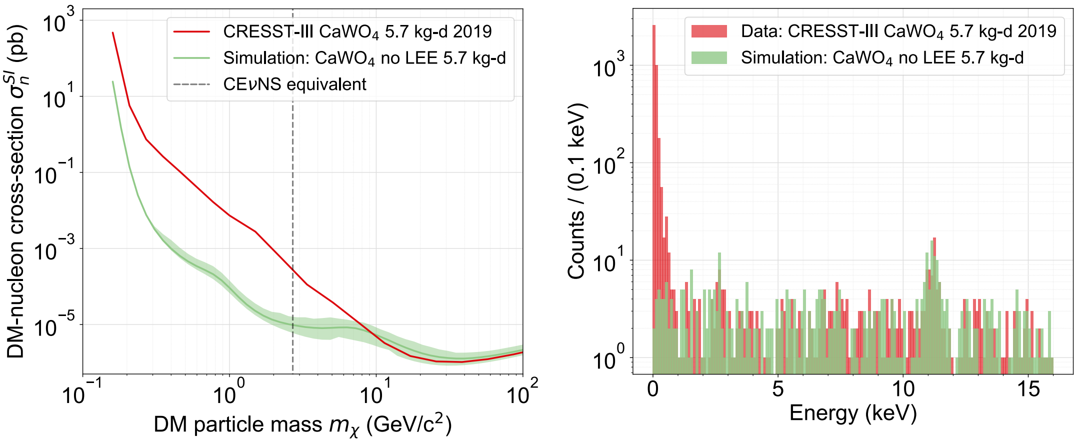

(a) (b)

Figure 1.13.: (a) Expected sensitivity of the CRESST-III 24 g $CaWO_4$ detector with a 30 eV threshold to SI elastic DM-nucleus scattering across various DM masses. The red line represents the upper limit on the interaction cross-section at a 90% confidence level, derived from data collected during the first CRESST-III data-taking campaign reported in [43]. The green line illustrates the limit obtained with a simulated spectrum that follows the measured one but is modified to exhibit a flat background level down to the threshold, showing the influence of the LEE on the sensitivity. The shaded area indicate the 90% confidence interval borders for the corresponding limits. For the simulated limits, the same detector performance as in [43] was assumed. (b) Comparison of the measured (red) and simulated (green) energy spectra.

Since the LEE populates the regions of interest for low-threshold solid-state cryogenic detectors, it remains the main obstacle to improving sensitivity for light DM and CE$\nu$NS detection. If the effects of the LEE are mitigated, a significant sensitivity improvement for $m_\chi < 10\,\mathrm{GeV/c^2}$ is anticipated. This effect is illustrated in Fig. 1.13. The measured energy spectrum with a CRESST-III $CaWO_4$ detector that led to the 2019 SI DM-nucleon interaction limits [43] was described with a likelihood framework for background modeling [132]. In this model, the LEE is approximated using an exponential function. The energy spectrum is then simulated according to this analytical description, excluding the LEE component. This simulated spectrum thus represents a scenario where the measured spectrum remains approximately flat down to the threshold while the other backgrounds are kept. Fig. 1.13b shows a comparison of the measured and simulated spectra. The DM exclusion limit, calculated at the 90% confidence level using the Yellin method [133, 134] for the simulated data – while maintaining the same detector performance and exposure as in [43] – is represented by the green line in Fig. 1.13a. For $m_\chi > 10\,\mathrm{GeV/c^2}$, the limit remains unaffected by the absence of the LEE, while for lighter DM, the sensitivity improves by up to two orders of magnitude.

Following the argument presented in [218], Fig. 1.13a additionally illustrates the impact of the LEE on CE$\nu$NS detection. The processes of direct DM detection and CE$\nu$NS are closely related, as both involve measuring low-energy nuclear recoils with similar spectral shapes. For example, the expected nuclear recoil energy spectrum from CE$\nu$NS, induced by reactor neutrinos, closely resembles that produced by a $2.7\,\mathrm{GeV/c^2}$ WIMP. Moreover, the interaction cross-sections for both processes scale coherently with the square of the neutron number (for DM, assuming $A \approx 2N$). This allows for a comparison of the LEE's impact on CE$\nu$NS sensitivity within the DM parameter space, assuming a DM mass of $2.7\,\mathrm{GeV/c^2}$.

For a $CaWO_4$ detector operating deep underground at LNGS, considered in Fig. 1.13a, the presence of the LEE degrades the CE$\nu$NS sensitivity by a factor of approximately 50. However, LEE rates measured at surface-level experiments, where most of the CE$\nu$NS experiments are conducted, have shown higher LEE rates. Consequently, the sensitivity improvement in the absence of the LEE would be more pronounced in such environments. On the other hand, the decaying nature of LEE rates suggests that the lower observed rates in underground experiments might be (partially) attributed to the extended cooldown times required due to shielding, as well as the later start of data-taking, compared to surface-level runs often dedicated to R&D. A more detailed discussion of these effects is provided in Sec. 4.1.

### 1.3.2. Calibration of low-energy nuclear recoils

Since both DM detection and CE$\nu$NS rely on observing nuclear recoils precise calibration of sub-keV nuclear recoils is crucial for these experiments. However, current low-energy calibration methods predominantly use electron recoils. For example, many experiments (e.g. [6, 22, 56, 59]) employ $^{55}$Fe sources that produce 5.9 keV and 6.5 keV lines, which are significantly higher than the region of interest for sub-GeV DM and CE$\nu$NS searches operating at eV-scale. To bridge this gap, in CRESST the detector response is mapped from these calibration lines to lower energies using artificially injected heater pulses, but this method assumes identical scaling between heater and particle pulses (see Sec. 6.4).

While this approach has proven to be effective, it still requires cross-calibration with an absolute energy scale based on different energy deposition mechanisms.

An extension of the method based on a $^{55}$Fe source can be realized using X-ray fluorescence (XRF). For instance, in a NUCLEUS measurement illustrated in Fig. 1.14a, a $CaWO_4$ detector was irradiated with a two-stage XRF source where a $^{55}$Fe source caused XRF in an aluminum target, producing lower-energy Al K$\alpha$ X-rays of 1.5 keV that then excite a second target made of various materials causing X-rays with even lower energies. This technique successfully provided calibration lines down to 677 eV from Fluorine $K_\alpha$, offering a detailed mapping of the detector's dynamic range [219]. However, the downside is that such sources populate the spectrum with additional lines, making them less suitable for in-situ calibration during rare-event searches.

Another effective method is the LED calibration, described e.g. in [220, 221] and illustrated in Fig. 1.14b, where an LED lamp shines on the absorber a controlled number of photons of a fixed energy. If the burst duration is significantly shorter than the signal rise time, the absorbed photons are perceived as a simultaneous energy input in the detector. Each burst consists of multiple photons of energy $E_p$, with an average number of absorbed photons denoted by $\langle N \rangle$.

The process of photon absorption follows Poisson statistics, leading to a standard deviation of $\sqrt{\langle N \rangle}$. For each phonon burst, the distribution of signal amplitudes is well-described by a Gaussian function with standard deviation $\sigma$. The relationship between $\sigma$ and the mean amplitude $\langle \text{Amplitude} \rangle$ is expressed as the combination of two uncorrelated terms added quadratically:

$$\sigma = \sqrt{\sigma_0^2 + R \cdot E_p \cdot \langle \text{Amplitude} \rangle} \tag{1.9}$$

where $\sigma_0$ represents the baseline noise energy resolution and $R$ is the energy calibration coefficient. By fitting the standard deviations of each peak against the measured amplitude using Eq. 1.9, the calibration coefficient $R$, which links the measured amplitude to energy, can be extracted. An advantage of this method is that no radioactive sources are located in vicinity of the detector and the energy of the calibration peaks can be adjusted.

While these methods offer reliable in-situ calibration, low-energy photons do not penetrate deep into crystals and often deposit energy near the surface. Certain crystals can be activated to produce calibration lines, providing a uniform distribution of events absorbed throughout the crystal bulk. For instance, when germanium is activated by a neutron source, the short-lived isotope $^{71}$Ge is produced, which decays via electron capture in the K, L, and M shells. This process generates de-excitation lines at 10.37, 1.30, and 0.16 keV, respectively [23]. Similarly, cosmogenic activation of $^{182}$W produces characteristic lines at 2.6 and 11.3 keV [43] in $CaWO_4$ detectors. However, this activation technique is only applicable to a limited range of target materials, and the resulting energies often exhibit low activity, with limited flexibility in adjusting the energy values for calibration.

All the methods mentioned so far rely on electron recoils, but understanding the detector's response to nuclear recoils, the signature of both DM and CE$\nu$NS, is essential. Below

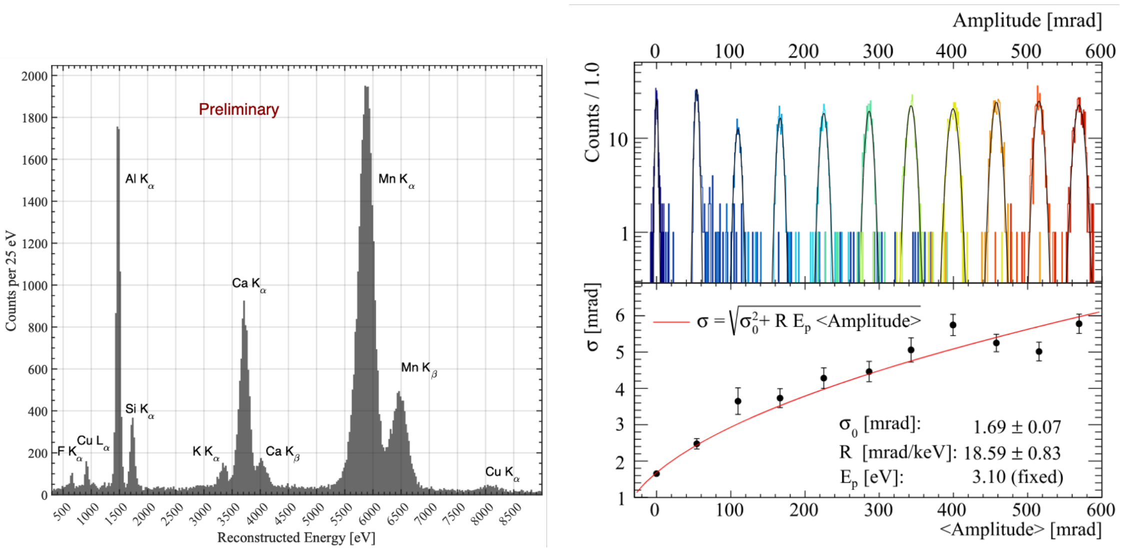

(a) Measured energy spectrum from the detector irradiated by a two-stage XRF-source described in the text. Various lines down to 677 eV are observed. Figure is provided by the NUCLEUS collaboration.

(b) Top: Distribution of the amplitude of the signals and Gaussian fits to the distributions for a controlled number of fast LED pulses shining increasing amounts of photons to the absorber. Bottom: Standard deviations versus their mean value (⟨Amplitude⟩) from the gaussian fits shown in the top panel. The red line shows the result of the fit of the dat with Eq. 1.9. Figure is taken from [220].

Figure 1.14.: Illustration of the the absolute energy calibration methods based on electronic recoils: (a) with an XRF source irradiating a NUCLEUS TES-based detector and (b) LED pulses shining on a CALDER KID-based detector.

several hundred eV, energy can be stored in crystal lattice defects, distorting the energy spectrum [222].

While neutrons pose a significant background by inducing nuclear recoils that can mimic the expected signal, they also provide a valuable tool for calibrating detector responses. Elastic neutron scattering off nuclei, combined with the measurement of the scattered neutron direction, produces nearly monoenergetic nuclear recoils, making this method widely used for calibration purposes. A comprehensive overview of neutron-based calibration techniques, including inelastic scattering and resonant photonuclear processes, can be found in [223].

A novel approach to directly calibrating low-energy nuclear recoils via thermal neutron capture was recently proposed by the CRAB collaboration [189]. For certain isotopes, when a nucleus captures a thermal neutron, the de-excitation process may involve the emission of a single MeV gamma, leading to a monoenergetic nuclear recoil. In the case of the $^{182}$W isotope, this process results in a nuclear recoil energy deposition of 112.5 eV. This monoenergetic nuclear recoil peak has been observed around the expected value in

$CaWO_4$ detectors, confirmed in a dedicated measurement by the CRAB and NUCLEUS collaborations [5], as presented in Ch. 5, and during neutron calibration campaigns of the CRESST-III experiment [224]. This method, combined with timing information [225], enables precise studies of the detector response across different target materials, such as $Al_2O_3$, Si, Ge, and $CaWO_4$. When used alongside electron-recoil sources, it significantly enhances the understanding of signal formation at low energies.

The precise calibration of low-energy nuclear recoils is vital for both reliable CE$\nu$NS measurements and potential DM discovery. It allows for accurate characterization of detector responses at the sub-keV scale, where potential signals from DM or CE$\nu$NS interactions are expected. In turn, these experiments enable the exploration of new physics beyond SM, offering opportunities to probe DM and study fundamental neutrino interactions with unprecedented sensitivity.

# 2. Data analysis workflow: from a data stream to an energy spectrum

Several measurements with the CRESST and NUCLEUS detectors are analyzed in the framework of this thesis. Since both experiments are based on the TES readout, the data formats are similar, and the first analysis steps often overlap. This chapter outlines the entire analysis workflow, from raw data processing to the final energy spectrum.

Sec. 2.1 provides a brief overview of the model for TES-based cryogenic particle detectors, including the expected pulse shape of the signal. Sec. 2.2 introduces the structure and format of the typical data collected. Sec. 2.3 explains the analysis process, covering triggering and pulse amplitude reconstruction. This is followed by Sec. 2.4, which discusses event selection. Sec. 2.5 focuses on the efficiency calculations for each analysis step, while Sec. 2.6 provides details on how the final detector performance parameters are evaluated.

## 2.1. Pulse-shape model

The simplified presentation of the working principles of cryogenic detectors in Sec. 1.1.1 and Fig. 1.1 assumes full thermal equilibrium between the absorber and sensor, neglecting the thermometer's properties. To fully describe the expected pulse shape in a TES-based cryogenic calorimeter, a detailed understanding of the signal formed by independent temperature systems like the absorber crystal, thermometer electrons, and phonons. This model was developed in [58].

The thermal system, shown in Fig. 2.1, consists of the heat capacities of the crystal ($C_c$) and thermometer electrons ($C_e$), both coupled to a thermal bath at temperature $T_b$ via thermal links $G_{cb}$ and $G_{eb}$, respectively. Since the thermometer is metallic, its electron heat capacity $C_e$ is proportional to temperature and is significantly larger than its phonon heat capacity, which is typically negligible.

The thermal coupling between phonons and electrons in the sensor, $G_{ep} \propto T^5$, is strongly suppressed at low temperatures due to electron-phonon decoupling. The transmission of thermal phonons at the interface between the thermometer and the absorber is defined by the Kapitza thermal conductance: $G_K \propto T^3$. The effective coupling between the sensor electrons and the absorber's thermal phonons can be expressed as $G_{ec} = (1/G_{ep} + 1/G_K)^{-1}$.

Due to the weak thermal coupling $G_{ec}$ between the crystal and the sensor, TES-based macrocalorimeters primarily detect athermal signals generated by particle interactions in the crystal. When a particle interacts, high-frequency optical phonons are produced, which quickly decay into acoustic phonons. These phonons propagate ballistically through the crystal until they thermalize at its surface. A fraction of these athermal phonons is absorbed by the TES film covering the crystal's surface, initiating the process shown in Fig. 1.2. The total power input is therefore split into two components: a direct signal from

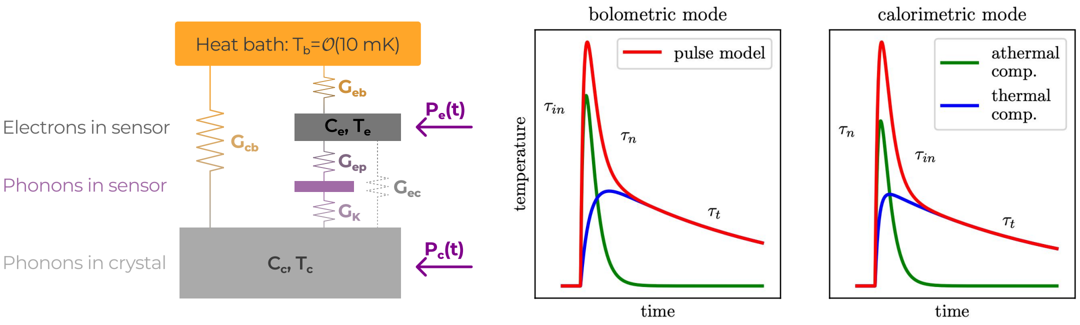

Figure 2.1.: Left: Schematic of the detector's thermal model adapted from [58]. $T_b$ represents the temperature of the heat bath, while $T_e$ and $T_c$ denote the temperatures of the electron system in the sensor and the phonon system in the crystal, respectively. $C_e$ and $C_c$ are their respective heat capacities, and $P_e$ and $P_c$ represent the power inputs from athermal phonons into the system. The thermal conductances are labeled with $G$. Right: Pulse models corresponding to Eq. 2.1, illustrating the bolometric regime ($\tau_{in} < \tau_n < \tau_t$, left) and the calorimetric regime ($\tau_n < \tau_{in} < \tau_t$, right). The relevant time scales are indicated on the pulses in each regime. The total pulse model (red) is the sum of the athermal component (green) and the thermal component (blue). The figure is taken from [40].

athermal phonons bypassing the weak coupling $G_{ec}$, modeled as a power input to the TES electrons ($P_e(t)$), leading to a temperature increase in the sensor, and a power input to the crystal ($P_c(t)$), leading to a secondary thermal component.

The temperature rise of the TES electron temperature, $\Delta T_e(t) = T_e(t) - T_b$, defines the observed change of the TES resistance and can be obtained by solving the differential equations for the power inputs $P_c(t)$ and $P_e(t)$ [58]. The overall pulse shape, governed by the coupled system of heat capacities and thermal conductances, is modeled as the superposition of two exponential functions with distinct rise and decay times, representing the athermal and thermal components of the signal.:

$$\Delta T_e(t) = \Theta(t - t_0) \cdot \left\{A_n \cdot \left(e^{-(t-t_0)/\tau_n} - e^{-(t-t_0)\tau_{in}}\right) + A_{th} \cdot \left(e^{-(t-t_0)/\tau_{th}} - e^{-(t-t_0)/\tau_n}\right)\right\}, \tag{2.1}$$

where

$\tau_{in} = {}^{C_e}/_{G_{eb}}$ is the relaxation timescale of the thermometer through the thermal link $G_{eb}$,

$\tau_t = {}^{C_c}/_{G_{ec}}$ is the relaxation timescale of the absorber crystal via the bottleneck $G_{ec}$,

$\tau_n$ is the athermal phonon lifetime, dependent on the thermalization timescales of the film and crystal surfaces,

$A_n$ is the amplitude of the athermal component, and

$A_{th}$ is the amplitude of the thermal component.

Depending on the relative order of the timescales ($\tau_{in}$, $\tau_n$, $\tau_t$), two operational regimes, illustrated on the right side of Fig. 2.1, are distinguished:

**Bolometric mode** ($\tau_{in} < \tau_n < \tau_t$): In this mode, the TES temperature stabilizes at a temporary equilibrium before the athermal energy input decays. The TES effectively measures the time-dependent power flux, and the pulse rise time is determined by $\tau_{in}$.

**Calorimetric mode** ($\tau_n < \tau_{in} < \tau_t$): Here, the thermometer begins to equilibrate only after the athermal energy input has finished. Thus the TES integrates over the total deposited energy, and the initial temperature rise is proportional to the total deposited energy ($A_n \propto \Delta E$). The rise time is described by $\tau_n$, while the fast decay component is determined by $\tau_{in}$.

In the current CRESST-III and NUCLEUS detectors, the calorimetric mode is preferred due to its improved energy resolution and signal response. Thus the amplitude of the measured pulses is proportional to the energy deposition into the crystal.

## 2.2. Data structure

Before introducing the analysis methods used in this thesis, this section provides a brief overview of the data formats and their typical content.

### 2.2.1. Data formats

In the CRESST and NUCLEUS experiments data from cryogenic detectors are usually recorded **continuously**. This minimizes deadtime and exploits advantages of offline triggering to minimize energy thresholds, which is critical for critical for the physics results. Additionally, continuous data collection allows for noise samples to be captured, facilitating the study of noise properties. Moreover, a **record window** - the length of the recorded waveform in samples - can be optimized in the specific analysis.

In CRESST, recording of a continuous data stream is handled by the Continuous Data Acquisition (CDAQ) system, described in [226]. This system operates two 16-bit resolution digitizers in parallel, alternating between sampling and reading out the data. The CRESST data discussed in Ch. 3 and 6 were recorded with a sampling frequency of 25 kHz.

In addition to continuous data, in CRESST also, pre-triggered or **hardware-triggered** data are recorded using a ring-buffer digitizer, as described, e.g., in [227]. After filtering, amplification, and shaping, signals that exceed a fixed threshold are saved to disk. This system was the primary data acquisition method in CRESST-I and II but is now mainly used for data monitoring and first analysis iteration, e.g., building template pulse and characterizing noise (Sec. 2.3).

The NUCLEUS experiment employs a next-generation Versatile Data Acquisition (VDAQ) system, developed specifically for cryogenic experiments like CRESST, COSINUS, and NUCLEUS, in HEPHY. VDAQ integrates detector optimization with data recording at sampling frequencies up to 1 MHz. The data presented in Ch. 4 and 5 were recorded using VDAQ.

When hardware-triggered data are unavailable, a simple trigger algorithm, based on the recorded signal exceeding a set number of standard deviations, can be used for the first manipulations with the data.

A continuous data stream of one run is typically stored in multiple files. A cryogenic **run** is defined as the period of time from cooling down a cryostat from room temperature to operating temperatures around 15 mK to warm-up. For CRESST, typical runs are usually long, above a year, and data-taking is regularly briefly interrupted for refilling cryogenic liquids in the wet cryostat, resulting in typical file lengths of about 50 hours. In NUCLEUS, which uses a dry cryostat, such interruptions are not required, and file lengths are determined by processing considerations or, in R&D runs, by the experimental schedule.

In addition to the data from the cryogenic detectors, additional files containing information from other systems, such as muon veto or general system monitoring parameters may ve available.

### 2.2.2. Data stream content

The data stream contains the voltage signal from the input coil of the SQUID operated in parallel with the TES as shown in Fig. 1.3. As discussed in Sec. 2.1, energy depositions in the target crystal, such as particle recoils, generate pulses in the data stream. In addition to these events, artificial voltage pulses, known as **heater pulses**, are periodically injected via an ohmic gold heater evaporated on the crystal surface. These pulses deposit fixed energy regulated by the injected amplitude $A_{inj}$ varying from 0 to 10 V. Two types of heater pulses are distinguished: control pulses and test pulses.

**Control pulses** inject a substantial amount of energy into the heater, causing a rapid rise in the signal until the TES reaches its normal conducting state. In this regime, further heat input does not significantly affect its electrical resistance, causing the detector response to control pulses to have a shape of saturated pulses, as shown in the upper left panel of Fig 2.2. The measured height of each control pulse, i.e., the distance from the baseline to saturation level, represents the difference between the TES's normal conducting state and its initial temperature before the pulse. Periodic control pulse heights provide input to a Proportional-Integral-Differential (PID) loop, which adjusts the heater power to stabilize the detector at the desired operating point. Additionally, the voltage response to these control pulses is used later in the analysis to select stable detector operation periods, as illustrated in Fig. 2.9.

**Test pulses**, the second type of heater pulses, have smaller injected energies than control pulses. These pulses are used to map the detector response across different energies within its dynamic range. Importantly, they allow this mapping to be performed continuously for each moment of time, which is crucial for long measurements, such as CRESST runs, where small drifts in detector response over time may occur. This method was used for data presented in Ch. 6 and is described in Sec. 6.4.

Fig. 2.2 shows an example of a data stream segment from a silicon wafer detector operated in a recent CRESST-III campaign. In this dataset, control pulses are injected every 10 s, while test pulses of fixed set of different injected amplitudes are fired every 20 s (see upper left and middle panels for zoomed-in views). Additionally, a particle pulse is displayed in the upper right panel. Given that the measurements are conducted in the low-background, deep-underground environment of LNGS, the particle rate is low.

The time positions of the heater pulses are recorded so that these artificial pulses can be easily identified during analysis. While heater pulses introduce dead time (depending on their frequency and the detector's response time), they play a crucial role in maintaining stable detector operation and significantly improve the precision of energy reconstruction.

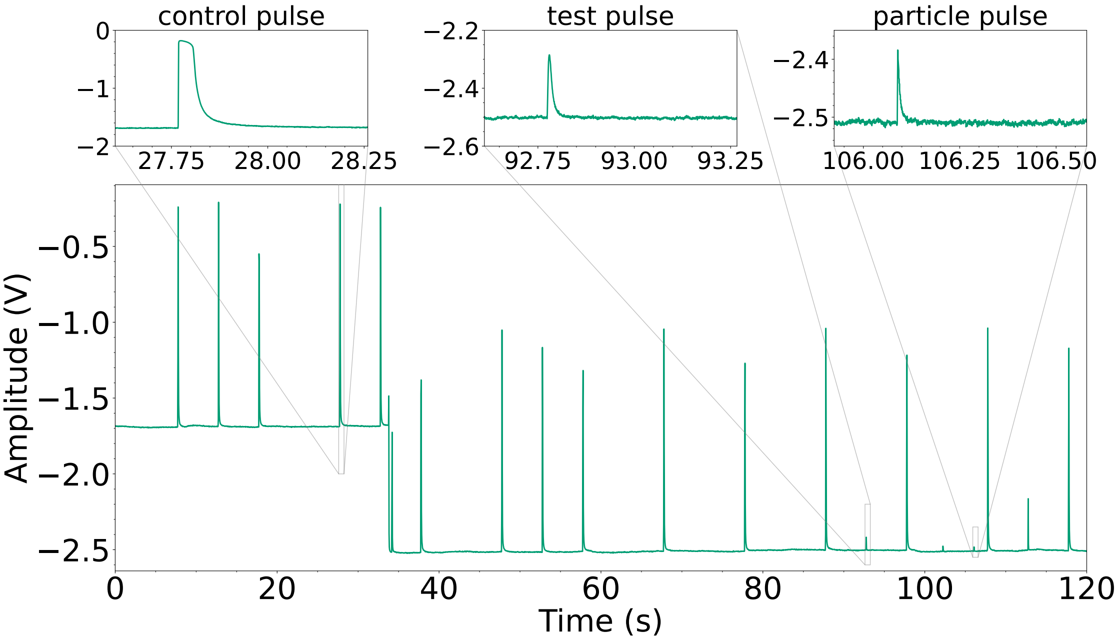

Figure 2.2.: Bottom panel: A portion of a continuous data stream from a silicon wafer detector operated during a recent CRESST-III data-taking campaign. Control pulses, which bring the TES into a normal conducting state and cause saturated pulses, are injected every 10 s; an example is shown in the upper left panel. Test pulses with a set of fixed injected energies are sent every 20 s, with an example depicted in the upper middle panel. The upper right panel illustrates a particle pulse.

The baseline level in the stream segment shown in Fig. 2.2 initially sits around -1.7 V and then abruptly shifts to -2.5 V. This behavior arises from the properties of SQUID operation. The SQUID electronics regulate the current in its feedback coil to keep the SQUID voltage at zero, and the output voltage signal is proportional to the input current. However, due to the periodic nature of the SQUID response, multiple feedback voltage values can satisfy the zero-voltage condition, resulting in an ambiguity caused by an offset of an integer number of flux quanta and multiple possible baseline levels. If the input signal changes rapidly by more than half a flux quantum, the SQUID can jump to the next working point, which explains the rapid baseline shift around 35 seconds in Fig.2.2. This phenomenon is a common artifact known as flux quantum loss (FQL). The identification of FQLs and other artifacts present in the data streams is described in Sec. 2.4.

## 2.3. Data analysis basics

The analysis of the stream data considered in this thesis generally follows the workflow illustrated in Fig. 2.3. It begins with characterizing the detector through building pulse template (Sec. 2.3.1) and the noise power spectrum (Sec. 2.3.2), using typical pulses and noise traces from the data stream. This is followed by triggering (Sec. 2.3.2) with optimized threshold (Sec. 2.3.3), event building (Sec. 2.3.4), and reconstructing pulse amplitudes (Sec. 2.3.5). Based on the parameters calculated for each pulse, event selection procedures are then defined (Sec. 2.4). Those analysis step are validated through event simulation and efficiency calculation (Sec. 2.5). Many of these steps are iterative, with adjustments and refinements made until they are finalized. The final outputs of this analysis stage, highlighted in green in Fig. 2.3, include both the energy spectrum and the detector performance parameters (Sec. 2.6), i.e., energy threshold and baseline resolution, required for the following data interpretation steps.

For this work, the analysis is performed with the ROOT[1]-based software Cryogenic Analysis Tools (CAT), which was primarily developed within [228] and is widely used in the CRESST and COSINUS collaborations. In this work It was adapted for the NUCLEUS data.

The main steps from the data stream to the energy spectra are outlined below. As can be seen, the analysis is an iterative process such that the same steps are usually refined and repeaed several times until the final result is obtained.

Although for illustrations, the CRESST-III silicon (Si) wafer and bulk detectors, discussed in detail in Ch. 6, are used, the same methods are applied to the other datasets presented in this thesis. Specific aspects of the analysis are addressed in dedicated chapters where relevant.

### 2.3.1. Pulse template

Since the pulse height of particle pulses is a measure of the energy deposition, accuracy in reconstructing the pulse amplitude is crucial. Several methods are used for this, as described in Sec.2.3.5. The foundation for all of them is the description of the detector response to particle pulses – **pulse template**.

As shown in Sec. 2.1, the pulse shape is expected to remain constant within the linear range of the detector response. To obtain the pulse template, several hundred valid events within the detector's linear range are summed. In the perfect case those events belong to the same energy, e.g. from a calibration peak. The summed pulse is then fitted with a well-established pulse shape model, described in [58] and reviewed in Sec. 2.1, to fully remove noise from the template. The summed particle pulse templates for the CRESST-III bulk detector, along with the fit, are shown in Fig. 2.4. The same procedure can be applied

---

[1] https://root.cern

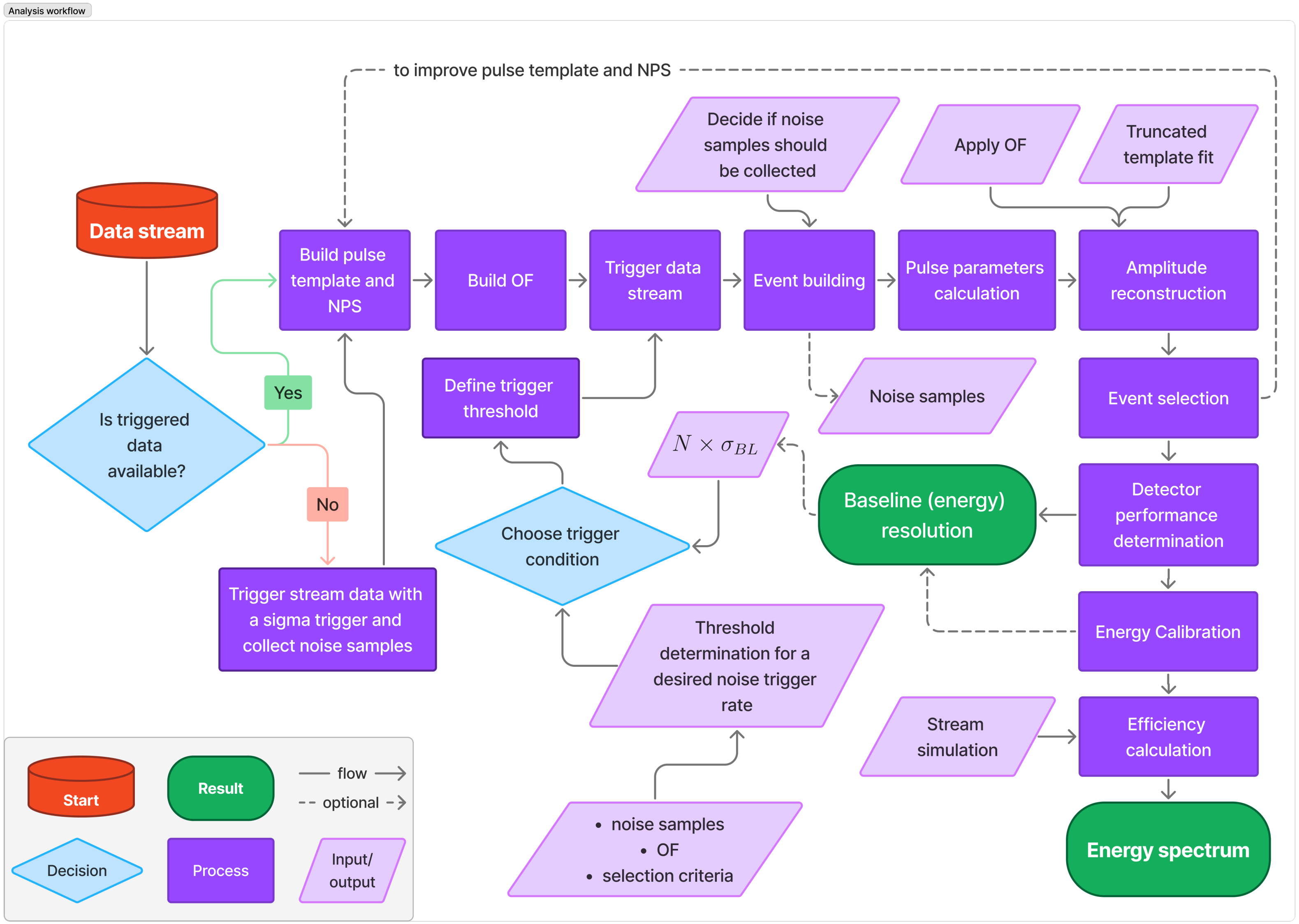

Figure 2.3.: Data analysis workflow indicating the main analysis steps described in the main text from the data stream (red) to the final results (green): evaluaion of the detector performance through the baseline energy resolution and final measured energy spectrum.

to test pulses in order to describe their pulse shape typically deviating from the one of particle events.

In most cases, building a pulse template is an iterative process that requires careful event selection and sufficient statistics.

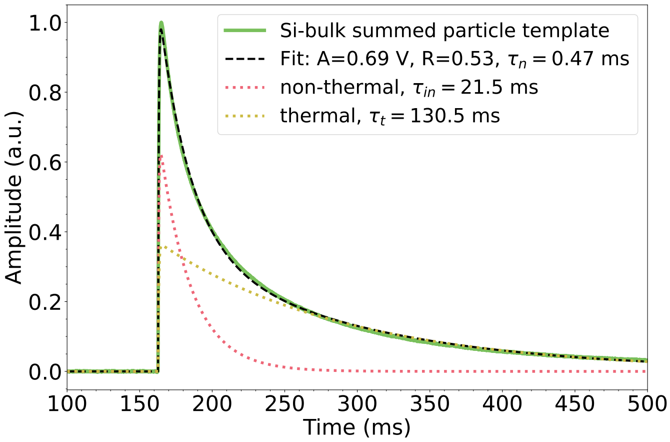

Figure 2.4.: Summed particle template for the CRESST-III Si bulk detector (green line), together with the best fit with the pulse shape model (Eq. 2.1) described in Sec. /refs:pulse-model (black dashed line). The two response components are displayed: the fast non-thermal component (dotted pink) and the slow thermal component (dotted yellow). Fit parameters are listed in the legend where $A$ is the amplitude of the non-thermal component and $R$ is the ratio of the thermal and non-thermal adamplitudes.

## 2.3.2. Triggering data stream

Recording the full data stream allows for the use of highly effective triggering algorithms during offline analysis. In experiments like CRESST and NUCLEUS, minimizing the energy threshold is critical, and methods that achieve the lowest possible threshold are prioritized. Triggering the data stream is done using the optimum filter approach described below.

### Optimum filter

Matched or optimum filter (OF) [229] is widely used in the low-threshold detectors community to maximize signal-to-noise ratio. Implementation of the OF approach to the CRESST data is described in detail in [226].

To construct the optimum filter, two components are necessary: the expected pulse shape of particle events, described in Sec. 2.3.1, and the typical noise power spectrum (NPS) of the detector.

**Noise Power Spectrum (NPS)** is determined by averaging a large number of noise traces from the data stream after they are Fourier transformed into the frequency domain. In the resulting NPS dominant noise frequencies are enhanced while random fluctuations are averaged out. An example NPS is shown in pink in Fig. 2.5, where the 50 Hz power supply noise is particularly prominent. The green line in Fig. 2.5 shows the power spectrum of the pulse template.

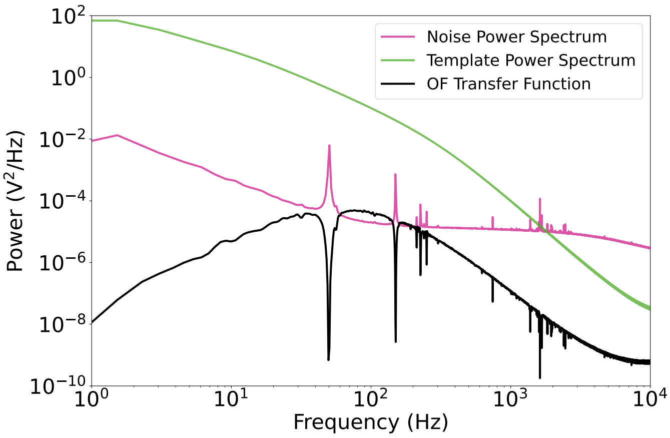

Figure 2.5.: Noise power spectrum obtained by averaging over a large number of clean empty traces (pink), power spectrum of the particle pulse templates from Fig. 2.4 (green), and transfer function of the optimum filter built from them (black) of the CRESST-III Si bulk detector.

Now, having characteristics of the typical noise present in the detector and pulse shape of desired signal, a frequency filter can be built to identify the signal within this noise, so-called matched or optimum filter (OF) [229] - widely used in the low-threshold detectors community. Implementation of the OF approach to the CRESST data is described in detail in [226].

With the detector's noise characteristics and the pulse shape of the desired signal in hand, the OF can be constructed to distinguish the signal from the noise. Each recorded event, $s(t)$, can be expressed as a sum of the scaled to the amplitude $A$ pulse template $s_0(t)$ and noise $n(t)$:

$$s(t) = As_0(t) + n(t). \tag{2.2}$$

The OF maximizes the signal-to-noise ratio using the given NPS and pulse shape. The OF transfer function $H(\omega)$ is proportional to the ratio of the complex conjugate of the Fourier-transformed pulse template $\hat{s}_0^*(\omega)$ and the NPS $N(\omega)$:

$$H(\omega) = K\frac{\hat{s}_0^*(\omega)}{N(\omega)}e^{i\omega\tau_{max}}, \tag{2.3}$$

where $\tau_{max}$ corresponds to the maximum position of the considered pulse, and $K$ is a normalization constant ensuring amplitude preservation. The transfer function, constructed from the NPS and the pulse template of the Si bulk detector, is shown by the black line in Fig. 2.5. As evident, the frequencies that dominate the NPS are weighted lower in the transfer function.

When OF is applied to a recorded trace or data stream, the original data is first transformed to the frequency domain, then multiplied by the transfer function and transformed back to the time domain. Fig. 2.6 shows a low-energy pulse before and after applying OF. A significant suppression of the noise is clearly visible, allowing to set the trigger threshold at lower values.

In the triggering process, all time stamps where the data exceeds the threshold after filtering are identified and stored. The specifics of triggering with the OF method are detailed in [226]. While OF preserves the amplitude of the pulse, the pulse shape is not saved in the filtered pulse. This is, however, not a problem since the amplitude is the measure for the energy deposition.

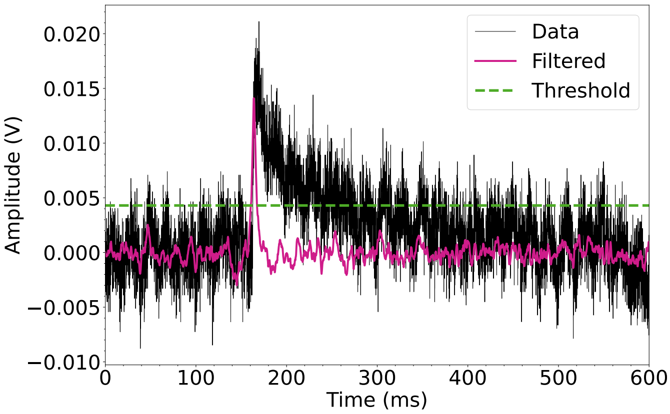

Figure 2.6.: A pulse of 58 eV measured by the CRESST-III Si bulk detector before (black) and after (magenta) applying the OF shown in Fig. 2.5. The green dashed line shows the triggering threshold for this data set defined to allow one noise trigger per kg-day of exposure as described in Sec. 2.3.3.

### 2.3.3. Threshold determination

After building the OF, the next step is to determine the appropriate triggering threshold. Several methods are available for this. The first simple option is to set the threshold at a specific number of baseline resolution values, e.g., $5\sigma_{BL}$. The procedure to calculate the baseline resolution is described in Sec.2.6.1. Alternatively, if control over the number of accepted noise triggers is necessary, the threshold can be set to allow only a certain number of triggers per unit of exposure. A procedure for this was developed in [230].

To implement it, a set of clean noise traces[2] is required. The OF is then applied to each noise trace, and the maximum values of the OF output are identified as potential triggers. The distribution of these maxima for the Si bulk detector, scaled by exposure, is shown in Fig. 2.7a. Assuming that each noise sample follows the distribution $P(x)$, the joint

---

[2] In reality, selecting traces containing only noise is not always trivial. The selection criteria used can affect the content of the noise traces set and, consequently, the result. Therefore, it is good practice to apply the same selection criteria that will be used in the final analysis to ensure relevant conditions for a given analysis. See Sec. 2.4 for commonly used selection criteria.

probability that one sample equals $x_{max}$ while all others are smaller can be modeled with a binomial distribution:

$$P_d\left(x_{\max}\right) = \frac{d!}{1!(d-1)!} \cdot P(x_{\max}) \cdot \left(\int_{-\infty}^{x_{\max}} P(x)dx\right)^{d-1}, \tag{2.4}$$

where $d$ represents the number of statistically independent samples within a trace. Under the assumption of the white noise, $P(x)$ takes the form of a Gaussian function, and the probability distribution can be rewritten as:

$$P_d\left(x_{\max}\right) = \frac{d}{\sqrt{2\cdot\pi}\cdot\sigma} \cdot e^{-\left(\frac{x_{\max}}{\sqrt{2}\sigma}\right)^2} \cdot \left(\frac{1}{2} + \frac{\operatorname{erf}\left(x_{\max}/(\sqrt{2}\sigma)\right)}{2}\right)^{d-1}, \tag{2.5}$$

where $\sigma$ is the standard deviation of the Gaussian distribution, and erf is the error function. This probability distribution function describes the observed distribution of OF maxima. The best fit of the histogram using Eq.2.5 is shown as a black line in Fig.2.7a. The corresponding values are listed in Tab. 2.1.

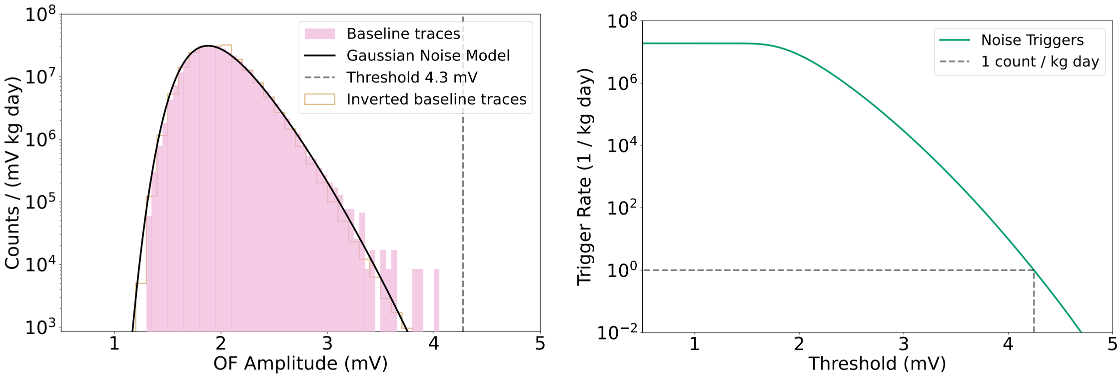

(a) (b)

Figure 2.7.: (a) Distribution of the baseline triggers normalized to the exposure obtained from applying OF to a set of clean noise traces (pink) with a fit function from 2.5 assuming normally distributed noise samples (black) for the CRESST-III Si bulk detector. Distribution of the OF maxima obtained with the coltage-inverted stream is shown with yellow. (b) Integral of the noise trigger model characterizing noise trigger rate (green). The threshold value of 4.3 mV is chosen to allow one noise trigger per kg-day of exposure and is shown with the black dashed line.

| Fit parameter | Value |
|---|---|
| $\sigma$ | (0.68±0.02) mV |
| $d$ | 315±5 |

Table 2.1.: The values of the free fit parameters of the Gaussian noise model obtained from a maximum likelihood fit of Eq. 2.5 to the baseline triggers shown in Fig. 2.7a.

The integral of this probability distribution gives the noise trigger rate (NTR) above a threshold $x_{thr}$:

$$NTR(x_{thr}) = \int_{x_{thr}}^{\infty} P_d(x_{\max}) dx_{\max}. \tag{2.6}$$

The NTR for different threshold values, based on the fit results from Fig.2.7a and Tab.2.1, is shown in Fig. 2.7b. This allows the selection of a triggering threshold based on the desired number of noise triggers per unit of exposure. For instance, one noise trigger per kg-day, a standard criterion in recent CRESST-III campaigns, was used for this detector and is illustrated by the dashed lines.

The validity of this trigger model can be confirmed by comparing the OF maxima distribution for the voltage-inverted data. In the case of symmetric noise, the distributions for the original and inverted noise traces should be identical. The distribution for the inverted data is shown as a yellow histogram in Fig. 2.7a, demonstrating that the noise fluctuates symmetrically in both directions.

While the assumption of white noise is sufficient for many detectors, selecting purely noise traces can be challenging when high signal rates are present in the low-energy region, such as in the case of a low-energy excess. In such cases, the OF maxima distribution will deviate from Eq.2.5, which assumes purely Gaussian-distributed samples. An extension of this model, which includes an exponentially distributed component to account for this effect, was developed in [231] and is discussed in Ch. 6.

### 2.3.4. Event building

During the triggering process, all time stamps where the filtered data stream exceeds the predefined threshold are identified. After this, a dedicated event-building algorithm is applied. In this step, triggers from multiple channels associated with the same detector module – such as the phonon-light technique in CRESST or double-TES detectors – are combined into events. Each event has a designated record window and includes data from a predetermined number of channels. Additionally, control and test pulses are identified based on their time stamps.

At this stage, noise traces can also be collected, typically by randomly sampling the data stream.

### 2.3.5. Amplitude reconstruction

The amplitude of the pulse is crucial for analysis, as it directly relates to the energy deposition in the crystal. When after the energy deposition the TES resistance remains within the linear part of its transition curve, recorded pulses have the same shape but vary in amplitude. In this regime, called the **linear range** of the detector response, the pulse amplitude is proportional to the energy deposited. For such pulses, the OF, discussed in Sec. 2.3.2, is applied to the events, with the pulse amplitude defined as the maximum of the filtered trace.

Another method for reconstructing amplitude involves fitting the data with a sum of the pulse template (Sec. 2.3.1) and a background model, typically a third degree polynomial. In this process, the template is scaled and shifted in time to minimize the root mean square (RMS) of the fit. While this method is less precise than OF in the linear range, often by a factor of 2-3, it becomes necessary when the energy deposition pushes the TES beyond the linear range, where pulse shapes are no longer preserved and OF-based amplitude reconstruction fails.

For such cases, a **truncated template fit** is used. This method fits the template to the portion of the pulse that still lies within the linear range, as shown in Fig. 2.8. The voltage level at which the pulse shape begins to deviate from the template is referred to as the **truncation limit**, which corresponds to 0.5 V in Fig. 2.8. Only the data points below this limit are used in the fit. The implementation of the truncated fit is described in detail in [228].

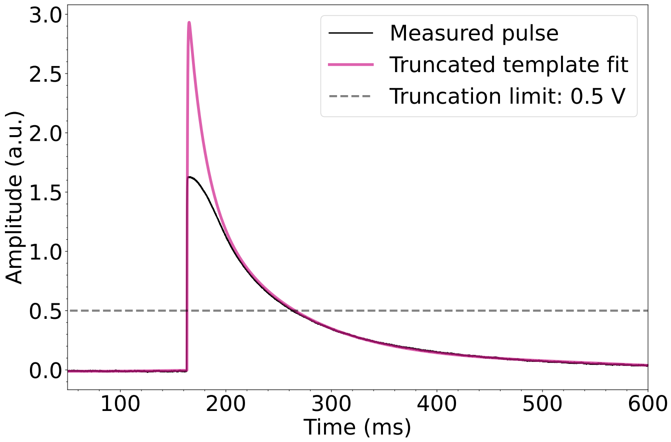

Figure 2.8.: Saturated pulse from the non-linear range of the detector response of about 15 keV measured by the CRESST-III Si bulk detector (black line). The pink line shows the truncated template fit that considers only the data points below the truncation limit indicated with the dashed line.

## 2.4. Event selection

After events are defined, a set of pulse parameters, primarily based on the moving average, is calculated for each trace. The selected parameters used in this work are defined as follows:

- **Baseline Offset**: This parameter represents the baseline level in the pre-trigger region, determined by fitting a linear function to this part of the trace. The slope of the fitted function is stored as a separate **Baseline Slope** parameter. And the RMS of this fit is saved to **Baseline RMS** parameter. This baseline model is subtracted from each trace so that the resulting baseline is centered at 0, as shown in Fig. 2.6. Pulses without this correction are illustrated in the top panels of Fig. 2.2.

- **Baseline Difference**: This is the difference between the average of the last 50 samples in the record window and the average of the first 50 samples. It is useful for identifying events where the baseline level before and after the pulse differs, as discussed in the Baseline Difference cut below.
- **Pulse Height**: The maximum value within the record window after applying the moving average. This serves as a rough initial estimate of the pulse height.
- **Peak Position**: This parameter records the position of the maximum within the record window. It can later be refined by a more precisely determined OF peak position.
- **Rise and Decay Times**: The rise time is defined as the time it takes for the pulse to increase from 10% to 90% of its height, and the decay time as the time it takes to fall from 90% to 10% of its height.
- **Minimum and Maximum Derivative**: These parameters capture the steepest rise and fall between two consecutive samples within the record window, characterizing rapid changes in the signal.

Additionally, both amplitude reconstruction methods, the OF and the template fit described in Sec. 2.3.5, provide a measure of how closely the recorded pulse matches the template pulse shape. For the template fit, this measure is the root mean square (**Fit RMS**) of the residuals. In the case of the OF, it corresponds to the RMS difference between the filtered data and the filtered template pulse scaled to the same amplitude - **OF RMS**. Furthermore, the RMS of the OF around the peak position is stored as a separate parameter, providing additional information into the agreement in this critical region.

The selection criteria are developed with the goal to only keep the events where reliable energy reconstruction can be ensured. Here commonly used cuts relevant for most of the data presented in this thesis are described and illustrated with the CRESST-III Si wafer detector presented in Ch. 6. Cuts additionally developed for specific data sets are then presented in corresponding chapters.

**Stability cut**

Events occurring during periods of unstable detector operation are excluded. To identify these intervals, the detector's response to control pulses is used. Control pulses fully saturate the TES, providing a reliable measure of how deep the detector is within the superconducting transition curve at any given time. To ensure data are collected only when the detector is at a desired operating point (i.e., at the same position on the transition curve), all time periods where the control pulse height deviates from the targeted value are excluded. The distribution of all measured control pulse heights for the Si wafer detector is shown in Fig. 2.9a, with stable control pulses marked in green. Periods where the control pulse height deviates by more than $2\,\sigma$ from the mean value are removed.

Fig. 2.9b illustrates the control pulse heights measured by the wafer detector over time, including an example of instability during data-taking. During this period, the control pulse height is clearly distorted, which also impacts the detector's response to smaller test pulses, as shown in the same figure. The stability cur successfuly removes this periods of disturbed detector response. Only events occurring during stable control pulse response, highlighted in green, pass the cut.

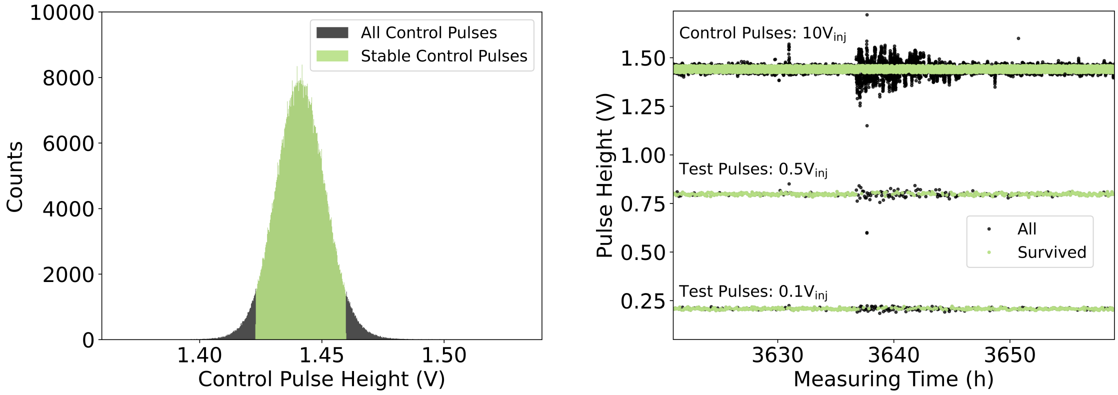

(a) Distribution of all control pulse heights (black), the stable inputs defined as those that are within 2 $\sigma$ from the mean value and shown in green.

(b) Pulse heights of control pulses and two test pulses with injected amplitude of 0.5 $V_{inj}$ and 0.1 $V_{inj}$ over measuring time (black). Events survived the stability cut are shown in green. An instability around 3640 hours is cleared up after applying the cut.

Figure 2.9.: Selection of stable periods of detector operation for the CRESST-III Si wafer detector.

**Quality cuts**

The goal of quality cuts is to remove the events where the trigger algorithm was fired by an artifact or the recorded puls was distorted.

One of the common artifacts is a electronic **delta spike**. An example of such an event is shown in the inset of Fig. 2.10a. Due to the instant change in output voltage in delta spikes, an effective method for removing these events is to apply a cut based on the ratio of the minimum derivative of the trace to the baseline RMS of the trace's pre-trigger range. The distribution of this parameter for all events is shown in Fig. 2.10a. Pulse-like events belong to the peak with the small negative values of this parameter shown in green while the spike artifacts form the structure with higher negative values and are rejected.

Another common artifact is the **flux-quantum loss of the SQUID**. This might occur when the input signal changes very rapidly and by more than half of a flux quantum, following the SQUID to jump to the next working point. As a result, the baseline level after the pulse differs from that before, as illustrated in the upper left inset of Fig. 2.10b. In this case, the baseline difference corresponds to one flux quantum. The distribution of the baseline difference parameter for all events is shown in black in Fig. 2.10b. For valid pulses, the baseline difference parameter is centered around 0, while pulses affected by flux-quantum losses have a distribution shifted to more negative values.

Additionally, amplitude reconstruction is degraded for pulses that occur on **decaying baselines** from a previous pulse (as seen in the lower right inset of Fig.2.10b). To account for this, such events are also rejected by imposing stricter limits on the baseline difference parameter. Events that the baseline difference cut are marked in green in Fig. 2.10b.

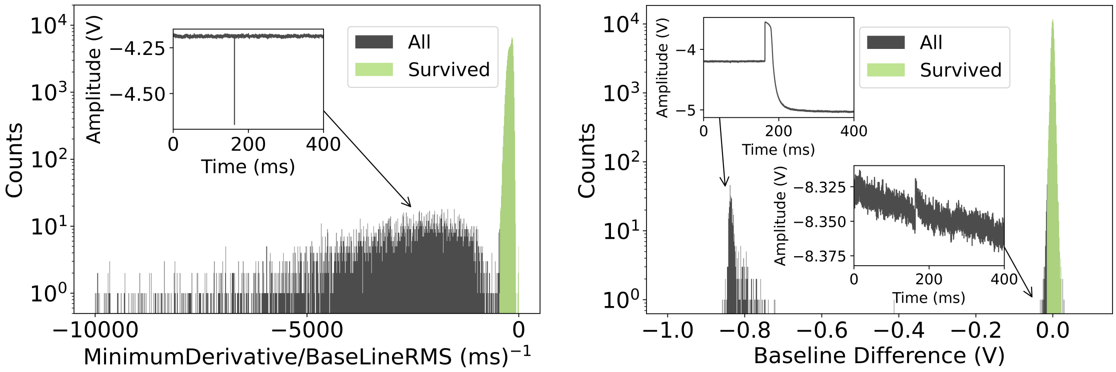

(a) Distribution of the ratio of the minimum derivative of the trace and the RMS of the pre-trigger baseline is shown in black. Cutting on this parameter removes electronic delta spike events such as the one shown in the inset. Events that survived the selection are shown in green.

(b) Distribution of the difference between baselines in the pre-trigger and post-trigger range (Baseline Difference parameter). The structure around -0.8 V contains purely events suffering from flux-quantum losses of the SQUID, such as the event from the left upper inset. The left shoulder of the peak around 0 contains pulses on decaying baselines, similar to this illustrated in the lower inset. Events that survived the selection are shown in green.

Figure 2.10.: llustration of the quality cuts for the CRESST-III Si wafer detector.

To reject events with distorted waveforms, only those with low values of OF RMS and Peak RMS are selected. Fig. 2.11 shows the OF RMS as a function of the OF Amplitude for all events that passed the previous cuts. The RMS value starts to increase around the truncation limit, 0.3 V for this detector, indicating the beginning of the detector's response becoming increasingly non-linear: the pulse shape first starts to deviate from the template and then measured pulses become fully saturated, resulting in an almost constant identified OF amplitude with very high RMS (left part of Fig. 2.11). In this region results from truncated template fit described in Sec. 2.3.5 are used for amplitude reconstruction and data cleaning.

The left inset zooms in on the low-amplitude region, where events passing the RMS selection are highlighted in green. The dotted magenta line represents the average OF RMS in the linear range, i.e., below 0.3 V. Beyond this amplitude, the RMS gradually increases. The right inset provides an example of an event excluded by this cut due to pile-up. The OF RMS cut is also effective to identify events occurring during noisy periods, which exhibit distorted pulses.

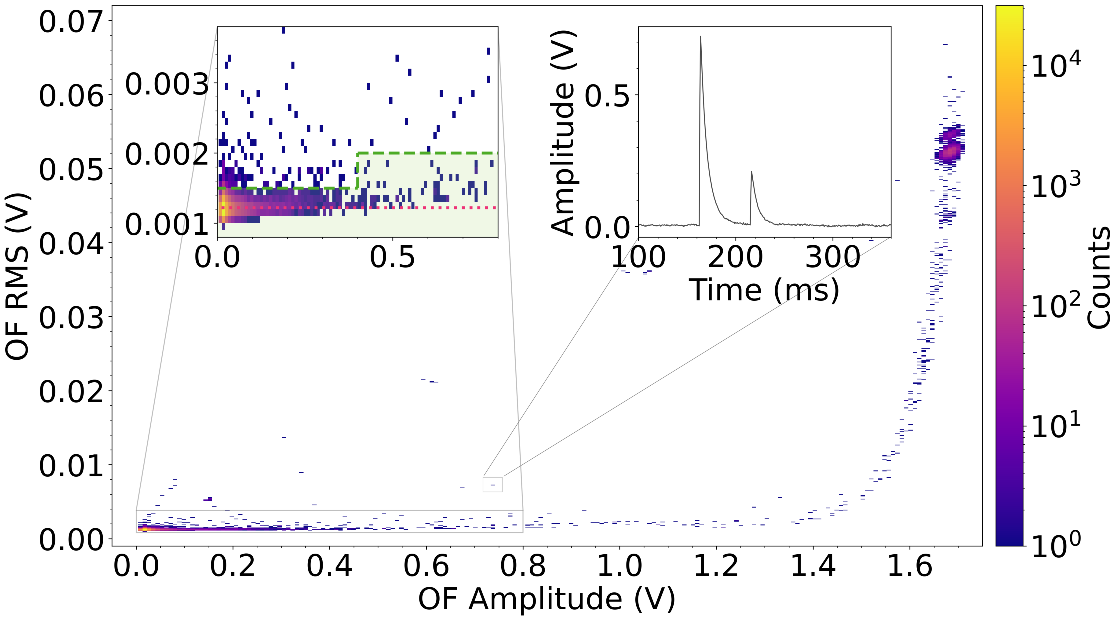

Figure 2.11.: OF RMS values as a function of OF Amplitude for the CRESST-III Si wafer derector. The RMS remains constant until it begins to rise above the truncation limit at around 0.3 V. Beyond this point, the OF is not used for amplitude reconstruction, as the pulse shape begins to deform, leading to full saturation, as for the population around 1.65 V corresponding to Fe calibration events. The left inset provides a zoom into the low-amplitude region. The dashed green line indicates the cut values, with the events that passed the selection shaded in green. Above 0.8 V, the OF RMS cut was not applied. The dotted magenta line represents the average OF RMS value in the linear range (below 0.3 V), marking the onset of RMS rise. The right inset shows an example of a rejected pulse, where the increased RMS value was caused by a pile-up. Pulses with distorted shapes are also effectively removed by the OF RMS cut.

Additionally, a cut on the template fit RMS is applied, particularly above the linear regime, to filter out distorted pulses at higher energies. If different pulse shapes appear in the dataset, both OF RMS and template fit RMS can be used to distinguish between different populations, as demonstrated in Sec. 4.3.2.4 and5.4.2.

**Coincidence cuts**

For rare-event searches, such as DM searches in CRESST, the signal is expected to originate only within the target detector. To ensure this, several coincidence cuts are applied. Events detected in the target that coincide with a signal in the muon veto within a defined time window, such as $\pm 5\,\mathrm{ms}$ for the Si wafer detector, are rejected.

When multiple detectors are operated simultaneously during the same run, the signal is not expected to occur in more than one detector at the same time. Therefore, coincidences between different cryogenic detectors are also excluded.

## 2.5. Trigger and cut efficiency calculation

To estimate the impact of the analysis on the data, the efficiency of the triggering process and event selection is evaluated. This is done using a so-called stream simulation, in which a scaled template pulse is superimposed onto the data stream at random time samples with a set frequency. This approach ensures that the simulated events closely resemble real events, as both a typical pulse shape and real noise conditions are used. The full analysis chain described earlier – from OF triggering to applying cuts – is then applied to the simulated stream. Unlike real data analysis, the timestamps of the simulated events are known, allowing for an accurate assessment of how many events survive each analysis step. For higher energies, a flat part of the resulting efficiency curve can be used as a rough estimate of efficiency.

The superimposed template pulse can be scaled to a selected amplitude value to investigate efficiencies for specific energy, and this process can be repeated for multiple energy values. In large datasets, like those collected in CRESST, a range of energies can be studied simultaneously by randomly scaling the amplitude in a chosen energy range, covering the linear region up to the truncation limit. Beyond this range, the pulse shape is no longer constant, so simply scaling the template pulse does not accurately represent the detector response. A description of pulse shape behavior in the non-linear regime was developed in [228], which could be implemented to extend stream simulations beyond the linear range. However, the region of interest for the data discussed in this thesis lies at low energies, so the stream simulation is performed for the linear ranges.

Fig. 2.12 shows efficiency curves that illustrate the cumulative effect of various analysis steps on the CRESST-III Si wafer detector as a function of simulated energy. In this case, events were uniformly distributed from 0 to 300 eV. The survival fraction for each curve is calculated as the ratio of the number of events that survive each step to the total number of simulated events in each energy bin.

After running the OF triggering algorithm, the fraction of triggered events was calculated for each energy. Occasionally, a real particle or heater event may overlap with the simulated one in the same record window. All heater pulses are marked by default, and the coinciding simulated events are lost from the analysis. For particle events, the triggering algorithm selects the event with the highest OF voltage output. Thus the total event rate, including the frequency of heater pulses, largely defines the trigger dead time. Since these scenarios can occur in real event analysis as well, the fraction of simulated events that successfully fire triggering provides the trigger efficiency. The flat part of the efficiency curve describes the trigger dead time, while the efficiency decreases as the threshold (at 10 eV for this detector) is approached, as shown in the inset plot.

Next, the selection criteria described in Sec. 2.4 are applied to the triggered simulated events to determine the fraction of valid pulses surviving them. Fig. 2.12 shows the cumulative impact of stability cuts, muon veto coincidence, and quality cuts applied one

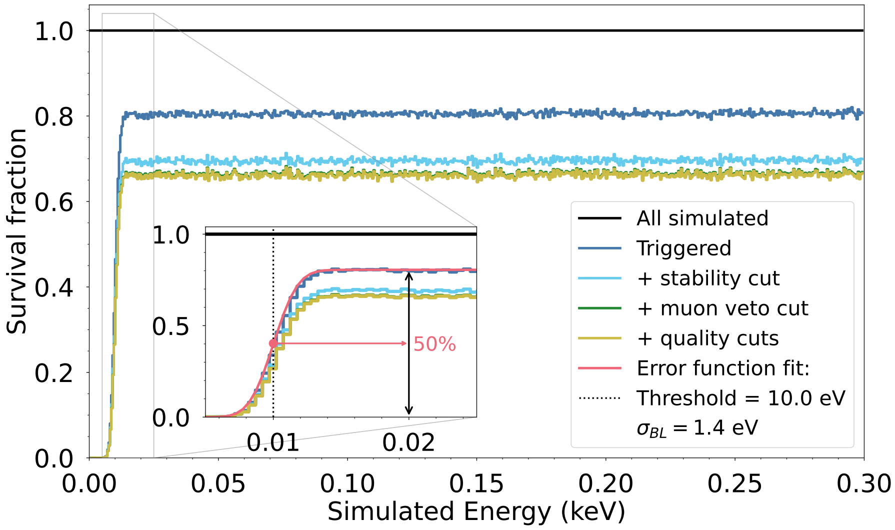

Figure 2.12.: Trigger and cut efficiency curves for simulated energies ranging from 0 to 300 eV for the CRESST-III Si wafer detector. For each energy bin, the survival fraction is calculated as the ratio of surviving events to the total number of simulated events. Before any analysis manipulation is applied the survival fraction stayes at 1, shown as the black line. The next analysis steps are applied sequentially, with the cumulative effect represented by the following lines: triggering (blue), stability cut (cyan), muon veto coincidence cut (green), and quality cuts (yellow). The inset provides a zoomed view of the low-energy region. The pink line represents an error function fit to the trigger efficiency curve, used to assess detector performance. The resulting threshold and baseline energy resolution are indicated in the legend.

after another. Since the dataset for this detector was of very high quality, the quality cuts remove only a small fraction of events of about 1% after the other cuts.

The final efficiency curve (yellow line in Fig. 2.12) is used to correct the energy spectra after applying the selection criteria by dividing the raw spectra by the efficiency value at a given energy. This correction accounts for the fraction of valid events lost due to trigger dead time and selection cuts. Additionally, stream simulations can be useful for fine-tuning cut values, especially when the real dataset has a low particle rateand thus lacks statistics for precice particle events charachterisation.

## 2.6. Detector performance

### 2.6.1. Baseline resolution

**Baseline energy resolution** $\sigma_{BL}$ refers to the detector's resolution at zero energy, where the accuracy of pulse amplitude reconstruction is limited only by noise fluctuation. While the energy resolution varies with energy, the baseline resolution is a key performance metric for cryogenic detectors, as it determines the minimum achievable trigger threshold.

The primary method used in this work to estimate baseline energy resolution involves superimposing a noiseless particle pulse template to a large set of randomly collected noise traces. In such way a set of particle-like events with a known amplitude are constructed. The same amplitude reconstruction method, typically OF, and selection criteria used in the actual analysis are applied to these simulated events. The reconstructed amplitudes normally form a Gaussian distribution centered around the original amplitude of the template, with the standard deviation representing the baseline resolution. This method provides a reliable estimate of the baseline resolution because it closely mimics real analysis conditions. Both the baseline resolution and trigger threshold, initially determined in Volt units, can be converted to energy units using a calibration factor.

Another method for assessing detector performance derives from the trigger efficiency curve. The width of the gradual rise in trigger efficiency at the threshold, shown in the inset of Fig. 2.12, reflects the detector's finite resolution. This rise can be modeled with an error function by convolving an ideal step function with a Gaussian detector resolution $\sigma$ at the triggering threshold $E_{thr}$ :

$$f(E) = \frac{A}{2}\left(1 + \mathrm{erf}\left(\frac{E - E_{thr}}{\sqrt{2}\sigma}\right)\right), \tag{2.7}$$

where $A$ represents the flat efficiency at higher energies. By fitting this function to the trigger efficiency curve, as shown in Fig. 2.12, the threshold and resolution at the triggering threshold – equivalent to the baseline resolution – are determined.

The results from the superimposition method and the error function fit serve as internal cross-checks to validate the detector's performance characteristics.

### 2.6.2. Energy calibration

The reconstructed pulse amplitude reflects the energy deposited in the crystal. As discussed in Sec. 1.3.2, the energy scale is usually obtained by using a radioactive source that emits X-rays of sufficient rate and known energy that are fully absorbed by the detector target, producing a distinct line in the amplitude spectrum. In the analyses presented in this thesis, a $^{55}$Fe source is used, providing calibration lines at 5.9 and 6.5 keV. In an ideal case, this amplitude is linearly proportional to the energy, and the detector's response remains stable over time. Under these simplified assumptions, a constant calibration factor can be determined and used to convert pulse amplitudes into energy, from calibration lines down to the threshold. This approach is employed in the analysis of the NUCLEUS detectors discussed in Ch. 4 and 5. However, several factors can introduce non-linearity, such as the non-linear shape of the superconducting transition curve or the bias circuit, which can reduce the accuracy of energy determination (see Sec. 5.4.1 for further discussion).

To enhance precision, the detector's response can be mapped using test pulses injected via the heater. Assuming that the reconstructed height of these test pulses scales with injected energy in the same manner as particle pulse heights allows the construction of the detector's response function in the entire dynamic range. Additionally, this method enables tracking deviations of the detector response in time. With this approach, the reconstructed amplitude of measured pulses is translated into the corresponding injected amplitude of test pulses, which is linearly proportional to the energy input. This method is used in the analysis of the CRESST Si detectors, discussed in Ch. 6, and is detailed in Sec. 6.4.

Having calibration lines directly in the region of interest of the experiment is beneficial to further reduce the uncertainties of the energy determination.

# 3. Low-energy excess in the CRESST-III experiment

As discussed in Sec. 1.3.1, the low-energy excess (LEE) currently stands as one of the primary challenges for the low-threshold cryogenic detectors searching for DM or aiming to measure CE$\nu$NS. The CRESST-III experiment marked a significant milestone by achieving an energy threshold of 30 eV in the first CRESST-III underground campaign [43]. Consequently, it was among the first to observe the LEE phenomenon in the measured energy spectra.

This chapter provides a summary of LEE observations in the CRESST experiment, with a focus on results obtained within the scope of this thesis. In Sec. 3.1, the first observations of the LEE in $CaWO_4$ and $Al_2O_3$ CRESST-III detectors are briefly reviewed. LEE-related results from the most recently concluded data-taking campaign of CRESST are discussed in Sec. 3.2[1] and concluded in Sec. 3.3.

## 3.1. First observations of the LEE in CRESST-III

Since the focus of the third phase of the CRESST experiment, CRESST-III, was set on probing light DM, the absorber's mass was reduced in comparison to the earlier phases, which allowed significantly lowering the energy thresholds from $\mathcal{O}(100\,\text{eV})$ to $\mathcal{O}(10\,\text{eV})$, reaching the part of the energy spectra affected by LEE.

### 3.1.1. First observation of the LEE in CRESST-III $CaWO_4$ detectors - Run34

The first data-taking campaign of CRESST-III was ongoing from October 2016 to April 2018 and is internally named *Run34*. Ten 24 g $CaWO_4$ crystals of $20\times20\times10\,\text{mm}^3$, paired with SOS light detectors, were operated in the standard CRESST-III modules shown in Fig. 1.8. Four detectors reached energy thresholds below 100 eV: detectors A, B, J, and E. The absorbers for all of those four detectors were cut from crystal ingots grown at TUM [232] - detectors A and J from the TUM56 crystal ingot and B and E from the TUM73 ingot. Detectors A, B, and E had the CRESST PD-M TES design and detector J - CRESST PD-L design. The CRESST-III TES designs used for detectors discussed in this work are shown in Fig. 3.1.

---

[1] Results from Sec. 3.2.2 and 3.2.5 are derived with the data from the Si2-wafer detector presented and analyzed in this work in Ch. 6 and are published in Ref. [6]. Results presented in Sec. 3.2.3-3.2.4 are obtained based on the analyses of various detectors performed by several people (see all the references in Tab. 3.1) and are in large part published in Ref [3]. Sec. 3.2.4, however, contains additional findings made in this work. My contributions to the mentioned publications are specified in .

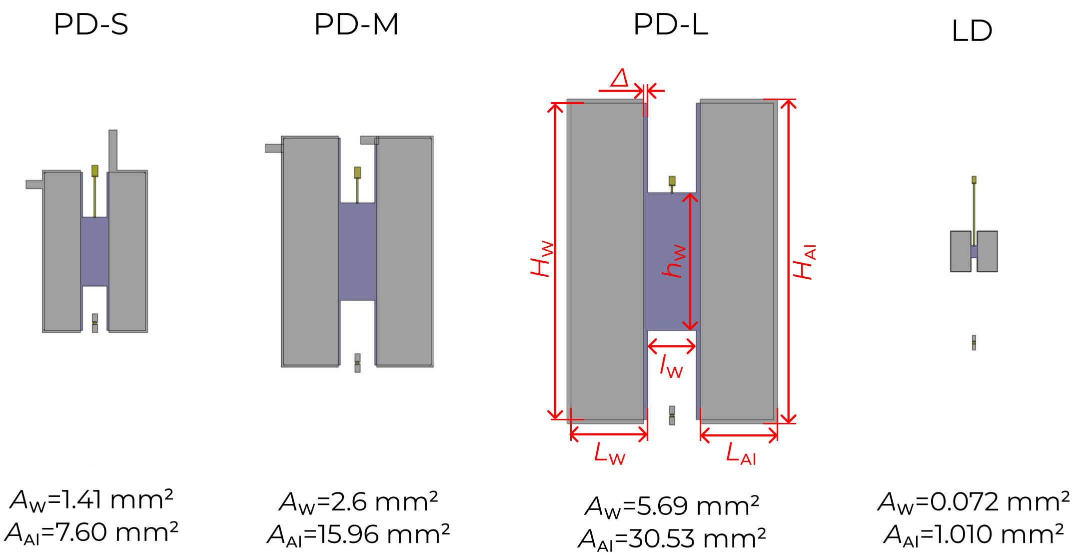

Figure 3.1.: Overview of the CRESST-III TES designs used in Run 34, 35, and 36. The purple color represents the tungsten layer with a thickness of ∼200 nm, the gray represents aluminum with a thickness of ∼1 $\mu$m, and the yellow represents gold. The tungsten films are deposited on a ∼50 nm thick layer of SiO2. In the PD designs, this SiO2 extends 0.2 mm outward from all sides of the W-layer, while in the LD designs, the SiO2 layer forms a circle with a 7 mm diameter. The aluminum phonon collectors are evaporated on the tungsten films, forming a bi-layer structure. The total surface areas for the tungsten inner part ($A_{\mathrm{W}}$) and aluminum phonon collectors ($A_{\mathrm{Al}}$) are provided for each design. The specific dimensions are listed in Tab. A.1 in App. A. This figure is adapted from [40].

Fig. 3.2a, adapted from [228], shows the low-energy parts of their spectra. Although the detectors were operated in identical modules, the LEE observed in each detector has different shapes and rates. The difference in the observed LEEs between the nearly identical detectors operated in Run34 suggested that particle-related origins, as well as DM, are unlikely to account for a major fraction of the observed events. Additionally, it was noted for the first time that the LEE rate decreases with measurement time [233]. The LEE rate evolution in time for one of the detectors operated in Run34 is shown in Fig. 3.2b. At that time, however, LEEs had only been observed by CRESST in detectors with $CaWO_4$ absorbers. To test whether this feature also occurs in the other absorber materials, $Al_2O_3$ crystals were operated in the next CRESST-III data acquisition campaign, internally known as *Run35*.

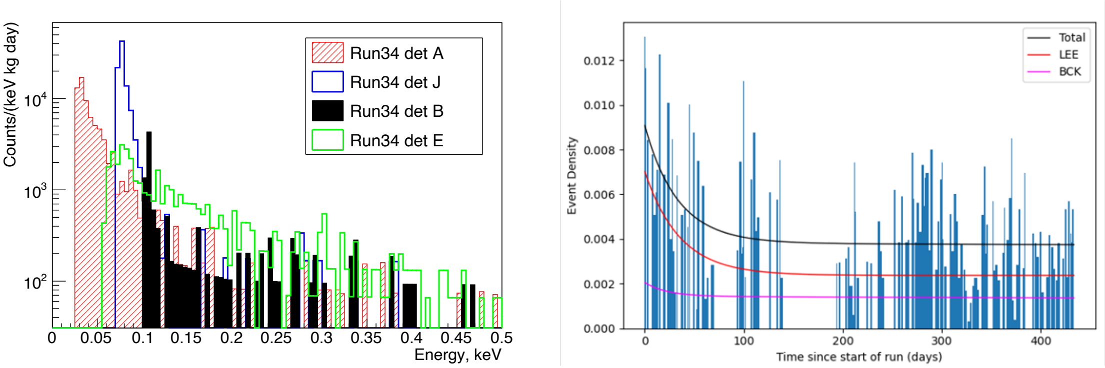

(a) LEE spectra measured in $CaWO_4$ detectors in Run34. Figure adapted from [228].

(b) Likelihood analysis of the time behavior of the rate at low energies measured by detector A. Two components are considered to describe the total event density over time shown with the blue histogram: LEE (red) and flat background (magenta) resulting in the total rate (black). While the background rate remains almost constant in time, the LEE rate is decreasing. The figure is taken from [233].

Figure 3.2.: LEE energy spectra and rate evolution in time measured by CRESST-III detectors in Run34.

### 3.1.2. Observation of the LEE in CRESST-III $Al_2O_3$ absorbers - Run35

Run35 was ongoing from September 2018 to October 2019. In addition to $CaWO_4$ detectors, two 16 g $Al_2O_3$ crystals of $20\times20\times10\,mm^3$ were operated in standard CRESST-III modules, shown in Fig. 1.8. Both detectors' TESs featured the CRESST PD-M design (see Fig. 3.1 and Tab. A.1). The analysis of those detectors was performed within the scope of this thesis following the procedure described in Ch. 2. The low-energy parts of the spectra measured by the $Al_2O_3$ detectors are shown in Fig. 3.3a. The LEE was observed in both detectors, with its rate decaying over time [233], indicating that this phenomenon is not exclusive to $CaWO_4$. While the shapes of the observed LEEs are similar: the slopes of the exponents match within 10% in the spectral shape fit [234]. The rates, however, vary by an order of magnitude between the two detectors, despite no apparent difference in the detector design[2]. This large difference further rules out a sole particle origin of the LEE. To investigate the impact of the different components of the detector modules on the observed LEEs, several modifications to the standard module design were made for the next data-taking campaign - *Run36*.

---

[2] Since one of the currently discussed hypotheses for the origin of LEE is the relaxation of the stress induced by the mechanical holders of a crystal, it may be worth noting that the external force of the holders on the crystal was not precisely controlled and therefore may differ between the two modules.

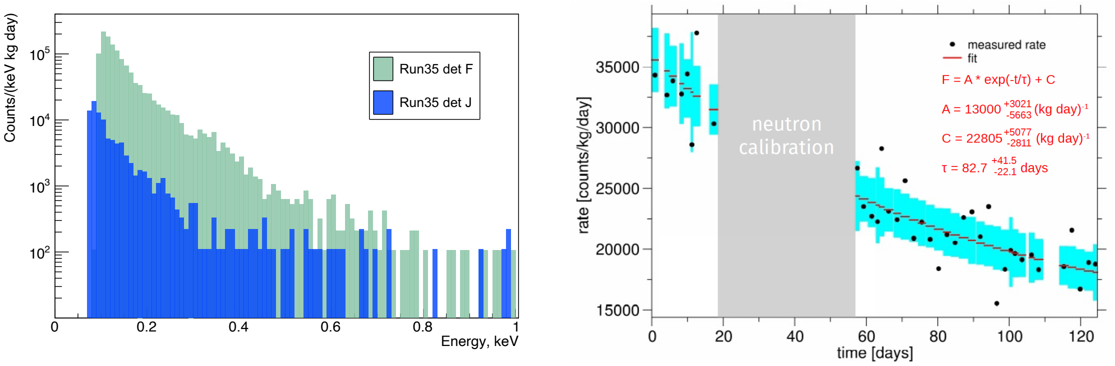

(a) LEE spectra measured in two $Al_2O_3$ detectors in Run35.

(b) Rate of events below 200 eV for det F. shown with the black dots. The red line shows the best fit with an exponential function, and the cyan band represents the $1\sigma$ band of the fit. Similar behavior is observed for det J.

Figure 3.3.: LEE energy spectra and rate evolution in time measured by CRESST-III $Al_2O_3$ detectors in Run35. Figures taken from [233].

## 3.2. CRESST LEE studies in Run36

### 3.2.1. Modified detector modules for LEE studies

Run36 was ongoing from August 2020 to February 2024. The main goal of this data-taking campaign was to study the LEE and to check if any component of the standard module design contributes majorly to the observed LEE rate. Therefore, several modifications were made to the detector modules, while the core and geometry of most modules stayed the same. The detector modules discussed in this work and their main characteristics are listed in Tab. 3.1. The modifications to the detector modules are reviewed below.

- **Absorber material.** In addition to $CaWO_4$ and $Al_2O_3$ absorbers, Si and $LiAlO_2$ were used as absorber materials in Run36 (Si2 and Li1 modules) to study the LEE behavior in a larger variety of materials.

- **$CaWO_4$ origin.** $CaWO_4$ of different origins were used: commercially available crystals for the Comm2 module and crystals grown in-house at TUM from extensively chemically purified raw materials for the TUM93A module. By maintaining control over each production step, it is possible to achieve high radiopurity, improved optical quality, and minimal crystal lattice stress compared to commercially produced crystals [125, 137, 232, 235]. Therefore, this modification serves two purposes: first, to check the impact of the intrinsic background on the LEE, and second, to investigate the influence of the crystal lattice stress on the LEE.

- **Holding structures.** Standard $CaWO_4$ holding sticks were replaced by copper sticks in most of the modules (Si2, Li1, Sapp1,2 modules) to exclude a signal leakage and scintillation light from them as an LEE origin. In the TUM93A module, one instrumented $CaWO_4$ was kept to study the radiopurity of the crystal [125, 139]. A completely different geometry of the supporting structures - bronze clamps - was used in the Comm2 module. Clamps are expected to introduce less external stress to the crystal, and therefore, the influence of external stress can be tackled with their help.

- **Housing of the module.** The standard module has the inner housing covered by a scintillating foil to improve the light collection efficiency. In [236], a fraction of the LEE observed in Run34 was attributed to particles hitting the foil. Thanks to the phonon-light technique, it was possible to identify and remove those events with the $LY$ parameter. In order to explore the scintillation light as a possible LEE origin, the foil was removed for some of the modules (Si2, Comm2, Sapp1,2 modules) so that the crystals are surrounded directly by copper walls.
- **Non-scintillating target crystal.** As an ultimate test of scintillation as a source of LEE, Si, i.e., non-scintillating, absorbers were used in the Si2 module. This was complemented by copper holding sticks and copper housings, so no scintillating materials were used in this module design. Since the absorbers face each other, it is also possible to study the contribution of surface contamination to the LEE with this module.

The resulting modules with those modifications applied are shown in Fig. 3.4, and their main characteristics are specified in Tab. 3.1.

All of the detectors discussed here were calibrated with low-activity $^{55}$Fe sources mounted on the wall of the modules. The sources are covered with a layer of glue to reduce the emission of Auger electrons and a thin layer of gold to make them light-tight. Although the presence of the $^{55}$Fe sources contributes to the low-energy background [40], the LEE was also observed in the detectors in Run34 where no $^{55}$Fe calibration sources were in the vicinity of the crystals (Fig. 3.2a).

As in the other CRESST campaigns, in Run36, after the cryostat successfully reached base temperature, a detector optimization period started with the goal to set the detectors up in the optimal working points, ensuring high sensitivity and good stability. After that, a calibration period with a $^{57}$Co source took place, followed by a background data-taking period and a neutron calibration campaign. In Run36, special thermal tests were performed to investigate the influence of the temperature changes on the LEE rate. For this, detectors were purposely warmed up to higher temperatures (from 200 mK to 130 K) and then cooled back down to their operating temperatures around $\mathcal{O}(10\,\text{mK})$, where data-taking was resumed. The impact of those thermal cycles is discussed in Sec. 3.2.4.

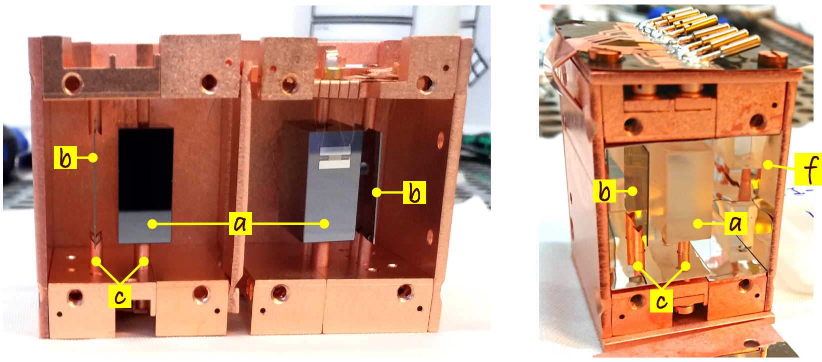

Si-module Li1-module

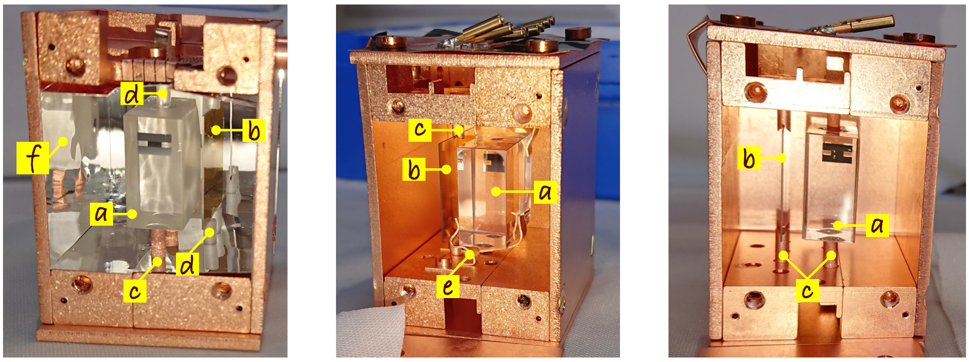

TUM93A-module Comm2-module Sapp1/2-module

Figure 3.4.: Photographs of the detector modules operated in Run36. Bulk target crystals of different materials (a) are paired with wafer detectors (b). Both are equipped with an individual TES. Different holding approaches are used: copper sticks (c), $CaWO_4$ sticks (d), or bronze clamps (e). Detectors are encapsulated in a copper housing in some modules covered with scintillating foil (f). Modifications in comparison to the standard CRESST-III detector module (Fig. 1.8) are listed in the text, and the main properties and performance of those modules are specified in Tab. 3.1.

| Detector | Absorber material | Geometry | Mass, g | Holding scheme | Foil? | TES design | Analysis threshold, eV | Ref. |
|---|---|---|---|---|---|---|---|---|
| Si2-wafer | Si | $20 \times 20 \times 0.4\,\mathrm{mm}^3$ | 0.35 | Cu sticks | No | LD | 10 | [3, 6], Ch. 6 |
| Si2-bulk | Si | $20 \times 20 \times 10\,\mathrm{mm}^3$ | 9 | Cu sticks | No | PD-S | 18 | Ch. 6 |
| Sapp1 | $Al_2O_3$ | $20 \times 20 \times 10\,\mathrm{mm}^3$ | 16 | Cu sticks | No | PD-M | 157 | [3, 115] |
| Sapp2 | $Al_2O_3$ | $20 \times 20 \times 10\,\mathrm{mm}^3$ | 16 | Cu sticks | No | PD-M | 52 | [3, 115] |
| TUM93A | $CaWO_4$ | $20 \times 20 \times 10\,\mathrm{mm}^3$ | 24 | 2 Cu + 1 $CaWO_4$ | Yes | PD-M | 54 | [3, 125] |
| Comm2 | $CaWO_4$ | $20 \times 20 \times 10\,\mathrm{mm}^3$ | 24 | Bronze clamps | No | PD-M | 29 | [3, 237] |
| Li1 | $LiAlO_2$ | $20 \times 20 \times 10\,\mathrm{mm}^3$ | 11 | Cu sticks | Yes | PD-M | 84 | [3, 140, 231, 237] |

Table 3.1.: Characteristics of the CRESST detector modules operated in Run36 and discussed in this work [3]. For the specifications of the TES designs see Fig. 3.1 and Tab. A.1. The thresholds listed in the table are the analysis thresholds defined in the works from the corresponding "Reference" column.

### 3.2.2. Excluding noise and data artifacts as origins of the low-energy excess

Before proceeding to the LEE observations in the different detector modules, a confirmation that the LEE does not consist of noise triggers is provided using the Si2-wafer detector. Details of the analysis of this module are presented in Ch. 6.

The black data points in Fig. 3.5 show the low-energy spectra of the Si2-wafer detector used for the DM search in [6] discussed in Ch. 6. As described in Sec. 6.3, for building the baseline trigger model, the optimum filter is applied to a set of baseline traces randomly collected from the data stream. The total baseline triggers model, shown as the dashed green line in Fig. 3.5, consists of two components: Gaussian noise trigger component and the exponential pollution component associated with the LEE. The right shoulder of the total baseline triggers distribution matches the energy spectrum measured close to threshold very well. This confirms the expectation that many of the randomly collected baselines are coincidental with small pulses from the LEE.

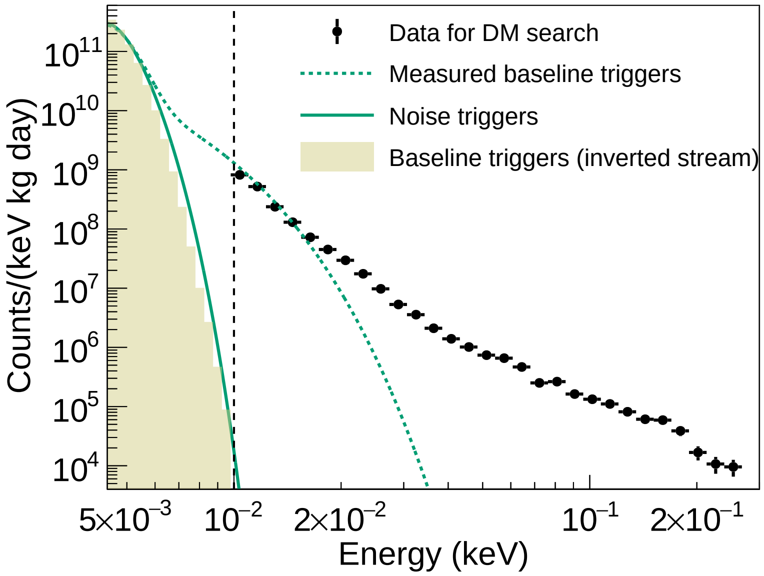

Figure 3.5.: The energy spectrum (black data points) below 300 eV used for the DM analysis from [6] presented in Ch. 6. The dashed green line shows the distribution of the baseline triggers derived from analyzing randomly collected traces. The solid green line shows the distribution of the noise triggers. A gap between this distribution and the data rules out noise triggers as the source of the LEE. The yellow histogram shows the distribution obtained from applying the optimum filter to the inverted data stream, which perfectly agrees with the noise trigger distribution.

The remaining Gaussian component of the baseline trigger model forms the detector noise distribution and is shown with the solid green line. As described in Sec. 6.3, this noise trigger model is additionally validated using the voltage-inverted data stream

---

[3] Here, only the details of the detector modules discussed in this work are presented. For the full overview of the detectors operated in Run36, see, e.g., [125].

where only true noise fluctuations can cause a trigger. The distribution of these upward fluctuations found in the inverted data stream is shown as the yellow histogram in Fig. 3.5. Its agreement with the solid green line confirms the validity of the noise trigger model.

This noise trigger model is used to apply the threshold determination method, allowing only one noise trigger per kg-day of exposure (see Sec. 6.3). It leads to a rather conservative threshold at the level of $7.35\,\sigma_{BL}$. As can be seen in Fig. 3.5, the contribution of the noise triggers (solid green line) to the LEE event rate above the threshold is negligible, which fully excludes noise triggers being responsible for the observed LEE. A similar picture unfolds when investigating the other CRESST detectors.

As an additional confirmation that the measured LEE does not consist of noise triggers or traces containing artifacts, averaged pulses were constructed based on events with energies that do not exceed the threshold by more than two times the baseline energy resolution of the detectors considered. These averaged pulses, therefore, represent a typical pulse shape of the LEE events. They are shown in Fig. 3.6 together with the particle templates used for energy reconstruction in the corresponding detectors. The LEE pulse shapes closely follow the pulse shapes of the analysis templates, confirming that the LEE consists of valid pulses with a pulse shape similar to that of particle recoil events. This also illustrates why the LEE events survive all the quality cuts applied and are not rejected based on the pulse shape parameters.

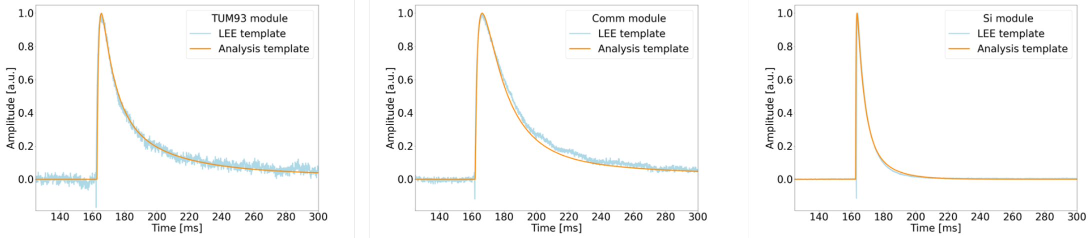

(a) TUM93A (b) Comm2 (c) Si2-wafer

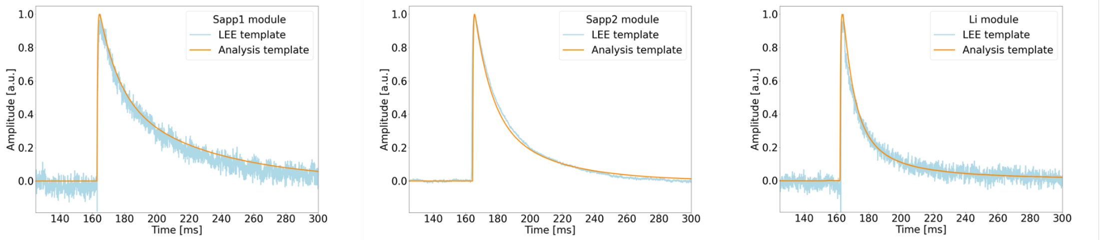

(d) Sapp1 (e) Sapp2 (f) Li1

Figure 3.6.: Pulse templates for particle interactions in the main absorber (orange) and a templates built from LEE events (light blue) for various CRESST-III detectors operated in Run36. The LEE templates are obtained by averaging events with energies that do not exceed the threshold by more than two times the baseline enregy resolution ($E < E_{thr} + 2\sigma_{BL}$) listed in Tab. 3.1.

### 3.2.3. Results obtained from the measured energy spectra

For the energy spectra comparison, detectors listed in Tab. 3.1 are considered. While the analysis of the Si2 module is presented in Ch. 6, the references containing details on the analyses of the other detectors are provided in Tab. 3.1. To achieve the most meaningful comparison across different modules, given the decaying nature of the LEE, a time interval from the background data-taking period where all considered detectors were operated stably was selected[4]. This results in a data set of 105.4 days of total measuring time collected between days 173 and 352 since the cooldown. The resulting energy spectra above the individual energy thresholds scaled with the exposure, as usually used in DM searches, are shown in Fig. 3.7a. Fig. 3.7b shows the same energy spectra scaled only with the measuring time. In both cases the spectra are corrected with the trigger and cut survival probabilities individually calculated for each detector. In addition to the spectra presented in [3], the spectrum measured by the Si2-bulk detector was added to the selection.

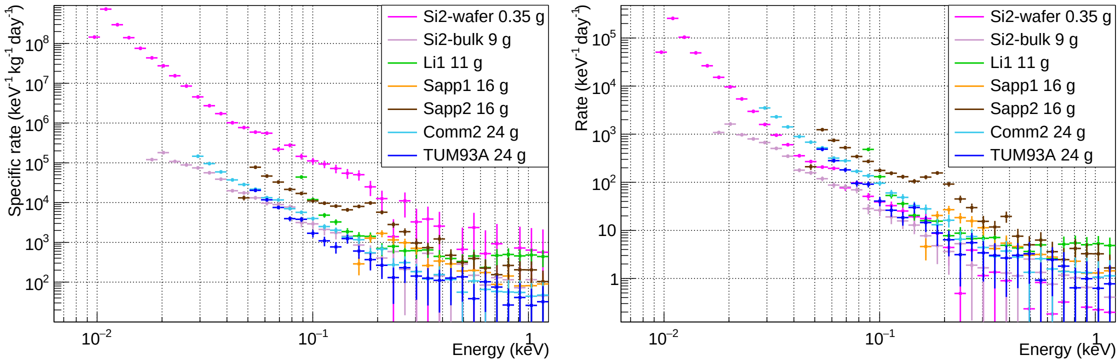

(a) Energy spectra scaled with measuring time and absorber's mass.

(b) Energy spectra scaled with measuring time.

Figure 3.7.: Low-energy spectra measured by various detectors in Run36. The error bars represent the statistical uncertainties.

| Detector | LEE event rate (60-120 eV) between 173 and 352 days since cooldown, day$^{-1}$ |
|---|---|
| Si2-bulk | 3.0±0.2 |
| Si2-wafer | 4.7±0.3 |
| TUM93A | 7.0±0.4 |
| Comm2 | 10.3±0.4 |
| Sapp2 | 21.5±0.5 |

Table 3.2.: LEE event rate in various detectors in Run36.

Despite the modifications to the detector modules presented in Sec. 3.2.1, the LEE was

---

[4] Operating points of the Li1 and Comm2 modules had to be re-adjusted in February 2021 to improve their stability.

observed in all detector modules. Generally, the LEE rates measured by all detectors have similar spectral shapes above ∼60 eV and fall within one order of magnitude when not scaled by the absorber's mass (Fig. 3.7b). Scaling with the mass makes the difference in rates larger - by up to two orders of magnitude (Fig. 3.7a). Rates of events with energies between 60 and 120 eV are provided in Tab. 3.2.

The conclusions from the measured energy spectra shown in Fig. 3.7 are manifold and will be examined case by case below [5]:

- LEE is observed in all absorber materials, confirming that the LEE is a general feature and cannot be attributed to one material only.
- The LEEs observed in $CaWO_4$ absorbers of different origins - TUM93A and Comm2 - have close LEE rates. Since TUM93A crystal has higher radiopurity and is grown with reduced internal stress compared to Comm2, this rules out the major role of the intrinsic background and the crystal lattice stress introduced during the growth process for the LEE formation.
- The LEE rate in the Comm2 detector, where the crystal was supported by an alternative holding scheme, is close to the rates observed in the other detectors. However, there was little control over the force applied from the holding structures to the crystal among the modules during the mounting process. Thus, given the unambiguous observations of LEE enhancement by external stress on the crystal in the SPICE TES-based detector [212], stress induced by the holding structures cannot be fully excluded as a significant contribution to the LEE yet. The CRESST observations could then be explained in case the clamps apply comparable stress as the sticks.
- The absence of the scintillating foil in Si2, Comm2, and Sapp1,2 detectors did not lead to a significant reduction of the LEE rate in comparison to the modules where the foil was present, which excludes foil-related events as a major origin of the LEE. However, as was shown in [140], in the absence of the light detector, foil-related events cannot be identified, and thus, they contribute to the total measured low-energy spectrum.
- The LEE is present and comparable to the other modules in both detectors operated inside the fully non-scintillating Si2 module - Si2-wafer and Si2-bulk. Therefore, the contribution of the local scintillation to the LEE is negligible.
- The LEE rate does not scale with the absorber's mass. This is particularly evident when comparing the energy spectra scaled by the absorber's mass of the Si2-wafer and Si2-bulk detectors, both using the same absorber material (Fig. 3.7a). In fact, the

---

[5] It is important to note that the observations and conclusions presented here are based on the Run36 detectors, where a single TES readout was employed. However, as will be demonstrated in the next Ch. 4, the LEE appears to have a multi-component structure. This suggests that the LEE observed in the Run36 detectors is likely a mixture of two components, complicating direct comparisons of the spectra and making the interpretation less straightforward.

spectra show less variation when not scaled by mass (Fig. 3.7b). Despite the bulk detector being 26 times heavier than the wafer, they exhibit similar LEE absolute rates above 40 eV. At lower energies, the rate increases more rapidly in the wafer detector. This observation makes the hypotheses where the event rate is expected to scale with the absorber mass, as well as DM, unplausible.

- The bulk and wafer detectors have significantly different TES dimensions. For example, the PD-M design, used in most bulk detectors (see Tab. 3.1), has an inner tungsten area 36 times larger and aluminum phonon collectors 16 times larger than the LD design (Fig. 3.1). If the LEE was related to the thermal contraction mismatch between the TES layers and the crystal, one might expect a lower LEE rate in detectors with smaller TES areas. This tendency is not observed. However, the tungsten layer is not evaporated directly onto the crystal surface but on top of an amorphous $SiO_2$ layer. The ratio of the SiO2 surface area is nearly twice as large in the LD design compared to the PD-M. Thus, the comparable absolute LEE rates observed in the Si2-wafer detector may suggest the importance of this $SiO_2$ layer in LEE production.
- In the spectrum of the Sapp2 detector, a bump-like structure occurs at about 180 eV and, similarly, albeit with less significance and at about 160 eV, in TUM93A. The origin of these features is yet not fully understood and is under further investigation. In [115], the time evolution of event rate in this structure in the Sapp2 detector was studied, and a good agreement with the half-life of the $^{55}$Fe was found pointing to the origin of the bump being related to the presence of the calibration source.

### 3.2.4. Results from the time dependence studies of the LEE rate in CRESST

As was observed in Run34 and Run35 detectors, the LEE event rate decayes with time [233]. The time dependence of the LEE rate in Run36 is shown in the top panel of Fig. 3.8a. The time is counted since the cryostat reached the base temperature. A common energy interval from 60 to 120 eV was selected to compare the evolution of the LEE rate with time among different detectors. Thus, the Sapp1 and Li1 detectors are excluded from this comparison due to their higher thresholds. Each data point shows the measured count rate within one week (livetime roughly 150 h, corresponding to three data files), corrected with their individual survival probabilities and measuring time of each period.

As can be seen from Fig. 3.8a, in the background data set, covering the time period from 90 to 380 days after the cooldown, the LEE rate in all detectors is decaying exponentially. Then, a neutron calibration was performed. A short additional background data set was taken right after the neutron calibration source was removed. During this period, no significant impact of the crystals being exposed to neutrons on the LEE rate.

Following the discussions at the EXCESS Workshop [190] and observations by the EDELWEISS collaboration [206], the data-taking was interrupted to investigate how the LEE rate reacts to a temperature change. During this break, the cryostat was warmed up to ∼60 K and then cooled down again to the operating temperature of ∼ 15 mK when the data-taking was resumed, corresponding to data points after 490 days in Fig. 3.8a. Directly after this manipulation, a much higher LEE rate in all detectors was observed, decaying faster than in the background period. Additional warm-ups to lower temperatures of 600 mK and 200 mK did not significantly influence the LEE rate.

To quantify these observations, the data points were fit with an exponentially decaying function $R(t) = A \cdot e^{-t/\tau} + C$ for each detector. Here the bck and after warm-up periods are considered separately. The resulting decay times $\tau$ of each fit are shown in Fig. 3.8b and Fig. 3.8c. The uncertainties of the decay time of the *Comm2* module are higher than in the other modules due to a reduced time range caused by a later start of the data-taking. The average decay time in the background period across different modules is $(149 \pm 40)$ days, while after the warm-up to 60 K it is $(18 \pm 7)$ days. At the bottom of Fig. 3.8a, the decay of the $^{55}$Fe event rate in TUM93A module is shown as a reference. Its decay time is much higher and is $(3.8 \pm 0.3)$ yr, which agrees with the literature value of 3.9 yr (corresponding to a half-life of 2.7 yr [238]).

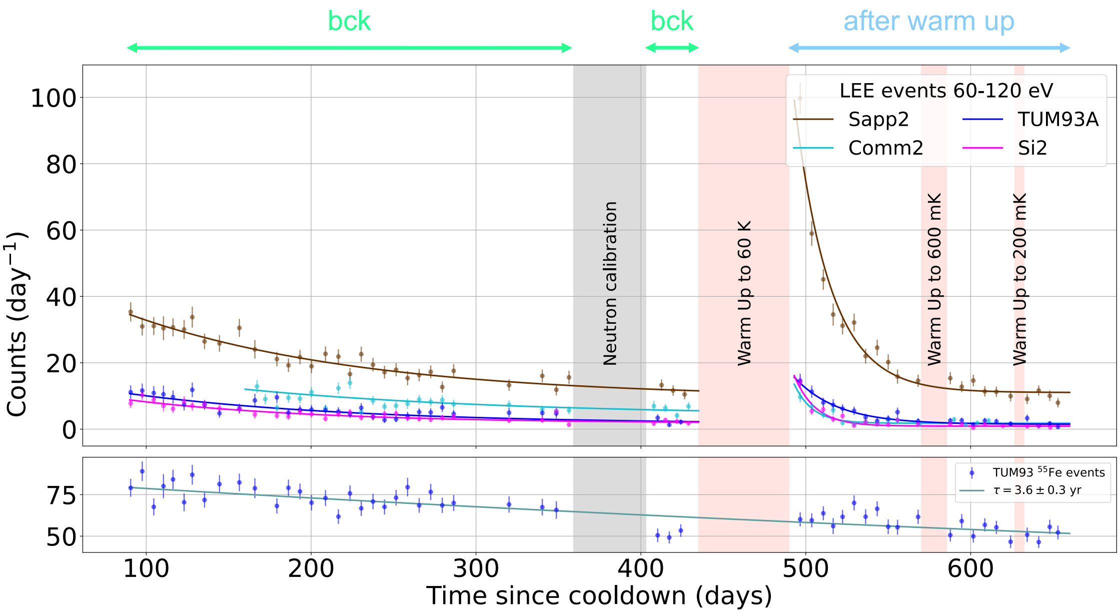

(a) Time evolution of the LEE rate for energies between 60 and 120 eV in different detector modules for bck (90-380 days) and after warm-up (495-670 days) data periods. Solid lines show the fitted functions ($R(t) = A \cdot e^{-t/\tau} + C$). As a reference, the $^{55}$Fe event rate measured in the TUM93A module is shown in the bottom panel. The resulting decay time agrees with the literature value of 3.9 yr [238]. The error bars indicate the statistical uncertainties.

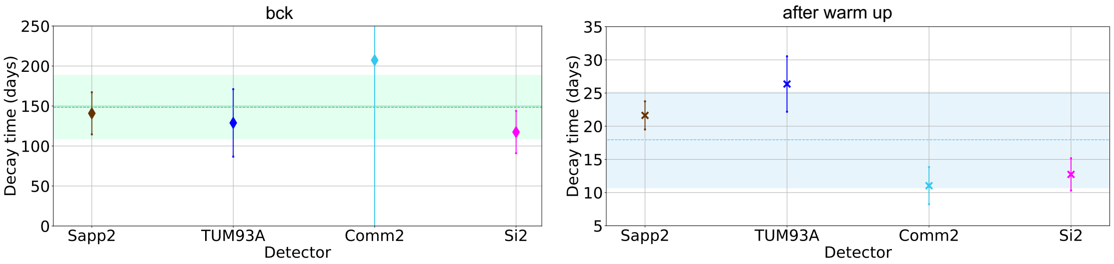

(b) Decay times from the fits for the background period.

(c) Decay times from the fits for the after warm-up period.

Figure 3.8.: Bahavior of the LEE rate with measuring time and after warm-up tests in different detector modules in Run36. The dashed lines and shaded areas in panels (b) and (d) represent the mean values and standard deviations of decay times across four modules.

In the continuation of Run36, more warm-up tests were performed. The cryostat was warmed up to about 3, 30, 11, and 130 K with the same goal of checking the impact of each thermal manipulation on the LEE rate. The evolution of the event rate between 12 and 200 eV in the Si2-wafer detector over the whole Run36 is shown in Fig. 3.9a. Each data point represents one data file of about 50 hours measuring time. The rate is enhanced after the warm-ups to 60, 30, 11, and 130 K, while warm-ups to the lower temperatures do not have a significant effect. It is notable that the impact is higher when warm-ups to higher temperatures are performed. The rate after the warm-up to 130 K, however, does not follow this observation, which might be explained by a longer cooling down period due to technical difficulties, which led to a delayed restart of data-taking. Moreover, the overall trend suggests that the slow decay rate (Fig. 3.9a) is unaffected by temperature manipulations and continues over the whole time of this measuring campaign.

The spectral shape's evolution in the Si2-wafer detector over time is illustrated in Fig. 3.9b. For this analysis, five distinct periods of the run, each spanning roughly 250 hours, were chosen. These periods are highlighted in Fig. 3.9a with corresponding colors for clarity. As anticipated, the spectrum during the latter part of the background period ("bck late") exhibits a reduced rate across all energies compared to the early part of the run ("bck early"). However, after the warm-up to 60 K, the energy spectrum does not uniformly scale up across different energies. While the energies above ~30 eV show a high increase, resulting in rates matching or exceeding those at the beginning of the run, the lower end of the spectrum experiences a lesser effect. The LEE rate is at its lowest at the end of the "after 11 K" period, when a long period of time has elapsed since the cooldown from room temperature, and the LEE component with the short lifetime which was (re)introduced by the warm-up tests has almost decayed away. After the warm-up to 130 K, a similar pattern as after 60 K is observed.

To illustrate this varying behavior across different energy ranges, the low-energy spectrum was divided into two intervals: from 12 to 30 eV and from 30 eV to 100 eV. The total rates within these intervals $R$ were plotted in Fig. 3.9c relative to the rates observed at the beginning of the background data-taking period ("bck early"). While the rates in both energy ranges decline similarly over time in the background period ($R_{\text{bck early}} \approx 5 R_{\text{bck late}}$), the increase in event rate above 30 eV following the warm-ups to 60 and 130 K is 7 to 9 times greater than that in the energy range below 30 eV. Thus, the LEE energy spectrum changes its shape after the warm-ups to $\mathcal{O}(10\,\text{K})$, which, together with the different decay times, strongly suggests the presence of the multiple LEE components that dominate at different energies. Additionally, only the fast-decaying, more highly energetic component seems to be repopulated when warming up the detector. A similar conclusion was made in the analysis of the Sapp2 detector presented in [115]. Detailed modeling of the time-dependent spectral shape for Run36 detectors is being done in the scope of [239].

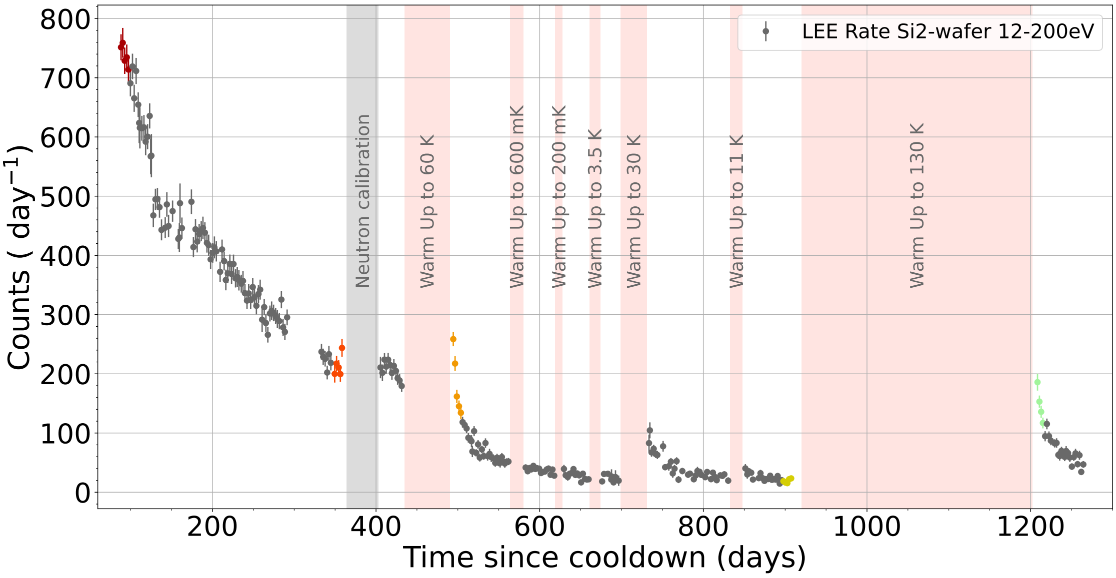

(a) Time evolution of the LEE rate for energies between 12 and 200 eV in the Si2-wafer detector. Each data point corresponds to one data segment of about 50 h. While the rate is decaying over the whole measuring time of the data-taking, the thermal cycles to 60, 30, 11, and 130 K resulted in a significant rate increase followed by a rapid decay. The error bars indicate the statistical uncertainties. The colors correspond to the selected periods whose spectra are shown in Fig. 3.9b.

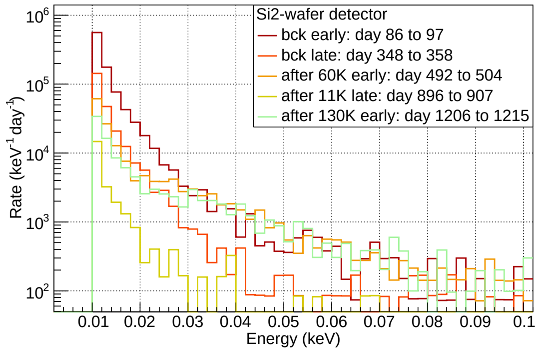

(b) Energy spectra measured by the Si2-wafer detector in different run periods indicated in Fig. 3.9a. Rate enhancement following the warm-ups is not uniform across different energies, resulting in the LEE spectral shape varying with the measuring time.

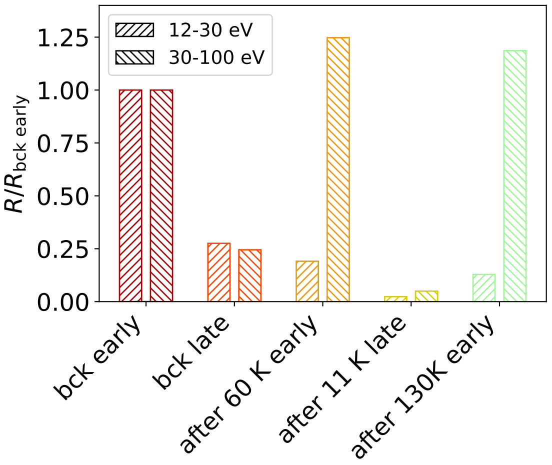

(c) Event rates $R$ in two energy intervals - 12-30 eV and 30-100 eV - measured in different run periods scaled to the rate at the beginning of the background data-taking $R_{\text{bck early}}$ Colors are indicated in Fig. 3.9a.

Figure 3.9.: Evolution of the LEE rate and spectral shape with time in the Si2-wafer detector in Run36.

### 3.2.5. Exploring crystal surface contaminations as a possible LEE origin

The fully non-scintillating Si module enables the comparison of signals simultaneously recorded in the wafer and bulk detectors facing each other. To investigate the crystal surface background contribution to the LEE (Fig. 3.4), the LEE events measured in the *wafer* detector are divided into three groups based on their energy $E_w$: from 10 to 15 eV, from 15 to 50 eV, and from 50 to 300 eV. The calibration lines $^{55}$Mn K$_\alpha$ and K$_\beta$ are used as reference. If an X-ray from the calibration source hits the wafer and deposits all of its energy in the wafer, no coinciding signal is expected to be measured by the bulk detector. Fig. 3.10a shows the energy in the bulk detector versus the energy measured in the wafer detector for the three LEE groups and the calibration lines, while Fig. 3.10b contains the corresponding density distributions of the energies measured by the bulk detector. In addition, the noise model obtained with the method described in Sec. 2.3.3 is plotted. The energy distributions closely follow the expected noise distribution, confirming that the LEE events measured by the wafer detectors do not cause a signal in the bulk detector.

As described in Ch. 6, the coincidence cut applied to the Si2-wafer detector data rejects all coincident triggers with the bulk detector within a recording window. This cut removes only a $(0.9 \pm 0.5)\%$ fraction of events below 300 eV. Therefore, the crystal surface background can be excluded as a dominant origin of the LEE.

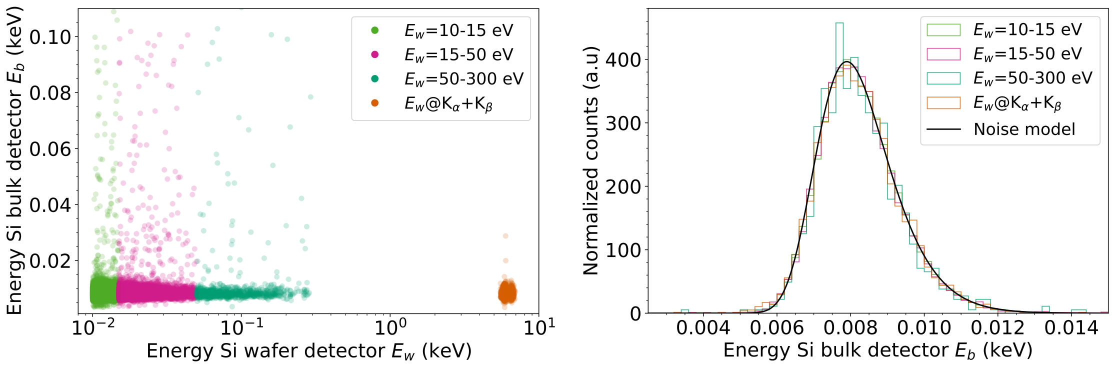

(a) Energy measured in the bulk detector vs. energy measured in the wafer detector for different groups of events in the wafer detector: LEE events in three energy ranges specified in the legend and the calibration $^{55}$Mn K$_\alpha$ and K$_\beta$ X-ray hits.

(b) Histograms show the density distributions of the energies measured by the bulk detector for the different groups of events measured by the wafer detector. The solid black line shows the noise trigger model for the bulk detector obtained in Sec. 2.3.3.

Figure 3.10.: Distribution of the energy measured by the Si2-bulk detector $E_b$ for the events in the Si2-wafer detector with different energies $E_w$.

## 3.3. Conclusions and outlook

The Low-energy excess (LEE) is currently the main challenge for CRESST in probing new parameter space for hypothetical low-mass, weakly interacting dark matter candidates.

With the data collected during the recent CRESST measurement campaign, numerous modifications to the standard detector design were implemented to probe the potential origins of the LEE. In the scope of this thesis and in collaboration with CRESST, I investigated several possible causes based on these data, leading to the following conclusions at this stage.

1. **The LEE is neither caused by noise triggers nor artifacts in the data stream.** The noise trigger distribution is well understood and does not contribute to the observed trigger rate above the threshold. The averaged pulse shape of the LEE events does not differ significantly from that of particle recoil events.
2. **The LEE is not specific to one material but rather a universal feature** for low-threshold detectors based on the CRESST technology.
3. Crystals made of the same material, but grown using different techniques by different producers, show similar LEE rates (TUM93A and Comm2 in Fig. 3.7a). Contrary to this, the crystals of the same origin show a difference in the LEE rates by more than an order of magnitude (det F and det J in Fig. 3.3a). From those two observations, we infer that **the LEE rate is not dominated by either intrinsic radioactive background or crystal lattice stress introduced during the growth process.**
4. Some modules were equipped with scintillating foil, while others were not; one module had no scintillating elements at all. Comparing the observed low-energy spectra **allows us to exclude foil-related events and local scintillation light as significant contributors to the LEE**.
5. Multiple detector modules, particularly the module containing both a wafer detector and a much heavier bulk detector of the same material, demonstrate that **the LEE does not directly scale with the absorber's mass**.
6. This module also enables the use of a coincidence analysis between the wafer and the bulk to tag events originating on the crystal surface, revealing that **surface contaminations do not contribute significantly to the LEE**.
7. The LEE rate decays exponentially with time since cooldown with a time constant of $(149 \pm 40)$ days. Furthermore, the LEE rate first rises sharply and then decays with a faster time constant of $(18 \pm 7)$ days after the detectors are briefly heated to $(O)(10\,\mathrm{K})$ and then cooled down to operating mK temperatures. These observations **rule out particle-induced backgrounds and point to solid-state effects as the dominant source of the LEE**.

This brings us to the two possible remaining hypotheses on the LEE origin.

First, although some detectors had different holding schemes, the possibility that a significant fraction of the LEE is introduced by **external stress from the holding structures** cannot be excluded at this time. Since the modules are assembled manually, the forces applied to the crystals can vary considerably, even when an identical approach to crystal holding is used. Thus the mechanical stress from the holders remains one of the most plausible hypotheses, especially in light of the direct comparison of the LEE measured in the ″low″ and ″high″ external stress implementations reported by the SPICE collaboration in [207].

To explore this possibility further, CRESST is operating various dedicated detectors in the recently started data-taking campaign. First, external stress from the holders is reduced by using so-called gravity-assisted holders introduced in [141], where absorbers are held in place solely by their own weight. If external stress from the holders plays a significant role in the overall LEE rate, one would expect a reduction, or at least some observable effect, in the measured LEEs in the modules featuring this holding scheme. The second approach to investigate the contribution of external stress to the LEE is based on the idea that such stress relaxation events are likely to form near the holder-crystal interface. If the holder itself is a crystal, the resulting phonon signal is expected to originate in both the target and holder crystals and/or to be transmitted between them. The effective propagation of the phonon signal through contact points has been confirmed by various CRESST measurements [240, 241]. To test this hypothesis, in the mini-Beaker design [141], the target crystal is attached via a glue spot to a ring-shaped crystal equipped with a TES. Thus, the ring functions as an instrumented holding structure. If both TESs – on the target crystal and the ring crystal – have sufficient sensitivity, studying the energy sharing and pulse shapes of coincident low-energy events should allow the identification of the event population caused by external stress at the contact points.

The second remaining plausible source of the LEE is **stress introduced at the interface between the crystal and the TES or in the TES structure itself.** To test it, several independent measurements were performed with crystals equipped with two TESs: by CRESST, reported in [211], by SPICE in [212], and by NUCLEUS in [4], which will be presented in Ch. 4. All of these measurements showed that some of the measured LEE events are seen by only one of the two TESs (“single”), while the remaining fraction is observed by both (“shared”), with roughly equal energy sharing. While the CRESST data discussed in this chapter do not allow us to distinguish these populations, several doubleTES modules [141] have been installed and are currently in operation in the recently started CRESST campaign. These detectors enable studying the different LEE contributions and their pulse shapes in a low-background environment. Another exciting insight expected from these data is the understanding of the total LEE rate evolution by investigating the time dependence of the single and shared LEE rates separately. In the next chapter, where the results of the NUCLEUS *double-TES* detector are presented, the discussion of possible applications of the double-TES detectors will be continued.

# 4. Results from the NUCLEUS *double-TES* detector

One of the hypotheses about the origin of the LEE in the TES-based detectors that remains plausible after the CRESST studies presented in Ch. 3 is the relaxation of stress induced at the interfaces between the TES films and the crystal surfaces. A natural approach to test this idea is to equip a detector with several phonon sensors and read out the signal from each of them simultaneously and separately. In this case, the signal originating in the crystal volume, such as particle recoils, is expected to be shared among the sensors. If there is a signal originating in the close vicinity to a TES, as in the case of TES-related events, the closer TES is expected to measure a higher fraction of the total deposited energy, if not all of it. Thus, using more than one TES channel should allow for the identification of the events in the absorber volume that are of interest in the DM and CE$\nu$NS searches.

A detector consisting of an absorber crystal with two TESs fabricated on its surface was developed within the CRESST collaboration and showed promising results in the identification of different LEE components [242]. Following this successful proof of principle, the NUCLEUS collaboration produced and operated two detectors, each with two TES channels, called here *double-TES*. Successfully achieving the low-energy thresholds well below 100 eV allowed measuring the LEE with high event statistics and addressing the following questions:

- Are the LEE events produced in the crystal?
- Is there a TES-related population in the measured LEE?
- What is the fraction of of the TES-related event population in the total LEE rate?

In this chapter, I begin by briefly reviewing previous LEE observations with the NUCLEUS prototype detectors in Sec. 4.1. Then I introduce the novel NUCLEUS *double-TES* detectors in Sec. 4.2, followed by a detailed analysis and the results from the first operation of these detectors in Sec. 4.3. Next, in Sec. 4.4, I present results from an extensive series of measurements with the *double-TES* detector conducted at TUM, under various background conditions. Sec. 4.5 summarizes the key findings from these measurements, and Sec. 4.6 offers a comprehensive discussion. Finally, Sec. 4.6 outlines the next steps in the NUCLEUS LEE investigation and mitigation strategy.

## 4.1. LEE observations in the NUCLEUS prototype measurements

The first NUCLEUS prototype measurement achieving a back then unprecedented low energy threshold of 19.7 eV was performed in 2017 with a 0.5 g $Al_2O_3$ detector. That was the first measurement ("Run1") in the series of NUCLEUS prototype measurements performed in 2017-2019 at Max Planck Institute for Physics presented in details in [40].

Here, the main observations regarding the LEE are briefly summarized and put in the context of the CRESST observations presented in Ch. 3.

The main goal of this series of measurements was testing different NUCLEUS components, such as instrumented inner and outer veto, discussed in Sec. 1.2.2.2. The sketches of the prototype detector components in different measurement runs are shown in Fig. 4.1a. In Run1, the target crystal was supported by the four $Al_2O_3$ spheres (three from below and 1 from above) with 1 mm diameter and a bronze clamp. In the second run - "Run2" - the target crystal was pressed between two elastic 200 $\mu$m thick silicon wafers, each equipped with a TES. Thus the wafers were playing the role of the inner veto. They supported the target crystal with pyramidal structures on their inner sides, providing point-like mechanical contacts. Thus the veto wafers have a cross-talk of the signal with the target crystal. Although the wafers were also instrumented with individual TESs, they were operated simultaneously with the target crystal only in one of the next runs - "Run4" [40].

Fig. 4.1b shows the low-energy parts of the measured energy spectra in the three considered runs. In Run1, the crystal was irradiated with a $^{55}$Fe source for energy calibration, while during Run2, the calibration source was removed. Comparing the LEE spectra of Run1 and Run2 allowed to conclude that while some low-energy background contribution can be expected from a $^{55}$Fe source, it is not responsible for a dominant contribution of the observed LEE [40].

Fig. 4.1b also contains the low-energy spectrum of the CRESST-III Sapp2 detector discussed in Sec. 3.2.3. The NUCLEUS prototype above ground measurements have up to almost three orders of magnitude higher LEE at 100 eV than the CRESST $Al_2O_3$ detector, operated at LNGS, when scaled by the target masses. The difference gets by a factor of 30 smaller when no scaling with the mass is considered.

One mechanism that could partially explain the difference in the observed LEE rates is the decaying nature of the LEE rate with time. As was shown in Sec. 3.2.4, the LEE observed in CRESST is decaying with time since cooldown. At day 90, the LEE rate in the 60 to 120 eV energy range in Sapp2 detector is (35.3±2.9) Counts/day (see Fig. 3.8a). The NUCLEUS prototype measurements were taken only a few days after the cryostat reached the base temperature, and the rate in the same energy range was (1026±104) Counts/day in Run1 and (589±78) Counts/day in Run4. Assuming the NUCLEUS LEE rate is also decaying with the decay time of (140.8±26.3) days obtained from the fits for Sapp2 detector in the background data-taking period (Fig. 3.8b), the expected reduction of the rate at day 90 is $^{R(t=2)}/_{R(t=90)} = 1.9 \pm 0.2$. However, assuming the fast decay time of $(21.6 \pm 2.1)$ days (Fig. 3.8c) expected to be observed right after the cooldowns from $\mathcal{O}(10\,\mathrm{K})$, the reduction factor is $^{R(t=2)}/_{R(t=90)} = 58.8 \pm 23.3$. The fast decay of the rate thus could partially[1] explain the observed difference in the rates between the surface measurements taken immediately after a cooldown and the CRESST measurements at LNGS, usually starting background data-taking several months after a cooldown. However, the reduction factor depends

---

[1] In case no scaling with the target mass is assumed, the fast exponential decay of the rate can fully explain the observed rate difference.

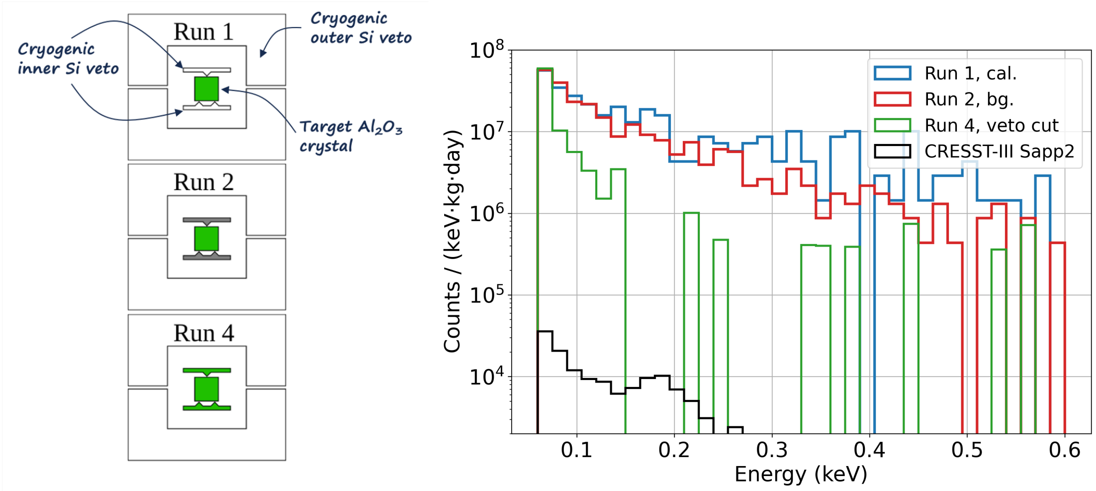

(a) Sketch of the prototype detector components. Green identifies components operated in a given run, grey - present but passive components, and white - not present components.

(b) Energy spectra at low energies for the three considered NUCLEUS runs. In Run1, the target crystal was irradiated with a $^{55}$Fe calibration source, while in Run2 the source was removed. In Run4, the inner veto was operated simultaneously, allowing performing a veto cut that reduced the observed LEE. The spectrum from the CRESST-III Sapp2 detector [3] discussed in Sec. 3.2.3 is shown for comparison.

Figure 4.1.: Overview of the LEE observations in the series of the above-ground NUCLEUS prototype measurements with a 0.5 g $Al_2O_3$ detector of 5 $mm^3$. The figures are adapted from [243], the measurements are discussed in detail in [40], and the results from Run1 are presented in [59, 64, 181], from Run4 in [187].

strongly on the amplitude ratio between the slow and fast decaying components of the LEE rates and the exact decay times. Not identical behavior of the spectral shape across different energies discussed in Sec. 3.2.4 makes this description even more complex and requires more dedicated studies, e.g., longer measurements at the surface facilities.

The active inner veto in Run4 enabled the use of an anticoincidence veto cut. This cut aims to select only events originating in the target crystal, such as particle recoils, by analyzing the amplitude ratios of the three channels (target crystal + two veto wafers). The spectrum after applying the veto cut, shown in Fig. 4.1b, remains flat down to ∼300 eV and has a sharp rise from 100 eV toward the threshold. This suggests that a portion of the observed LEE was successfully removed using information from the veto's TESs. However, this result may have different interpretations of the origin of the removed LEE events, such as: (i) local low-energy radiation may have been absorbed by the veto, preventing it from reaching the target crystal, (ii) those events could originate at the interfaces between the crystal and its holding structures (e.g., stress-related), causing the deposited energy to be shared differently between the channels compared to particle recoils within the crystal, (iii) events might leak into the crystal through the holders and remain in the final spectrum in the case of non-instrumented holders (e.g. Run1 or Run2). The next generation of measurements with an active inner veto, currently in preparation, has the potential to provide a definitive answer to these possibilities.

## 4.2. *Double-TES* detector description

To test the TES-related origin of the LEE, NUCLEUS operated a crystal equipped with not one, but two TES – the *double-TES* detector. Due to the standard NUCLEUS detector production procedure, obtaining the *double-TES* detectors did not require a dedicated R&D process. NUCLEUS absorber cubes are usually cut from a crystal substrate only after the TES fabrication process. Since, in this case, the TESs experience the same fabrication process, this unifies the performance among different detectors. An $Al_2O_3$ substrate containing a 4×4 detector array is shown in Fig. 4.2a. Normally, 16 detectors would be cut from it, each equipped with one of the TESs shown in white. The TES design used for this 4×4 detector array and its dimensions are shown in Fig. 4.3. It is noteworthy that in this design, the phonon collectors are made purely from aluminum in contrast to the TESs used in the CRESST and NUCLEUS experiments so far, where phonon collectors were W/Al bilayers as in Fig. 3.1.

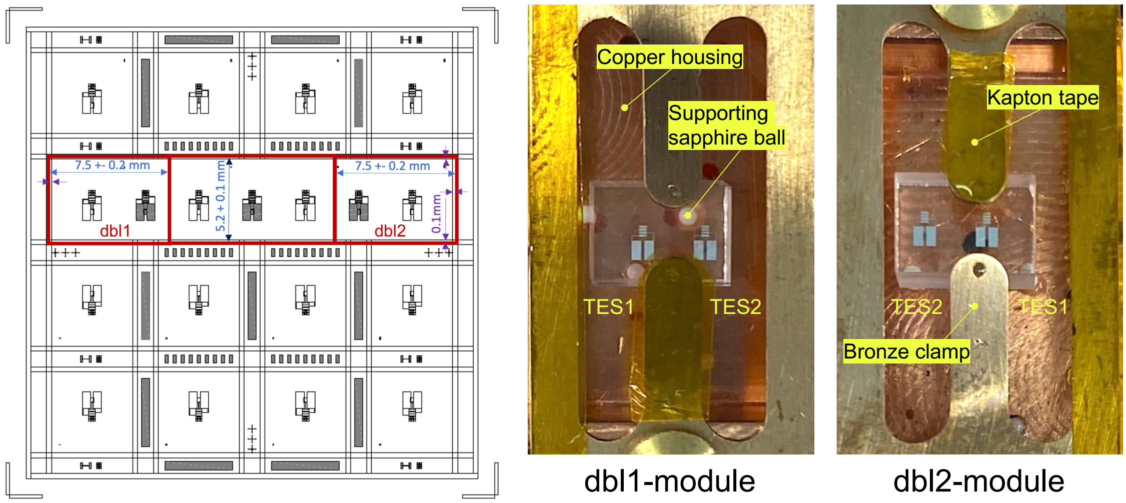

(a) (b)

Figure 4.2.: (a) Scheme of a 4×4 cube array with TESs fabricated on its surface before cutting into separate detector cubes. The TESs initially intended for testing purposes are depicted in dark grey. Normally, cutting is done according to the black lines shown. A new cutting approach following the red lines and using the test TESs allowed the production of two *double-TES* modules and one absorber with three TES attached. (b) Photos of the two *double-TES* modules: *dbl1* and *dbl2*. The crystal absorbers are each supported by two bronze clamps with 1 mm sapphire balls underneath each clamp and three sapphire balls from below partially visible and exemplarily indicated in the photo of *dbl1*. Kapton tape covers certain spots, providing an isolation layer to prevent the bond wires from touching the housing or the clamps.

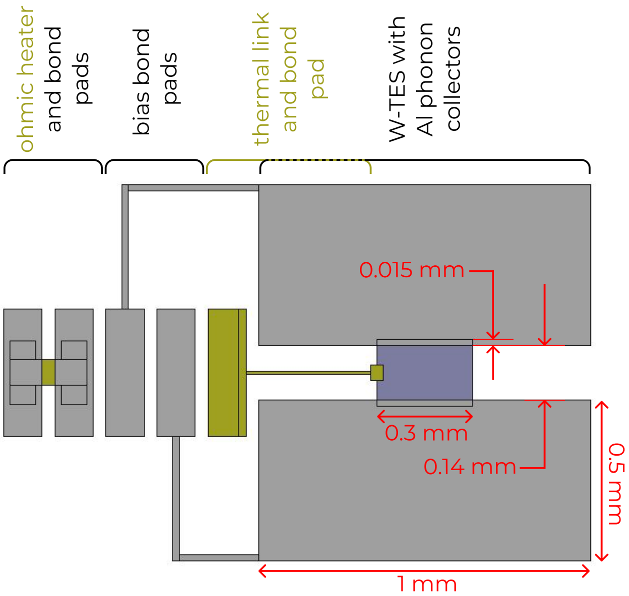

Figure 4.3.: Geometry of the TES used for the NUCLEUS *double-TES* detectors. Purple color represents the tungsten layer of ~180 nm thickness, gray - aluminum of ~1 $\mu$m, and yellow - gold of ~80 nm for the heater and thermal link and ~700 nm for the thermal link contact pad. The tungsten and aluminum parts are evaporated on a ~50 nm thick layer of $SiO_2$. In each *double-TES* detector, two of those structures are used, as shown in Fig. 4.2. The scheme is provided by Johannes Rothe (TUM).

The second row of the array has additional three TESs fabricated for testing purposes, marked with dark grey, which are otherwise fully identical to the other TESs on this substrate. The cutting pattern in the second row was changed and was performed following the red lines in Fig. 4.2a, resulting in one detector equipped with three TESs and two detectors with two TESs - *double-TES*.

These two $Al_2O_3$ *double-TES* absorbers with the dimensions of $5 \times 5 \times 7\,\mathrm{mm}^3$ and $5 \times 5 \times 7.5\,\mathrm{mm}^3$ were mounted into separate modules - *dbl1* and *dbl2* - shown in Fig. 4.2b. Three sapphire balls with 1 mm diameter support the crystals from below and are partially visible in Fig. 4.2b. From above, the crystals are fixed at their positions by two bronze clamps, each of which has a sapphire ball underneath as a contact point to the crystal. The module's housings are made of copper. A $^{55}$Fe calibration source is mounted above the detectors shining on the side of the crystal where the TESs are fabricated.

## 4.3. First NUCLEUS measurements with the *double-TES* detectors

### 4.3.1. Data description

Both *dbl1* and *dbl2* detector modules were operated in a Bluefors dry dilution refrigerator installed in a laboratory located on the first floor of the Physics Department of the Technical

University of Munich. The vibrations from the pulse tube were effectively attenuated by a two-stage spring decoupling system [185], and no additional shielding against the backgrounds was used. The measurements were taken between June 26 and July 4, 2023.[2]

The standard way of optimizing detectors equipped with a single TES relies on adjusting the bias current through the TES circuit (Fig. 1.3). Detectors are then put to the desired operating point on the transition curve with the help of an ohmic heater, as described in 2.2.2. In the case of the NUCLEUS *double-TES* detectors, each of the TESs is part of a separate current circuit and has its own heater. However, optimizing the TESs independently is impossible due to severe cross-talk between them through the crystal volume. Therefore, only one of the heaters was used to stabilize both TESs at their operating points - heater of TES2 in *dbl1* and heater of TES1 on *dbl2*. Due to the similar transition curve shapes shown in Fig. 4.4, for the *dbl2* module, the same bias current of 2 $\mu$A was used for both TESs. For *dbl1* module, different bias currents were required to overlap the optimal working points at the same heater voltage value (1.5 $\mu$A and 3 $\mu$A).

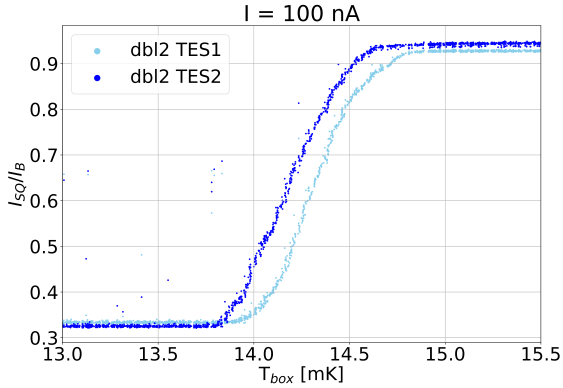

Figure 4.4.: Transition curves of TES1 and TES2 of the *dbl2* module measured with the bias current of 100 nA.

Both modules were operated successfully and showed good performances: 9.9 eV and 4.7 eV BL resolution in two TESs of the *dbl1* module and 6.7 eV and 6.2 eV in *dbl2*. In this work, I will focus on the analysis and the results obtained from the data taken with the *dbl2* module since its TESs had more similar performance, which is beneficial for the LEE studies. The main properties of the module and the data included in this analysis are presented in Tab. 4.1.

The data were continuously recorded in the VDAQ2 (Sec. 2.2.1) format with 100 kHz sampling frequency for three channels: ch 0 - heater stream, ch1 - TES1, ch2 - TES2. Control pulses are injected every 9 seconds via the heater of TES1. Two test pulses are fired between each control pulse with the sequential amplitudes of 0.18%, 2.36%, 6.19%, 15.2%, 67%, and 78% of the control pulse amplitude.

---

[2] Detector optimization and data taking were performed by Nicole Schermer and Johannes Rothe, Technical University of Munich

The total duration of the measurement considered here is 17.08 h. File list is provided in App. C.1. The stability of both TESs during this measurement time can be seen in Fig. 4.5. Only the periods with the stable detector response, 12.0 h in total, marked with green, were manually selected and are in the analysis described in the next section.

| *dbl2* module | TES1 | TES2 |
|---|---|---|
| Absorber material | $Al_2O_3$ | |
| Absorber mass | 0.75 g | |
| Sampling rate | 100 kHz | |
| Record window | 2048 samples ⇔ 20 ms | |
| Date of the measurement | 27 June 2023 (2-3 days after cooldown) | |
| Measuring time | 17.08 h | |
| Stable measuring time | 12.0 h | |
| Control pulses | Every 9 seconds | |
| Test pulses | 2 test pulses between each 2 control pulses | |
| Test pulse amplitudes | 0.18%, 2.36%, 6.19%, 15.2%, 67%, 78% of CP | |
| Linear range | below 0.2 V ⇔ 1.3 keV | below 0.2 V ⇔ 1.6 keV |
| Trigger threshold | 4.2 mV | 3.12 mV |
| Energy threshold[3] | $(27.2 \pm 0.8)$ eV | $(24.8 \pm 0.8)$ eV |
| Baseline resolution | $(1.05 \pm 0.03)$ mV ⇔ $(6.8 \pm 0.2)$ eV | $(0.78 \pm 0.03)$ mV ⇔ $(6.2 \pm 0.2)$ eV |
| Calibration factors | 6.47 keV/V | 7.89 keV/V |

Table 4.1.: Characteristics of the *dbl2* module and the dataset analyzed and presented in this chapter.

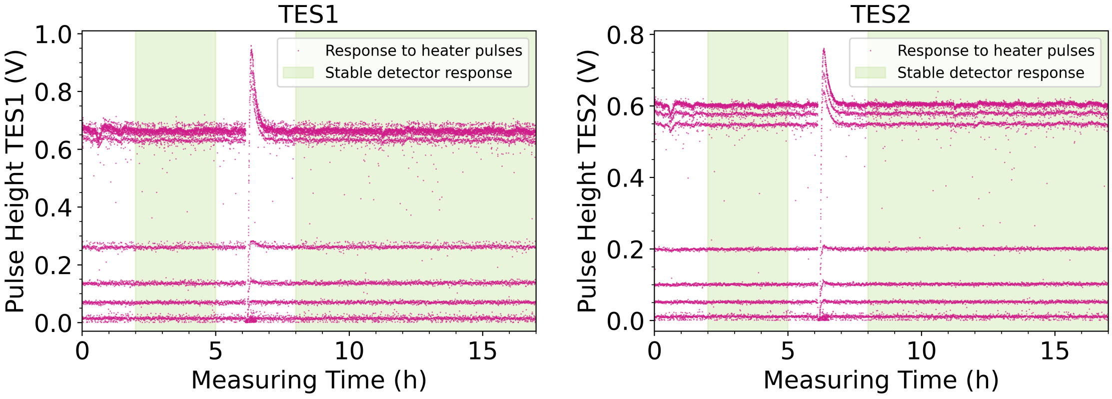

(a)

(b)

Figure 4.5.: Stability of the *dbl2* module over the measuring time. Magenta dots show the detector's responses to heater pulses. Only the periods with the stable detector response shaded with green were used for the analysis.

---

[2] The values quoted here represent $4\sigma_{BL}$ level in both channels. Simultaneous triggering at this level in both channels allows having a negligible contribution of noise triggers, as discussed in Sec. 4.3.2.1. However, identification of different event populations on event-by-event basis at this level is strongly limited and becomes effective only at higher energies of around 40 eV (Sec. 4.3.3.3).

### 4.3.2. Special aspects of analysis

While the analysis of the *double-TES* detector presented here follows the main principles described in Ch. 2, the presence of the second channel opens up new opportunities and requires extending the standard analysis workflow. In this subchapter, I focus on the data processing and analysis approaches required by the two-channel read-out while still listing all the steps for completeness.

#### 4.3.2.1. Triggering

Two TES data streams were both triggered with OF at $4\,\sigma_{BL}$ thresholds of 4.2 mV and 3.12 mV for TES1 and TES2 respectively. A triggered event consists of two simultaneously recorded windows of 2048 samples corresponding to 20.5 ms - one for each TES channel, as shown in Fig. 4.6. In case both channels are triggered within one record window, as illustrated in Fig. 4.6a and 4.6b, the priority is always given to TES1. This means that the TES1 trigger, i.e., the maximum of the filtered trace, is set to the default triggering position at $^1/_4$ of the record window, and the traces for both channels are recorded around this position. In case TES1 and TES2 triggers are not caused by a simultaneous pulse, as in Fig. 4.6b, the pulse in TES2 might be away from the triggering position and is not considered as a main pulse in the following analysis. This leads to a slightly higher deadtime of the TES2 channel than that of TES1.

To estimate time delays between the pulses in two channels caused by the same energy deposition in the absorber (as in Fig. 4.6a), the difference between the maximum positions of the filtered traces in two channels $\Delta t$ was calculated. Only simultaneously triggered pulses with the amplitudes above $8\,\sigma_{BL}$ were considered to ensure a high signal-to-noise ratio and, therefore, a precise maximum position evaluation. The distribution of $\Delta t$ is shown in Fig. 4.7. Here and throughout this chapter, pulses are defined as "simultaneous" if $|\Delta t| \leq 50\,\mu$s, which corresponds to 5 time samples and falls within $4\sigma$ boundaries.

Usually, the triggering threshold is set at higher values of 5-7 $\sigma_{BL}$ in order to minimize the number of noise triggers, e.g., how it was done in the data presented in Ch. 5 and 6. However, physical events in the crystal volume are expected to cause simultaneous pulses in both channels and thus cause triggers in both TESs at the same time. Therefore, only *simultaneous* noise triggers would contribute to the final measured energy spectrum of interest, while noise triggers in only one of the channels get rejected. This allows to choose lower threshold values for the *double-TES* detectors.

The expected number of individual and simultaneous noise triggers is estimated based on the voltage-inverted stream. As was discussed in Sec. 3.2.2, only noise fluctuates in both directions and thus can cause a trigger in the inverted data stream. First, as in the case of a single read-out, following the procedure described in Sec. 2.3.3 for the inverted data stream, we obtained the OF amplitude distributions for TES1 and TES2 channels, shown as the pink histograms in Fig. 4.8a and Fig. 4.8c. Those distributions are fit under the assumption of the Gaussian noise with the function from Eq. 2.5. The fits are shown with the solid black lines. Using these noise models we estimate the noise trigger rates

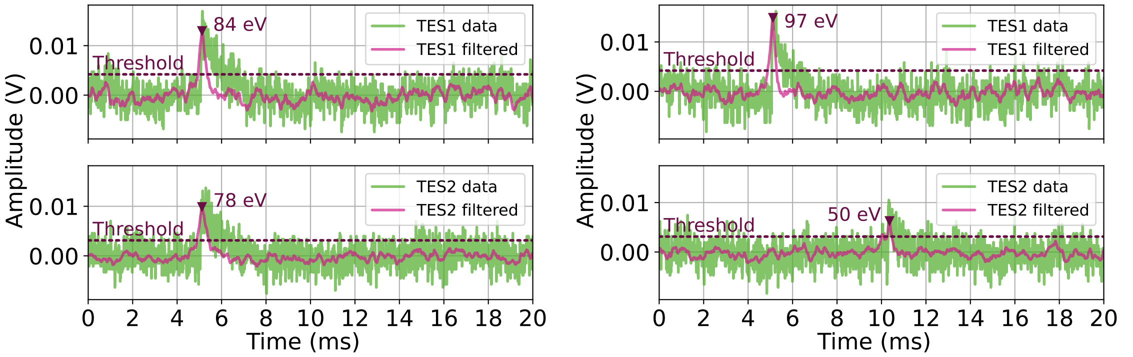

(a) TES1 and TES2 triggered simultaneously.

(b) TES1 and TES2 triggered at different positions within one record window. The triggering position of the event is assigned to the TES1 trigger.

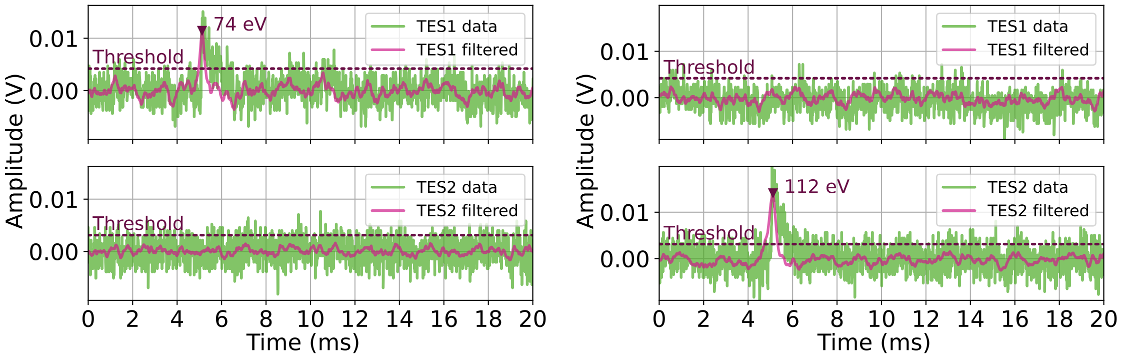

(c) Only TES1 triggered.

(d) Only TES2 triggered.

Figure 4.6.: Examples of the triggered events in the *dbl2* module. Raw data are shown in green, while the filtered traces are illustrated with magenta.

at any threshold value for each channel independently shown with the solid black line in Fig. 4.8b and Fig. 4.8d. The energy threshold of $4\,\sigma_{BL}$ results in $7.8{\cdot}10^7$ noise counts per kg-day of exposure in TES1 and $6.1{\cdot}10^7$ in TES2. Compared to the actual trigger rate from the original data stream, those numbers translate to 20% and 19% of the total single-channel trigger rate, respectively. The numbers are provided in Tab. 4.2.

However, recording two channels significantly decreases the noise trigger rate when only simultaneous events are selected. To obtain the distribution of the simultaneous noise triggers, only the events where the OF maxima exceed the $4\,\sigma_{BL}$ thresholds in both channels within $\pm 50\,\mu$s are selected from the original distributions (pink histograms). Those events are shown as the yellow histograms in Fig. 4.8a and Fig. 4.8c, which are also fit with Eq. 2.5. These fits, shown as the green lines, provide the simultaneous trigger model, which allows estimation of the number of expected *simultaneous* noise triggers as a function of the triggering threshold, shown as the green line in Fig. 4.8b and Fig. 4.8d. For triggering both channels at $4\,\sigma_{BL}$, the simultaneous noise triggers occupy only about 0.1% of the total simultaneous trigger rate (see Tab. 4.2).

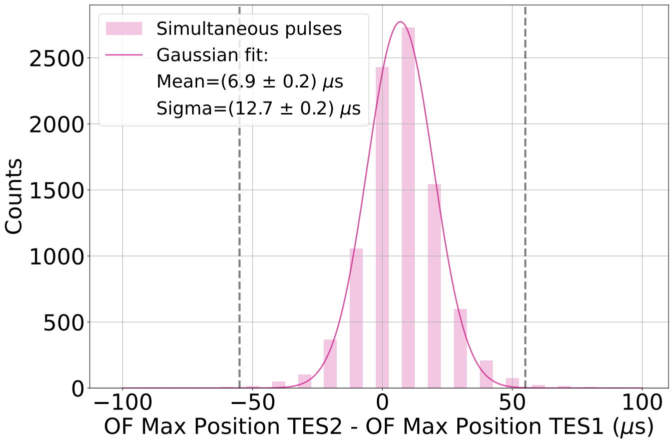

Figure 4.7.: Difference between the OF Maximum Positions in TES2 and TES1 for simultaneous pulses in the linear range of the detector response. Only pulses with the Amplitude higher than 8 $\sigma_{BL}$ in both channels are included to ensure high precision of the maximum position identification.

The strong suppression of noise triggers clearly highlights the advantage of the double read-out system: by selecting only simultaneous pulses, the triggering thresholds can be set lower compared to a single-TES detector. In the case considered here, to achieve a noise trigger rate of 0.1% of the total simultaneous trigger rate (shown by the horizontal dashed green line in Fig.4.8b and Fig.4.8d), the threshold for a single read-out system must be set at approximately 5.5 $\sigma_{BL}$. In contrast, for the double-TES system, to keep the same trigger rate the threshold can be reduced by 30% down to 4 $\sigma_{BL}$. It is possible to lower the threshold even further when a less strict requirement on the noise trigger fraction is applied. While this analysis uses a threshold of 4 $\sigma_{BL}$, future studies could optimize the threshold based on the desired noise trigger fraction. Therefore, the double-TES approach is highly advantageous for DM and CE$\nu$NS experiments exploring the low-energy frontier.

Fig. 4.8b and Fig. 4.8d also show that at higher amplitudes, the expected rates of simultaneous and individual noise triggers get closer to each other. This fact indicates the presence of a noise component that is not completely independent between the two channels, but is correlated between them. Thus, the next step to further improve the detector's sensitivity is to investigate correlations of noise between the two channels, e.g., following the method from [244].

| | Single-channel trigger rate $R_{1TES}$ | Estimated single-channel noise trigger rate | Simultaneous trigger rate within ±50 μs $R_{2TES}$ | Estimated simultaneous noise trigger rate |
|---|---|---|---|---|
| TES1 | $3.9{\cdot}10^8$counts/(kg-day) | $7.8{\cdot}10^7$counts/(kg-day)<br>→ 19.7% of $R_{1TES}$ | $1.1{\cdot}10^8$counts/(kg-day) | $8.1{\cdot}10^4$counts/(kg-day)<br>→ 0.07% of $R_{2TES}$ |
| TES2 | $3.2{\cdot}10^8$counts/(kg-day) | $6.1{\cdot}10^7$counts/(kg-day)<br>→ 18.8% of $R_{1TES}$ | | $1.1{\cdot}10^5$counts/(kg-day)<br>→ 0.1% of $R_{2TES}$ |

Table 4.2.: Results of the noise trigger rate estimation for the trigger thresholds set at $4\sigma_{BL}$ level in the *dbl2* module.

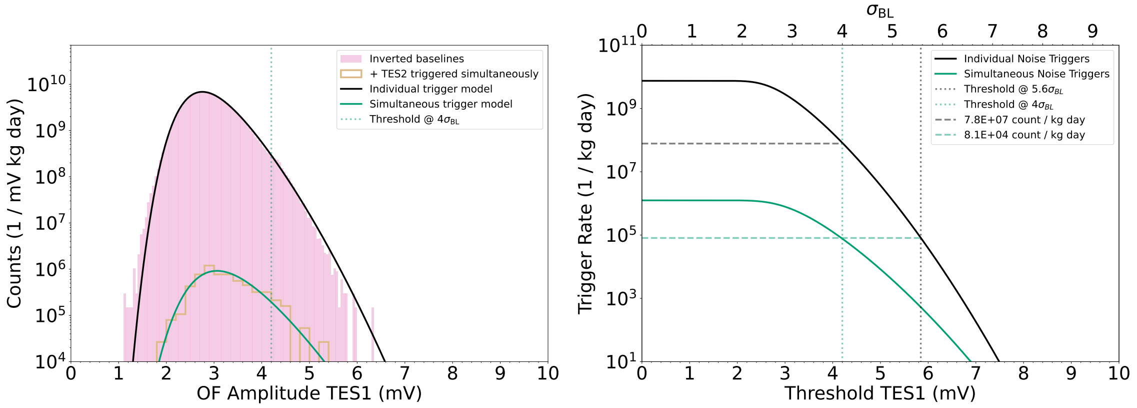

(a) Noise trigger distribution for TES1.

(b) Noise trigger rate evaluation for TES1.

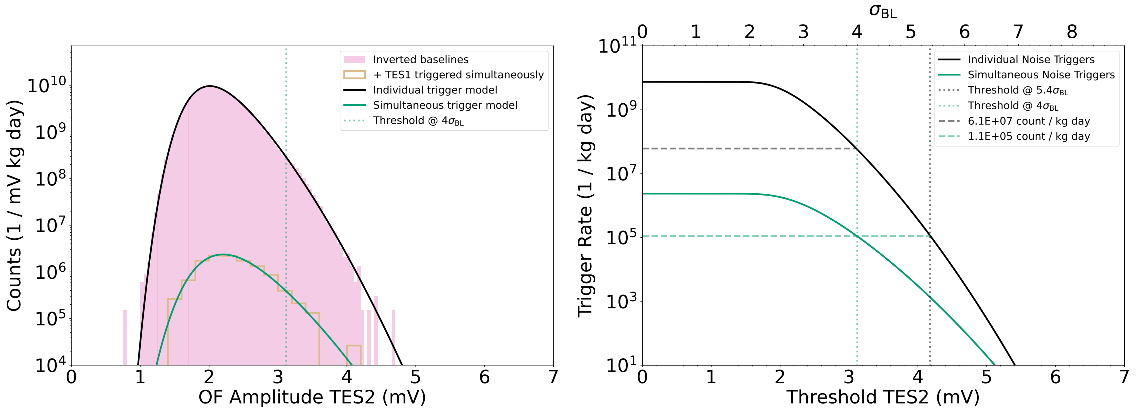

(c) Noise trigger distribution for TES2.

(d) Noise trigger rate evaluation for TES2.

Figure 4.8.: (a) and (c): Distributions of the noise triggers in TES1 and TES2 operated as individual channels (pink) and simultaneous triggers (yellow) obtained with the voltage-inverted data stream. Both distributions are fit with Eq. 2.5 shown with the black and green solid lines. (b) and (d): Noise trigger rates as a function of the threshold evaluated with the individual (black) and simultaneous (green) trigger model. Expected noise trigger rates at the trigger threshold of $4\,\sigma_{BL}$ for both models are highlighted with the dashed lines and printed in the legends. Additionally, the thresholds required in the single-TES approach to achieve the same rate of individual triggers as the simultaneous triggers in the double-TES at $4\,\sigma_{BL}$ are indicated by the vertical black dotted lines.

### 4.3.2.2. Pulse amplitude reconstruction

The detector response is linear below 1.3 keV for TES1 and 1.6 keV for TES2. Following the procedure described in Chapter 2, the amplitudes of the pulses in the linear range were reconstructed with OF; above the linear range, the truncated template fit approach was used. The pulse templates were constructed from the simultaneous pulses in the linear range of both channels and are shown in Fig. 4.20. The maximum search region for the amplitude reconstruction algorithms is limited to a narrow time range around the trigger position ±50 $\mu$s, giving a preference to simultaneous pulses.

#### 4.3.2.3. Detector performance

Energy calibration is based on the $^{55}$Mn $K_\alpha$ line (5.9 keV) from the $^{55}$Fe source. The detector response is linearized down from the calibration line to 0 with constant calibration factors of 6.47 keV/V and 7.89 keV/V for TES1 and TES2, respectively. Fig. 4.9 shows the $^{55}$Mn $K_\alpha$ and $K_\beta$ lines for the TES1 and TES2 channels. The $^{55}$Mn $K_\beta$ (6.5 keV) line was used as a reference cross-check point. Its reconstructed energy is approximately 1.5% lower than the expected value due to unaccounted-for nonlinearities in the detector response, which might originate from the readout circuit and the distorted shape of the transition curve. A more detailed discussion of these effects is provided in Sec.5.4.1. In the future, these effects could potentially be compensated for by mapping the detector response using heater pulses, as described in Sec. 6.4.

By superimposing a pulse template to a set of noise traces, the baseline resolution values of $(1.05 \pm 0.03)$ mV for TES1 and $(0.78 \pm 0.03)$ mV for TES2 were obtained. Those values translate to $(6.8 \pm 0.2)$ eV and $(6.2 \pm 0.2)$ eV respectively. Thus, both TES channels have a very similar and excellent performance, which allows to study the LEE down to low energies.

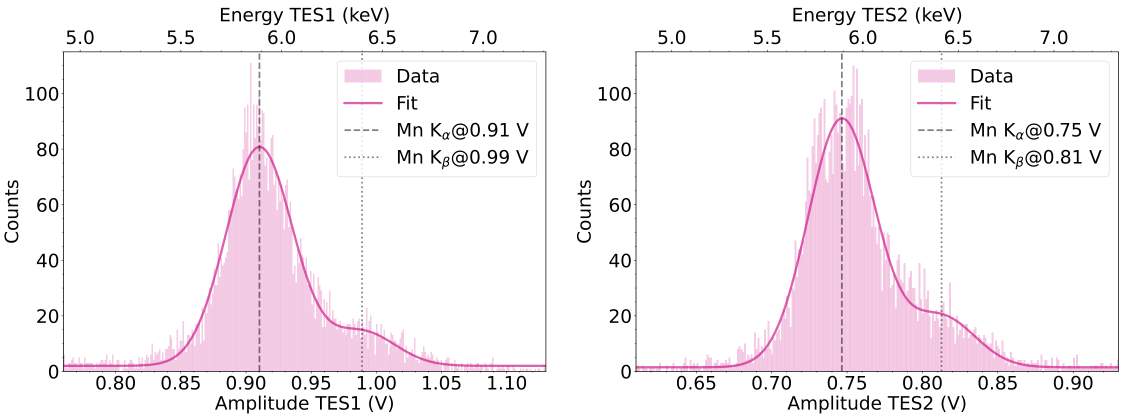

(a) (b)

Figure 4.9.: Calibration lines from the $^{55}$Fe source measured by TES1 (a) and TES2 (b) in the *dbl2* module.

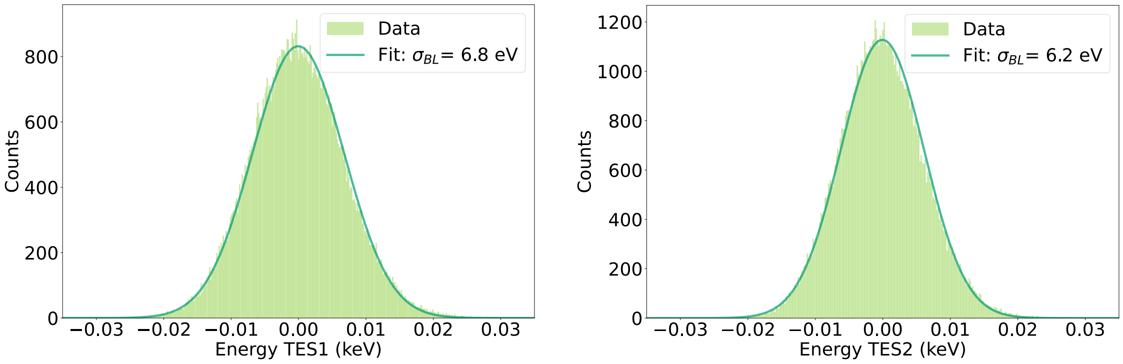

(a) (b)

Figure 4.10.: Baseline resolution determination for TES1 (a) and TES2 (b) in the *dbl2* module. A particle template of a fixed amplitude $A_{sim}$ was superimposed to the set of noise traces, and these events were fed to the analysis chain. The x-axis shows the difference between the reconstructed energy value and the simulated one: $E_{reco} - E_{sim}$, so the distributions are centered around 0.

#### 4.3.2.4. Event selection

A dedicated set of cuts was developed to reject the artifacts and ensure reliable amplitude reconstruction. The definitions of the used parameters are presented in Sec. 2.4.

First, it was noticed that interference of the SQUID of the TES1 with the electronics disturbed the pulses recorded at one of the offset points and led to deviations in the amplitude reconstruction. This effect is illustrated in Fig. 4.11. Heater pulses are used for convenience since they have fixed and known energy depositions. The SQUIDs working point can be identified by the baseline offset parameter (Sec. 2.4). The baseline offset distribution for heater pulses measured by TES1 is shown in Fig. 4.11a. Events in the problematic working point have the baseline offset around -8 V and are highlighted with pink. As can be seen in Fig. 4.11b, where the distribution of the SE fit amplitude for heater pulses is shown, the highlighted events have their amplitudes reconstructed around values different from the others (compare pink and gray distributions). To avoid amplitude mis-reconstruction caused by this effect, events recorded at this SQUID operating point were removed from further analysis. This selection removes about 9% of the total number of events. The SQUID channel used for TES2 does not show a similar effect.

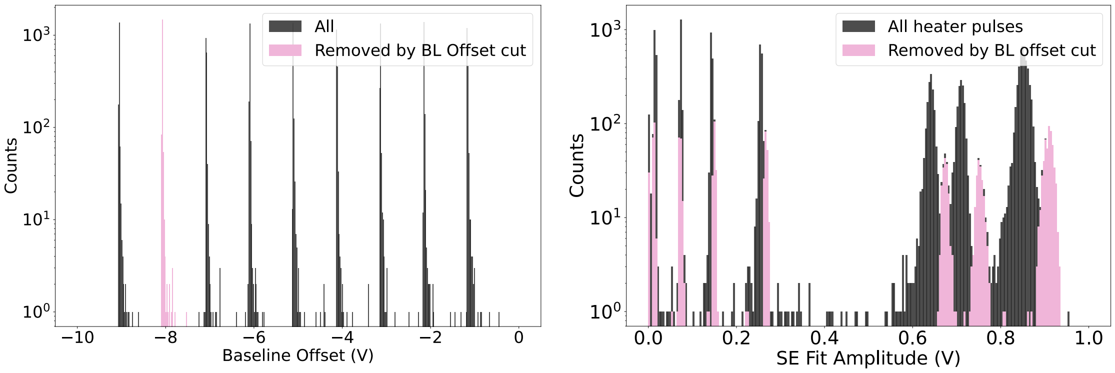

(a) Distribution of the baseline offset parameter for heater pulses measured by TES1.

(b) Distribution of the Amplitude reconstructed with SE Fit for heater pulses measured by TES1.

Figure 4.11.: Illustration of the baseline offset cut. Events with the SQUID working point corresponding to baseline offset value around -8 V marked with pink are excluded from further analysis.

Several types of artifacts were present in the data stream. One of them - flux quantum losses illustrated in Fig. 4.12c - are removed by applying a cut on the baseline difference parameter shown in Fig. 4.12a.

Another peculiar artifact present in this data set is *slow pulses* illustrated in Fig. 4.13. Those slow pulses have a completely different time scale in comparison to regular particle pulses: 250 ms versus 0.7 ms decay time. Therefore, the record window of 20 ms used in this analysis is not long enough for a slow pulse to start falling back to the original baseline level. Thus, slow pulses do not exhibit a pulse-like shape within the recorded window, and the baseline difference cut is effective at identifying and rejecting these pulses down to ∼40 eV, as shown in Fig. 4.12b. Nevertheless, they may become harmful at lower energies, potentially contributing to the background rate in the region of interest for the NUCLEUS experiment. Similar slow pulses have been observed in several NUCLEUS R&D measurements using different absorber materials and TES designs, including the setup described in Sec. 5.2. However, their origin is not yet fully understood and remains under investigation. Measurements with the *double-TES* detector revealed that these slow events are present in both channels, constituting about 1-2% of the data stream. Since they consistently occur in anticoincidence between the two TES, an absorber-related origin of these events can be ruled out.

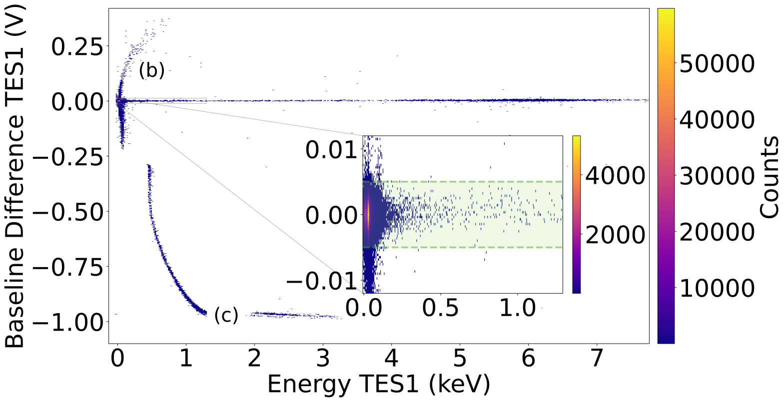

(a) 2D histogram of the baseline difference parameter versus the measured energy in TES1.

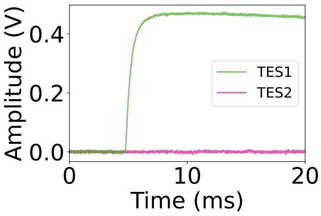

(b) Slow pulse in TES1.

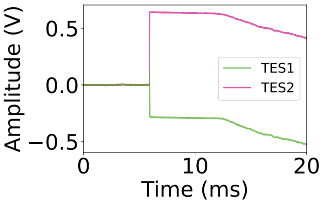

(c) Flux quantum loss in TES1.

Figure 4.12.: Baseline difference cut for TES1 channel. (a): Undisturbed particle pulses have similar baseline levels at the beginning and end of the record window, forming a horizontal line around the 0 baseline difference value. The population marked with (b) is formed by the slow pulses that do not decay back to the original baseline value within the standard record window. An example of such a trace is shown in panel (b). A similar slow pulse is shown with an extended record window in Fig 4.13. The populations marked with (c) are formed by flux quantum losses, such as the one in panel (c). The inset shows a zoom into the energies within the linear range. In the linear region, only events with BL Difference $\in (-0.005\,\mathrm{V}, 0.005\,\mathrm{V})$, shaded with green, are selected for further analysis.

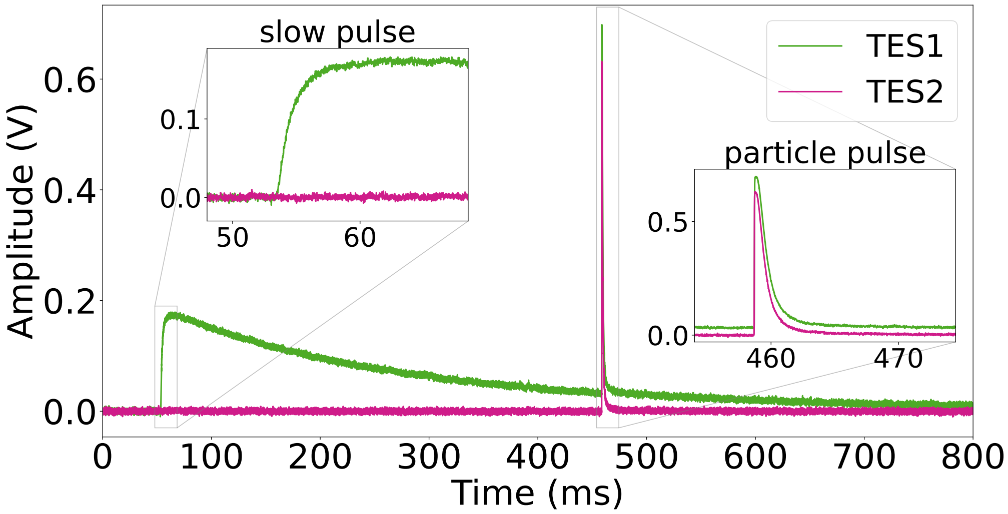

Figure 4.13.: Example from the data streams of a slow pulse with a decay time of about 250 ms in the TES1 channel, followed by a simultaneous particle event. The insets show how those events look like in the analysis where the record window is set to 2048 samples. Such slow pulses form the population (c) in Fig. 4.12.

To remove events with distorted pulse shapes, a cut on the OF RMS parameter is performed. The OF RMS is shown versus the Energy for TES1 in Fig. 4.14a. This cut removes very noisy events, marked with (b), present in the TES1 data stream and illustrated in Fig. 4.14b. Additionally, in the OF RMS-Energy plane, one can notice the band marked with (c). This band is formed by events originating in the supporting sapphire balls and transmitted to the main crystal through the contact points. While in those events similar energies are measured in two TESs, they have a slower pulse shape compared to the particle recoils in the target crystal due to their signal propagation. The comparison is shown in Fig. 4.14c. Similar observations were made in CRESST detectors operated in instrumented iStick holders [236] and CRAB measurements with the NUCLEUS $CaWO_4$ detector presented in Ch. 5.

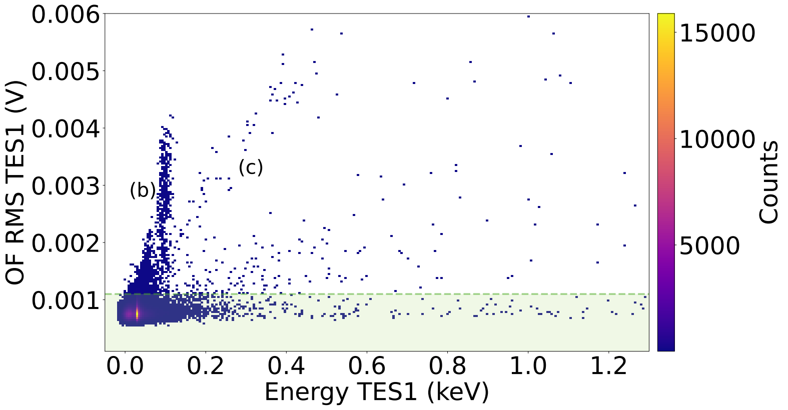

(a) 2D histogram of the OF RMS versus the measured energy for the linear range of the detector response in TES1.

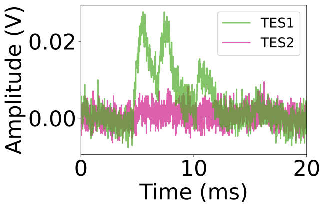

(b) Noisy event in TES1.

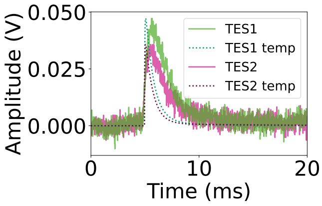

(c) Event transmitted to the target crystal through the contact point with one of the supporting sapphire balls.

Figure 4.14.: OF RMS cut for TES1 channel. (a): Events with template-like pulse shapes have small and roughly constant RMS values. Only events that fall in the green-shaded region with OF RMS $< 0.0011$ V in the linear range are selected for further analysis. The structure marked with (b) consists of very noisy events like the one shown in panel (b). The band marked with (c) consists of events originating in the supporting sapphire balls transmitted to the target crystals, thus they have a slower pulse shape in comparison to the particle template. An example of such an event is shown in panel (c) with the solid lines. The particle templates used for the amplitude reconstruction are shown with the dotted lines for comparison.

Additionally, to remove distorted pulses outside the linear range, a SE Fit RMS cut was applied, as illustrated in Fig. 4.15.

The analogous cuts were applied to the TES2 channel. TES2 data stream contains similar artifacts except for noisy events from Fig. 4.14b and has a lower rate of the flux quantum losses.

For the sake of LEE investigations, in the next section, we consider all events that survived the cuts in *both* channels and triggered *at least one channel*.

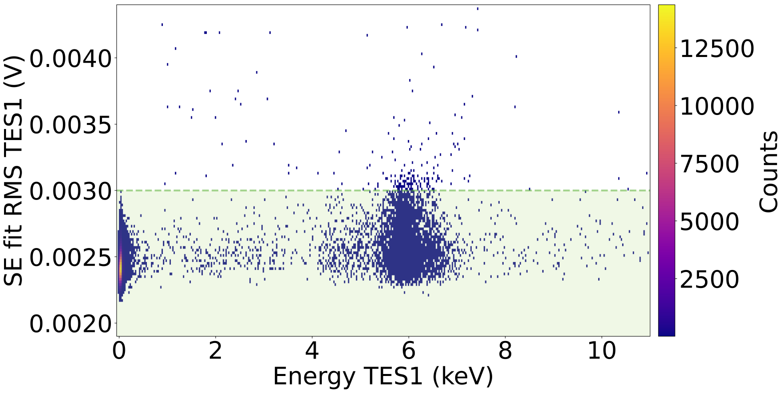

Figure 4.15.: SE Fit RMS cut for TES1 channel. 2D histogram of the SE Fit RMS versus the measured energy in TES1. The green-shaded area corresponds to SE Fit RMS $< 0.003$ V and highlights events that survived this cut.

#### 4.3.2.5. Trigger and cut efficiency

In order to take into account the effect of the triggering and the cuts, the corresponding efficiencies are calculated as described in Sec. 2.5. Events of the same energy are simulated in coincidence in two channels with $\Delta t = 10\,\mathrm{ms}$ (one time sample shift in TES2), corresponding to the most probable scenario encountered in the data (see Fig. 4.7). The resulting efficiencies for the low-energy range are shown in Fig. 4.16. As in the analysis of the real events, the starting point is the list of events where at least one of the channels caused a trigger (black), and then the quality cuts described in Sec. 4.3.2.4 are applied to both channels (blue). In the analysis of a standard single-TES detector, this would be the final cut efficiency, but in the case of the *double-TES* detector, the additional information from comparing the two channels is available. Namely, it can be checked which fraction of the simulated events caused the triggering of TES1 (green), TES2 (pink), or both channels simultaneously (cyan). While at the lowest accessible energies, some of the simultaneously simulated events do not cause simultaneous triggers, which leads to the sharp fall of the efficiencies in that region, above 40 eV all coincidences are found (the cyan curve reaches the blue one), and the efficiencies stay flat at the (84.3±1.3)% level.

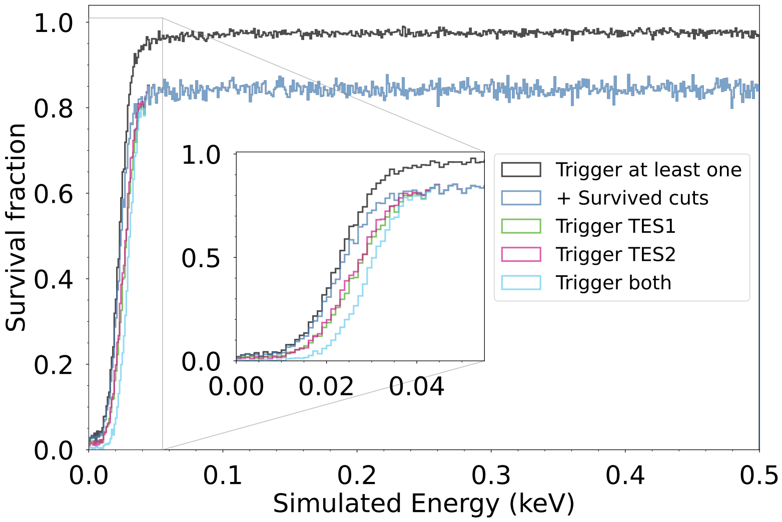

Figure 4.16.: The fraction of simulated events that caused a trigger of at least one of the TESs (black) and passed all selection criteria (blue). From the events that survived the cuts, those that triggered TES1 are shown in green and TES2 in pink, while the cyan histogram contains the fraction of simultaneous triggers. The inset shows a zoom into the low-energy part where the trigger probability is highly energy dependent.

### 4.3.3. Energy sharing between two TES channels

The energy deposited within the target crystal is expected to be shared equally between two TES channels. This is indeed confirmed by this measurement, as can be seen from the energy sharing plot in Fig. 4.17a, where the energy measured by TES2 $E_{TES2}$ is shown against the energy measured by TES1 $E_{TES1}$. While X-rays from the calibration source form the most prominent structure in the plot around 6 keV in both channels, the backgrounds over the wide energy range follow the $E_{TES2} = E_{TES1}$ line.

However, the calibration lines structure has tails with non-equal energy sharing in both directions. Since for events in the tails $E_{TES1} + E_{TES2} \approx 2 \cdot E_{K_{\alpha/\beta}}$, their origin is still attributed to the X-rays from the calibration source. The disturbed sharing can be explained by the different positions of the X-ray hits. Since the non-collimated calibration source was shining on the crystal's side where the TESs are fabricated, an X-ray can directly hit the TES or phonon collectors' surface. In this case, a part of the energy is deposited within the films and does not reach the target crystal. Thus, the signal in the TES, which was hit, appears to be higher, and the second TES measures less energy than in the case of a crystal hit. The relatively lower occurrence of events where $E_{TES1} > E_{TES2}$ compared to the opposite direction is explained by the fact that events with $E_{TES1} > E_{K_{\alpha/\beta}}$ are suffering from the flux quantum losses in TES1 and therefore are mostly rejected by the baseline difference cut, described in Sec. 4.3.2.4.

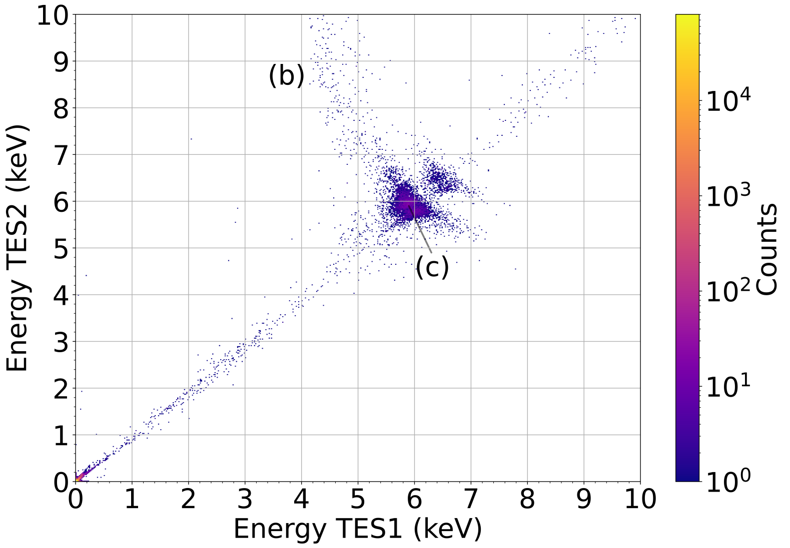

(a) 2D histogram of the energies measured in two TES channels.

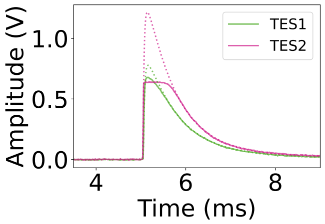

(b) $^{55}$Mn X-ray hit with unequal energy sharing between TES1 and TES2 likely caused by direct TES hits.

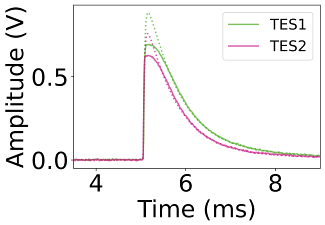

(c) Typical $^{55}$Mn X-ray hit with equal energy sharing between TES1 and TES2.

Figure 4.17.: Energy sharing between two TES channels. In the wide energy range, an equal energy sharing between two channels is observed. The prominent structure marked with (c) around 6 keV in both channels is formed by the $^{55}$Mn $K_\alpha$ and $K_\beta$ X-rays emitted by the calibration source. A typical event from that region is shown in panel (c). The tails in both directions from the structure (c) are visible. A typical pulse from the tail where $E_{TES2} > E_{TES1}$ marked with (b) is exemplarily shown in panel (b). Note that the raw pulses are not calibrated to the energy units, and therefore, the amplitude ratio does not represent the energy ratio due to the different calibration factors for two channels (see Tab. 4.1).

#### 4.3.3.1. Energy sharing at low energies

The most exciting results of this measurement can be found in the low-energy region. The energy sharing plot below 300 eV is shown in Fig. 4.18c. Several populations of events can be clearly seen. The main band along the $E_{TES2} \approx E_{TES1}$ line continues from higher energies into the low-energy region. An example of an event from this population is shown in Fig. 4.18d. In addition, there are clearly separated populations of events where the signal is present in only one of the channels. Examples of such TES1-only and TES2-only events are shown in Fig. 4.18e and Fig. 4.18b, respectively. While in one of the channels there is a clear pulse-shaped signal, in the other one the trace is noise-like. This clearly shows that a fraction of the LEE does not originate or propagate through the crystal.

Moreover, there is a prominent substructure above the main shared band with a slightly asymmetric energy sharing, where $E_{TES2}$ is larger than $E_{TES1}$. It contains events with the particle-like pulse shape; an example of an event from this structure is shown in Fig. 4.18a. The asymmetric energy sharing is additionally confirmed by investigating the heater pulses. In Fig. 4.19, they are shown on top of the 2D histogram with the events that triggered the detector, same as shown in Fig. 4.18c. As expected, the heater pulses lie perfectly to the equal energy-sharing band.

From Fig. 4.18c, one can see that while a fraction of the LEE has a signal in only one of the channels, a substantial part belongs fully to the main shared band. The contribution of different event groups to the measured energy spectra is discussed in Sec. 4.3.3.3.

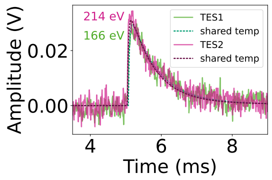

(a) Event from the asymmetric energy sharing band.

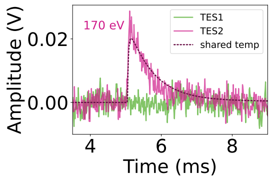

(b) TES2-only event.

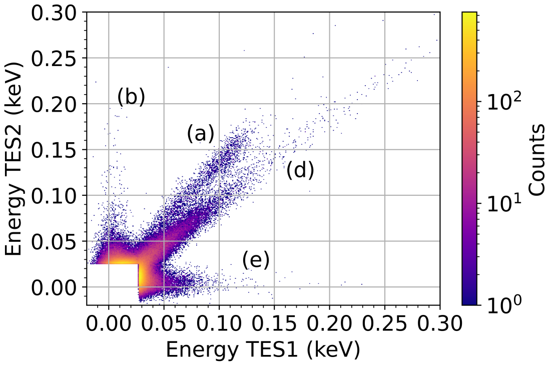

(c) 2D histogram of the Energies measured in two TES channels at low energies.

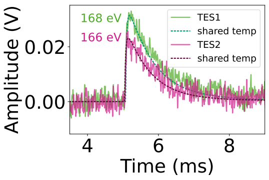

(d) Event from the main shared band with $E_{TES2} \approx E_{TES1}$.

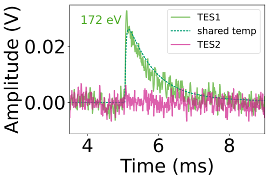

(e) TES1-only event.

Figure 4.18.: Energy sharing between two TES channels at low energies. The population with $E_{TES2} \approx E_{TES1}$ continues the shared band from Fig. 4.17a. An example of an event from this group is shown in panel (d). Close to the main band, a population with a slightly different and asymmetric energy sharing is prominent (an example is shown in panel (a)). Additionally, there are clear populations with the signal present in only one of the TESs. A TES1-only event is shown in panel (e), and a TES2-only event in panel (b). The particle templates used for the amplitude reconstruction are shown with the dashed lines. Note that the pulses are not calibrated to the energy units, and therefore, the amplitude ratio does not represent the energy ratio due to the different calibration factors for the two channels (see Tab. 4.1).

#### 4.3.3.2. Pulse shapes of different event classes

The cuts discussed in Sec. 4.3.2.4 were developed with the goal of selecting events featuring the pulse shape of particle events, and all events presented in Fig. 4.17 and 4.18 passed those cuts. At low energies, though, the signal-to-noise ratio gets lower, and it gets increasingly difficult to distinguish between different pulse shapes. However, it is possible

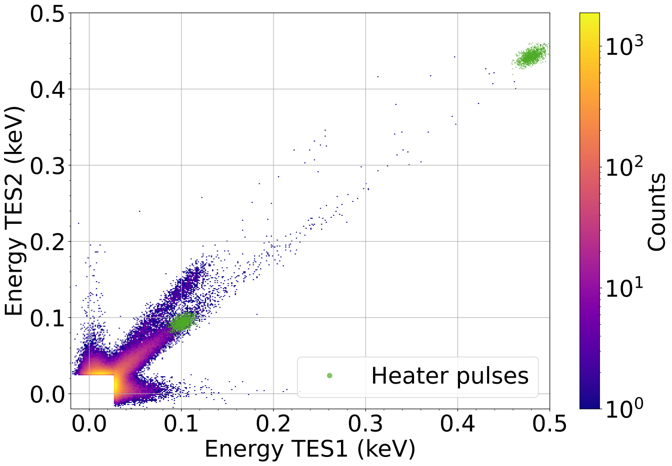

Figure 4.19.: Energy sharing between two TES channels at low energies. The 2D histogram shows the energy sharing for events triggered in at least one of the TESs as in Fig. 4.18c. The green data points on top of it are the calibrated heater pulses. They fall on the band with equal energy sharing, where events caused by energy deposition in the absorber are expected to appear.

to select events with different energy sharing discussed in Sec. 4.3.3.1 and build an average pulse shape for each of them. Due to significant statistics of events for each of the groups - equal sharing, asymmetric sharing, TES1-only, and TES2-only - one can obtain pulse shapes with little noise contribution. The resulting pulse shapes are shown in Fig. 4.20 together with the noiseless particle template used for amplitude reconstruction. To compare the pulse shapes of different populations, the residuals between the summed templates of each group and the particle template are shown in the bottom panels. It is evident that events with equal and asymmetric energy sharing have similar pulse shapes and closely follow the shape of the particle template. The pulse shape of single TES events appears to be faster that the particle template, especially for TES2. This observation supports the idea that these events originate from within the TES structures, given the expected shorter signal development times in such case. The exact prediction of the pulse shape, however, depends upon the exact process underlying the occurrence of single TES events.

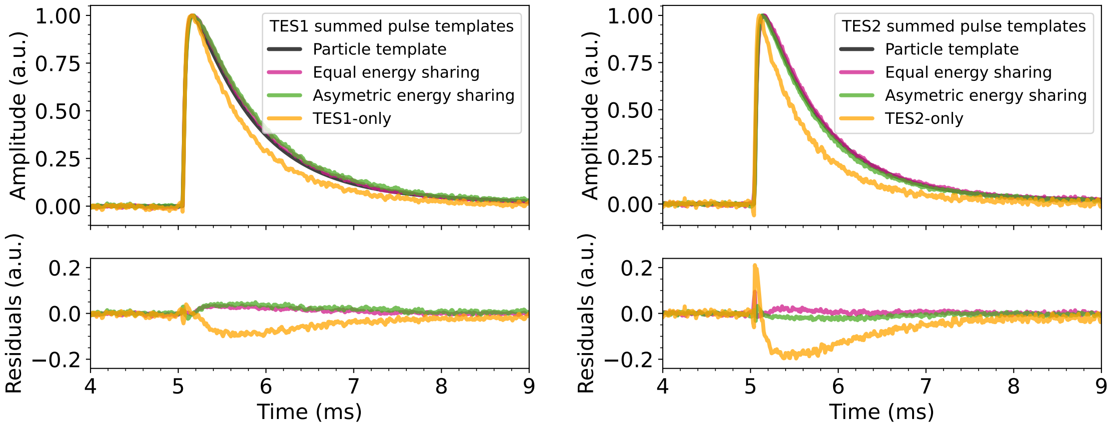

(a) (b)

Figure 4.20.: Top: Summed pulse templates for different energy sharing groups for TES1 (a) and TES2 (b) compared to the particle templates (black lines). The templates built from the events from the equal energy sharing band are shown with the pink lines, from the asymmetric sharing - with the green lines, and events with a signal in only one of the channels - with the orange lines. Bottom: residuals between the summed templates from the different event groups and the particle template are shown with corresponding colors.

#### 4.3.3.3. Spectral shapes of different event classes

To investigate the spectral shapes of the event classes with different energy sharing, they were identified using the difference in the energies measured by two channels. This parameter is shown against the energy measured by TES1 in Fig. 4.21. By definition, the band with equal energy sharing is located around 0; the energy difference for TES1-only events is increasing with $E_{TES1}$ since the signal in TES2 for those events stays comparable to noise. The band with asymmetric energy sharing ($E_{TES2} > E_{TES1}$) is clearly identified above the equal energy sharing population. While the separation of the equal sharing and the asymmetric band is clear around 100 eV, the separation of these two populations becomes difficult at lower energies. The figure contains only events with the measured energy above 40 eV in both channels, where the separation of the simultaneous events and single-TES events is possible, which is confirmed by the fact that the efficiency of the coincidence cut stays flat above this energy (see Fig. 4.16).

Using this grouping, the energy spectra of the three populations for each TES are shown in Fig. 4.22. Several insights can be taken from these spectra. First, the largest fraction of the LEE starts around 150 eV and consists of events with equal energy sharing (pink histogram). Secondly, the single-TES population (orange) starts at lower energies around 100 eV and is rapidly rising towards lower energies. The rates of single-TES events are presumably taking over the rates of shared events at energies below 40 eV. Thirdly, events from the asymmetric energy sharing band have a peculiar spectral shape and form a bump-like structure in the spectra of both channels at $E_{TES1} \approx 80 - 130\,\mathrm{eV}$ and $E_{TES2} \approx 110 - 160\,\mathrm{eV}$. At these energies, the bump-like structure dominates the total rate over the other components and, therefore, is prominent in the total spectra, especially for TES2. The bump-like structure is not aligned with the equal sharing band, where the particle recoils are expected to fall. This might hint towards the origin of those events happening in close vicinity of TES2. Similar bump-like spectral features were observed in the CRESST data, in an $Al_2O_3$ detector at around 190 eV [3, 115] and in a $CaWO_4$ at around 150 eV [125]. In [115], the time evolution of event rate in this structure was studied, and a good agreement with the half-life of the $^{55}$Fe was found pointing to the origin of the bump being related to the presence of the calibration source.

No structures in time were found in the distributions for the waiting times between the events from the different groups at low energies and with the hits by X-rays from the calibration source. Therefore, events from one group are unlikely to cause events from another.

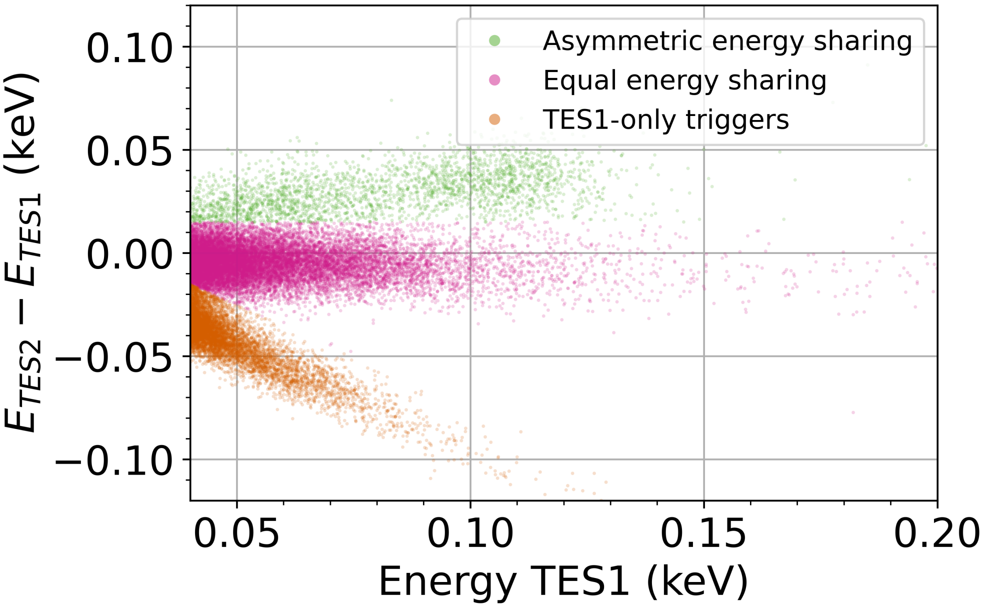

Figure 4.21.: Difference in the measured energies in two channels vs. energy measured by TES1. Pink data points show events with roughly equal energy sharing, and green points represent events with asymmetrical energy sharing ($(E_{TES2} - E_{TES1}) > 15\,\mathrm{eV}$). Events where only TES1 got triggered are shown in orange. Only events above 40 eV are included.

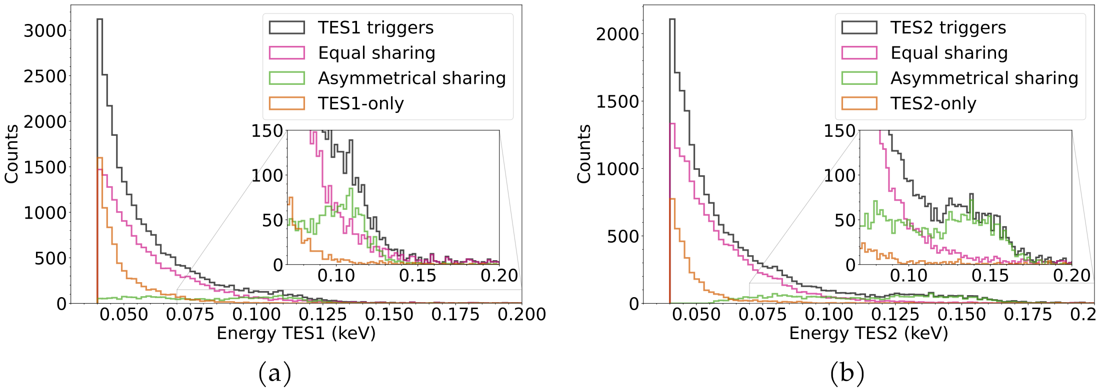

(a) (b)

Figure 4.22.: Energy spectra of the populations with different energy sharing measured by TES1 (a) and TES2 (b): all events after the selection criteria are shown with black. The coloring follows Fig. 4.21 for the different event populations: events from the band with equal energy sharing are shown in pink, events with asymmetric energy sharing - in green, and events that caused a trigger in only one of the channels - in orange. Only events above 40 eV, where such separation is possible, are shown. Insets zoom into the y-axis to illustrate the bump-like spectral shape of the asymmetric energy-sharing population.

#### 4.3.3.4. Impact of the *double-TES* approach on the measured low-energy spectrum

To estimate the influence of the *double-TES* approach as a tool to suppress the LEE, the measured energy spectra before and after the coincidence cut are compared. The spectra before the coincidence cut correspond to those that would be measured in the classical case of a single-TES detector, i.e., a mixture of the shared and single TES events. If an event caused a simultaneous (i.e., $|\Delta t| < 50\,\mu$s) trigger in both channels, it survives the coincidence cut. The spectra measured by two channels before and after the coincidence cut corrected by the corresponding efficiencies discussed in Sec. 4.3.2.5 are shown in Fig. 4.23. Since, as was shown in Sec. 4.3.3.3, the spectral populations of single TES events appear below 100 eV and rise steeply towards the lower energies, the coincidence cut has an impact only at low energies.

The spectra measured by two TES are almost identical at the higher energies. The only prominent difference is the higher event rate in TES1 between 4 and 5 keV. This is explained by the alternated energy sharing for the calibration X-rays (see the tails of the calibration lines in the 2D histogram in Fig. 4.17a)[4]. Such position-dependent effects in the energy spectra can be overcome by using, e.g., the mean of the energies reconstructed in the two channels as the final measure for energy. Additionally, a more sophisticated

---

[4] This effect is not compensated by the efficiency correction since, in the current implementation described in Sec. 2.5, efficiency indicates the fraction of “good” events in a given data stream that survive the cuts. However, it does not estimate the leakage of artifacts into the final dataset. Here, the number of pulses affected by FQLs increases with energy. This effect was not considered in the efficiency simulations because it is only relevant at high energies above the calibration lines, while the main focus of this analysis is on the sub-keV part of the spectrum.

coincidence cut can be developed, which would allow the choice of only events with close measured energy values.

The energy range below 100 eV, where the effect of the coincidence cut becomes prominent, is shown in the inset plot of Fig. 4.23. The fraction of coinciding events, shown in orange, decreases towards the lower energies, reaching 50% at 40 eV for TES1. The energy spectra after the coincidence cut of TES1 and TES2 have only a minor discrepancy of up to 20%, which can likely be attributed to the energy reconstruction uncertainties. The spectra are only shown above 40 eV, where the single-TES and shared events are clearly separated, and the coincidence cut efficiency is flat. To investigate the behavior of the LEE at even lower energies with this data set, a leakage estimation from the single-TES populations is required. This is left for future work.

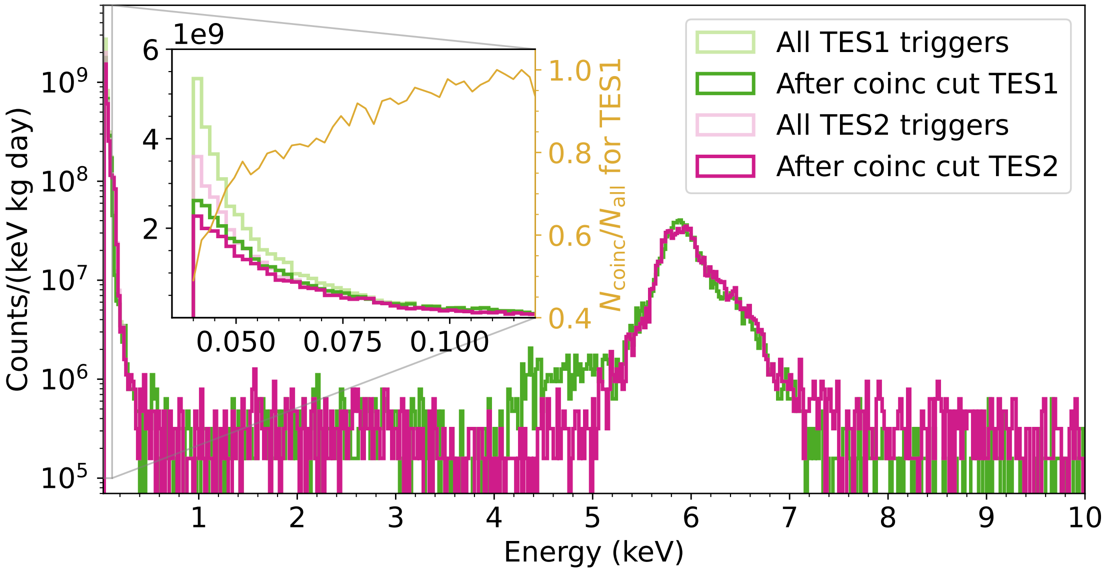

Figure 4.23.: Comparison of the energy spectra measured by two TESs before and after the coincidence cut. The x-axis shows the corresponding energy - measured by TES1 for the green spectra and measured by TES2 for the pink ones. The spectra are corrected with the corresponding efficiencies. The inset plot shows the effect of the coincidence cut at low energies, where the orange line indicates the ratio between the spectra of coinciding events to all TES1 triggers.

## 4.4. Further series of measurements with the *double-TES* detector

After the first successful operation of the *double-TES* detector, presented in Sec. 4.3, that established the multi-component nature of the observed LEE, the NUCLEUS collaboration had a chance to study the impact of different external factors on the LEE's rate while progressing with the setup commissioning and preparing for the first full-system operation at TUM. Since the *double-TES* detector showed the advantages for the LEE studies, it was installed in most of the coming cryogenic R&D runs. This led to a series of measurements with the *double-TES* dbl2 detector, conducted in two different setups with varying background levels, from summer 2023 to summer 2024, presented in this section.

Since many measurements were performed and analyzed in these studies, for convenience, the datasets are named according to their setup, as indicated in Tab. 4.3, which summarizes their main properties. The analysis of all datasets closely followed the procedure described in Sec. 4.3.2.

| | | surf1 | surf2 | UGL1-1 | UGL1-2 | surf3-1 | surf3-2 | UGL2 |
|---|---|---|---|---|---|---|---|---|
| Setup location | | 1st floor | 1st floor | UGL | | 1st floor | | 1st floor |
| Starting date of the run | | 2023/06/25 | 2023/07/09 | 2024/03/25 | | 2024/05/29 | | 2024/06/20 |
| External shielding | | No | No | PE, Pb | | No | | PE, Pb |
| Iron source | | Yes | No | Yes | Yes | Yes | Yes | Yes |
| Measurement time (h) | | 12 | 7 | 85.3 | 24.1 | 19.4 | 91.7 | 64.1 |
| Day since cooldown for the start of the measurement | | 2 | 2 | 3 | 14 | 2 | 3 | 2 |
| Calibration factor (keV/V) | TES1 | 6.47 | 6.47 | 12.13 | 6.87 | 3.80 | 3.93 | 3.49 |
| | TES2 | 7.89 | 7.89 | 14.89 | 7.95 | 6.34 | 6.04 | 4.99 |
| Baseline resolution (eV) | TES1 | 6.8 | 6.7 | 16.5 | 8.7 | 6.1 | 6.7 | 8.1 |
| | TES2 | 6.2 | 6.7 | 14.6 | 7.2 | 7.9 | 8.2 | 6.6 |
| Triggering threshold at $4\sigma_{BL}$ (eV) | TES1 | 27.2 | 26.8 | 66.0 | 34.8 | 24.4 | 26.8 | 32.4 |
| | TES2 | 24.8 | 26.8 | 58.4 | 28.8 | 31.6 | 32.8 | 16.4 |
| Analysis threshold (eV) | | 60 | 60 | 110 | 60 | 60 | 60 | 60 |

Table 4.3.: Characteristics of the series of measurements with the *dbl2* module. The datasets are named according to their setup location: "surf" refers to measurements taken at the surface facility on the 1st floor of the TUM Physics Department, while "UGL" indicates data collected in the TUM shallow underground laboratory [245]. The dataset labeled "surf1" corresponds to the measurement discussed in Sec. 4.3. The statistical uncertainties of the baseline resolution and corresponding triggering threshold determination, not specified in the table, are within 5% for all the measurements. The analysis threshold was selected as the energy above which different LEE populations can be reliably distinguished. A common analysis threshold is used for all measurements except UGL1-1 due to its sub-optimal performance. File lists used for each period are specified in App. C.1.

### 4.4.1. Observations of the shared LEE component in the different *double-TES* measurements

The first data-taking labeled **surf1** in Tab. 4.3 performed in June 2023 was presented in detail in Sec.4.3. It was shown that the LEE consists of two main components: (i) simultaneous events causing similar energy deposition in two TESs - *shared LEE*, (ii) events with a signal in only one of the TESs - *single-TES LEE*. Here, the series of measurements will be presented in chronological order, highlighting the changes between them. First, I will focus on the observations on the shared LEE. The single-TES component is then discussed in the next Sec. 4.4.2.

The shared LEE component in all measurements was defined by simultaneous triggering in both TESs (recall Sec. 4.3.2.1). Only in the surf1 measurement an additional selection criterion was applied, as illustrated in Fig. 4.21, to exclude the asymmetric structure from the shared LEE band. In subsequent runs, however, no such asymmetric structures were observed, and therefore, this selection was not needed.

The next measurement (**surf2**) focused on testing the impact of irradiating the crystal with the calibration $^{55}$Fe source on the LEE rate. For this test, the *double-TES* detector was operated in the same configuration and setup as in the surf1 measurement. The only modification was the removal of the calibration source from the module. LEE events associated with the calibration source are expected to occur within the crystal and thus fall into the shared LEE band. Fig. 4.24a shows the total and shared LEEs measured with and without the source. The similarity in the shape and rate of the shared LEE spectra confirms that the $^{55}$Fe source has no observable impact, at least at this level of the LEE rate.

Shortly after this, the detector was mounted into a Bluefors dry dilution refrigerator[5] in the shallow underground laboratory (UGL) at TUM. It has an overburden of ~15 m.w.e. which leads to the muon flux reduction by a factor of 3 and blocks the hadronic component of the cosmic radiation [245]. Additionally, an external shielding of several layers of lead and polyethylene was installed around the cryostat. Such configuration is a partial implementation of the final NUCLEUS shielding shown in Fig. 1.11. In the scope of assembling the full NUCLEUS setup in the UGL, 13 thermal cycles from the room to mK temperatures were required until the optimal conditions were fulfilled. The *double-TES* detector was mounted inside the cryostat during this debugging period for monitoring purposes. When the optimal conditions and required temperature were reached, after about nine months from the surf1 run, the detector was measured in the UGL setup for the first time. This **UGL1** dataset is split into two parts: **UGL1-1** and **UGL1-2**. First, during the UGL1-1 period, the detector was operated in a sub-optimal conditions, which resulted in a two times worse baseline energy resolution in comparison to the usual value (see Tab. 4.3 for the values). After the conditions were optimized, a better resolution of about 8 eV in both TESs was achieved in the UGL1-2 period, which enabled the spectrum below 100 eV. The total and shared spectra obtained during those two periods are shown in Fig. 4.24b. In the overlapping energy region, the shared LEEs have close rates, thus only the UGL1-2 period is used for the further spectral comparisons in this chapter.

The shared LEE observations in UGL1-2 and in surf1 are shown together in Fig. 4.25. The spectrum taken in the UGL shows a reduction of the shared LEE by up to two orders of magnitude. This suggests a significant impact of the total background level on the LEE rate since otherwise, the detector was unchanged. For convenience, the rates at 100 eV measured in different runs are provided in Tab. 4.4.

---

[5] The model and configuration of the cryostat in the UGL is the same as the ones in the surface laboratory.

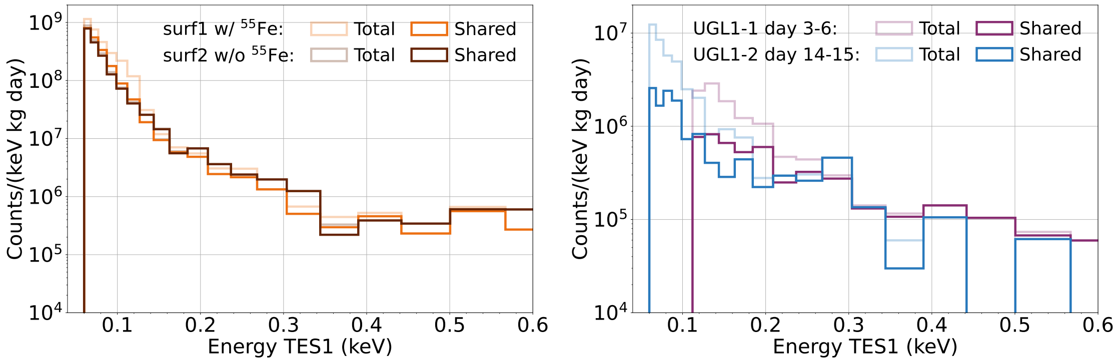

(a) The LEE measured in the same configuration with and without the $^{55}$Fe source shining on the target crystal.

(b) The LEE measured in UGL1-1 and UGL1-2 periods.

Figure 4.24.: The LEE spectra observed in different measurements specified in Tab. 4.3 are shown. The total measured LEE is represented by the lighter-colored lines, while the shared component is highlighted with the brighter lines. The energy measured by TES1 is used as an example here; a similar behavior is observed in TES2.

After the UGL1 run, the detector was taken back to the surface laboratory in order to remeasure the spectrum and confirm the dependence of the LEE rate on the background level. However, a cleaning procedure scheduled in the NUCLEUS detector preparation program took place before the next data-taking. For this, the detector module was dismounted in order to clean and etch all the parts surrounding the crystal, such as housing and clamps. Additionally, the simulations indicated a large fraction of the expected particle background originating from the commercially printed circuit board (PCB) facing the crystal. Therefore, it was exchanged with custom-manufactured copper-kapton-copper traces glued to a copper plate. The modifications of the detector module are shown in Fig. 4.27.

The *double-TES* detector in this modified module was operated in the surface laboratory providing the **surf3** dataset. It is split into two parts - surf3-1 and surf3-2 - since two different operating points were used. The measured shared LEE component in the surf3-1 period is shown in Fig. 4.25 together with the previous runs. The observed rate is increased in comparison to the UGL1 measurement (e.g., by a factor of $69 \pm 22$ at 100 eV) and is close to the surf1 rate, even though the spectral shape has changed. This increased LEE rate in the surface run, at first glance, seems to confirm the hypothesis of the shared LEE rate related to the external background level.

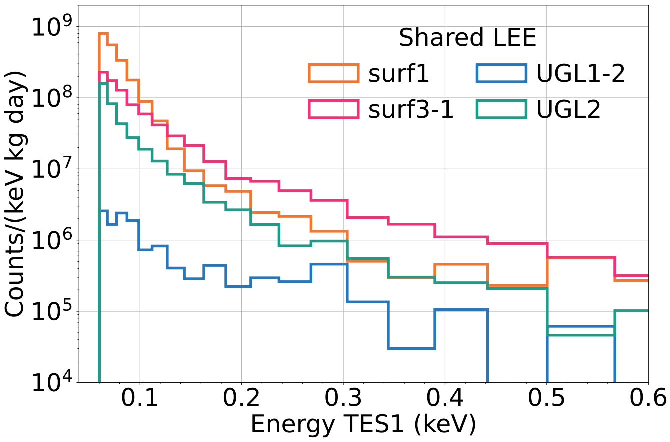

Figure 4.25.: The shared LEE spectra observed in different measurements specified in Tab. 4.3. The energy measured by TES1 is used as an example here; a similar behavior is observed in TES2 due to the close to equal energy sharing between the two channels.

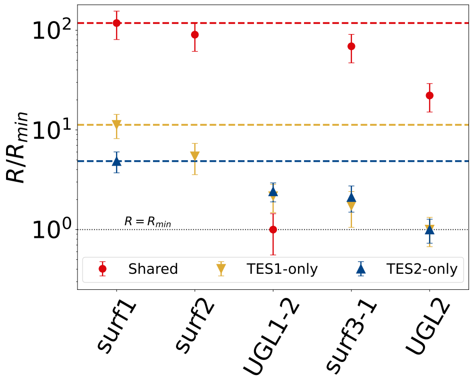

Figure 4.26.: Visualization of Table 4.4. The plot shows the ratio of the rates at 100 eV $R$ of the different LEE components to their respective minimum values $R_{min}$ across various NUCLEUS double-TES measurements. The dashed lines indicate the maximum ratios for each LEE population: the ratio for the shared LEE (red) reaches up to $121 \pm 37$, for TES1-only (yellow) up to $11 \pm 3$, and for TES2-only (blue) up to $4.9 \pm 1.5$. The black dotted line represents the $^{R}/_{R_{min}} = 1$ line.

| | Rate at 100 eV $R$, day$^{-1}$ | | |
|---|---|---|---|
| | Shared | TES1-only | TES2-only |
| surf1 | $1205 \pm 55$ | $117 \pm 17$ | $53.5 \pm 11.7$ |
| surf2 | $921 \pm 59$ | $56.6 \pm 14.6$ | n/a |
| UGL1-2 | $10.2 \pm 3.2$ | $22.5 \pm 4.8$ | $26.6 \pm 5.2$ |
| surf3-1 | $704 \pm 36$ | $18.0 \pm 5.7$ | $23.3 \pm 6.5$ |
| UGL2 | $226 \pm 11$ | $10.4 \pm 2.4$ | $11.0 \pm 2.5$ |
| CRESST-III<br>Sapp2 in Run36 | $2.59 \pm 0.19$ | | |

Table 4.4.: The rates at 100 eV of the shared and single-TES components of the LEE observed in different measurements with the NUCLEUS *double-TES* detector. The characteristics of the measurements are provided in Tab. 4.3. Due to the short measurement time the the surf2 measurement has an empty bin at 100 eV (see Fig. 4.30). For comparison, the rate from the CRESST-III sapphire detector (Sapp2) discussed in Sec. 3.2 is listed. This detector had a single TES readout and thus no separation of the LEE population was possible.

To obtain definitive evidence of the impact of the background level, the *double-TES* detector was measured again in the UGL. Even though the spectra in this **UGL2** measurement shown in Fig. 4.25 appear to be slightly lower than in the surf3 period (by a factor of $3.1 \pm 0.2$ at 100 eV), it is by more than an order of magnitude higher than in the UGL1 measurement. Since the background conditions in the UGL setup did not change in UGL2 compared to UGL1[6], the repeated measurements do not support a major contribution of the particle background to the shared LEE.

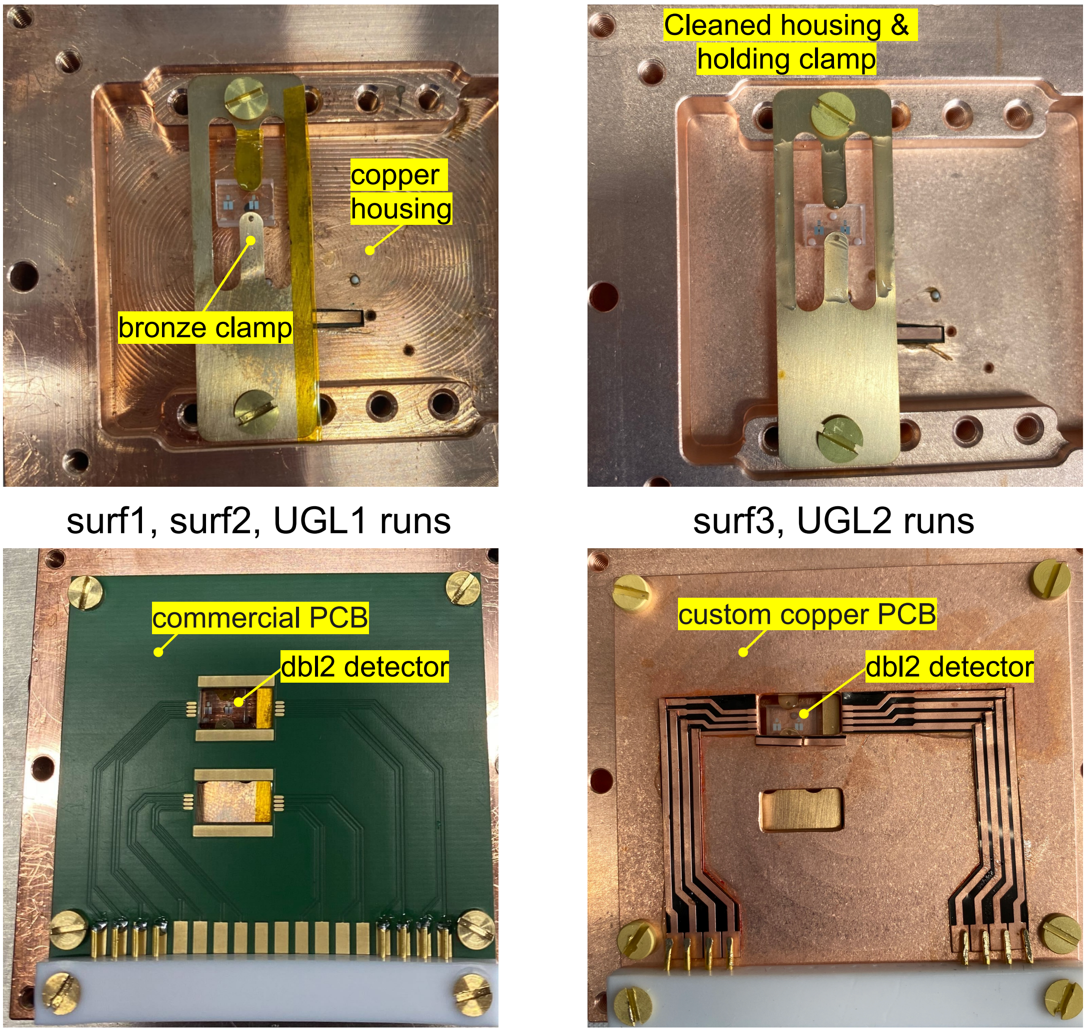

(a) (b)

Figure 4.27.: Photographs of the NUCLEUS dbl2 detector module before (a) and after (b) the modifications performed between the UGL1 and surf3 measurements. After disassembling the module, the copper housing and brass clamps were cleaned and etched, and the commercial PCB was replaced with the custom copper PCB.

---

[6] The overall particle background is actually expected to be lower in the UGL2 measurements due to the cleaning of the material surrounding the crystal shown in Fig. 4.27.

To provide a comprehensive overview of the observations, the rates of the different LEE components – shared, TES1-only, and TES2-only – across all measurements are plotted against real-time in Fig. 4.28. Each data point represents one recorded data segment, resulting in some measurement periods containing multiple points. Due to the varying durations of the data segments (ranging from one hour to a full day), the statistics among the data points differ. This figure might assist in following the evolution of the shared LEE rate throughout the runs discussed above.

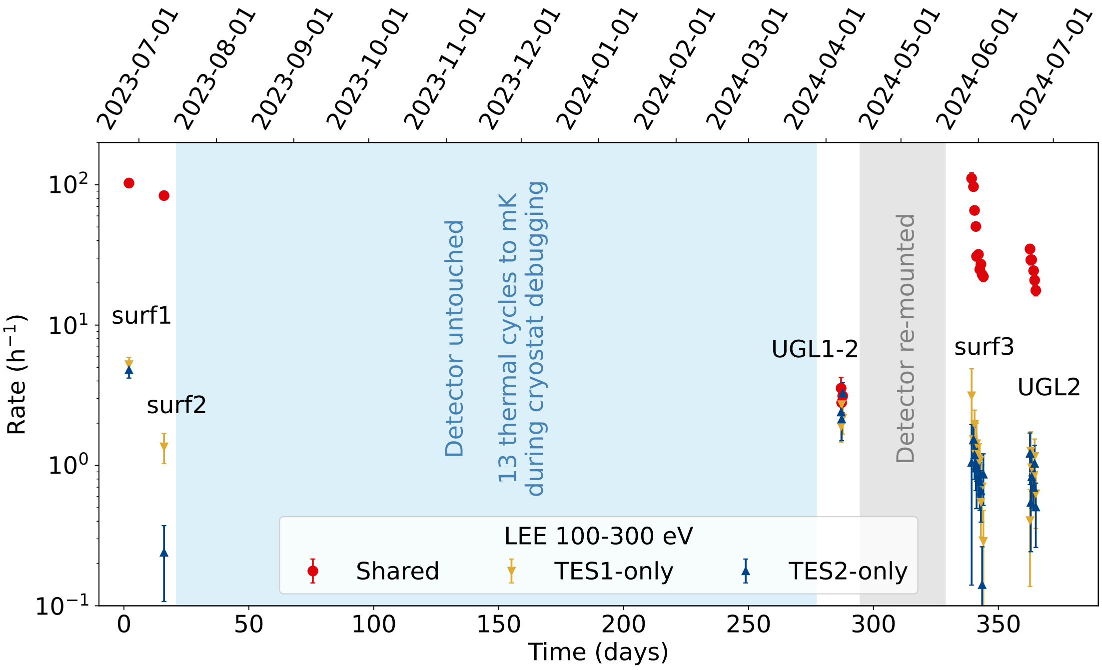

Figure 4.28.: Rate of the shared and single-TES LEE events with energy between 100 and 300 eV versus time since the cooldown of the surf1 run (bottom x-axis) and real-time (top x-axis). The characteristics of the measurements are specified in Tab. 4.3. Data points for the UGL1-1 period are not displayed due to the sub-optimal performance of the detector in this period.

Additionally, the time evolution of the shared LEE rate within a single run is shown in Fig.4.29 for the surf3 measurement, which has the longest duration for the energy range between 100 and 300 eV.[7] The rate appears to exponentially decrease with a decay time of $1.4 \pm 0.2$ days. This is faster than in the CRESST surface measurements with an SOS doubleTES detector, where the shared component was shown to have decay times of $(7.4 \pm 1.1)$ days and $(12.4 \pm 1.5)$ days in two different measurements [211]. However, longer measurements are required to precisely study the time dependence of the LEE rates in the NUCLEUS detectors.

---

[7] While the UGL1 run has a comparable total measurement time, the performance of the TESs in the UGL1-1 period does not allow proper discrimination of the different LEE components down to 100 eV.

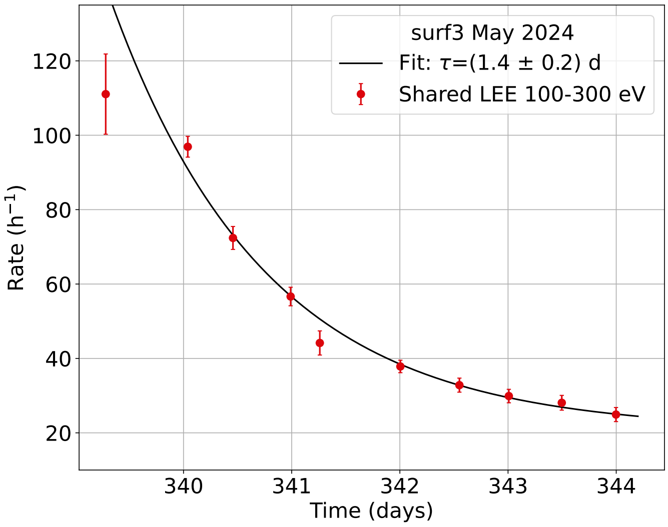

Figure 4.29.: Shared LEE rate measured by the NUCLEUS *double-TES* detector in the surf3 measurement versus the time since the beginning of the first *double-TES* measurement in surf1. Each red data point represents the rate calculated in one data segment, with the error bars indicating statistical uncertainties. The best fit using the function $F(t) = A \cdot e^{-(t-t_0)/\tau} + C$, where $t_0$ is the time of the cooldown in the surf3 run, is shown with the black line.

### 4.4.2. Observations of the single-TES LEE component in the different measurements

So far, we have focused only on the shared component of the observed LEE, which is relevant for DM or CE$\nu$NS searches. With the *double-TES* approach, the other component, single-TES LEE, can be removed from the final energy spectrum by using the signal ratio between the two channels. However, the single-TES component becomes more prominent at lower energies, and it is uncertain whether its origin is entirely unrelated to that of the shared component. Therefore, it is important to investigate the single-TES LEE as well. In this section, observations on the single-TES LEE are presented.

The spectral shape of the single-TES component is steeper than of the shared LEE (see Fig. 4.22). The spectra of the single-TES LEE components observed in TES1 and TES2 in the measurements discussed here are shown in Fig. 4.30. The shapes of the single-TES spectra appear similar in different runs. From Tab.4.4, the maximum ratio between the rates at 100 eV in different *double-TES* runs is $R^{\mathrm{surf1}}_{\mathrm{TES1-only}}/R^{\mathrm{UGL2}}_{\mathrm{TES1-only}} = 11 \pm 3.1$ for the TES1-only LEE and $R^{\mathrm{surf1}}_{\mathrm{TES2-only}}/R^{\mathrm{UGL2}}_{\mathrm{TES2-only}} = 4.9 \pm 1.5$ for the TES2-only LEE, as visualized in Fig. 4.26. Interestingly, the relative spread of the LEE rate values is an order of magnitude higher for the shared LEE component ($R^{\mathrm{surf1}}_{\mathrm{shared}}/R^{\mathrm{UGL1-2}}_{\mathrm{shared}} = 121 \pm 37$) compared to the single-TES components.

The behavior of the single-TES LEE component over time since cooldown within a single run is less conclusive compared to the shared LEE shown in Fig 4.29, due to the

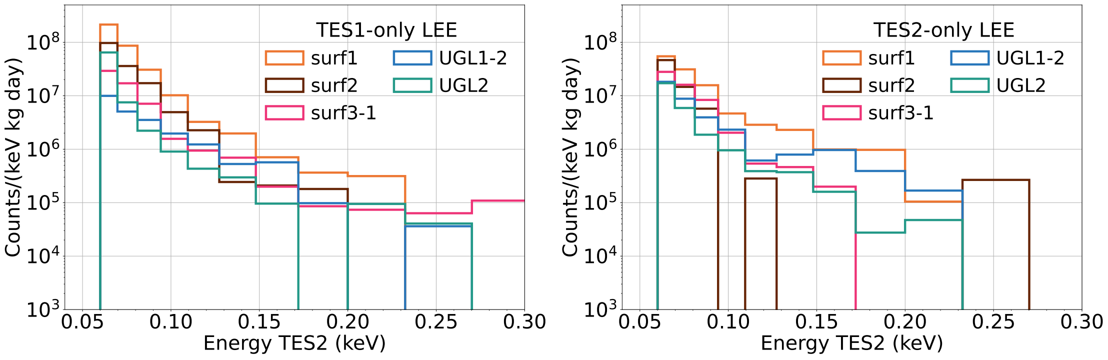

(a) (b)

Figure 4.30.: Energy spectra of the single-TES components–TES1-only (left) and TES2-only (right)–in the different runs listed in Tab. 4.3.

lower number of counts. A more detailed statistical analysis is required to investigate this further, and is planned for future work. Additionally, longer measurement periods would be beneficial for this analysis. However, as shown in Fig. 4.28, the single-TES LEE rates do not appear to be affected by the numerous thermal cycles or detector re-mounting. This suggests that the single-TES LEEs are more likely to originate from the internal structure of the TES or the readout system, which remained unchanged throughout these measurements.

## 4.5. Summary of the observations from the NUCLEUS *double-TES* measurement series

The NUCLEUS *double-TES* detector presented in this chapter has demonstrated very good and nearly identical performance in both channels and across multiple runs (spreading from 6.1 eV to 8.7 eV BL energy resolution – see Tab. 4.3). High resolution in both channels is essential for the main goal of the DM or CE$\nu$NS experiments – selecting events originating in the absorber's volume by comparing the measured energies of the two TESs. In this section, I will summarize the main findings of the NUCLEUS *double-TES* measurements presented in this chapter regarding the LEE. Most of these findings can be followed by looking at Fig. 4.28.

1. The LEE observed by each TES contains at least **two populations of events**.
2. The first population of events is measured in both TESs with nearly equal energy – **shared LEE**. These events are associated with the signal originating in, or at least propagating through, the absorber crystal.
    a) **The shared LEE decays over time since cooldown within one run**, with a decay time on the order of days.

   b) The shared LEE rate varies by up to two orders of magnitude across different runs. **The lowest rate was measured** during the UGL1 run, which took place **nine months after the detector was mounted into the module and after experiencing 13 thermal cycles from room to mK-temperatures**.
   c) After the detector was re-assembled, the rate of the shared LEE was measured at similarly high levels ($\mathcal{O}(100\,\mathrm{counts/day})$ at 100 eV) across different background setups (surface and UGL with shielding). **This indicates that re-clamping the detector resets the shared LEE rate to the higher values** observed in otherwise unchanged setups. The decaying behavior of the shared LEE, along with this observation, strongly suggests that external stress (e.g., from mechanical holding) plays a significant role in the formation of the shared LEE.
   d) Additionally, all available information leads to the conclusion that, at least at the currently measured rates, **the particle background does not significantly contribute to the observed LEE**, even at surface facilities.
   e) **No impact of the presence of the $^{55}$Fe calibration source** in the vicinity of the crystal on the LEE rate was observed.

3. The second LEE population consists of events observed by only one of the TESs, while the simultaneously measured traces in the other channel appear noise-like – **single-TES LEE**. The signal forming the single-TES population does not propagate through the crystal medium. Instead, it is expected to originate where minimal leakage between the two channels occurs, e.g., at the interfaces between the corresponding TES films and the crystal, within the TES's internal structures, or directly within the readout system.
   a) The spread in the rate of the single-TES LEE measured across different runs reaches a factor of 10, which is generally smaller than that for the shared LEE. So far, no clear dependence on external factors has been identified; **the single-TES LEE appears unaffected by thermal cycles, re-assembling the detector, or lower particle background**.
   b) The spectral shape of the single-TES component is steeper than that of the shared LEE. As a result, **the single-TES LEE becomes dominant at lower energies**, with the exact energy at which this occurs depending on the rates of both components and varying across different measurements, e.g. at $\sim$40 eV in surf1 and $\sim$ 200 eV in UGL1, (see Fig. 4.24).
   c) **The pulses corresponding to single-TES events appear to be slightly faster** than the pulses from the shared LEE.

4. **As shared LEE rates decrease, the single-TES LEE increasingly dominates.** Consequently, the fraction of the total LEE that can be removed varies across different measurements and with time since the cooldown.

5. In the first measurement with the NUCLEUS *double-TES* detector - surf1 - an additional substructure with asymmetric energy sharing ($E_{TES2} > E_{TES1}$) is observed at low energies; it forms a bump-like structure in the measured energy spectra. The exact origin of this structure is not yet identified and is currently under investigation. Interestingly this asymmetric feature was not pronounced in any of the later runs with the same detector.

6. The *double-TES* approach significantly reduces the number of noise triggers by requiring coincident signals in two channels. As a result, to meet the criterion of 0.1% noise triggers from the total simultaneous trigger rate in the first NUCLEUS *double-TES* measurement, **the threshold could be lowered by approximately 30% compared to the standard single-TES approach**.

## 4.6. Discussion

While the majority of LEE observations in the community have been obtained using single-channel phonon readout (e.g., CRESST-III [3, 43], NUCLEUS [59, 187], EDELWEISS [22, 23, 69], Ricochet [25], SuperSDMS-CPD [56], SuperCDMS-HVeV [205], Spice/HeRALD [207]), several independent measurements employing the double-TES readout approach at surface facilities are also available. In addition to the one presented in this work, these include measurements by the CRESST collaboration with $CaWO_4$ and SOS detectors [211], and by the SPICE collaboration with a QET-based silicon detector [212]. Despite differences in the detector and TES designs, all these measurements confirm the presence of single-TES events, along with a prominent fraction of LEE belonging to the shared component.

In those measurements, the CRESST, SPICE, and NUCLEUS experiments used different approaches for holding the target crystals. In the NUCLEUS detector, the crystal is firmly clamped in place with a bronze holder, whereas CRESST and SPICE aim to minimize mechanical stress on the crystal. For this, CRESST employs gravity-assisted holders, where the crystal is fixed at its position solely by its own weight, while SPICE suspends its crystal on bond wires[8]. Although CRESST and SPICE detectors were designed to experience minimal external stress, a large fraction of events is still shared between the two TESs. This indicates that stress from the holders may not be the only source of the shared LEE. A recent hypothesis suggests that relaxation in the aluminum films, propagated through the crystal medium by dislocations, could be a potential source of these events [217]. Performing dedicated measurements with different aluminum coverage of the crystal surface could be one way to test this idea.

In the CRESST surface measurements with the SOS double-TES detector, the shared component decays with timescales of $(7.4 \pm 1.1)$ days and $(12.4 \pm 1.5)$ days in two separate

---

[8] An earlier dedicated SPICE measurement [207] demonstrated that a crystal glued to its holder experienced more than two orders of magnitude higher LEE rates compared to a crystal suspended on bond wires. This difference was attributed to the relaxation of thermally induced stress between the glue and crystal, suggesting that high external stress on the crystal enhances LEE.

measurements, while the single-TES components remained roughly constant over a measurement duration of approximately 17 days [211]. In the NUCLEUS measurement, the shared LEE component appeared to decay more rapidly (see p. 2a in Sec. 4.5), and longer measurements are required to conclusively determine whether the single-TES component also decays over time since cooldown.

It is notable that the shared LEE level achieved in the UGL1 run is unprecedentedly low for NUCLEUS surface measurements. In Fig. 4.31, the highest (surf1) and lowest (UGL1) LEE rates measured in this series are compared to those observed in Run1 of the NUCLEUS prototype (discussed in Sec.4.1) and in Sapp2 detector operated in Run36 of CRESST-III (discussed in Sec. 3.2). All these detectors use sapphire as target crystals, albeit with different masses. Since the LEE rate does not seem to scale obviously with target mass (see Sec. 3.2.3), the comparison is presented in absolute rate units, normalized only by the measuring time, not exposure.

At 100 eV, the CRESST-III Sapp2 rate measured between 6 to 12 months (173 to 352 days) after cooldown is only $4 \pm 1$ times lower than the shared LEE observed in the shallow facility two weeks after cooldown (UGL1-2), see Tab. 4.4 for the numbers. This difference can be fully explained considering the exponentially decaying nature of the LEE observed in CRESST, even only the slow decay component with $\tau = (140.8 \pm 26.3)$ days in the Sapp2 detector. Accounting for the fast decay time of $\tau = (21.6 \pm 2.1)$ days for Sapp2 can further compensate for the difference, even when scaling the LEE rate by detector mass.

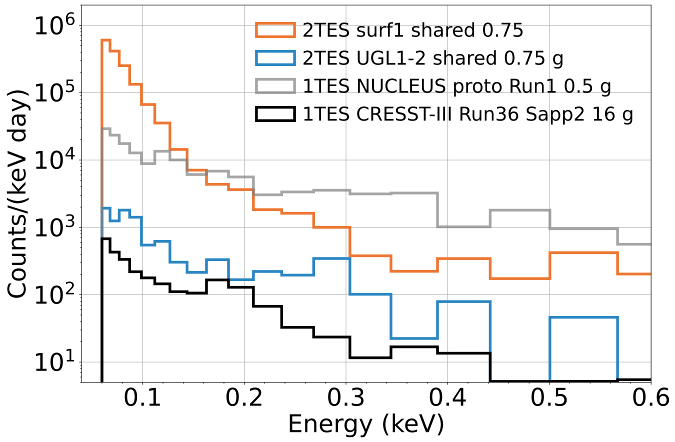

Figure 4.31.: Energy spectra of the shared LEE component measured in the NUCLEUS dbl2 module during the surf1 and UGL1-2 runs (Tab. 4.3), compared to the LEE observed in Run1 of the NUCLEUS prototype measurement campaign (Sec.4.1) and in the Sapp2 detector operated by CRESST-III during Run36 (Sec. 3.2). Since the NUCLEUS prototype and Sapp2 detectors used a single TES readout, selecting the shared LEE was not possible for those measurements. All measurements used sapphire absorbers with the corresponding crystal masses provided in the legend. The spectra are normalized by time, not exposure.

The LEE rate in the NUCLEUS dbl2 detector, comparable to the levels observed in underground measurements, was obtained after the detector had undergone a dozen thermal cycles to mK temperatures. Interestingly, the CPD collaboration reported that the LEE rate in their QET-based silicon detector appears to decay additively with cold time [246]. This raises the question of whether stress on the crystal is permanently released during thermal cycling. If this is the case, thermal cycles could provide a promising strategy to mitigate the shared LEE.

Additionally, it is interesting to compare the *double-TES* observations with the Run4 NUCLEUS prototype measurement, discussed in Sec. 4.1. In Run4, the target cube was operated between two silicon holding wafers, each equipped with a TES, forming a so-called inner veto [40, 187] (see Fig. 4.1a). In this configuration, the target crystal was operated within instrumented holding structures, allowing for the reduction of LEE through a signal ratio cut between the crystal and the veto. However, Run4 employed a *single-TES* readout for the target crystal.

It is plausible to assume that the LEE fraction removed by the veto cut originated from events propagating through the veto to the target crystal or vice versa. It implies that if a second TES channel had been available for the target in Run4, the removed events would have fallen into the shared LEE population. However, since the target crystal in Run4 was equipped with only one TES, there was no way to identify the TES-related population, and the remaining LEE after the veto cut could correspond to single-TES LEE events.

Building on this assumption, Fig. 4.32 illustrates the spread of the single-TES LEE component in the dbl2 detector from the measurements presented in this chapter together with the LEE observed in the NUCLEUS prototype during Run4 after the veto cut. Both spectra start steeply rising below 150 eV. Interestingly, the remaining LEE observed in the single-TES detector during Run4, after the veto cut, aligns with the spread of the single-TES LEE and shares a similar spectral slope. This provides a compelling hint that the steeper LEE remaining in Run4 could have originated from TES-related events.

Continuing with this speculation, let's also consider the Run1[9] of the NUCLEUS prototype measurements (see Sec.4.1). In Run1, the single-TES target was mounted in non-instrumented holders and was supported by sapphire balls, similar to the setup used in the *double-TES* detector presented here. Consequently, no veto cut was available in either case. In Fig. 4.32, the low-energy spectrum measured in Run1 is compared to the spread of shared LEE components measured in different *double-TES* runs. The UGL1 measurement was excluded from the band, as the shared LEE in this run exhibited rates up to two orders of magnitude lower, possibly due to long waiting times or thermal cycles that are irrelevant to the NUCLEUS prototype measurements.

For both cases – Run1 and the shared LEE in the *double-TES* measurements – the single-TES component and the Run4 spectrum are subdominant down to the very low energies and rise steeper. Additionally, the spectra from Run1 and the shared LEE in the *double-TES* measurements start rising at higher energies of several hundred eV. While the Run1 spectrum shows moderate agreement with the shared component band above 100 eV, it

---

[9] It might seem more logical to use the Run4 before the veto cut spectrum here, but it is heavily populated by leakage signals from events originating in the veto (see Fig. 8.41 in [40]).

has a lower rate at the lowest energies. However, if the dominant contribution to the shared band indeed arises from stress in the holders, this discrepancy could be expected, given the differences in applied forces and their magnitude. This is partially supported by the different steepness of the shared LEE spectra in surf1 (before detector re-mounting) and surf3 (after re-mounting) (see Fig. 4.25).

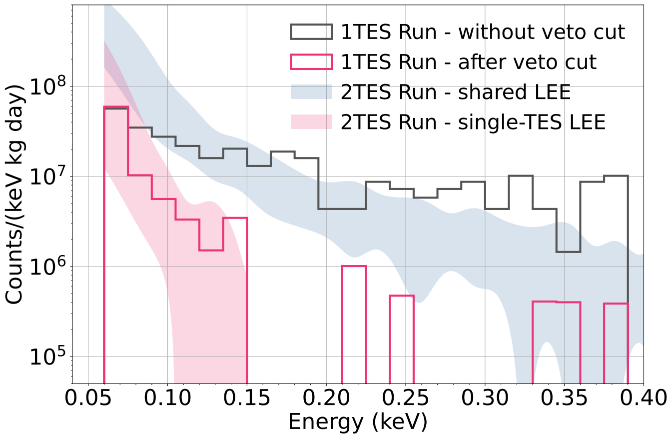

Figure 4.32.: Energy spectra from Run1 (gray line) and Run4 after the veto cut (magenta line) of the NUCLEUS prototype measurements described in Sec. 4.1, obtained with a target crystal equipped with a single TES. The pink shaded area represents the spread of the single-TES LEE across different runs listed in Tab. 4.3, measured in TES1 and TES2 (shown in Fig. 4.30). The gray shaded area shows the spread of all shared LEE spectra from different runs listed in Tab. 4.3, excluding the UGL1 measurement, which had up to two orders of magnitude lower rates. The shaded areas indicate the corresponding minimum and maximum values for each group, including statistical uncertainties. The similarity between the Run4 spectra and single-TES LEE suggests that the veto cut may be effective in reducing the shared LEE component.

## 4.7. Outlook

The results obtained with the NUCLEUS *double-TES* detector turned out to be crucial for developing a strategy to address the LEE observed in the experiment. Several specific tests and measurements are proposed here as promising next steps to further reduce the LEE and better understand its origin.

Given the encouraging findings from the LEE studies presented in this chapter, the dbl2 detector was installed for the first background run of the fully assembled NUCLEUS setup, which began in the UGL in the summer of 2024. With a longer measurement period, these data will allow for a more detailed study of the time dependence of various LEE contributions. Understanding the evolution of LEE components over time is critical for defining an effective mitigation strategy.

The unprecedentedly low LEE rates of only about 10 counts per day at 100 eV observed in the UGL1 measurement may provide a pathway to a controlled mitigation approach. To investigate whether thermal cycling can reduce the LEE, a dedicated series of measurements is currently being conducted at TUM in collaboration with MPP. This experiment involves first measuring the LEE levels in several *double-TES* detectors, followed by controlled thermal cycling between 300 K to 4 K by slowly immersing the detectors in liquid helium. The number of cycles can be chosen to be similar to that reported in the series of measurements presented here - around a dozen - or even increased by an order of magnitude to possibly enhance the effect. After a set number of cycles the LEE rate will be remeasured and directly compared to the initial data. This test will determine whether temperature cycling has an impact on the LEE rate. If it does, a deeper investigation into the underlying solid-state physics processes will be needed, supported by experimental efforts to identify the precise temperatures and timescales relevant to these effects.

In parallel, new tools are being developed within the NUCLEUS collaboration to enhance pulse shape discrimination. Since, as was shown in this chapter, different LEE populations display subtle variations in pulse shape, this approach could complement existing techniques to select absorber-only events [247].

At the same time, NUCLEUS is developing a detector module where the target crystal is fully enclosed by a silicon inner veto, which is also equipped with a TES. As illustrated in Fig. 4.32, combining such *instrumented inner veto* with a *double-TES* target offers a promising opportunity to address both LEE components: shared LEE could be reduced via the veto cut, while single-TES events can be eliminated through energy sharing between the two TES channels of the target crystal. The module with both features is currently being developed and tested at TUM as part of [248] and is expected to be operated in 2025.

# 5. Observation of a neutron-induced nuclear recoil peak at 100 eV scale in a NUCLEUS $CaWO_4$ detector

Measurements of CE$\nu$NS and searches for DM-nucleus scattering rely on detecting the nuclear recoil energy deposited in the target. In low-threshold cryogenic experiments, such as NUCLEUS and CRESST, the region of interest lies in the sub-keV energy range. However, currently-available low-energy calibration sources are primarily based on electron recoils (see 1.3.2). Additionally, at recoil energies below several hundred eV, a significant fraction of energy might be stored in crystal lattice defects. This would result in a deformation of the measured energy spectra and thus affect their interpretations [222, 249]. Therefore, gaining a detailed understanding of the detector response to nuclear recoils at low energies is of the utmost importance.

In this chapter, after a brief review of the CRAB method for direct nuclear recoil calibration via thermal neutron capture, I will present the dedicated measurements performed at TUM with a NUCLEUS $CaWO_4$ detector exposed to a $^{252}$Cf neutron source, where the mono-energetic nuclear recoil peak at the 100 eV scale was observed for the first time. This observation led to the publication [5]. In the scope of this thesis, I performed one of the two independent analyses of the data reported in the article as “Analysis 2”.

## 5.1. The CRAB method for nuclear recoil energy calibration

A novel approach to direct energy calibration of nuclear recoils based on thermal neutron capture was proposed by the CRAB (Calibrated nuclear Recoils for Accurate Bolometry) collaboration in [189]. The process is illustrated in Fig. 5.1 and can be described as follows: After a target nucleus captures a thermal neutron with a negligible kinetic energy, a compound nucleus in an excited state close to the neutron separation energy $S_n$ is created. The de-excitation process to the ground state typically goes through a multi-$\gamma$ cascade. However, a single MeV-$\gamma$ transition from excited to ground state is possible. In this case, the nucleus will experience a mono-energetic recoil with $E_R = {}^{E_\gamma}/_{2M}$, where $E_\gamma$ is the energy of the emitted $\gamma$, and $M$ is the nucleus mass. When a cm-scale target crystal is operated, the high-energy $\gamma$ escapes and the only remaining energy measured by the detector is nuclear recoil energy on the 100 eV scale.

Parameters that ensure a substantial probability for such a process include a high natural abundance of the target isotope in the crystal, a high thermal neutron capture cross-section of the target nucleus, as well as a considerable branching ratio for the single-$\gamma$ transitions. According to the FIFRELIN simulation code developed within [189], the most prominent mono-energetic nuclear recoil peak for $CaWO_4$ targets is expected for the $^{182}$W isotope with a natural abundance of 26.5%. The branching ratio of this single-$\gamma$ transition is 13.94% and the corresponding $E_\gamma = 6191$ keV and $E_R = 112.5$ eV. For other W isotopes, capture reactions lead to less significant peaks at 85 and 160 eV. Since this is exactly in the region of interest of the experiment, a dedicated measurement was performed by the NUCLEUS and CRAB collaborations presented next.

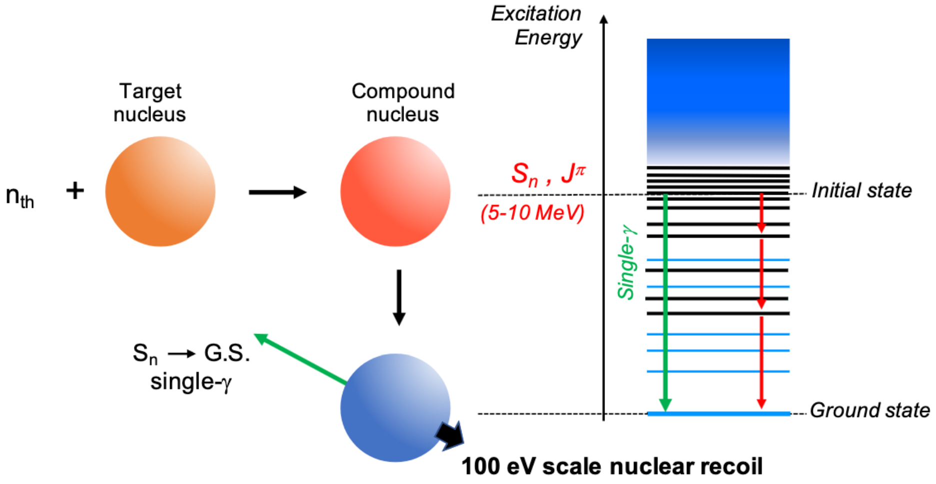

Figure 5.1.: Illustration of the process in which the mono-energetic nuclear recoil peak is induced in the target crystal: A thermal neutron capture by a target nucleus creates a compound nucleus in an excited initial state. The desired signal is the nuclear recoil energy from the de-excitation process through a single-$\gamma$ emission. The illustration is taken from [189].

## 5.2. Experimental setup description

Following the CRAB idea for nuclear recoil calibration, a dedicated measurement was performed at TUM where a $CaWO_4$ NUCLEUS detector was irradiated by a $^{252}$Cf neutron source. A 0.75 g detector cube with a side of 0.5 cm equipped with a W-TES was held by a bronze clamp, as shown in Fig. 5.2 left. The point-like contacts between the crystal and the flexible bronze clamps were realized using sapphire spheres of 1 mm diameter. The crystal was continuously exposed to a $^{55}$Fe source for energy calibration. The detector encapsulated into a copper housing was operated in a dry dilution refrigerator Bluefors LD400 installed in the facility on the first floor of the Physics Department of the Technical University of Munich. The vibrations from the pulse tube cooling system were effectively attenuated by a two-stage spring decoupling system[185], and no additional shielding around the detector against backgrounds was used.

The setup was exposed to a commercial $^{252}$Cf neutron source with an activity of 3.54 MBq. Spontaneous fission, with a branching ratio of 3%, provides an average of 3.77 neutrons per fission, with an average energy of 2.12 MeV. The source was located outside the cryostat in a multi-layered shielding box on a movable platform. The configuration of the layers (Fig. 5.2 right) was optimized in the scope of [250] to maximize the flux of thermal neutrons emitted in the direction of the detector and to reduce the fast neutron and $\gamma$ background from the source based on inputs from simulations. The source capsule was installed inside a polyethylene (PE) cube with a side length of 10 cm. A 5 cm thick layer of PE was placed in the direction of the detector to thermalize the emitted neutrons. To reduce the gamma background, a 7 cm thick layer of lead was positioned in front of it. The source was surrounded on the other sides by graphite blocks to slow down and reflect neutrons and by blocks of borated PE for radiation protection. The source was located (80±1) cm from the detector.

A comprehensive model of the detector and its surrounding environment, including the entire cryostat and the neutron source configuration, was implemented in a Geant4 Monte Carlo simulation. The FIFRELIN code was used to predict the particle flux emitted from the fission of $^{252}$Cf and the de-excitation of tungsten nuclei following neutron capture. This simulation predicts a thermal neutron rate of approximately 0.25 $n_{th}$/s at the surface of the cryogenic detector.

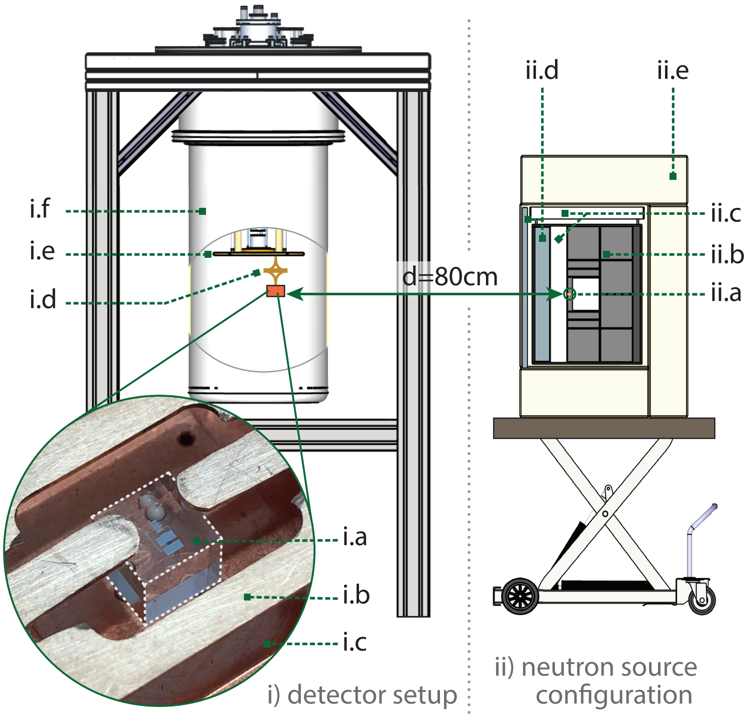

Figure 5.2.: Detector setup (i) and configuration of the neutron source (ii) in the CRAB measurements at TUM. The NUCLEUS $CaWO_4$ detector (inset on the left) is equipped with a W-TES (i.a), fixed at its position with a bronze clamp (i.b), and is encapsulated in a copper housing (i.c). This detector module is installed in the dry dilution refrigerator (i.f) and is decoupled from the mixing chamber (i.e) by a two-stage spring decoupling system (i.d). The $^{252}$Cf neutron source was installed outside the cryostat on a movable platform. The source was installed inside a PE cube (ii.a) surrounded by layers of graphite (ii.b), PE (ii.c), lead (ii.d), and borated PE (ii.e). The illustration is taken from [5].

## 5.3. Data description

The measurement was performed at TUM by the NUCLEUS and CRAB teams. Two datasets were obtained in this setup during one cryogenic run in July 2022. First, a *background* dataset of 18.9 h total time was collected in the absence of the neutron source to optimize the detector and characterize the background rate. From this, a stable period of 15.7 h was used in the analysis presented in this work. A neutron source was then installed next to the cryostat as described in Sec. 5.2 and shown in Fig. 5.2. A *source* dataset of the total measuring time of 40.2 h was collected over the next few days. The data stream was continuously recorded with the VDAQ2 acquisition system (Sec. 2.2.1) with a sampling frequency of 10 kHz. Control pulses were injected through the ohmic heater every 10 seconds and were used for active detector stabilization and to identify stable periods in offline analysis. The main characteristics of the two datasets are listed in Tab. 5.1.

| | background data | source data |
|---|---|---|
| Absorber material | CaWO$_4$ | |
| Absorber mass | 0.75 g | |
| Sampling rate | 10 kHz | |
| Record window | 2048 samples ⇔ 205 ms | |
| Date of the measurement | Jul 28 - 29 2022 | Jul 29 - 31 2022 |
| Measuring time | 15.7 h | 40.2 h |
| Control pulses | Every 10 s | |
| Linear range | below 1 V ⇔ 9.3 keV | below 1 V ⇔ 9.0 keV |
| Trigger threshold | 3.25 mV | |
| Analysis threshold | 50 eV | |
| Baseline resolution | $(0.654 \pm 0.004)$ mV ⇔ $(6.06 \pm 0.04)$ eV | $(0.674 \pm 0.004)$ mV ⇔ $(6.07 \pm 0.04)$ eV |
| Calibration factors | $(9.261 \pm 0.002)$ keV/V | $(9.005 \pm 0.002)$ keV/V |

Table 5.1.: Characteristics of the datasets collected in the CRAB measuring campaign with a NUCLEUS detector at TUM. File lists used in the analysis are provided in App. C.2.

## 5.4. Special aspects of analysis

Since the main goal of this measurement campaign was to verify the existence of the predicted nuclear recoil peak induced in CaWO$_4$ by thermal neutrons around 112 eV, an unbiased analysis of the *source* dataset was essential. To achieve this, the analysis procedure was developed on the *background* dataset and then blindly applied to the *source* data.

The analysis generally follows the steps described in Ch. 2. Triggering was performed offline with an optimum filter (OF) approach at the threshold corresponding to $5\sigma_{BL}$. Triggered events were stored in record windows of 2048 samples, corresponding to 205 ms. Amplitude reconstruction was performed by re-applying OF to the triggered record windows.

In this section, I focus on the analysis aspects unique to the data discussed.

### 5.4.1. Detector performance

The detector response is linear up to 9.3 keV in the *background* data and 9.0 keV in the *source* data. This allows the particle pulse template shown in Fig. 5.9a to be built from the $K_\alpha$ events. Energy calibration was performed with a $^{55}$Fe source shining on the crystal. It provides two closely located X-ray lines: $K_\alpha$ at 5.895 keV and $K_\beta$ at 6.49 keV shown in Fig. 5.3a. The calibration factor, which converts amplitude to energy, is obtained by fitting a linear function to the three data points: (0,0), $K_\alpha$, and $K_\beta$, as shown in Fig. 5.3b. This results in $(9.261 \pm 0.002)$ keV/V for the *background* data and $(9.005 \pm 0.002)$ keV/V for the *source* data. The calibration factor was kept constant in each respective dataset since the detector response was stable over the measuring time, as shown in Fig. 5.4.

The calibration performed under this simple linearization from the calibration lines at $\sim 6$ keV down to the threshold does not address potential nonlinearities in the detector response. Such effects may arise from the intrinsic nonlinearity of the readout circuit, described, e.g., in [251], or from the shape of the transition curve. As a result, there is a significant combined systematic uncertainty conservatively estimated as $[-18; 25]\%$ in [5] on the energy reconstructed around the expected nuclear recoil peak at the 100 eV scale. The lower uncertainty of $-18\%$ was estimated by the NUCLEUS analysis team by studying the impact of the truncation limit value on the amplitude reconstruction. A shift of calibration factor for lower truncation limits might hint towards a small distortion of the transition curve between the calibration peaks and the sub-keV part of the spectrum. The higher uncertainty limit of $25\%$ was calculated by estimating the effect of bias current splitting between the TES and the shunt resistor. Using the readout circuit shown in Fig. 1.3 results in a nonlinear relationship between the SQUID voltage output and the energy deposition under the assumption that the TES resistance change is linearly proportional to the energy deposition. Both effects could possibly be compensated to improve the energy reconstruction precision by mapping the detector response in the region of interest with heater pulses as described in Sec. 6.4.

The baseline resolution was determined by superimposing a template pulse on a set of randomly collected noise traces as described in Sec. 2.6.1. This procedure gives $\sigma_{BL} = (6.06 \pm 0.04)$ eV for the *background* data and $\sigma_{BL} = (6.07 \pm 0.04)$ eV for the *source* data. Thus, while the particle count rate in the detector increased from 0.5 cps to 0.7 cps after the source was installed, the detector performance did not suffer from the presence of the neutron source.

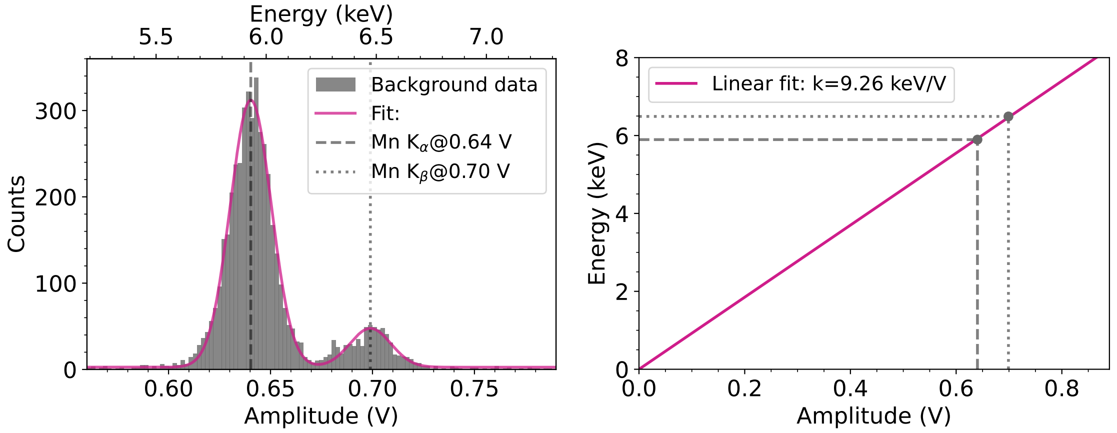

(a) Fit of the measured K$_\alpha$ and K$_\beta$ lines from the $^{55}$Fe source with a double Gaussian function. The positions of the fit are used to obtain the linear function of the detector response shown in Fig. 5.3b.

(b) The detector response function obtained as a linear fit through the point of origin and positions of the K$_\alpha$ and K$_\beta$ lines defined in Fig. 5.3a.

Figure 5.3.: Energy calibration procedure for the *background* data.

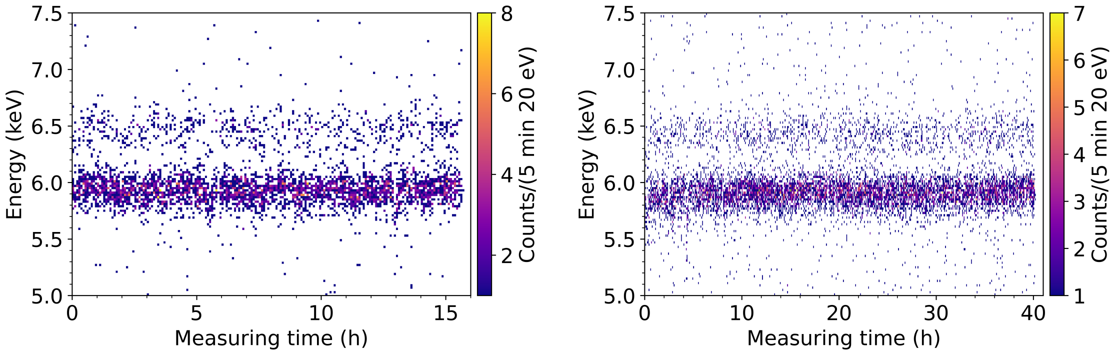

(a) Background data

(b) Source data

Figure 5.4.: Stable detector response to the $^{55}$Fe K$_\alpha$ and K$_\beta$ lines over the measuring time.

### 5.4.2. Event selection

To ensure correct energy reconstruction, only events with undisturbed particle-like pulse shapes were selected for the final energy spectrum. An example of such a particle event is shown in Fig. 5.5a.

In addition to pulses caused by particle recoils, the data stream contains different types of artifacts that cause triggering. One of them originates from the sapphire balls of the holding structure (Fig. 5.2). Signals in the balls are transmitted to the target crystal through the contact points. Since in this case the phonons travel through the interface, such events exhibit slower pulse shapes compared to particle recoils in the target crystal, as can be seen in Fig. 5.5b. Another type of events present in the stream is shown in Fig. 5.5c. Within the record window used in this analysis, such events do not fall back to the baseline level. Only an extended record window reveals the pulse-like nature of these slow events (see Fig. 5.5c right). They exhibit 5 times slower decay times than particle pulses. The origin of these slow events remains to be determined. Both - events caused by transmitted signals from the holding balls and slow pulses - were also observed in the *double-TES* detector data and are discussed in Sec. 4.3.2.4.

A peculiar artifact that required special treatment was present in these data. It is characterized by an instantaneous jump in the baseline level as shown in Fig. 5.5d and is most likely caused by the electronics. In addition, the data contains standard artifacts such as flux quantum losses (FQLs) (Fig. 5.6), pile-up events, and pulses sitting on decaying baselines. A careful selection of events, particularly in the region of interest, was essential for this analysis to prevent artifacts from compromising the observation of the neutron calibration peak at the 100 eV scale, while also preserving valuable statistics. The following selection criteria were developed on the *background* dataset and then applied to the *source* data to minimize selection bias.

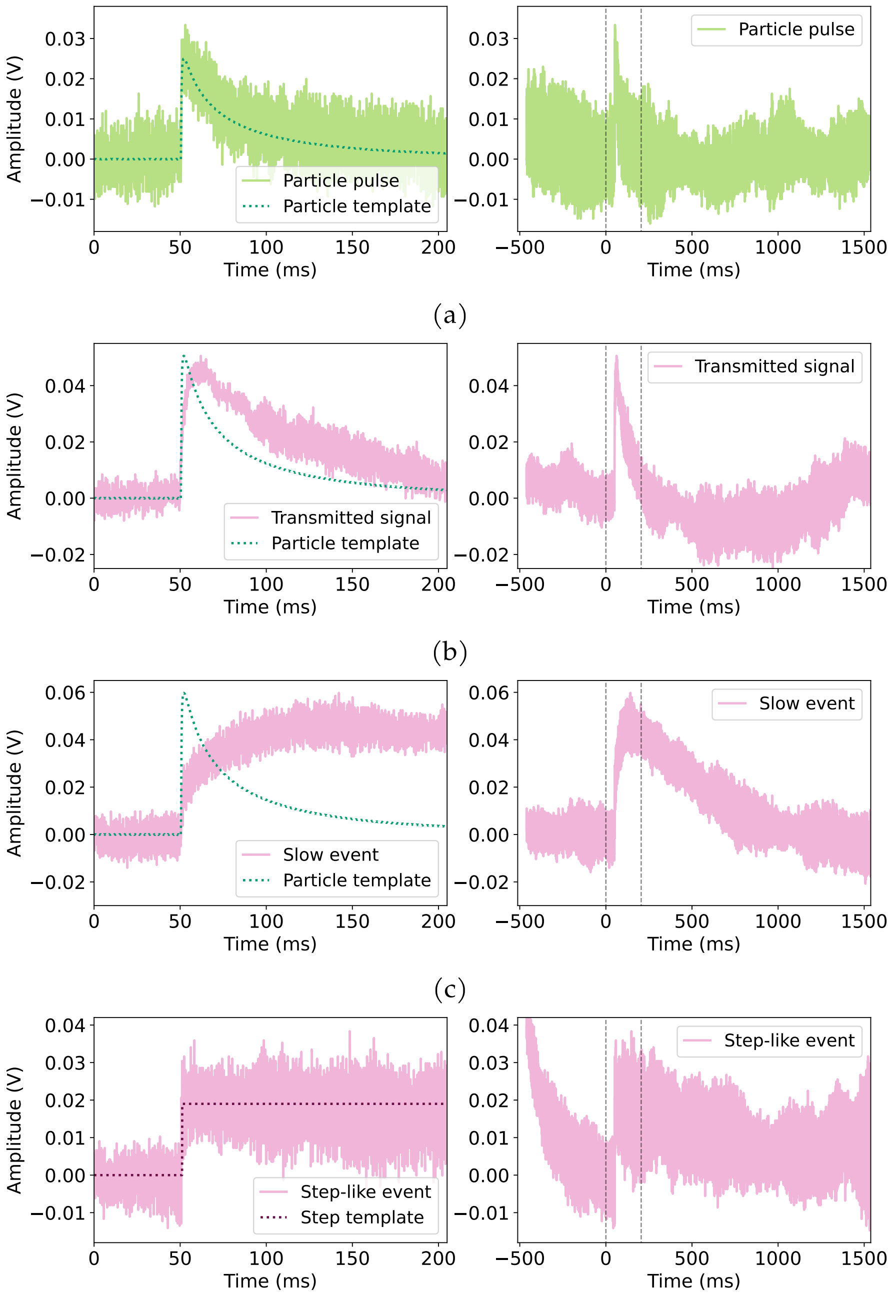

(a)

(b)

(c)

(d)

Figure 5.5.: Examples of triggered events in a record window of 205 ms used in the analysis on the left side and in the extended by 10 times record window on the right side. (a) Example of a pulse survived the selection criteria, (b-d) examples of different event classes rejected by the selection criteria. Particle and step templates are shown on top of the measured pulses to exemplarily highlight the similarities and differences in the pulse shapes. The vertical dashed lines in the right panels indicate the original 205 ms record windows shown on the left.

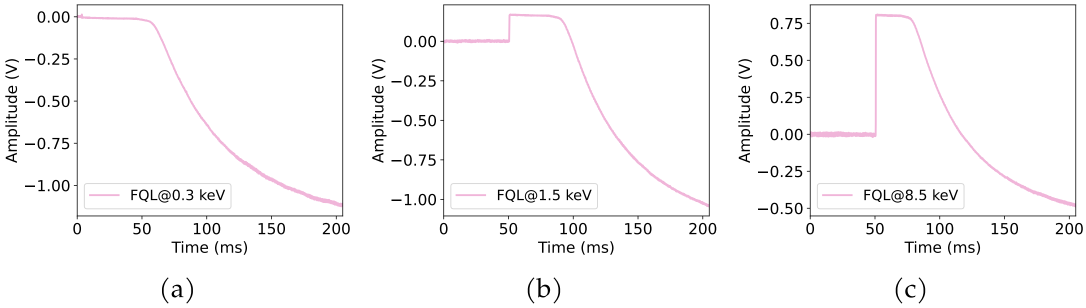

Figure 5.6.: Different types of FQL artifacts present in the data populating the raw energy spectrum around 0.3, 1.5 and 8.5 keV and rejected by the selection criteria (see Fig. 5.10).

1. **Stability cut** was performed to exclude periods of detector operation with strongly deviating response, defined as periods where the control pulse height deviates from its mean by more than $10\sigma$.

2. **Rate cut** was applied to identify periods of increased trigger rate observed in these data, as shown in Fig. 5.7. During these periods, the detector suffers from additional unidentified noise that causes false positive triggers at low energies.

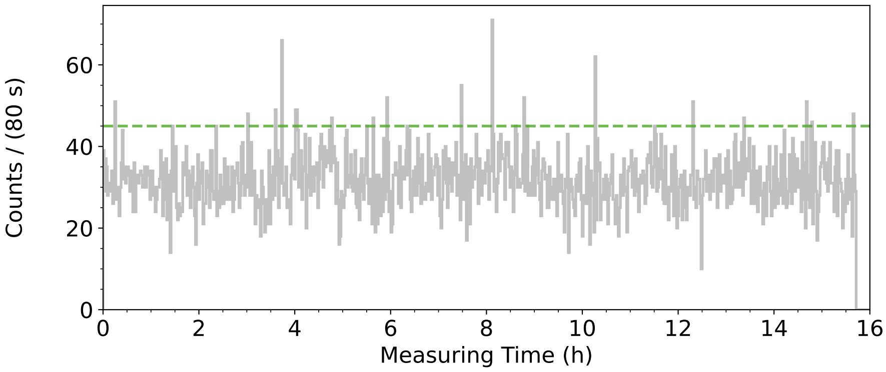

Figure 5.7.: Illustration of the rate cut for the *background* data. The total trigger rate per 80 seconds is shown versus measuring time. The events falling in the time periods where the trigger rate exceeds 45 counts per 80 seconds, marked with the green dashed line, were excluded from further analysis.

3. **Maximum position cut:** Only events with the maximum position within ±1 ms from the default trigger position were selected to ensure only the pulse that caused the trigger is considered.

4. **Cut on OF and SE fit RMS values** was performed to select events with pulse shapes close to the particle template. This cut is effective in identifying and rejecting pulses with slower pulse shapes, such as those from the signal transmitted through the supporting sapphire balls shown in Fig. 5.5b. It also helps against FQLs shown in Fig. 5.6, since the shape of these events is very different from the particle-like pulse.

5. **Cut on the ratio of the BL Difference and the OF Amplitude:** To reject pulses on decaying baselines (see Sec. 2.4), a cut based on the BL Difference parameter is used. Since particle pulses do not fully relax within the recording window as the energy increases, the baseline level at the end of the recording will begin to deviate from the level at the beginning[1]. To compensate for this effect, a ratio of the BL Difference and the OF Amplitude was used instead, which allowed using a flat cut on this new parameter, as illustrated in Fig. 5.8. Additionally, this cut is effective against slow events present in the data stream. An example of such an event is shown in Fig. 5.5c.

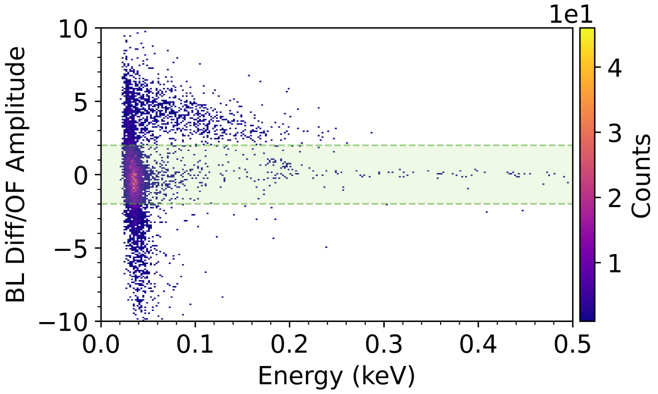

Figure 5.8.: The ratio of the BL Difference parameter and the OF Amplitude is plotted against the reconstructed energy for the *background* data. Only events with $|\text{BL Diff/OF Amplitude}| < 2$ were selected. Events above the green region contain mostly slow events, such as the one shown in Fig. 5.5c, which do not decay to the baseline level within the record window.

6. **Relative RMS difference cut against step-like events:** While the BL Difference cut rejects step-like events at high energies (i.e., with a high signal-to-noise ratio), a special selection criterion was necessary to identify such step-like events at low energies. A step-like template was created to describe the typical shape of these artifacts. It is shown in Fig. 5.9a together with the particle template. For each registered event, two fits were performed: with the particle template and with the step-like template. In both cases, a third-degree polynomial function was added to describe the baseline (see Sec. 2.3.5 for details on the fitting procedure). As expected, particle pulses are poorly described by the step-like template and vice versa. The resulting RMS values of the fits were compared via the relative difference, defined as $(RMS_{step}-RMS_{particle})/(RMS_{step}+RMS_{particle})$, and only events better described by the particle template were selected, as shown in Fig. 5.9b.

---

[1] This effect can be corrected by increasing the recording window. In this case, the pulses would fall back completely within the record. However, due to the high overall rate, this would increase the number of pile-up events, which increases the dead time.

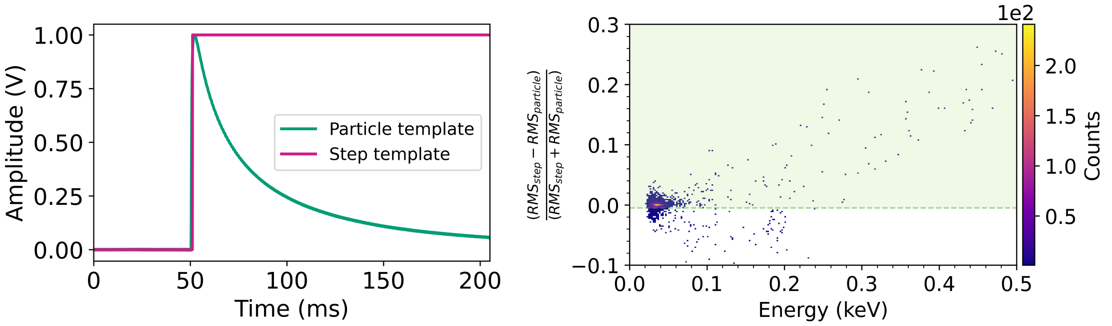

(a) The particle template built from the $^{55}$Fe $K_\alpha$ events is shown in green. The magenta line shows the step template, which describes the step-like events like the one in Fig. 5.5d.

(b) Relative difference of the RMS values from the particle and step template fits vs. the energy of the events. Events from the green shaded area were selected.

Figure 5.9.: Illustration of the relative RMS difference cut on the *background* data.

The impact of the selection criteria applied one after the other in the listed order on the energy spectrum of the *background* data is shown in Fig. 5.10a. The broad peaks reconstructed around 1.5 and 8.5 keV consist of FQLs (Fig. 5.6b and 5.6c) and are effectively rejected by the OF and SE fit RMS cut. The structure between 0.3 and 0.4 keV is attributed to FQL's tails (Fig. 5.6a) and is removed by the maximum position cut. A large fraction of events reconstructed below 200 eV consists of slow pulses (Fig. 5.5c), identified by the BL Difference cut. The peak-like structure around 190 eV is formed by the step-like events (Fig. 5.5d) and is rejected by the relative RMS difference cut.

The same selection criteria were applied to the *source* data. The only adjustment was made to the rate cut due to the increase in total rate in the presence of the source. As can be seen from Fig. 5.10b, the spectrum of the *source* data contains similar features reconstructed at the same positions as in the *background* data, and thus the cuts were effective against these artifacts.

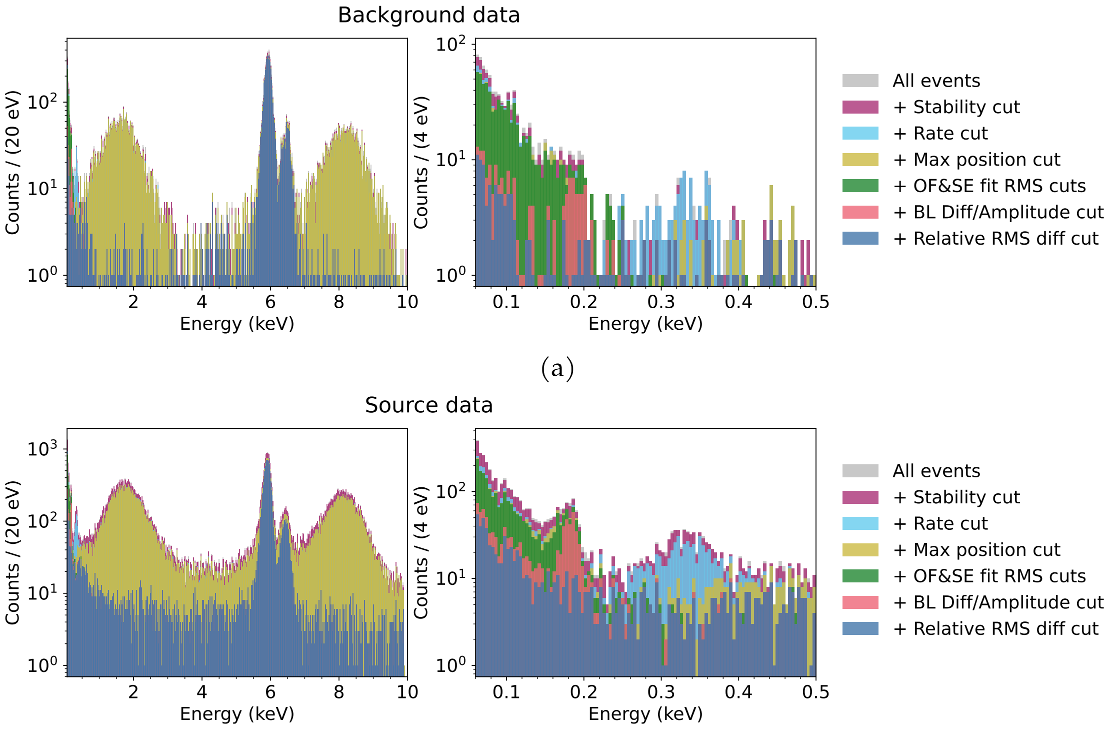

(a)

(b)

Figure 5.10.: Energy spectra measured in the *background* (a) and *source* (b) data set after successive application of the selection criteria described in Sec. 5.4.2.

### 5.4.3. Trigger and cut efficiency

The trigger efficiency was calculated by superimposing a scaled particle template at random times in the data stream and applying the same trigger algorithm used in the main analysis, as described in Sec. 2.5. The efficiency is then defined as the ratio of triggered superposed events to the total number of simulated events for each energy. The trigger efficiency is roughly flat above the analysis threshold of 50 eV, corresponding to $\sim 8\sigma_{BL}$, and is equal to (84.2±0.8)% in the *background* data and (77.5±0.3)% in the *source* data. This value is a measure of the dead time of the detector due to the heater pulses and pile-up events. Thus, the higher overall rate in the presence of the source explains the lower trigger efficiency in this data-taking period.

To calculate the cut efficiency, simulated events are constructed in a manner similar to that described in Sec. 2.5. The particle template, corresponding to a fixed energy value within the linear range of the detector response, is superimposed on a set of randomly collected noise traces. To increase the statistics, the same noise set is used for calculating the cut efficiency at each simulated energy value. The selection criteria outlined in Sec. 5.4.2 are then applied to these constructed events, and the fraction of events that pass the cuts determines the efficiency at a given energy. The cut efficiency is flat above $\sim 0.7$ keV and decreases towards lower energies. This energy dependence is introduced by the relative RMS difference cut. Although we normally try to avoid strong energy dependence in event selection efficiency, in the presence of the unusual step-like artifact, such energy dependence was tolerated to ensure that the region of interest for the nuclear recoil peak was cleared.

The total efficiency of the analysis procedure is defined as the product of the trigger and cut efficiency and is shown in Fig. 5.11.

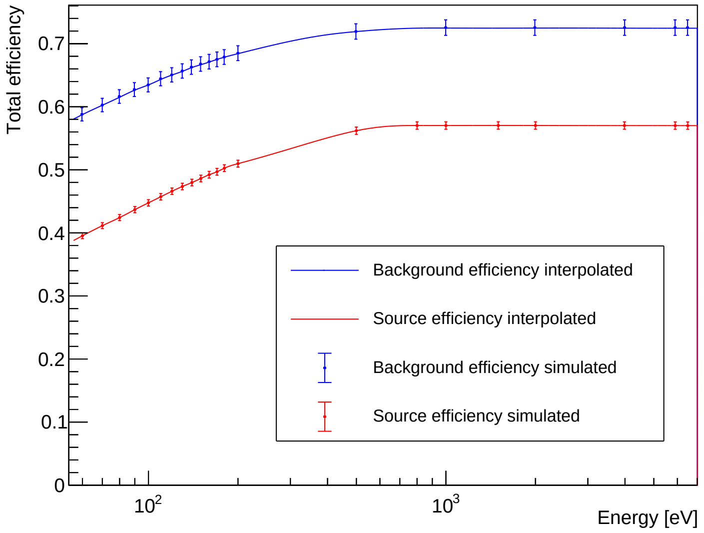

Figure 5.11.: Total efficiency of the analysis for the *background* (blue) and *source* (red) datasets, defined as the cumulative effect of the constant trigger efficiency and the energy-dependent cut efficiency. The data points show the discrete energies used in the cut efficiency calculation, covering the considered energy range of the detector response, with the error bars representing the statistical uncertainties. The solid lines show the extrapolation between the data points.

## 5.5. Energy spectra

Efficiency-corrected energy spectra after applying the selection criteria for the *background*, and *source* data are shown in Fig. 5.12. While the total background rate is generally higher in the *source* data, the intensity of the iron peaks remains constant around 0.12 cps within 2% in both data sets, confirming the robustness of the efficiency calculations.

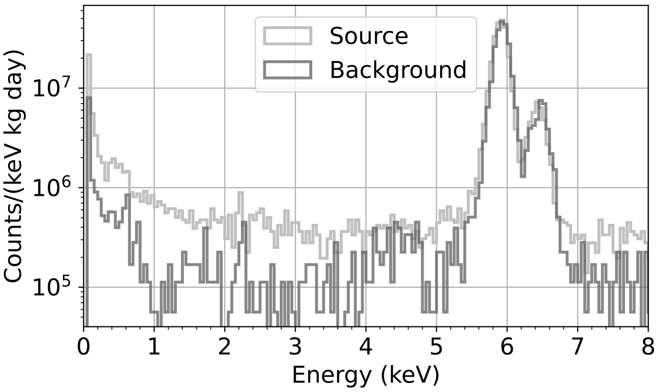

Figure 5.12.: Energy spectra measured in the *background* (dark grey) and *source* (light grey) data sets corrected with the efficiencies from Fig. 5.11.

### 5.5.1. Nuclear-recoil peak observation

In the low-energy part of the *source* spectrum shown in Fig. 5.13, a peak-like structure is observed around 112.5 eV, which is expected from the $^{182}$W nuclear recoil induced by thermal neutrons. Analogous to the results of the independent analysis reported in [5], a likelihood ratio test developed in [252] was performed to evaluate the significance of the observed peak above the background. The peak was described by a Gaussian function, while the background was represented by a sum of two exponential functions[2]. Thus, the total fit function, including both contributions, is written as:

$$F(x) = a \cdot e^{-b \cdot x} + c \cdot e^{-d \cdot x} + \frac{g}{\sqrt{2\pi} \cdot \sigma} \cdot e^{-\frac{(x-\mu)^2}{2\sigma^2}} . \tag{5.1}$$

Two binned likelihood ($L$) fits were performed on the energy spectra between 60 and 300 eV with ($L_{Bck+Sig}$) and without ($L_{Bck}$) the contribution of the Gaussian peak. All fit parameters were left free. The best fits are shown in Fig. 5.13. The statistical test is constructed as $t = -2ln(L_{Bck}/L_{Bck+Sig})$. The resulting $t = 13.9$ confirms the presence of the peak with a significance of $2.9\sigma$. The best fit reconstructs the peak at $\mu_{peak} = 106.3^{+2.3}_{-2.3}$ eV with a standard deviation of $\sigma_{peak} = 8.52^{+1.95}_{-1.44}$ eV. All fit parameters are listed in Tab. 5.2.

The reconstructed mean position of the peak agrees with the predicted 112.5 eV within the rather large systematic uncertainty of the energy reconstruction discussed in Sec. 5.4.1. The measured number of counts in the peak defined by the integral of the Gaussian function is $60^{+13}_{-12}$. Taking into account the analysis efficiency from Fig. 5.11, the ratio between the measured and the predicted number of events in the nuclear recoil peak by the FIFRELIN code is $1.2 \pm 0.4$. Thus, the measured peak is fully compatible with the

---

[2] The choice of the background model was validated by the quality of the fit to the data outside the peak region.

predictions within the uncertainties. In addition, the resulting fit parameters of the peak are fully compatible with the other analysis presented in [5] also listed in Tab. 5.2.

| | $a$ (Counts) | $b$ (eV)$^{-1}$ | $c$ (Counts) | $d$ (eV$^{-1}$) | $g$ (Counts eV$^{-1}$) | $\mu_{peak}$ (eV) | $\sigma_{peak}$ (eV) |
|---|---|---|---|---|---|---|---|
| "Analysis 1" | $3270^{+356}_{-339}$ | $0.0730^{+0.0016}_{-0.0015}$ | $12.6^{+0.8}_{-0.8}$ | $0.0055^{+0.0003}_{-0.0004}$ | $149.2^{+38.7}_{-35.8}$ | $106.7^{+1.9}_{-2.0}$ | $6.04^{+1.64}_{-1.38}$ |
| "Analysis 2" (this work) | $2867^{+265}_{-254}$ | $0.0666^{+0.0013}_{-0.0012}$ | $15.5^{+0.8}_{-0.8}$ | $0.0043^{+0.0003}_{-0.0003}$ | $240.1^{+52.3}_{-49.4}$ | $106.3^{+2.3}_{-2.3}$ | $8.52^{+1.95}_{-1.44}$ |

Table 5.2.: Best fit parameters with the presence of the peak describing the *source* spectrum with Eq. 5.1 for two independent analyses done for [5]. The parameters of the neutron calibration peak are fully compatible between the two. "Analysis 2" corresponds to the one done in the scope of this thesis, and the results of the fit are shown in red in Fig. 5.13.

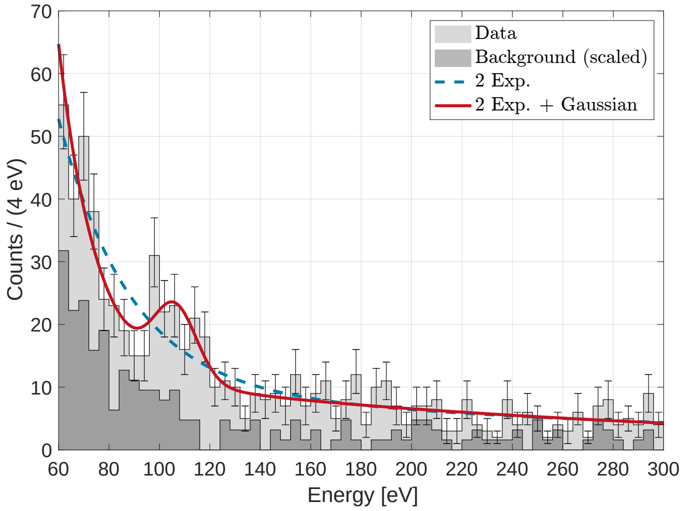

Figure 5.13.: Energy spectra measured in the *background* (light gray) and *source* (dark gray) datasets. The background spectrum is scaled to match the source exposure. The error bars represent the Poisson uncertainties. The dashed blue line shows the best fit with the background-only function, and the solid red line shows the best fit with the presence of the peak using Eq. 5.1 and the parameters listed in Tab. 5.2. The figure is provided by Sebastian Dorer (TU Wien) and the CRAB and NUCLEUS collaborations.

## 5.6. Discussion and outlook

The measurement presented in this chapter, performed with a NUCLEUS $CaWO_4$ detector irradiated by a $^{252}$Cf neutron source, provided the first observation of the monoenergetic nuclear recoil peak on the 100 eV scale induced by thermal neutrons[3]. The observed peak is fully compatible with the predictions for the $^{182}$W isotope after neutron capture and demonstrates the potential of the new method to calibrate nuclear recoils in the region of interest of low-threshold cryogenic experiments.

---

[3] This was followed by similar observations by the CRESST collaboration for the $^{182}$W isotope in a $CaWO_4$ detector reported in [224] and for the $^{27}$Al isotop in the $Al_2O_3$ detector presented in [115].

Simultaneous calibration with low-energy sources based on X-ray fluorescence or LED pulses, described in Sec. 1.3.2, will enable a comparison of the detector response between nuclear and electronic recoils. This provides an opportunity to gain a detailed understanding of the phonon detector response at the 100 eV-scale.

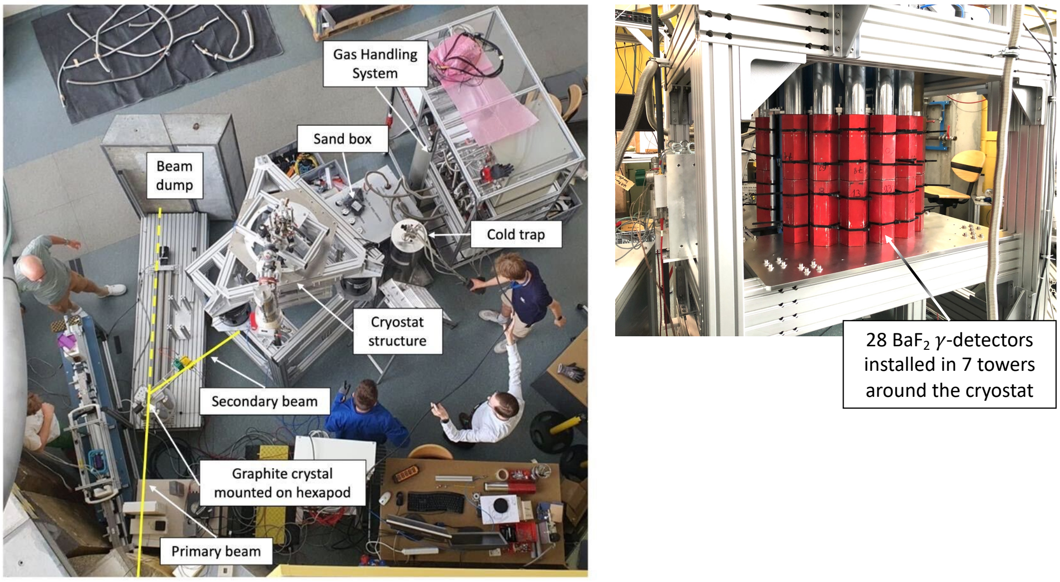

Figure 5.14.: Left: Photograph of the experimental setup for the upcoming CRAB campaign, commissioned at the TRIGA-Mark II research reactor in summer 2024. The beam will deliver a flux of thermal neutrons, which is expected to significantly reduce source-related background compared to the measurements with a neutron source described in this chapter. The beam is focused on the cryogenic detectors, installed inside the cryostat, where various materials can be used as absorbers. Right: An array of 7×4 $\gamma$-detectors around the cryostat, based on inorganic $BaF_2$ scintillator, is used to measure the $\gamma$ energy in coincidence with the recoils in the cryogenic detector. The pictures are provided by Andreas Erhart (TUM) and the CRAB and NUCLEUS collaborations.

Tagging the $\gamma$-rays emitted by nuclear deexcitation with external detectors as suggested in [189] would allow selecting events in the crystal that coincide with the $\gamma$ energies expected for particular transitions (e.g. $S_n$ from Fig. 5.1). For $CaWO_4$ detectors, this tagging would allow accessing the peak at even lower energies around 85 eV expected from the $^{186}$W isotope and enhancing the significance of the 112.5 and 160.3 eV peaks by rejecting background multi-$\gamma$ events. This allows probing the local linearity of the energy scale in the 100 eV range. Moreover, as shown in [225], for many isotopes commonly used as targets in cryogenic detectors, there are deexcitation cascade configurations in which the nucleus can temporarily remain at an excited level within the cascade between $\gamma$ emissions. This leads, if the probability is sufficient, to unique spectral features at low energies when the time evolution of the nuclear recoil and $\gamma$ emission processes is taken into account. Coincident detection of emitted $\gamma$'s opens up the opportunity to determine the direction of the recoil and to study its impact on the observed processes. Additionally, such measurements can provide a direct experimental test of the solid-state physics simulations and nuclear models.

Another application is the direct observation of the predicted effect of energy loss due to crystal defects created by nuclear recoils on the expected mono-energetic peaks [222, 249]. It is particularly important to understand this effect at low energies, as it could alter the expected nuclear recoil energy spectra of DM and CE$\nu$NS. Furthermore, it could provide insight into the origin of the LEE. As shown in [204], if the observed LEEs are nuclear recoil in nature, distinguishable spectral features at low energies are expected for materials with a sharp defect creation threshold.

Using a mobile commercial fission neutron source, like the one employed in the measurements presented in this chapter, allows for non-intrusive calibration and can be easily installed at most experimental sites. This source can also be used within the same cryogenic run to ensure identical detector operating conditions between background and calibration data-taking periods. However, such measurements inevitably involve high background levels from fast neutrons and gammas.

Using a thermal neutron beam from a nuclear research reactor, as proposed in [189], would allow a significant reduction of the source-related background and provide a high flux of thermal neutrons. The next phase of the CRAB measurements with various detectors (e.g., NUCLEUS $CaWO_4$ and $Al_2O_3$ and novel TES-based detector developed within [216]) is currently in preparation in the scope of work done in [250, 252] at the Triga-Mark II reactor [253] at TU Wien and is expected to start in late 2024. The setup sketched in Fig. 5.14 consists of the thermal neutron beam from the reactor guided to the cryostat. Inside the cryostat, cryogenic phonon detectors are mounted. The cryostat is surrounded by the $BaF_2$-based $\gamma$-detectors to enable $\gamma$ tagging. Additional lead shielding around the $\gamma$-detectors is foreseen to reduce the external background. The first measurement campaign aims to extend the calibration method presented in this chapter to a high-precision measurement of nuclear recoil peaks for different tungsten isotopes, taking advantage of $\gamma$ tagging. However, absorbers of different materials can be operated as cryogenic detectors.

This facility could also be of interest to the wider community working with ionization detectors. In widely used semiconductors like silicon and germanium, there is currently no consensus on the quenching factor–a measure of the ionization efficiency of nuclear recoils relative to that of gamma–for energies below a few keV [223]. The well-established Lindhard model [254], which predicts the quenching factor, appears to break down at low energies. Accessing low-energy neutron capture lines in these materials could significantly improve understanding in this area critical for experiments based on nuclear recoils. As a result, after the successful demonstration of the method presented in this chapter, the CRAB collaboration is entering an exciting phase, with a rich program that ranges from studying signal formation at low energies for DM and neutrino experiments to testing predictions in solid-state and nuclear physics.

# 6. Dark matter results with a CRESST-III ultra-low threshold silicon detector

The CRESST-III experiment continues to push the sensitivity of its detectors to sub-GeV dark matter (DM). In the recent CRESST-III data-taking campaign, a 0.35 g silicon wafer detector, operated in anti-coincidence mode with a bulk silicon detector, improved the previously best CRESST threshold by three times, achieving 10 eV. This sensitivity enabled the exploration of a new parameter space region for the elastic DM-nucleus scattering cross-section, which led to the CRESST collaboration publication [6]. This chapter presents and details the analysis done for this publication.

The design of the CRESST-III silicon detector module is presented in Sec. 6.1, while the data sets used in this analysis are introduced in Sec. 6.2. Following this, selected analysis aspects are discussed, including triggering and amplitude reconstruction in Sec. 6.3, and the construction of a time-dependent detector response using heater pulses for precise energy calibration in Sec. 6.4. The final data set used for the DM search, along with the corresponding energy spectrum, is detailed in Sec. 6.5. The chapter concludes with the results on the upper limit for the spin-independent DM-nucleon scattering cross-section in Sec. 6.6.

## 6.1. Detector design

In the recent CRESST-III data-taking campaign at LNGS, referred to as Run36 in Ch. 3, a novel silicon (Si) detector module was employed. This module contains four Si crystals: two thin *wafers* of 0.35 g each, with dimensions of $(20 \times 20 \times 0.4)\,\mathrm{mm}^3$, and two *bulk* crystals of 9.32 g each, with dimensions of $(20 \times 20 \times 10)\,\mathrm{mm}^3$. The targets are made from commercially produced Si, and all surfaces were polished after cutting, except for the thin edges of the wafers. This marks the first time a Si target has been operated within the CRESST framework at LNGS. The crystals are supported by three copper sticks each and encapsulated in a copper housing, as depicted in Fig. 6.1a. Since Si is a non-scintillating material and is surrounded by copper, no scintillation light is expected to be generated within this module, in contrasts to the standard CRESST-III design, which uses scintillating $CaWO_4$ targets [43].

Each of the crystals is equipped with its own tungsten TES. The TES for the wafers follows the LD TES design, while the bulk crystals use the PD-S design (see Fig. 3.1 for descriptions of these designs). The four crystals within this module can be thus considered as individual detectors positioned face-to-face. In this configuration, 50% of all detector surfaces face another detector, allowing the study of coincidences between them.

This chapter focuses on one pair of detectors, consisting of a wafer and a bulk crystal highlighted in Fig. 6.1a and schematically represented in Fig. 6.1b. Due to technical issues, it was not possible to operate the other wafer and bulk crystal.

An absolute energy calibration was achieved using a low-activity ($\sim 1\,\mathrm{mBq}$) $^{55}$Fe source attached to one of the module walls, exposing both crystals, as shown in Fig. 6.1b. The source is covered with a layer of glue to suppress Auger electrons from reaching the crystal, and an additional layer of gold was applied on top to shield the detectors from potential scintillation light produced in the glue.

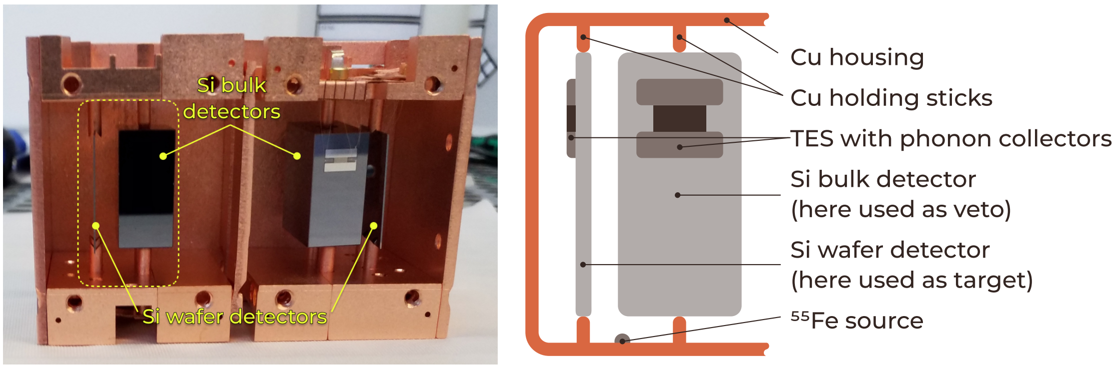

(a) (b)

Figure 6.1.: (a): Picture of the complete CRESST-III Si detector module containing four Si crystals (two wafers and two bulk), each equipped with a TES. Two operated detectors analyzed in this work are highlighted with the dashed rectangular shape. (b): Schematic drawing of the operated part of the Si detector module. The crystals are equipped with TES, held by three copper sticks, and mounted inside a copper housing. The $^{55}$Fe calibration source encapsulated with concentric layers of glue and gold is attached to the module's wall. The drawing is not to scale.

## 6.2. Data sets

Data from the wafer and bulk detectors in the Si module were continuously recorded with a sampling frequency of 25 kHz, as is standard in CRESST. Additional details on the data acquisition process are provided in Sec. 2.2.1. The CRESST-III data-taking campaign, Run36, was ongoing from August 2020 to February 2024, with several periods dedicated to different studies, as outlined in Ch. 3. For the DM search in this chapter, data from 186.9 days of measurements during the background data-taking period were used. This dataset was divided into two parts: a training set and a blind set. The analysis procedure was first optimized using the training dataset of a total of 29.6 days of measurement. The remaining 157.3 days of data were blinded. Once the analysis procedure was finalized, it was applied unchanged to the blinded data set, minimizing the risk of selection bias when defining the cuts.

The wafer detector exhibited better sensitivity than the bulk detectors, achieving a baseline resolution of 1.4 eV compared to 2.7 eV for the bulk detector. Consequently, the wafer detector was used for the DM results presented later in this chapter (Sec. 6.6), while the bulk detector was used as a veto in the analysis. Additionally, energy calibration for the bulk detector proved to be challenging, as discussed in Sec. B. Therefore, this chapter focuses primarily on the wafer detector, although key aspects of the bulk detector analysis are included for completeness. A summary of the properties and main performance parameters of the two detectors, as obtained from the analysis discussed in the next section, is provided in Tab. 6.1.

| | Wafer detector | Bulk detector |
|---|---|---|
| Absorber material | Si | |
| Absorber mass | 0.35 g | 9.3 g |
| Sampling rate | 25 kHz | |
| Record window | 16384 samples → 655.36 ms | |
| Training set measuring time | 29.6 days | |
| Blind measuring time | 157.3 days | |
| Training set exposure | 0.010 kg day | 0.28 kg day |
| Blind exposure | 0.055 kg day | 1.46 kg day |
| Linear range | below 0.3 keV | below 2 keV |
| Trigger threshold | 12.8 mV | 4.3 mV |
| Energy threshold | $(10.0 \pm 0.2)$ eV | $(17.7^{+1.4}_{-1.2})$ eV |
| Baseline resolution | $(1.7 \pm 0.06)$ mV ⇔ $(1.36 \pm 0.05)$ eV | $(0.63 \pm 0.08)$ mV ⇔ $(2.7^{+0.4}_{-0.4})$ eV |

Table 6.1.: CRESST-III Si detector module characteristics. File list used for the analysis is provided in App. C.3.

## 6.3. Triggering and amplitude reconstruction

Triggering is performed offline using the optimum filter (OF) approach, as discussed in Sec. 2.3.2. After applying the OF to the data stream, traces where the filtered signal exceeds a defined threshold are selected and stored in record windows containing 16384 data samples, corresponding to 655.36 ms, for further analysis.

According to the threshold determination procedure based on applying OF to a set of noise traces described in Sec. 2.3.3 and illustrated in Fig. 2.7, the triggering threshold of the bulk detector is set to the value of 4.3 mV that allows one noise trigger per kg-day of exposure.

For the wafer detector, however, the distribution of the OF maxima from the baseline traces, shown in Fig. 6.2a, cannot be fully described by Eq. 2.5 due to the presence of the right shoulder. This shoulder is attributed to the high rate of LEE events coinciding with the selected traces. While the standard procedure, which assumes Gaussian-distributed noise, is sufficient in most cases, it encounters problems when the LEE rate is so high that it significantly contributes to the noise traces. For comparison, the LEE rate at the threshold for the wafer detector is more than two orders of magnitude higher than for the bulk detector (see Fig. 3.7b).

To account for this effect, the original model, which assumed Gaussian noise with a standard deviation of $\sigma$, was extended by introducing an additional "pollution" component. This pollution component follows an exponentially rising distribution toward low amplitudes, characterized by the rate parameter $\lambda$. The extended probability that a sample within a trace equals $x_{max}$ while all other samples are smaller is given by:

$$\begin{aligned} P_d(x_{max}) = &\lambda e^{-(\lambda x_{max})} \cdot \left( \frac{1}{2} + \frac{\mathrm{erf}\left(x_{\mathrm{max}}/(\sqrt{2}\sigma)\right)}{2} \right)^{d-1} \\ &+ \left(1 - e^{-\lambda x_{max}}\right) \cdot (d-1) \\ &\cdot \frac{1}{\sqrt{2\cdot\pi}\cdot\sigma} \cdot \left( e^{-\left(\frac{x_{\mathrm{max}}}{\sqrt{2}\sigma}\right)^2} \right) \cdot \left( \frac{1}{2} + \frac{\mathrm{erf}\left(x_{\mathrm{max}}/(\sqrt{2}\sigma)\right)}{2} \right)^{d-2} , \end{aligned} \tag{6.1}$$

where *d* is the number of statistically independent samples within one trace. The resulting probability function, Eq. 6.1, is then fit to the OF maxima distribution of the wafer detector. In Fig. 6.2a, the Gaussian noise component is shown in green, the additional exponential pollution component in orange, and the cumulative function (Eq. 6.1) in black. The corresponding fit parameters are listed in Tab. 6.2. As discussed in Sec. 3.2.2 and illustrated in Fig. 3.5, the pollution component matches the energy spectrum measured near the threshold, which is fully dominated by LEE events.

| Fit parameter | Value |
|---|---|
| $\sigma$ | (1.889±0.004) mV |
| $d$ | 416±7 |
| $\lambda$ | (0.403±0.002) $\mathrm{mV}^{-1}$ |

Table 6.2.: The values of the best fit parameters of the cumulative model obtained from a maximum likelihood fit of Eq. 6.1 to the baseline triggers shown in Fig. 6.2a.

To validate this extended trigger model, the OF maxima distribution for the voltage-inverted data stream was produced. In this case, all real events become negative and are no longer detected by the trigger algorithm: triggering selects only the noise signal, which fluctuates in both directions. The resulting distribution is shown as a yellow histogram in Fig. 6.2a. The OF amplitude distribution from the inverted stream aligns with the noise component of the fit (green line in Fig. 4.10b), confirming the validity of the extended trigger model.

After distinguishing the two components – Gaussian noise and exponential pollution – it is possible to calculate the expected rates as a funcion of the threshold for both of them. The normalized integrals of the two components are shown in Fig. 6.2b. The pure noise component (green) is used to set the threshold with the same requirement of one noise trigger per kg-day as for the bulk detector, resulting in a trigger threshold of 12.8 mV for the wafer detector. The LEE events from the pollution components are triggered above this threshold and contribute to the final energy spectrum.

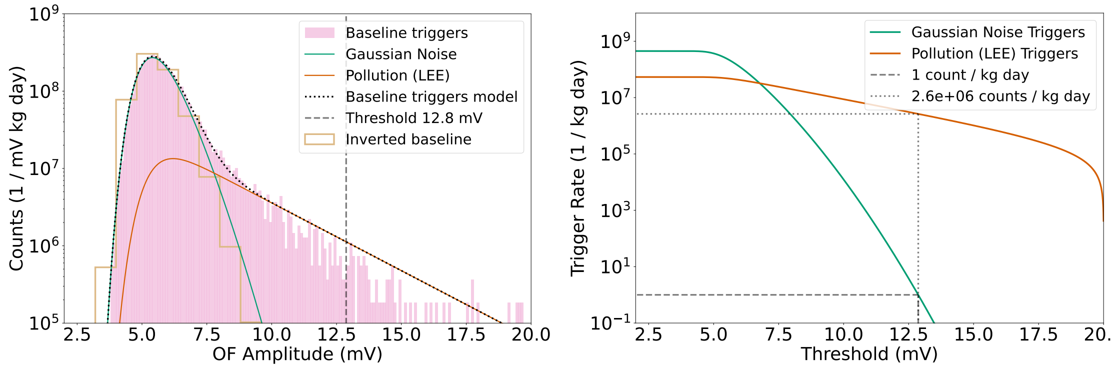

(a) (b)

Figure 6.2.: (a) Distribution of the OF maxima normilized by exposure obtained by applying OF to a set of randomly collected noise traces (pink) with a fit function from Eq. 6.1 (black dotted) assuming normally distributed noise samples (green) and exponentially distributed pollution component (orange) for the wafer detector. (b) Normalized to exposure integral of the pollution component (orange) and the Gaussian noise trigger model characterizing noise trigger rate (green). The threshold value of 12.8 mV is chosen to allow one noise trigger per kg-day of exposure and is shown with the black dashed line.

The same OF is used to reconstruct pulse amplitudes in the linear range of the detector response. For higher pulses, where the pulse shape is not preserved anymore, truncated template fit is applied, as described in Sec. 2.3.5. The linear range of the bulk detector extends to 0.5 V while for the wafer detector to 0.3 V.

## 6.4. Energy calibration with time-dependent response function

The energy calibration is based on electron capture in the $^{55}$Fe source that provides $^{55}$Mn $K_\alpha$ and $K_\beta$ X-ray lines at 5.9 and 6.5 keV respectively [238]. Therefore, a double structure with a known branching ratio is expected to be seen in the measured amplitude spectrum. However, due to instabilities of the detector response over the long data-taking period, a smeared structure in the amplitude spectrum shown in Fig. 6.3a is observed instead. The inset figure shows how the detector response was evolving with time - several jumps and drifts over time are clearly visible resulting in the distortion of the calibration lines shape. Thus, a time-dependent correction of the detector response is required.

To account for such instabilities, the detector response over time is tagged with the help of artificial pulses - *test pulses* - sent periodically every 20 seconds via the gold heater, as described in Sec. 2.2.2. They have fixed discrete injected amplitudes ($A_{inj}$), which correspond to the energy values from threshold up to 17 keV. The amplitude of test pulses are reconstructed using the same approach as for particle pulses, adjusting only the pulse templates. The measured amplitudes of those test pulses over the time of one data segment are shown as pink dots in Fig. 6.3b. A spline function is used for each of the fixed injected amplitudes to get the detector response at each moment of time. The resulting splines are shown as green lines in Fig. 6.3b. The inset figure shows a zoom into the response to the test pulse with the lowest injected amplitude. The smearing seen in Fig. 6.3a originates from jumps in the detector response like the one around 18 hours.

Now a detector response function between the injected and measured amplitude for each moment of time can be built. In Fig. 6.3c, the magenta dots show the values for the measured amplitudes from the spline functions in Fig. 6.3b for one moment of time with respect to the fixed and knows injected amplitude values. To get a continuous detector response function, a cubic spline interpolation between data points is used. The resulting function is shown as the green line in Fig. 6.3c. The inset shows a zoom into lo-amplitudes. As expected, below the truncation limit, the detector response is linear and starts to deviate from the linear behavior above this value.

Under the assumption of the same scaling between test and particle pulses with energy, such function describes the detector response over the entire dinamic range for each moment of time. Therefore, the measured amplitude of each particle event can be converted to an equivalent of the injected amplitude using the detector response function built with the test pulses, as illustrated in Fig. 6.3c. After the time-dependent conversion from measured amplitudes to an equivalent of injected amplitudes is done, the smeared structure shown in Fig. 6.3a becomes the expected clean double Gaussian structure shown in Fig. 6.3d.

This enables absolute recoil energy calibration since the injected amplitude is linearly proportional to the energy. A double Gaussian function is fit to the data to obtain the position of the calibration lines. The fit is shown as the solid magenta line in Fig. 6.3d. The detector response function from Fig. 6.3c can now be rescaled to energy units using the so-called *CPE* (Convert Pulse height to Energy) factor, which relates the energy to the injected amplitude as:

$$E\,[\mathrm{keV}] = \mathrm{CPE}\,[\mathrm{keV/V}] \cdot A_{\mathrm{inj}}\,[\mathrm{V}].$$

Using the $\mathrm{K}_\alpha$ position from the fit, $A_{\mathrm{inj}}(K_\alpha) = 3.43\,\mathrm{V}$, the *CPE* for the wafer detector is calculated as:

$$\mathrm{CPE} = \frac{E(K_\alpha)}{A_{\mathrm{inj}}(K_\alpha)} = 1.72\,\mathrm{keV/V}.$$

Multiplying the injected amplitude values by the $CPE$ factor provides the energy scale for the detector response function from Fig. 6.3c (see the y-axis on the right hand) and obtain the energy spectrum, as illustrated for the calibration peaks with the top x-axis in Fig. 6.3d. The described procedure is used to convert the measured amplitude within the dynamic range to energy at each moment of measuring time. More details on building the detector response can be found in e.g. [228].

A similar approach was used for the bulk detector. However, the bulk detector showed a splitting of the calibration lines after correction of the detector response with test pulses. The absence of splitting in the test pulses suggests that this effect has a physical origin, probably related to position-dependent detector response rather than an artifact or TES instability. This effect increases the uncertainty of the energy determination for this detector. The energy calibration for the bulk detector is described in detail in App. B.

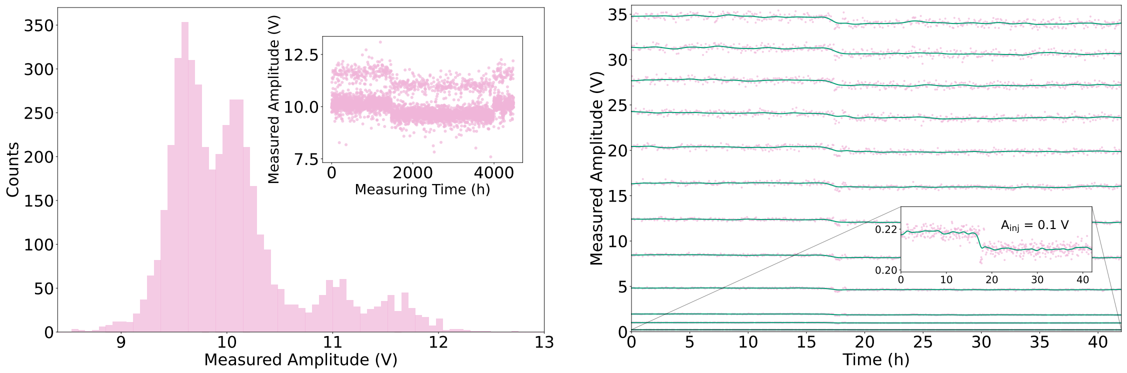

(a) Histogram of the measured amplitudes in the region of the $^{55}$Mn $K_\alpha$ and $K_\beta$ X-ray lines from the calibration source. The detector response is smeared due to time instabilities illustrated in the inset.

(b) Measured amplitudes for the artificially injected test pulses (pink dots) over time and the spline interpolation between them (green line) used for continuous detector response monitoring. The inset shows a zoom into the smallest test pulse with the injected amplitude of 0.1 V.

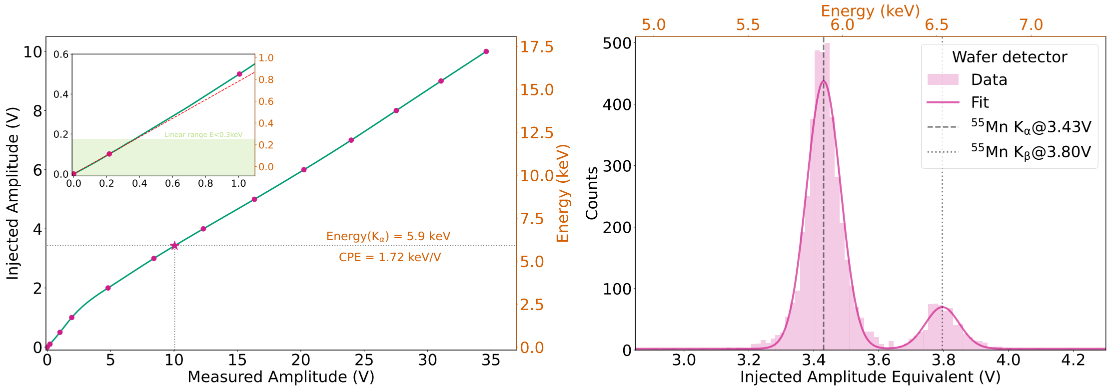

(c) Detector response function at one point in time establishing a correspondence between the measured amplitude and injected amplitude of test pulses (left-hand side y-axis). Data points for the injected test pulses are shown as magenta dots, and the green line shows a cubic spline interpolation between them. Using the injected amplitude equivalent value for the $K_\alpha$ peak shown as a magenta star, the $CPE$ factor is obtained to relate the injected amplitude to the energy (right-hand side y-axis). The inset presents a zoom into the low-energy part. In the region shaded with light green, the detector response is linear and follows the linear function (red dashed line).

(d) Detector response to the $^{55}$Mn $K_\alpha$ and $K_\beta$ X-rays after converting the measured amplitudes to the injected amplitude equivalent (pink histogram), which removed the smearing effect from instabilities present in (a). Fit with a double Gaussian function (magenta line) indicates the positions of the $K_\alpha$ and $K_\beta$ lines (dashed lines). The equivalent of the injected amplitude is converted to energy (top x-axis) with the constant $CPE$ factor.

Figure 6.3.: Illustration of the energy calibration and detector response description with test pulses.

## 6.5. DM data set for the silicon wafer detector

Wafer detector was considered as the main target in the DM search. To obtain DM data set, only the wafer detector was triggered. Simultaneous signal in the bulk detector is recorded and used as an auxiliary channel (e.g., for removing coinciding pulses as discussed in Sec. 6.5.4). All analysis steps were first adjusted based on the training set and then applied to the blind set. The figures in this section illustrate the final results obtained with the blind set.

### 6.5.1. Event selection

After triggering, the goal is to select only valid particle-like events for which precise amplitude evaluation can be ensured. For that, a set of cuts is developed to reject events that are suffering from artifacts, detector instabilities, or distorted pulse shapes. The cut values are defined based on the training data. The cuts used for the Si wafer detector were shown and exemplarily discussed in Sec. 2.4.

For the DM search, the following coincidence cuts are applied: First, any pulses coinciding with a muon veto panel trigger within a $\pm 5\,\mathrm{ms}$ window are rejected, discarding 4.5% of events. Since DM particles are not expected to scatter in multiple detectors simultaneously, pulses with a coincident signal in any other detector module within $\pm 10\,\mathrm{ms}$ are also removed, though this step eliminates only 0.12‰ of events. Additionally, all events coinciding with signals in the Si bulk detector within the same module are discarded, treating the bulk detector as surface events veto. The effect of the last cut is discussed later in Sec. 6.5.4.

### 6.5.2. Trigger and cut efficiency

To evaluate the probability of a valid event passing all selection criteria described above, the developed analysis scheme is applied to $3.8 \times 10^6$ simulated events. These events have the pulse shape of the particle template and energies uniformly distributed between 0 and 300 eV (upper limit of the linear detector response). The simulated events are superimposed on the real data stream at random times (for more information on the simulation procedure, see Sec. 2.5).

During the simulation process, it is possible that a real event is present in the same record window. The triggering algorithm then selects the event with the highest OF voltage output value as the one that caused triggering. To avoid that a nearby pulse triggered and reconstructed instead of the simulated pulse, a cut on the time stamps was applied. The difference between the position of a known simulated pulse and the trigger position should not exceed two rise times of a typical particle pulse in the detector, i.e.: $|T_{trigger} - T_{Sim}| < 2 \cdot \tau_{rise}$, where $\tau_{rise} = 0.3\,\mathrm{ms}$ for the Si wafer detector.

After applying the trigger algorythm to the stream with simulated events, a fraction of those that caused a trigger defined the trigger efficiency, shown in black in Fig. 6.4. Its flat part corresponds to a survival fraction of $(80.53 \pm 0.02)\%$ where the remaining events are lost due to the trigger dead time and coincidences with heater pulses.

The trigger efficiency decreases close to the threshold. As discussed in Sec. 2.6.1, the energy threshold is defined the trigger efficiency reaches 50% from its flat value (dashed line in the inset of Fig. 6.4). This corresponds to 40.3% of the survival traction after triggering The fit of Eq. 2.7 to the trigger efficiency results in an energy threshold of $E_{\mathrm{thr}} = (10.0 \pm 0.2)\,\mathrm{eV}$, a detector baseline resolution of $\sigma_{\mathrm{BL}} = (1.36 \pm 0.05)\,\mathrm{eV}$, and is shown as the orange line.

Next, the selection criteria from Sec. 6.5.1 are applied to the triggered simulated events to assess the fraction of valid pulses that survive the analysis chain. To prevent overestimation of the survival probability due to misidentified events, all outliers where the difference between reconstructed and simulated energies exceeds three times the baseline resolution are additionally excluded. This removes events coinciding with noise fluctuations greater than $3\,\sigma_{\mathrm{BL}}$. This approach to handling sub-threshold simulated events sets the lower mass limit for the DM search, making the results more conservative. The cumulative probability for a simulated event with a given energy to be triggered and pass all cuts is shown as the green line in Fig. 6.4. Above 14 eV, the survival probability stabilizes at $(65.91 \pm 0.03)\%$, indicating that the applied cuts do not introduce any significant energy dependence.

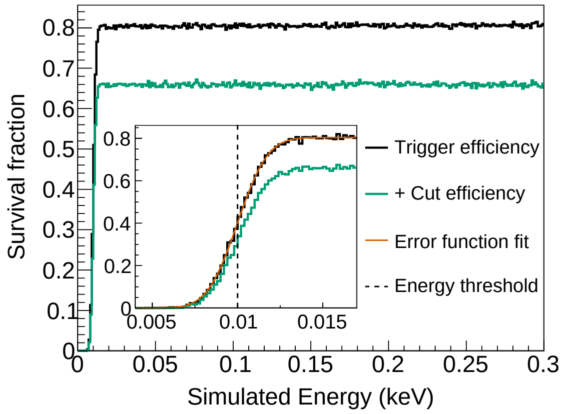

Figure 6.4.: The fraction of simulated events that caused a trigger (black) and passed all selection criteria (green). The inset shows a zoom into the low-energy part where the trigger probability is highly energy dependent. The solid orange line shows the error function fit that gives an energy threshold of $(10.0 \pm 0.2)\,\mathrm{eV}$ (dashed black line) and baseline resolution of $(1.36 \pm 0.05)\,\mathrm{eV}$ for the Si wafer detector.

### 6.5.3. Detector performance

By fitting the trigger efficiency with an error function, values for the energy threshold $E_{\mathrm{thr}} = (10.0 \pm 0.2)\,\mathrm{eV}$ and the detector baseline resolution $\sigma_{\mathrm{BL}} = (1.36 \pm 0.05)\,\mathrm{eV}$ are obtained.

Those values are confirmed by alternative methods to estimate the energy threshold and baseline resolution. The nominal trigger threshold voltage value is converted to energy units, giving $(10.24 \pm 0.15)$ eV. Following the procedure described in Sec. 2.6.1, the baseline resolution is estimated by superimposing a noiseless pulse template to a set of noise traces randomly collected over the measuring time. In this case, the amplitude reconstruction is only distorted by the baseline noise fluctuations and thus gives a measure for the baseline resolution of $(1.35 \pm 0.02)$ eV. The latter values agree with the ones from the error function fit within the uncertainties and thus additionally validate their robustness.

This outstanding performance represents the best baseline resolution achieved in CRESST in comparison to the previous results[1]. On one hand, it enables probing new DM parameter space, as presented in Sec. 6.6. On the other hand, it extends the range for studying low-energy excess (LEE) down to 10 eV, as discussed in Ch. 3.

### 6.5.4. Observed energy spectrum

The recoil energy spectrum measured by the wafer detector, after applying all selection criteria described in Sec. 6.5.1, is shown in black in Fig. 6.5a, where several features are prominent. The spectrum is presented without applying the trigger and cut efficiencies, which remain approximately constant above 14 eV and, therefore, do not affect the spectral shape. The dashed orange lines indicate the $^{55}$Mn K$\alpha$ 5.9 keV and K$\beta$ 6.5 keV lines from the $^{55}$Fe source used for energy calibration. The Si escape line from the K$\alpha$ X-ray is marked with the dotted pink line. This process occurs when an X-ray from the calibration source excites a Si atom in the wafer crystal, and the Si X-ray escapes the detector. Consequently, the expected energy deposition in the wafer detector is 4.16 keV, corresponding to the difference between the K$\alpha$ energy from the source and the Si X-ray (1.74 keV). This line was measured at $(4.18 \pm 0.02)$ keV, which is in agreement with the expected value, serving as a cross-check for the calibration procedure at lower energies. This line is significantly reduced after removing coinciding energy deposition events in the bulk detector facing the wafer. Fig. 6.5b shows the energy deposition in the bulk detector versus the energy in the wafer detector, where the Si escape line forms a prominent feature due to the high probability of catching the escaping Si X-ray in the bulk detector. The Si X-ray line does not appear in the wafer detector's energy spectrum because the source is not positioned in the center of the gap between the wafer and bulk crystals (see Fig. 6.1b), leading to a significant difference in the solid angles covered by the two facing crystal sides, confirmed by simulations.

Additionally, a peak structure in the wafer detector's energy spectrum is observed after the coincidence cut at $(2.4 \pm 0.1)$ keV. This energy value suggests a scenario in which two Si X-rays escape the crystal after a $^{55}$Mn K$_\alpha$ X-ray is absorbed by the wafer, with the

---

[1] After the results presented here were published, another wafer detector, a silicon-on-sapphire device that was originally operated as a light detector in the same CRESST-III data-taking campaign, was considered as a separate target and analyzed accordingly. Its performance achieved even lower baseline energy resolution of 1 eV [61].

expected remaining energy deposition of 2.42 keV. Ongoing simulation studies aim to clarify whether such a process could occur, for instance, at the wafer's edges or on rough surfaces. Although the origin of this structure remains under investigation, its presence does not affect the DM results presented in this chapter, as it lies well outside the region of interest.

The coincidence cut also eliminates background events originating from surface contamination of the crystals and events introduced by the presence of the calibration source in the module. In the energy range of (0.5–2) keV, a significant event rate reduction of $(76 \pm 5)\%$ is observed. To understand the coincident events arising from the calibration source, a Monte Carlo simulation was performed with the source placed inside the module, as shown in Fig. 6.1b. For this the ImpCRESST physics simulation code [128, 129], based on Geant4 [255–257] version 10.06 patch 3, was used[2]. The results suggest that a significant fraction of coinciding events is due to multiple scattering of X-rays from the calibration source, supported by results from an $Al_2O_3$ detector operated with a removable $^{55}$Fe source described in [40]. The remaining events removed by the coincidence cut are attributed to radioactive backgrounds accumulated on the crystal surfaces.

Another prominent feature in the energy spectrum (Fig. 6.5a) is the sharp rise in the event rate below 300 eV, corresponding to the LEE, discussed in Sec. 3.

---

[2] The simulations were performed by Samir Banik (HEPHY, TU Wien).

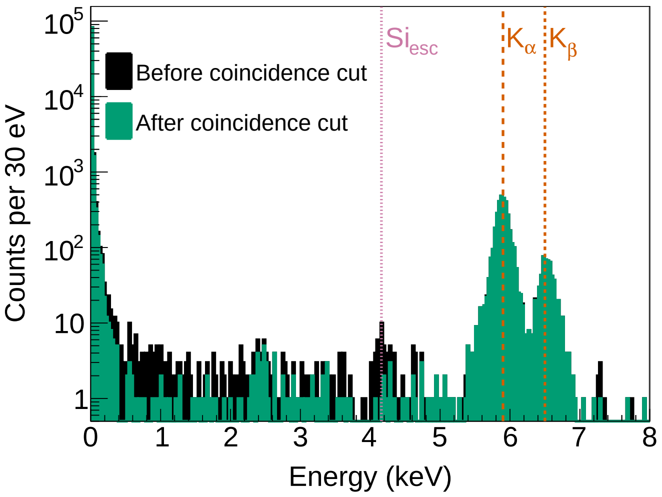

(a)

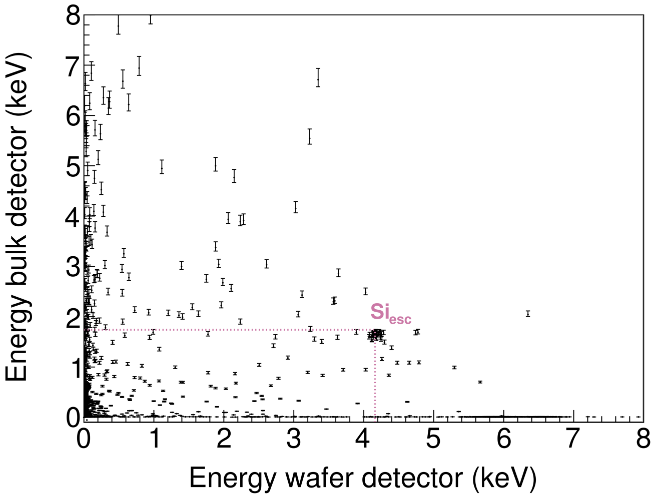

(b)

Figure 6.5.: (a) Measured energy spectrum of the Si wafer detector in the blind data set before the coincidence cut with the bulk detector (black) and after the coincidence cut (green). The dashed orange lines indicate the $^{55}$Mn $K_\alpha$ (5.9 keV) and $K_\beta$ (6.5 keV) lines from the source used for the energy calibration. The dotted pink line shows the Si escape line from the $K_\alpha$ X-ray at 4.16 keV. (b) The energy measured by the bulk detector is shown versus the energy of the wafer detector. The error bars indicate the uncertainties of the energy measured by the bulk detector due to the ambiguity of the detector response discussed in Sec. B. As indicated by the pink dotted line, the Si X-rays that escape from the wafer detector deposit energy of about 1.74 keV in the bulk detector, leading to simultaneous energy deposition in two channels.

## 6.6. Results on spin-independent DM-nucleus interaction

All events that pass the selection criteria outlined in Sec. 6.5.1 with $E > E_{\text{thr}}$ are treated as potential DM signals from elastic DM-nucleus scattering. The gross exposure of the blind data set used for the DM search is 55.06 g-day. Since precise estimation of the trigger and cut survival probability can only be performed for the linear range of the detector response below 300 eV, events outside this range are excluded from the DM search. The resulting region of interest (ROI) is displayed in green in Fig. 6.6.

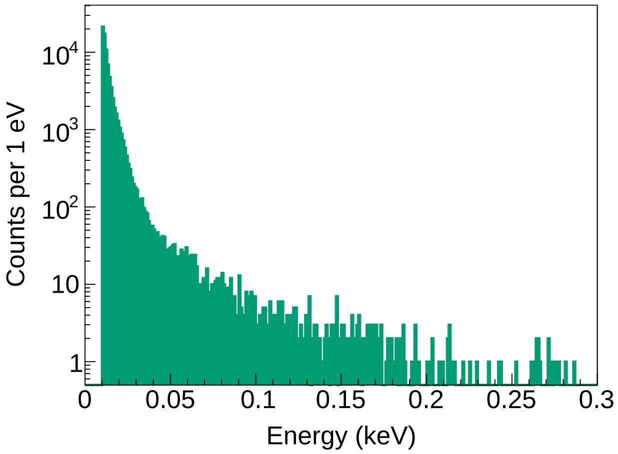

Figure 6.6.: Energy spectrum in the region of interest for the CRESST-III Si wafer detector, showing events within the linear response range used for DM limit calculations.

The expected differential energy spectrum for each DM mass is calculated based on the assumptions of the standard DM halo model [89], which includes a local DM mass density of $\rho_{\text{DM}} = 0.3\,(\text{GeV}/\text{c}^2)/\text{cm}^3$ [88], a Maxwellian velocity distribution with an asymptotic velocity of $v_{\odot} = 220\,\text{km/s}$ [258], and a galactic escape velocity of $v_{\text{esc}} = 544\,\text{km/s}$ [90], as discussed in Sec. 1.2.1. If DM particles of a given mass interact with the detector material, the expected recoil energy spectrum would be observed, but with distortions due to the finite energy resolution of the detector, the trigger algorithm, and the analysis chain. This cumulative effect is estimated through the simulations described in Sec. 6.5.2, allowing the calculation of the expected energy spectrum for any given DM mass as detected by the system.

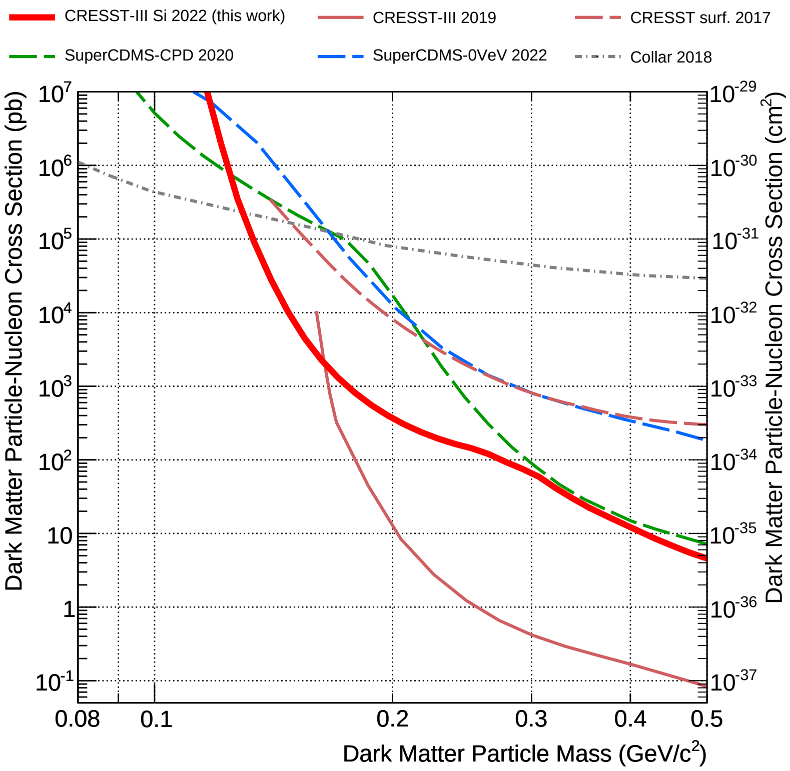

Figure 6.7.: Upper limit on the elastic spin-independent DM-nucleon scattering cross-section at 90% confidence level. The thick solid red line shows the result of this work obtained with a Si detector. The previous CRESST-III result from a $CaWO_4$ crystal operated underground [43] is depicted with the darker red solid line. Constraints obtained by the solid-state cryogenic detectors operated above ground are shown by dashed lines: dark red for CRESST-surf with an $Al_2O_3$ target [64]; green for SuperCDMS-CPD [56] and blue for SuperCDMS-0VeV [205], both operating a Si target. The dash-dotted gray line shows results of hydrogenated organic scintillators by J. I. Collar [110].

Fig. 6.7 presents the 90% confidence level upper limit on the spin-independent elastic DM-nucleon scattering cross-section for DM particles with masses between 0.115 GeV/$c^2$ and 0.5 GeV/$c^2$, obtained using Yellin's optimum interval algorithm [133, 134]. Yellin's method is a statistical approach used for setting conservative exclusion limits in DM searches when background events cannot be reliably modeled. Instead of incorporating background contributions, the method focuses on gaps between events in the data, assuming all events within the ROI are potential signal events[3]. The results from the Si wafer detector explore a new DM parameter space by improving the existing limits on

---

[3] Background descriptions from Geant4-based simulations for CRESST detectors can be integrated into the framework for obtaining DM limits using a profile likelihood ratio test [132]. However, the primary background in the region of interest for sub-GeV DM is the LEE excess. While it can be reasonably approximated by one or two exponential functions, as shown in [132], the exact physically motivated model is still under discussion. In this context, Yellin's method offers more conservative results.

the DM nucleon scattering cross-section for DM masses from 130 MeV/c$^2$ to 165 MeV/c$^2$ by up to a factor of 20 compared to previous studies.

For high interaction cross-sections, the detector is shielded from DM by the atmosphere and the rock overburden. A conservative estimate of the maximum cross-section detectable in a deep underground laboratory, such as LNGS, is provided in [259]. Furthermore, the VERNE package [260, 261] is used to estimate the effect of the shielding at LNGS in this work. Both estimations yield an upper boundary for the spin-independent cross-section of $\mathcal{O}(10^6\,\mathrm{pb})$. Consequently, the new parameter space explored in this work is expected to be accessible in the LNGS deep underground laboratory, unaffected by Earth shielding.

While the improved performance of the wafer detector has extended the DM search to lower masses, its sensitivity to DM with masses above 165 MeV/c$^2$ is reduced compared to the 2019 CRESST-III search with a $CaWO_4$ crystal. This reduction is attributed to the higher LEE rate per kg day and lower exposure, underscoring the importance of understanding and mitigating the LEE in future measurements to exploit the full potential of the CRESST technology to DM search.

# 7. Conclusion and outlook

Cryogenic particle detectors have proven to be effective tools for measuring small particle recoil energies down to eV-scale, making them essential for applications requiring such high sensitivities. This thesis explores two fundamental applications in astroparticle physics. The first one is revealing the nature of dark matter (DM), one of the most pressing questions in modern physics. With the absence of positive signals from classical weakly interacting massive particles (WIMPs), the search has extended to probe lighter DM masses below 1 GeV/c$^2$. The CRESST experiment employs crystals equipped with transition-edge sensors (TESs) as cryogenic calorimeters operated at 15 mK in a low background environment of the Laboratori Nazionali del Gran Sasso (LNGS) to detect DM-induced nuclear recoils. Due to its sensitivity to low energies, CRESST is currently among the leading experiments in sub-GeV DM searches.

The second application is the measurement of coherent elastic neutrino-nucleus scattering (CE$\nu$NS) with reactor neutrinos, the core goal of the NUCLEUS experiment, which employs technology derived from CRESST for its target detector. CE$\nu$NS offers a pathway to studying fundamental neutrino properties and probing physics beyond the Standard Model. Both CRESST and NUCLEUS rely on detecting low-energy nuclear recoils and face common challenges, such as the low-energy excess and nuclear recoil calibration at the 100 eV-scale, which are two focus topics of this thesis. As the third focus, new DM results obtained from the recent CRESST-III data are presented in this work.

After cryogenic detectors accessed energies below hundreds of eV, an unexpected spectral feature has been systematically observed – a steep rise in event rates toward low energies. Since this rate exceeds all known background expectations, it is often referred to as **low-energy excess (LEE)**. Such LEEs are observed by various experiments operating different target materials and phonon sensors at various background levels. Since the LEE occupies the region of interest for sub-GeV DM and CE$\nu$NS experiments and, moreover, exhibits a spectral shape similar to the sought-after signals, it poses a primary global challenge to the low-threshold cryogenic detectors community. While it is still under discussion whether the origins of the LEEs in different experiments are the same, this thesis investigates the LEE in the CRESST and NUCLEUS detectors.

In this thesis, data from two silicon detectors were analyzed, and compared to results from other detectors employing different target materials, such as $CaWO_4$, $Al_2O_3$ and $LiAlO_2$, all operated in the recent CRESST-III campaign. Due to the varying densities and crystal geometries, the masses range from 0.35 to 24 g. The LEE was observed in all detectors, confirming it is a universal rather than a material-specific feature. The analysis ruled out noise triggers and data artifacts as potential LEE causes. By comparing the spectra from the $CaWO_4$ crystals grown with different methods by different producers, it was concluded that the LEE rate is not dominated by either intrinsic radioactive background or crystal lattice stress introduced during the growth process. With a dedicated analysis, it was demonstrated that surface contaminations can contribute only (0.9±0.5)% of the LEE and thus can be excluded as a significant origin of the LEE as well as local scintillation light. Additionally, comparing the energy spectra from the absorbers of different masses does not indicate a consistent scaling of the LEE rate with the crystal mass.

In addition to the spectral analysis, an evolution of the LEE rate with time was studied. In all detectors, the LEE rate decays exponentially over time within one data-taking period with the average time constant of (149±40) days. In dedicated tests, where the detectors were warmed up to tens of K for a short time and then cooled back down to mK operating temperatures, a sharp increase of the LEE rate was observed, followed by a faster decay with a time constant of (18±7) days. These observations strongly suggest that the LEE is dominated by solid-state effects rather than particle-induced backgrounds. Two possible remaining origins identified in this thesis are the relaxation of external stress on the crystal from its holding structures and events forming at the crystal-TES interfaces or within the TES structure itself. To address these possibilities, the ongoing CRESST campaign–Run 37–operates detectors with reduced holder stress, double-TES readouts, and instrumented holders.

To investigate the TES-related LEE, a sapphire detector equipped with two TESs was operated in the NUCLEUS R&D phase. This double-TES configuration allows for the simultaneous readout of signals from both sensors, enabling the identification of events originating in the absorber volume, such as particle recoils, by comparing the energies measured by the two channels. For events occurring in the crystal, the energy is expected to be shared roughly equally between both TESs. However, the analysis of these data presented in this work revealed two distinct LEE components: events with equal energy sharing and events producing a signal in only one TES. These single-TES events are attributed to events generated at the interface between the crystal and the TES, or within the TES itself. The spectral shape of the single-TES component is steeper than that of the shared LEE and becomes dominating at low energies. Excluding single-TES component from the spectrum in the region of interest reduces the background, e.g., by 50% at 40 eV.

The remaining shared LEE was further reduced by two orders of magnitude after 13 thermal cycles from room to mK temperatures over the course of nine months during the cryostat debugging. The lowest absolute rate of the shared LEE component reached 10 counts per day at 100 eV, which is only a factor of 5 higher than the total LEE observed in a 20 times heavier CRESST-III sapphire detector operated at LNGS. However, after the crystal was re-assembled into its holders in the next measurement the LEE rate increased to its initial higher level. The shared LEE shows a decay with time within one run on the scale of days. The reduction of the shared LEE rate after frequent temperature changes and the strong enhancement after the force on the crystal from the holding structures was reapplied, strongly supports the significant role of external stress in the shared LEE formation. Thus, temperature cycling of the detector is proposed to be tested as a controlled method to mitigate the shared LEE. Operating a double-TES detector within an instrumented inner veto, acting also as a holding structure, developed with the NUCLEUS framework, should allow for identifying both TES-related and holder-induced LEE components.

The double-TES configuration also significantly reduced noise triggers, allowing the detection threshold for shared events to be lowered from 34 eV to 25 eV under the condition of only 0.1% of noise triggers in the total simultaneous trigger rate. This improvement highlights another advantage of the double-TES configuration for enhancing detector sensitivity in addition to mitigating the LEE.

A major challenge in the low-energy regime is the lack of a reliable calibration method for nuclear recoils. While most currently available low-energy calibration sources are based on electronic recoils, such as X-rays or LED photon bursts, it is nuclear recoils that are the detection signature for CE$\nu$NS and DM particle scattering with nuclei. The CRAB collaboration recently proposed a **novel approach to direct energy calibration of nuclear recoils based on neutron capture**. After a target nucleus captures a thermal neutron, there is a probability that the compound nucleus de-excites to the ground state via a single MeV-$\gamma$ transition. In this case, the nucleus experiences a mono-energetic recoil on the 100 eV scale.

This thesis presents the analysis of data collected with a NUCLEUS $CaWO_4$ detector irradiated by a flux of moderated neutrons from a strong $^{252}$Cf source at a TUM facility. This measurement resulted in the first observation of a monoenergetic nuclear recoil peak at 112.5 eV from the $^{182}$W isotope after thermal neutron capture. This observation provides the first demonstration of the CRAB method for calibrating low-energy nuclear recoils. The precision of this approach can be further improved if the signal-to-background ratio is enhanced by reducing neutron-induced backgrounds. In this case, more tungsten nuclear recoil peaks are expected to become available, as well as peaks in the other commonly used target materials, such as sapphire, germanium, and silicon. The future CRAB facility at the Triga-Mark-II reactor in Vienna will exploit thermal neutron beams for precise non-intrusive calibration for low-threshold cryogenic detectors while also contributing to valuable tests for a broader physics program, including solid-state and nuclear physics.

In the recent CRESST-III data-taking campaign, the energy threshold was lowered in comparison to the earlier results to 10 eV with a 0.35 g silicon wafer detector. A comprehensive analysis of the data collected with this detector is presented in this thesis. This reduction of the threshold resulted in an **improvement of the existing limits for spin-independent DM-nucleus interaction cross-section** by a factor of up to 20 compared to previous results for DM masses from 130 MeV/c$^2$ to 165 MeV/c$^2$, excluding a new region of parameter space. Accounting for the LEE rate decrease over time could be incorporated as an extra degree of freedom in the limit calculation procedure in the future. However, understanding the LEE is key for fully exploiting CRESST's potential in sub-GeV dark matter detection. A further improvement of the sensitivity with CRESST requires LEE reduction, for example, by exploiting the strategies proposed in this thesis.

The findings of this thesis contribute to the ongoing detector design development for the NUCLEUS experiment and future CRESST campaigns. Specifically, the insights gained into the LEE have identified the most promising mitigation strategies, such as thermal cycling and operating double-TES detectors in instrumented holders. These approaches are planned to be tested in the near future. Disentangling different LEE populations and studying their temporal behavior is essential to gain a better understanding of their origin processes and determine the most effective mitigation strategies.

While working on my thesis, I co-initiated the international EXCESS workshop series, which reached its fifth iteration in 2024. The workshop has sparked a global discussion about the LEEs observed in various experiments by bringing together leading experts in the field of low-threshold cryogenic detectors. Over the course of the years, the number of participants exceeded 300 in an online format and remained at about 60 in later in-person meetings. The insights gained from the workshop significantly enriched the research presented in this thesis. For instance, the idea to study the time evolution of the LEE rate, now widely adopted in the community, and the dedicated series of warm-up tests performed in the recent CRESST-III campaign were originally inspired by observations of the EDELWEISS collaboration, shared during the first EXCESS workshop. Another example is exploiting the two-channel readout approach now used by the SPICE/HeRALD, CRESST, and NUCLEUS collaborations, which opens up great potential for cross-learning from the results. The findings of this thesis confirm and further establish the broad consensus in the cryogenic detector community that solid-state effects, rather than particle-induced backgrounds, dominate the LEE.

However, I would like to acknowledge that the list of hypotheses considered for the origin of LEE may be incomplete at the moment. Moreover, many of the proposed ideas involve solid-state physics at very low energies and cryogenic temperatures, where detailed microphysics models are lacking. As a result, quantifying conclusions remains challenging at this stage. The results presented here are based on the best available knowledge and focus on the dominant LEE contributions. Further description and modeling of the exact processes are needed, underscoring the need for collaboration with solid-state physicists.

Cryogenic detectors with superconducting phonon sensors are unique tools to achieve world-leading energy thresholds and the required sensitivities for detection of sub-GeV DM and CE$\nu$NS. However, their operation in the new low-energy regime is not free of challenges. Implementation of novel nuclear recoil calibration methods, such as the one presented in this work, is required to reduce uncertainties in the energy reconstruction in the region of interest for these experiments. At the same time, testing the LEE mitigation strategies proposed in this thesis makes another step towards understanding the LEE origin. Reduction of the LEE will lead to an immediate extraordinary sensitivity boost. These advancements are not only essential for enabling discoveries and precise measurements with the current generation of DM and CE$\nu$NS detectors, but they also enhance our understanding of low-energy phonon signal formation, potentially leading to technological improvements and novel approaches for future experiments and new physics applications.

# List of Abbreviations

| **Abbreviation** | **Definition** |
|---|---|
| BSM | Beyond the Standard Model |
| CCD | Charge Coupled Device |
| CDAQ | Continuous Data Acquisition |
| CDMS | Cold Dark Matter Search |
| CE$\nu$NS | Coherent Elastic Neutrino-Nucleus Scattering |
| CMB | Cosmic Microwave Background |
| CP | Control Pulse |
| CPE | Convert Pulse height to Energy |
| CRAB | Calibrated nuclear Recoils for Accurate Bolometry |
| CRESST | Cryogenic Rare Event Search with Superconducting Thermometers |
| DAQ | Data Acquisition |
| DM | Dark Matter |
| HEPHY | Institute of High Energy Physics (Austria) |
| HPGe | High-Purity Germanium |
| KID | Kinetic Inductance Detector |
| LEE | Low-Energy Excess |
| LNGS | Laboratori Nazionali del Gran Sasso |
| MMC | Metallic Magnetic Calorimeter |
| MPP | Max-Planck-Institut for Physics |
| NTD | Neutron Transmutation Doped |
| NTL | Neganov-Trofimov-Luke (effect) |
| OF | Optimum Filter |
| PC | Phonon Collectors |
| QET | Quasiparticle-trap-assisted Electrothermal-feedback TES |
| ROI | Region of Interest |
| SD | Spin-Dependent (interaction) |
| SI | Spin-Independent (interaction) |
| SM | Standard Model (of particle physics) |
| SNS | Spallation Neutron Source |
| SQUID | Superconducting Quantum Interference Device |
| TES | Transition Edge Sensor |
| TP | Test Pulse |
| TUM | Technical University of Munich |
| UGL | Shallow Underground Laboratory at TUM |
| VDAQ | Versatile Data Acquisition |
| VNS | Very Near Site |
| WIMP | Weakly Interacting Massive Particle |
| XRF | X-Ray Fluorescence |

# A. Dimensions of the CRESST-III TES designs

| | $l_W$, mm | $h_W$, mm | $L_W$, mm | $H_W$, mm | $L_{Al}$, mm | $H_{Al}$, mm | $\Delta$, mm |
|---|---|---|---|---|---|---|---|
| PD-S | 0.60 | 1.70 | 0.95 | 3.90 | 0.950 | 4.00 | 0.050 |
| PD-M | 0.85 | 2.40 | 1.40 | 5.60 | 1.400 | 5.70 | 0.050 |
| PD-L | 1.20 | 3.40 | 1.90 | 7.80 | 1.900 | 8.00 | 0.100 |
| LD | 0.14 | 0.30 | 0.500 | 1.00 | 0.495 | 1.02 | 0.015 |

Table A.1.: Dimensions of the CRESST-III TES designs shown in Fig. 3.1 repeated below for convinience.

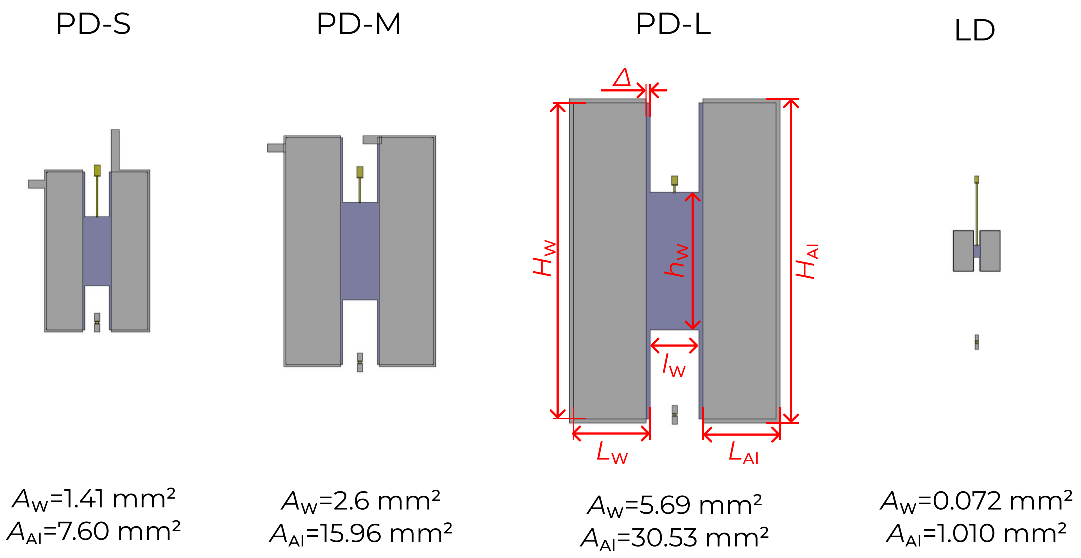

# B. Multi-component detector response in the CRESST-III silicon bulk detector

The calibration procedure described in Sec. 6.4 was also applied to the bulk detector data. However, after correcting the detector response using test pulses, a splitting of the calibration lines was observed. As illustrated in the pink histogram of the injected amplitude equivalent shown in Fig. B.1a[1], both $^{55}$Mn $K_\alpha$ and $K_\beta$ lines exhibit splitting into at least two peaks. While the spectrum is disturbed, the origin of the lines from the calibration source is beyond doubt, as their event rate is consistent with that expected from the source, and no other background source of such activity is expected at the LNGS facility. This splitting persists throughout the entire measurement period, as shown in Fig. B.1b, without any abrupt changes.

The adequacy of the detector response function was verified by examining the test pulse with an injected amplitude of 2 V, which overlaps with the energy of the calibration lines. The green histogram in Fig. B.1a shows the injected amplitude equivalent distribution for these test pulses, centered around 2 V after applying the same detector response function. No splitting was observed in the test pulses: the response has a Gaussian shape, with no indications for any irregularities. Typically, detector operating point instabilities or irregularities in the transition curve can cause splitting in the detector response. However, such effects should also manifest in test pulses of the same energy, as they involve the same part of the transition curve. The absence of this effect in the test pulses suggests that the observed splitting of the calibration lines likely has a physical origin, rather than being an artifact of analysis or TES response instability.

Moreover, all selected events in Fig. B.1a have identical pulse shapes, ruling out different mechanisms or unreliable amplitude reconstruction as the cause of the splitting.

Two possible explanations for the splitting of the calibration lines remain. The first is partial energy deposition in the crystal for some events, e.g., when a gamma escapes the crystal after Compton scattering before depositing its full energy. In this scenario, the response to the $^{55}$Fe calibration source would be distorted. However, Geant4 simulations of the calibration source with the given detector configuration do not support this explanation, as $^{55}$Mn $K_\alpha$ and $K_\beta$ X-rays are expected to fully deposit their energy in the crystal[2]. Additionally, coincident energy deposition into the wafer detector appears consistent with noise.

The second possibility is a position-dependent detector response. In this case, the distance between the energy deposition site and the TES may affect the signal,i.e., a closer energy deposition produces a stronger signal. Similar position-dependent signal losses have been observed in a Si beaker-shaped detector developed within CRESST, presented in [241], where the detector's geometry affected phonon propagation, leading to distortion

---

[1] The same step for for the wafer detector is illustrated in Fig. 6.3d.

[2] There is a small probability that a Si X-ray escapes the crystal, but this would result in a significantly lower measured energy, reduced by 1.74 keV from the original value. However, the observed splitting is on the order of a few percent, which does not align with this scenario.

of the calibration lines. Although this position dependence is not expected in standard CRESST-III bulk detectors, it cannot be completely excluded. Currently, this geometrical effect remains the most plausible hypothesis for the observed splitting, although further investigation is needed.

To obtain the $CPE$ factor for the bulk detector, it was assumed that the detector response consists of two components randomly distributed in time across the energy range, causing the observed calibration line splitting. A sum of two Gaussian functions with identical widths was fitted to the main $^{55}$Mn $K_\alpha$ calibration line, as shown by the solid magenta line in Fig. B.1a. For each component, the corresponding $CPE$ factors, $CPE_{left}$ and $CPE_{right}$, were calculated. Assuming equal contribution from the two detector response components, the weighted average of the Gaussian amplitudes was taken, yielding $CPE_{av} = 3.09\,\mathrm{keV/V}$. The conversion of the injected amplitude equivalent to energy for the entire data set was then performed as: $E = CPE_{av} \cdot A_{inj}$. All relevant values are summarized in Tab.B.1. This means that for each measured amplitude, the corresponding energy could lie anywhere between two values, $E_{left}$ and $E_{right}$, calculated using $CPE_{left}$ and $CPE_{right}$, respectively. This leads to increased asymmetric uncertainty for the determined energy $E$, with the lower uncertainty being $|E - E_{right}|$ and the upper uncertainty $|E - E_{left}|$. The uncertainties scale linearly with energy and are defined by the relative difference between the $CPE$ factors (percentage values are provided in the last column of Tab. B.1). The uncertainties are asymmetric because data points are more likely to fall within the more prominent right-hand part of the detector response. Fig. B.1a includes an x-axis converted to energy units using the $CPE_{av}$ factor. The dashed gray line indicates the $^{55}$Mn $K_\alpha$ energy, appearing between the two peaks. The orange error bars represent the asymmetric uncertainties of the reconstructed energies for the peak positions of the split calibration line, which overlap with the $K_\alpha$ energy.

This procedure enables the calibration of the bulk detector, allowing it to be used as a veto detector for the wafer detector. It is used to study simultaneous energy deposition, as shown in Fig. 6.5b, or to investigate coincidences with LEE events, as discussed in Sec. 3.2.5.

| $i$ | Maximum position, $A_{inj}$ | Amplitude (weight) | $CPE_i$ | $CPE_{av}$ | $\frac{\Delta E_i}{E} = \lvert\frac{(CPE_{av} - CPE_i)}{CPE_{av}}\rvert$ |
|---|---|---|---|---|---|
| left | 1.842±0.002 V | 189±12 | 3.202 keV/V | 3.09 keV/V | 3.4% |
| right | 1.948±0.002 V | 304±15 | 3.028 keV/V | | 2.1% |

Table B.1.: Parameter values for the calculation of the $CPE$ factors for the bulk detector energy calibration. Maximum positions and amplitudes of the fit with a double Gaussian function shown in Fig. B.1a. The amplitudes are used as weights for the $CPE_{av}$ calculation. Last column contains the relative uncertainty of the energy reconstruction inroduced by the splitting of the detector response.

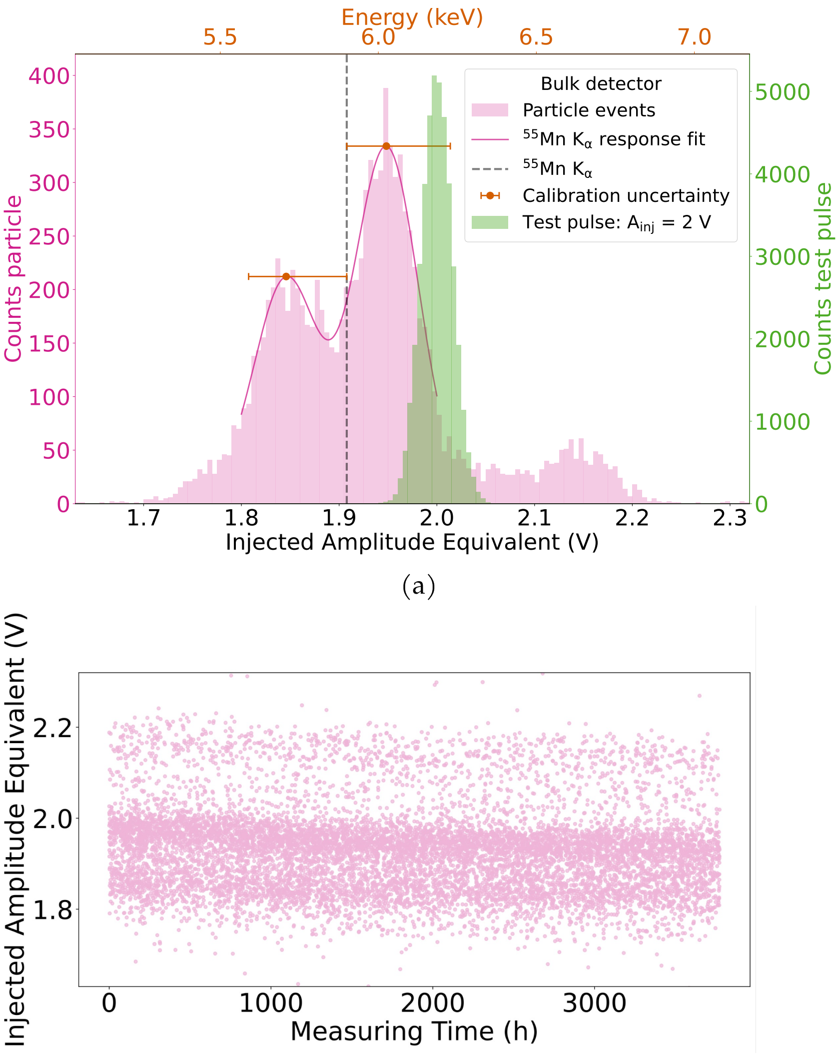

(a)

(b)

Figure B.1.: (a) Pink histogram shows the detector response of the bulk detector to the $^{55}$Mn K$_\alpha$ and K$_\beta$ X-rays after converting the measured amplitudes to the injected amplitude equivalent. Since splitting of the calibration lines is observed, a double Gaussian function (solid pink line) is fit to the K$_\alpha$ line. The top x-axis shows the conversion to energy units with the $CPE_{av}$ factor (see text for details) and the dashed gray line indicates the K$_\alpha$ energy. The orange error bars indicate the uncertainties of the energy determination for the maxima positions of the fit. The green histogram shows the distribution of the injected amplitude equivalent after applying the time-dependent detector response function for the test pulse with the injected amplitude of 2 V. (b) Injected amplitude equivalent of the $^{55}$Mn K$_\alpha$ and K$_\beta$ X-ray hits over the measuring time. Splitting is present over the whole data-taking.

# C. Data file lists used for analyses

## C.1. NUCLEUS *double-TES* measurement series

| **surf1** |
|---|
| c1_r0057_00013_dbl2_W1-710-12_T4_2uA_2uA |
| **surf2** |
| c1_r0058_0001_dbl2_W1-710-12_T4_2uA_2uA |
| **UGL1-1** |
| c2_r016_003_0001_W1-710-T1_1uA5_W1-710_T2_1uA5_100kHz |
| c2_r016_003_0002_W1-710-T1_1uA5_W1-710_T2_1uA5_100kHz |
| c2_r016_003_0004_W1-710-T1_1uA5_W1-710_T2_1uA5_100kHz |
| c2_r016_003_0005_W1-710-T1_1uA5_W1-710_T2_1uA5_100kHz |
| c2_r016_003_0006_W1-710-T1_1uA5_W1-710_T2_1uA5_100kHz |
| **UGL1-2** |
| c2_r016_005_0002_W1-710-T1_3uA_W1-710_T2_3uA_100kHz |
| c2_r016_005_0003_W1-710-T1_3uA_W1-710_T2_3uA_100kHz |
| c2_r016_005_0004_W1-710-T1_3uA_W1-710_T2_3uA_100kHz |
| **surf3-1** |
| c1_r085_0001_W1-710-dbl2_12_1u5A_T4_1uA_htr12 |
| c1_r085_0002_W1-710-dbl2_12_1u5A_T4_1uA_htr12 |
| **surf3-2** |
| c1_r085_0004_W1-710-dbl2_12_1u5A_T4_1uA_htr12 |
| c1_r085_0005_W1-710-dbl2_12_1u5A_T4_1uA_htr12 |
| c1_r085_0006_W1-710-dbl2_12_1u5A_T4_1uA_htr12 |
| c1_r085_0007_W1-710-dbl2_12_1u5A_T4_1uA_htr12 |
| c1_r085_0008_W1-710-dbl2_12_1u5A_T4_1uA_htr12 |
| c1_r085_0009_W1-710-dbl2_12_1u5A_T4_1uA_htr12 |
| c1_r085_0010_W1-710-dbl2_12_1u5A_T4_1uA_htr12 |
| c1_r085_0011_W1-710-dbl2_12_1u5A_T4_1uA_htr12 |
| **UGL2** |
| c2_r020_001_0002_W1-710-12_2uA_W1-710-T4_2uA_shieldingclosed |
| c2_r020_001_0003_W1-710-12_2uA_W1-710-T4_2uA_shieldingclosed |
| c2_r020_001_0004_W1-710-12_2uA_W1-710-T4_2uA_shieldingclosed |
| c2_r020_001_0005_W1-710-12_2uA_W1-710-T4_2uA_shieldingclosed |
| c2_r020_001_0006_W1-710-12_2uA_W1-710-T4_2uA_shieldingclosed |
| c2_r020_001_0007_W1-710-12_2uA_W1-710-T4_2uA_shieldingclosed |

Table C.1.: Data files analyzed for different measurement periods listed in Tab. 4.3 presented in Ch. 4.

## C.2. CRAB measuring campaign at TUM

| **Background Data Set** |
|---|
| c1_r0029_W1-681-4_2u5A_bg_lineardrive_00047 |
| c1_r0029_W1-681-4_2u5A_bg_lineardrive_00048 |
| c1_r0029_W1-681-4_2u5A_bg_lineardrive_00049 |
| c1_r0029_W1-681-4_2u5A_bg_lineardrive_00050 |
| c1_r0029_W1-681-4_2u5A_bg_lineardrive_00051 |
| **Source Data Set** |
| c1_r0029_W1-681-4_2u5A_crabsrc_pos3_Pb_2cm_00056 |
| c1_r0029_W1-681-4_2u5A_crabsrc_pos3_Pb_2cm_00057 |
| c1_r0029_W1-681-4_2u5A_crabsrc_pos3_Pb_2cm_00058 |
| c1_r0029_W1-681-4_2u5A_crabsrc_pos3_Pb_2cm_00059 |
| c1_r0029_W1-681-4_2u5A_crabsrc_pos3_Pb_2cm_00060 |

Table C.2.: Background and source data sets from Run29 in the CryoLab cryostat analysed in Ch. 5.

## C.3. CRESST-III silicon detectors

| **Training set** | **Blind set** | | | |
|---|---|---|---|---|
| bck_003 | bck_009 | bck_034 | bck_066 | bck_093 |
| bck_004 | bck_010 | bck_036 | bck_067 | bck_094 |
| bck_005 | bck_011 | bck_037 | bck_070 | bck_095 |
| bck_006 | bck_012 | bck_038 | bck_071 | bck_096 |
| bck_007 | bck_013 | bck_045 | bck_072 | bck_097 |
| bck_008 | bck_014 | bck_046 | bck_073 | bck_098 |
| bck_018 | bck_016 | bck_047 | bck_074 | bck_099 |
| bck_028 | bck_017 | bck_049 | bck_077 | bck_100 |
| bck_039 | bck_019 | bck_050 | bck_079 | bck_101 |
| bck_048 | bck_020 | bck_051 | bck_080 | bck_120 |
| bck_058 | bck_021 | bck_052 | bck_081 | bck_121 |
| bck_069 | bck_022 | bck_053 | bck_082 | bck_122 |
| bck_078 | bck_024 | bck_054 | bck_083 | bck_123 |
| bck_089 | bck_025 | bck_055 | bck_084 | bck_124 |
| | bck_026 | bck_056 | bck_085 | bck_125 |
| | bck_027 | bck_057 | bck_086 | bck_127 |
| | bck_030 | bck_060 | bck_087 | bck_128 |
| | bck_031 | bck_061 | bck_088 | bck_129 |
| | bck_032 | bck_062 | bck_090 | bck_130 |
| | bck_033 | bck_063 | bck_091 | bck_131 |

Table C.3.: List of files from Run36 for the training and blind sets used for the CRESST-III silicon detectors presented in Ch. 6.

# Bibliography

[1] M. Kaznacheeva and K. Schaeffner. "Scintillating low-temperature calorimeters for direct dark matter search." In: *Journal of Advanced Instrumentation in Science* 2024.1 (Aug. 2024). DOI: `https://doi.org/10.31526/jais.2024.514`. URL: `https://jais.andromedapublisher.org/index.php/JAIS/article/view/514`.

[2] P. Adari, A. Aguilar-Arevalo, D. Amidei, et al. "EXCESS workshop: Descriptions of rising low-energy spectra." In: *SciPost Phys. Proc.* (2022), p. 001. DOI: `10.21468/SciPostPhysProc.9.001`. URL: `https://scipost.org/10.21468/SciPostPhysProc.9.001`.

[3] G. Angloher, S. Banik, G. Benato, et al. "Latest observations on the low energy excess in CRESST-III." In: *SciPost Phys. Proc.* (2023), p. 013. DOI: `10.21468/SciPostPhysProc.12.013`. URL: `https://scipost.org/10.21468/SciPostPhysProc.12.013`.

[4] M. Kaznacheeva. "New excess measurements from NUCLEUS." EXCESS24 Workshop. 2024. URL: `https://agenda.infn.it/event/39007/contributions/235288/`.

[5] H. Abele, G. Angloher, A. Bento, et al. "Observation of a Nuclear Recoil Peak at the 100 eV Scale Induced by Neutron Capture." In: *Phys. Rev. Lett.* 130 (21 May 2023), p. 211802. DOI: `10.1103/PhysRevLett.130.211802`. URL: `https://link.aps.org/doi/10.1103/PhysRevLett.130.211802`.

[6] G. Angloher, S. Banik, G. Benato, et al. "Results on sub-GeV dark matter from a 10 eV threshold CRESST-III silicon detector." In: *Phys. Rev. D* 107 (12 June 2023), p. 122003. DOI: `10.1103/PhysRevD.107.122003`. URL: `https://link.aps.org/doi/10.1103/PhysRevD.107.122003`.

[7] F. Simon. "Application of low temperature calorimetry to radioactive measurements." In: *Nature* 135.3418 (1935), pp. 763–763.

[8] D. H. Andrews, R. D. Fowler, and M. C. Williams. "The Effect of Alpha-particles on a Superconductor." In: *Phys. Rev.* 76 (1 July 1949), pp. 154–155. DOI: `10.1103/PhysRev.76.154.2`. URL: `https://link.aps.org/doi/10.1103/PhysRev.76.154.2`.

[9] E. Fiorini and T. Niinikoski. "Low-temperature calorimetry for rare decays." In: *Nuclear Instruments and Methods in Physics Research* 224.1 (1984), pp. 83–88. ISSN: 0167-5087. DOI: `https://doi.org/10.1016/0167-5087(84)90449-6`. URL: `https://www.sciencedirect.com/science/article/pii/0167508784904496`.

[10] A. Drukier and L. Stodolsky. "Principles and applications of a neutral-current detector for neutrino physics and astronomy." In: *Phys. Rev. D* 30 (11 Dec. 1984), pp. 2295–2309. DOI: `10.1103/PhysRevD.30.2295`. URL: `https://link.aps.org/doi/10.1103/PhysRevD.30.2295`.

[11] B. Cabrera, L. M. Krauss, and F. Wilczek. "Bolometric detection of neutrinos." In: *Phys. Rev. Lett.* 55 (1 July 1985), pp. 25–28. DOI: `10.1103/PhysRevLett.55.25`. URL: `https://link.aps.org/doi/10.1103/PhysRevLett.55.25`.

[12] M. W. Goodman and E. Witten. "Detectability of certain dark-matter candidates." In: *Phys. Rev. D* 31 (12 June 1985), pp. 3059–3063. DOI: `10.1103/PhysRevD.31.3059`. URL: `https://link.aps.org/doi/10.1103/PhysRevD.31.3059`.

[13] K. Pretzl, N. Schmitz, and L. Stodolsky. *Low Temperature Detectors for Neutrinos and Dark Matter: Proceedings of a Workshop, Held at Ringberg Castle, Tegernsee, May 12–13, 1987*. Springer Berlin, Heidelberg, 1987. DOI: `https://doi.org/10.1007/978-3-642-72959-1`.

[14] N. Rando, D. Lumb, M. Bavdaz, et al. "Space science applications of cryogenic detectors." In: *Nuclear Instruments and Methods in Physics Research Section A: Accelerators, Spectrometers, Detectors and Associated Equipment* 522.1 (2004). TRDs for the Third Millenium. Proceedings of the 2nd Workshop on Advanced Transition Radiation Detectors for Accelerator and Space Applications, pp. 62–68. ISSN: 0168-9002. DOI: `https://doi.org/10.1016/j.nima.2004.01.019`. URL: `https://www.sciencedirect.com/science/article/pii/S0168900204000865`.

[15] D. McKinsey et al. "The TESSERACT Dark Matter Project." In: *Snowmass 2021 - Letter of Interest* (). URL: `https://www.snowmass21.org/docs/files/summaries/CF/SNOWMASS21-CF1_CF2-IF1_IF8-120.pdf`.

[16] R. Essig, G. K. Giovanetti, N. Kurinsky, et al. *Snowmass2021 Cosmic Frontier: The landscape of low-threshold dark matter direct detection in the next decade*. arXiv:2203.08297. 2023. arXiv: `2203.08297 [hep-ph]`.

[17] B. von Krosigk, K. Eitel, C. Enss, et al. "DELight: A Direct search Experiment for Light dark matter with superfluid helium." In: *SciPost Phys. Proc.* (2023), p. 016. DOI: `10.21468/SciPostPhysProc.12.016`. URL: `https://scipost.org/10.21468/SciPostPhysProc.12.016`.

[18] C. Enss. *Cryogenic particle detection*. Vol. 99. Springer Berlin, Heidelberg, 2005. DOI: `https://doi.org/10.1007/b12169`.

[19] E. E. Haller, K. M. Itoh, J. W. Beeman, et al. "Neutron transmutation doped natural and isotopically engineered germanium thermistors." In: *Instrumentation in Astronomy VIII*. Ed. by D. L. Crawford and E. R. Craine. Vol. 2198. International Society for Optics and Photonics. SPIE, 1994, pp. 630–637. DOI: `10.1117/12.176771`. URL: `https://doi.org/10.1117/12.176771`.

[20] N. Wang, F. C. Wellstood, B. Sadoulet, et al. "Electrical and thermal properties of neutron-transmutation-doped Ge at 20 mK." In: *Phys. Rev. B* 41 (6 Feb. 1990), pp. 3761–3768. DOI: `10.1103/PhysRevB.41.3761`. URL: `https://link.aps.org/doi/10.1103/PhysRevB.41.3761`.

[21] L. Hehn, E. Armengaud, Q. Arnaud, et al. “Improved EDELWEISS-III sensitivity for low-mass WIMPs using a profile likelihood approach.” In: *Eur. Phys. J. C* 76 (2016), pp. 1–10. DOI: `10.1140/epjc/s10052-016-4388-y`. URL: `https://doi.org/10.1140/epjc/s10052-016-4388-y`.

[22] E. Armengaud et al. “Searching for low-mass dark matter particles with a massive Ge bolometer operated above ground.” In: *Phys. Rev. D* 99 (8 Apr. 2019), p. 082003. DOI: `10.1103/PhysRevD.99.082003`. URL: `https://link.aps.org/doi/10.1103/PhysRevD.99.082003`.

[23] Q. Arnaud et al. “First Germanium-Based Constraints on Sub-MeV Dark Matter with the EDELWEISS Experiment.” In: *Phys. Rev. Lett.* 125 (14 Oct. 2020), p. 141301. DOI: `10.1103/PhysRevLett.125.141301`. URL: `https://link.aps.org/doi/10.1103/PhysRevLett.125.141301`.

[24] C. Augier, G. Beaulieu, V. Belov, et al. “Ricochet Progress and Status.” In: *Journal of Low Temperature Physics* 212.3 (Aug. 2023), pp. 127–137. ISSN: 1573-7357. DOI: `10.1007/s10909-023-02971-5`. URL: `https://doi.org/10.1007/s10909-023-02971-5`.

[25] C. Augier et al. “First demonstration of 30 eVee ionization energy resolution with Ricochet germanium cryogenic bolometers.” In: *Eur. Phys. J. C* 84.2 (2024). DOI: `https://doi.org/10.1140/epjc/s10052-024-12433-1`.

[26] B. S. Neganov and V. N. Trofimov. “Calorimetric method measuring ionizing radiation.” In: *Otkryt. Izobret.* 146 (1985), p. 215.

[27] P. N. Luke. “Voltage-assisted calorimetric ionization detector.” In: *J. Applied Phys.* 64 (1988), p. 6858. DOI: `https://doi.org/10.1063/1.341976`.

[28] P. K. Day, H. G. LeDuc, B. A. Mazin, et al. “A broadband superconducting detector suitable for use in large arrays.” In: *Nature* 425.6960 (2003), pp. 817–821. DOI: `https://doi.org/10.1038/nature02037`.

[29] L. J. Swenson, A. Cruciani, A. Benoit, et al. “High-speed phonon imaging using frequency-multiplexed kinetic inductance detectors.” In: *Appl. Phys. Lett.* 96.26 (July 2010), p. 263511. ISSN: 0003-6951. DOI: `10.1063/1.3459142`. eprint: `https://pubs.aip.org/aip/apl/article-pdf/doi/10.1063/1.3459142/13499261/263511\_1\_online.pdf`. URL: `https://doi.org/10.1063/1.3459142`.

[30] D. C. Moore, S. R. Golwala, B. Bumble, et al. “Position and energy-resolved particle detection using phonon-mediated microwave kinetic inductance detectors.” In: *Appl. Phys. Lett.* 100.23 (June 2012), p. 232601. ISSN: 0003-6951. DOI: `10.1063/1.4726279`. eprint: `https://pubs.aip.org/aip/apl/article-pdf/doi/10.1063/1.4726279/14247421/232601\_1\_online.pdf`. URL: `https://doi.org/10.1063/1.4726279`.

[31] O. Wen, T. Aralis, R. Basu Thakur, et al. “Performance of a phonon-mediated detector using kids optimized for sub-gev dark matter.” In: *J. Low Temp. Phys.* 209.3-4 (2022), pp. 510–517. DOI: `https://doi.org/10.1007/s10909-022-02764-2`.

[32] J. Colas, M. Calvo, J. Goupy, et al. “Improvement of contact-less KID design using multilayered Al/Ti material for resonator.” In: *J. Low Temp. Phys.* (2023), pp. 1–8. DOI: `https://doi.org/10.1007/s10909-023-02976-0`.

[33] A. Cruciani, L. Bandiera, M. Calvo, et al. “BULLKID: Monolithic array of particle absorbers sensed by kinetic inductance detectors.” In: *Appl. Phys. Lett.* 121.21 (Nov. 2022), p. 213504. ISSN: 0003-6951. DOI: `10.1063/5.0128723`. eprint: `https://pubs.aip.org/aip/apl/article-pdf/doi/10.1063/5.0128723/16487869/213504\_1\_online.pdf`. URL: `https://doi.org/10.1063/5.0128723`.

[34] S. R. Bandler, C. Enss, R. E. Lanou, et al. “Metallic magnetic bolometers for particle detection.” In: *J. Low Temp. Phys.* 93:3-4 (Nov. 1993). ISSN: 0022-2291. URL: `https://www.osti.gov/biblio/5478445`.

[35] A. Fleischmann, C. Enss, and G. Seidel. “Metallic Magnetic Calorimeters.” In: *Cryogenic Particle Detection*. Ed. by C. Enss. Berlin, Heidelberg: Springer Berlin Heidelberg, 2005, pp. 151–216. ISBN: 978-3-540-31478-3. DOI: `10.1007/10933596_4`. URL: `https://doi.org/10.1007/10933596_4`.

[36] M. Krantz, F. Toschi, B. Maier, et al. “Magnetic microcalorimeter with paramagnetic temperature sensors and integrated dc-SQUID readout for high-resolution x-ray emission spectroscopy.” In: *Appl. Pys. Lett.* 124.3 (Jan. 2024), p. 032601. ISSN: 0003-6951. DOI: `10.1063/5.0180903`. eprint: `https://pubs.aip.org/aip/apl/article-pdf/doi/10.1063/5.0180903/18573262/032601\_1\_5.0180903.pdf`. URL: `https://doi.org/10.1063/5.0180903`.

[37] B. J. e. a. Alenkov V. Bae H.W. “First results from the AMoRE-Pilot neutrinoless double beta decay experiment.” In: *Eur. Phys. J. C* 79 (2019), p. 791. DOI: `doi.org/10.1140/epjc/s10052-019-7279-1`.

[38] K. D. Irwin, S. W. Nam, B. Cabrera, et al. “A quasiparticle-trap-assisted transition-edge sensor for phonon-mediated particle detection.” In: *Rev. Sci. Instrum.* 66.11 (Nov. 1995), pp. 5322–5326. ISSN: 0034-6748. DOI: `10.1063/1.1146105`. eprint: `https://pubs.aip.org/aip/rsi/article-pdf/66/11/5322/8806468/5322\_1\_online.pdf`. URL: `https://doi.org/10.1063/1.1146105`.

[39] P. Ferger, P. Colling, C. Bucci, et al. “Cryogenic particle detectors with superconducting phase transition thermometers.” In: *Nucl. Instrum. Methods Phys. Res., Sect. A* 370.1 (1996), pp. 157–159. ISSN: 0168-9002. DOI: `https://doi.org/10.1016/0168-9002(95)01068-8`. URL: `https://www.sciencedirect.com/science/article/pii/0168900295010688`.

[40] J. Rothe. "Low-Threshold Cryogenic Detectors for Low-Mass Dark Matter Search and Coherent Neutrino Scattering." PhD thesis. Technische Universität München, 2021. URL: `http://mediatum.ub.tum.de/?id=1576351`.

[41] A. I. Braginski. "Superconductor electronics: Status and outlook." In: *J. Supercond. Nov. Magn.* 32 (2019), pp. 23–44. DOI: `https://doi.org/10.1007/s10948-018-4884-4`.

[42] B. A. I. and C. John. John Wiley & Sons, Ltd, 2004. ISBN: 9783527603640. DOI: `https://doi.org/10.1002/3527603646`. eprint: `https://onlinelibrary.wiley.com/doi/pdf/10.1002/3527603646`. URL: `https://onlinelibrary.wiley.com/doi/abs/10.1002/3527603646`.

[43] A. H. Abdelhameed et al. "First results from the CRESST-III low-mass dark matter program." In: *Phys. Rev. D* 100 (10 2019), p. 102002. DOI: `http://dx.doi.org/10.1103/PhysRevD.100.102002`. URL: `https://link.aps.org/doi/10.1103/PhysRevD.100.102002`.

[44] G. Angloher, F. Ardellier-Desages, A. Bento, et al. "Exploring CENS with NUCLEUS at the Chooz nuclear power plant." In: *The European Physical Journal C* 79.12 (Dec. 2019), p. 1018. DOI: `https://doi.org/10.1140/epjc/s10052-019-7454-4`.

[45] C. Goupy, H. Abele, G. Angloher, et al. "Exploring coherent elastic neutrino-nucleus scattering of reactor neutrinos with the NUCLEUS experiment." In: *SciPost Phys. Proc.* (2023), p. 053. DOI: `10.21468/SciPostPhysProc.12.053`. URL: `https://scipost.org/10.21468/SciPostPhysProc.12.053`.

[46] M. Pyle, P. Brink, B. Cabrera, et al. "Quasiparticle propagation in aluminum fins and tungsten TES dynamics in the CDMS ZIP detector." In: *Nucl. Instrum. Methods Phys. Res., Sect. A* 559.2 (2006), pp. 405–407. ISSN: 0168-9002. DOI: `https://doi.org/10.1016/j.nima.2005.12.022`. URL: `https://www.sciencedirect.com/science/article/pii/S0168900205024137`.

[47] R. Agnese, A. J. Anderson, D. Balakishiyeva, et al. "Demonstration of surface electron rejection with interleaved germanium detectors for dark matter searches." In: *Appl. Phys. Lett.* 103.16 (Oct. 2013), p. 164105. ISSN: 0003-6951. DOI: `10.1063/1.4826093`. eprint: `https://pubs.aip.org/aip/apl/article-pdf/doi/10.1063/1.4826093/13676279/164105\_1\_online.pdf`. URL: `https://doi.org/10.1063/1.4826093`.

[48] R. Agnese, Z. Ahmed, A. J. Anderson, et al. "Silicon detector results from the first five-tower run of CDMS II." In: *Phys. Rev. D* 88 (3 Aug. 2013), p. 031104. DOI: `10.1103/PhysRevD.88.031104`. URL: `https://link.aps.org/doi/10.1103/PhysRevD.88.031104`.

[49] R. Agnese, T. Aralis, T. Aramaki, et al. "Search for low-mass dark matter with CDMSlite using a profile likelihood fit." In: *Phys. Rev. D* 99.6 (Mar. 2019), p. 062001. DOI: `10.1103/PhysRevD.99.062001`. URL: `https://link.aps.org/doi/10.1103/PhysRevD.99.062001` (visited on 04/08/2019).

[50] R. Agnese, A. J. Anderson, T. Aramaki, et al. "Projected sensitivity of the SuperCDMS SNOLAB experiment." In: *Phys. Rev. D* 95 (8 Apr. 2017), p. 082002. DOI: `10.1103/PhysRevD.95.082002`. URL: `https://link.aps.org/doi/10.1103/PhysRevD.95.082002`.

[51] M. F. Albakry, I. Alkhatib, D. W. P. Amaral, et al. *A Strategy for Low-Mass Dark Matter Searches with Cryogenic Detectors in the SuperCDMS SNOLAB Facility*. arXiv:2203.08463. 2023. arXiv: `2203.08463 [physics.ins-det]`.

[52] R. Ren, C. Bathurst, Y. Y. Chang, et al. "Design and characterization of a phonon-mediated cryogenic particle detector with an eV-scale threshold and 100 keV-scale dynamic range." In: *Phys. Rev. D* 104 (3 Aug. 2021), p. 032010. DOI: `10.1103/PhysRevD.104.032010`. URL: `https://link.aps.org/doi/10.1103/PhysRevD.104.032010`.

[53] R. Agnese, T. Aralis, T. Aramaki, et al. "First Dark Matter Constraints from a SuperCDMS Single-Charge Sensitive Detector." In: *Phys. Rev. Lett.* 121 (5 Aug. 2018), p. 051301. DOI: `10.1103/PhysRevLett.121.051301`. URL: `https://link.aps.org/doi/10.1103/PhysRevLett.121.051301`.

[54] D. W. Amaral et al. "Constraints on low-mass, relic dark matter candidates from a surface-operated SuperCDMS single-charge sensitive detector." In: *Phys. Rev. D* 102 (9 Nov. 2020), p. 091101. DOI: `10.1103/PhysRevD.102.091101`. URL: `https://link.aps.org/doi/10.1103/PhysRevD.102.091101`.

[55] C. W. Fink, S. L. Watkins, T. Aramaki, et al. "Performance of a large area photon detector for rare event search applications." In: *Appl. Phys. Lett.* 118.2 (Jan. 2021), p. 022601. ISSN: 0003-6951. DOI: `10.1063/5.0032372`. eprint: `https://pubs.aip.org/aip/apl/article-pdf/doi/10.1063/5.0032372/13706989/022601\_1\_online.pdf`. URL: `https://doi.org/10.1063/5.0032372`.

[56] I. Alkhatib, D. W. P. Amaral, T. Aralis, et al. "Light Dark Matter Search with a High-Resolution Athermal Phonon Detector Operated above Ground." In: *Phys. Rev. Lett.* 127 (6 Aug. 2021), p. 061801. DOI: `10.1103/PhysRevLett.127.061801`. URL: `https://link.aps.org/doi/10.1103/PhysRevLett.127.061801`.

[57] R. Anthony-Petersen, A. Biekert, C. L. Chang, et al. *Applying Superfluid Helium to Light Dark Matter Searches: Demonstration of the HeRALD Detector Concept*. arXiv:2307.11877. 2023. arXiv: `2307.11877 [physics.ins-det]`.

[58] F. Pröbst, M. Frank, S. Cooper, et al. "Model for cryogenic particle detectors with superconducting phase transition thermometers." In: *J. Low Temp. Phys.* 100.1 (1995), pp. 69–104. DOI: `https://doi.org/10.1007/BF00753837`.

[59] R. Strauss, J. Rothe, G. Angloher, et al. "Gram-scale cryogenic calorimeters for rare-event searches." In: *Phys. Rev. D* 96 (2 July 2017), p. 022009. DOI: `10.1103/PhysRevD.96.022009`. URL: `https://link.aps.org/doi/10.1103/PhysRevD.96.022009`.

[60] G. Angloher, A. Bento, C. Bucci, et al. "Results on light dark matter particles with a low-threshold CRESST-II detector." In: *Eur. Phys. J. C* 76 (2016), pp. 1–8. DOI: `https://doi.org/10.1140/epjc/s10052-016-3877-3`.

[61] C. Collaboration, G. Angloher, S. Banik, et al. *First observation of single photons in a CRESST detector and new dark matter exclusion limits*. 2024. arXiv: `2405.06527 [astro-ph.CO]`. URL: `https://arxiv.org/abs/2405.06527`.

[62] A. Abdelhameed, G. Angloher, A. Bento, et al. "A low-threshold diamond cryogenic detector for sub-GeV dark matter searches." In: *Eur. Phys. J. C* 82.9 (2022), p. 851. DOI: `https://doi.org/10.1140/epjc/s10052-022-10829-5`.

[63] G. Angloher, S. Banik, G. Benato, et al. "Light dark matter search using a diamond cryogenic detector." In: *Eur. Phys. J. C* 84.3 (2024), pp. 1–6. DOI: `https://doi.org/10.1140/epjc/s10052-024-12647-3`.

[64] G. Angloher, P. Bauer, A. Bento, et al. "Results on MeV-scale dark matter from a gram-scale cryogenic calorimeter operated above ground." In: *Eur. Phys. J C* 77.9 (2017), pp. 1–6.

[65] N. Ferreiro Iachellini, L. Pattavina, A. Abdelhameed, et al. "Operation of an Archaeological Lead PbWO 4 Crystal to Search for Neutrinos from Astrophysical Sources with a Transition Edge Sensor." In: *J. Low Temp. Phys.* 209.5-6 (2022), pp. 872–878. DOI: `https://doi.org/10.1007/s10909-022-02823-8`.

[66] G. Angloher, M. R. Bharadwaj, I. Dafinei, et al. "Deep-underground dark matter search with a COSINUS detector prototype." In: *Phys. Rev. D* 110 (4 Aug. 2024), p. 043010. DOI: `10.1103/PhysRevD.110.043010`. URL: `https://link.aps.org/doi/10.1103/PhysRevD.110.043010`.

[67] R. Agnese, A. J. Anderson, T. Aralis, et al. "Low-mass dark matter search with CDMSlite." In: *Phys. Rev. D* 97 (2 Jan. 2018), p. 022002. DOI: `10.1103/PhysRevD.97.022002`. URL: `https://link.aps.org/doi/10.1103/PhysRevD.97.022002`.

[68] E. Armengaud, Q. Arnaud, C. Augier, et al. "Performance of the EDELWEISS-III experiment for direct dark matter searches." In: *J. Instrum.* 12.08 (Aug. 2017), P08010. DOI: `10.1088/1748-0221/12/08/P08010`. URL: `https://dx.doi.org/10.1088/1748-0221/12/08/P08010`.

[69] E. Armengaud, Q. Arnaud, C. Augier, et al. "Search for sub-GeV dark matter via the Migdal effect with an EDELWEISS germanium detector with NbSi transition-edge sensors." In: *Phys. Rev. D* 106 (6 Sept. 2022), p. 062004. DOI: `10.1103/PhysRevD.106.062004`. URL: `https://link.aps.org/doi/10.1103/PhysRevD.106.062004`.

[70] N. Aghanim, Y. Akrami, M. Ashdown, et al. "Planck 2018 results - VI. Cosmological parameters." In: *Astron. Astrophys.* 641 (2020), A6. DOI: `10.1051/0004-6361/201833910`. URL: `https://doi.org/10.1051/0004-6361/201833910`.

[71] F. Zwicky. "Die Rotverschiebung von extragalaktischen Nebeln." In: *Helvetica Physica Acta* 6 (Jan. 1933), pp. 110–127.

[72] V. C. Rubin, W. K. Ford Jr, and N. Thonnard. "Rotational properties of 21 SC galaxies with a large range of luminosities and radii, from NGC 4605/R= 4kpc/to UGC 2885/R= 122 kpc." In: *Astrophysical Journal, Part 1, vol. 238, June 1, 1980, p. 471-487.* 238 (1980), pp. 471–487. DOI: `10.1086/158003`.

[73] J. P. Ostriker, P. J. Peebles, and A. Yahil. "The size and mass of galaxies, and the mass of the universe." In: *Astrophysical Journal, vol. 193, Oct. 1, 1974, pt. 2, p. L1-L4.* 193 (1974), pp. L1–L4. DOI: `10.1086/181617`.

[74] J. Einasto, A. Kaasik, and E. Saar. "Dynamic evidence on massive coronas of galaxies." In: *Nature* 250.5464 (1974), pp. 309–310. DOI: `https://doi.org/10.1038/250309a0`.

[75] D. Clowe, M. Bradač, A. H. Gonzalez, et al. "A Direct Empirical Proof of the Existence of Dark Matter*." In: *The Astrophysical Journal* 648.2 (Aug. 2006), p. L109. DOI: `10.1086/508162`. URL: `https://dx.doi.org/10.1086/508162`.

[76] R. Massey, T. Kitching, and J. Richard. "The dark matter of gravitational lensing." In: *Reports on Progress in Physics* 73.8 (July 2010), p. 086901. DOI: `10.1088/0034-4885/73/8/086901`. URL: `https://dx.doi.org/10.1088/0034-4885/73/8/086901`.

[77] G. Jungman, M. Kamionkowski, and K. Griest. "Supersymmetric dark matter." In: *Physics Reports* 267.5 (1996), pp. 195–373. ISSN: 0370-1573. DOI: `https://doi.org/10.1016/0370-1573(95)00058-5`. URL: `https://www.sciencedirect.com/science/article/pii/0370157395000585`.

[78] R. D. Peccei and H. R. Quinn. "CP Conservation in the Presence of Instantons." In: *Phys. Rev. Lett* 38.1440-1443 (1977), p. 328.

[79] C. Bœhm, P. Fayet, and J. Silk. "Light and heavy dark matter particles." In: *Phys. Rev. D* 69 (10 May 2004), 101302(R). DOI: `10.1103/PhysRevD.69.101302`. URL: `https://link.aps.org/doi/10.1103/PhysRevD.69.101302`.

[80] C. Bœhm and P. Fayet. "Scalar dark matter candidates." In: *Nuclear Physics B* 683.1 (2004), pp. 219–263. ISSN: 0550-3213. DOI: `https://doi.org/10.1016/j.nuclphysb.2004.01.015`. URL: `https://www.sciencedirect.com/science/article/pii/S0550321304000306`.

[81] D. Hooper and K. M. Zurek. "Natural supersymmetric model with MeV dark matter." In: *Phys. Rev. D* 77 (8 Apr. 2008), p. 087302. DOI: `10.1103/PhysRevD.77.087302`. URL: `https://link.aps.org/doi/10.1103/PhysRevD.77.087302`.

[82] J. L. Feng and J. Kumar. "Dark-Matter Particles without Weak-Scale Masses or Weak Interactions." In: *Phys. Rev. Lett.* 101 (23 Dec. 2008), p. 231301. DOI: `10.1103/PhysRevLett.101.231301`. URL: `https://link.aps.org/doi/10.1103/PhysRevLett.101.231301`.

[83] D. E. Kaplan, M. A. Luty, and K. M. Zurek. "Asymmetric dark matter." In: *Phys. Rev. D* 79 (11 June 2009), p. 115016. DOI: `10.1103/PhysRevD.79.115016`. URL: `https://link.aps.org/doi/10.1103/PhysRevD.79.115016`.

[84] H. Baer, K.-Y. Choi, J. E. Kim, and L. Roszkowski. "Dark matter production in the early Universe: Beyond the thermal WIMP paradigm." In: *Phys. Rep.* 555 (2015), pp. 1–60. ISSN: 0370-1573. DOI: `https://doi.org/10.1016/j.physrep.2014.10.002`. URL: `https://www.sciencedirect.com/science/article/pii/S0370157314003925`.

[85] G. B. Gelmini. "Light weakly interacting massive particles." In: *Rep. Prog. Phys.* 80.8 (June 2017), p. 082201. DOI: `10.1088/1361-6633/aa6e5c`. URL: `https://dx.doi.org/10.1088/1361-6633/aa6e5c`.

[86] A. Boveia and C. Doglioni. "Dark Matter Searches at Colliders." In: *Annual Review of Nuclear and Particle Science* 68.Volume 68, 2018 (2018), pp. 429–459. ISSN: 1545-4134. DOI: `https://doi.org/10.1146/annurev-nucl-101917-021008`. URL: `https://www.annualreviews.org/content/journals/10.1146/annurev-nucl-101917-021008`.

[87] J. M. Gaskins. "A review of indirect searches for particle dark matter." In: *Contemporary Physics* 57.4 (2016), pp. 496–525. DOI: `10.1080/00107514.2016.1175160`. eprint: `https://doi.org/10.1080/00107514.2016.1175160`. URL: `https://doi.org/10.1080/00107514.2016.1175160`.

[88] P. Salucci, F. Nesti, G. Gentile, and C. F. Martins. "The dark matter density at the Sun's location." In: *Astron. Astrophys.* 523 (2010), A83. DOI: `https://doi.org/10.1051/0004-6361/201014385`.

[89] F. Donato, N. Fornengo, and S. Scopel. "Effects of galactic dark halo rotation on WIMP direct detection." In: *Astropart. Phys.* 9.3 (1998), pp. 247–260. DOI: `https://doi.org/10.1016/S0927-6505(98)00025-5`.

[90] M. C. Smith, G. R. Ruchti, A. Helmi, et al. "The RAVE survey: constraining the local Galactic escape speed." In: *Mon. Notices Royal Astron. Soc.* 379.2 (July 2007), pp. 755–772. ISSN: 0035-8711. DOI: `10.1111/j.1365-2966.2007.11964.x`. URL: `https://doi.org/10.1111/j.1365-2966.2007.11964.x`.

[91] D. Baxter, I. M. Bloch, E. Bodnia, et al. "Recommended conventions for reporting results from direct dark matter searches." In: *Eur. Phys. J. C* 81.10 (Oct. 2021). ISSN: 1434-6052. DOI: `10.1140/epjc/s10052-021-09655-y`. URL: `http://dx.doi.org/10.1140/epjc/s10052-021-09655-y`.

[92] R. H. Helm. "Inelastic and Elastic Scattering of 187-Mev Electrons from Selected Even-Even Nuclei." In: *Phys. Rev.* 104 (5 Dec. 1956), pp. 1466–1475. DOI: `10.1103/PhysRev.104.1466`. URL: `https://link.aps.org/doi/10.1103/PhysRev.104.1466`.

[93] J. Lewin and P. Smith. "Review of mathematics, numerical factors, and corrections for dark matter experiments based on elastic nuclear recoil." In: *Astropart. Phys.* 6.1 (1996), pp. 87–112. ISSN: 0927-6505. DOI: `https://doi.org/10.1016/S0927-6505(96)00047-3`. URL: `https://www.sciencedirect.com/science/article/pii/S0927650596000473`.

[94] E. Aprile, K. Abe, F. Agostini, et al. “First Dark Matter Search with Nuclear Recoils from the XENONnT Experiment.” In: *Phys. Rev. Lett.* 131 (4 July 2023), p. 041003. DOI: `10.1103/PhysRevLett.131.041003`. URL: `https://link.aps.org/doi/10.1103/PhysRevLett.131.041003`.

[95] J. Aalbers, D. S. Akerib, C. W. Akerlof, et al. “First Dark Matter Search Results from the LUX-ZEPLIN (LZ) Experiment.” In: *Phys. Rev. Lett.* 131 (4 July 2023), p. 041002. DOI: `10.1103/PhysRevLett.131.041002`. URL: `https://link.aps.org/doi/10.1103/PhysRevLett.131.041002`.

[96] Y. Meng, Z. Wang, Y. Tao, et al. “Dark Matter Search Results from the PandaX-4T Commissioning Run.” In: *Phys. Rev. Lett.* 127 (26 Dec. 2021), p. 261802. DOI: `10.1103/PhysRevLett.127.261802`. URL: `https://link.aps.org/doi/10.1103/PhysRevLett.127.261802`.

[97] R. Ajaj, P.-A. Amaudruz, G. R. Araujo, et al. “Search for dark matter with a 231-day exposure of liquid argon using DEAP-3600 at SNOLAB.” In: *Phys. Rev. D* 100 (2 July 2019), p. 022004. DOI: `10.1103/PhysRevD.100.022004`. URL: `https://link.aps.org/doi/10.1103/PhysRevD.100.022004`.

[98] P. Agnes, I. F. M. Albuquerque, T. Alexander, et al. “Search for low-mass dark matter WIMPs with 12 ton-day exposure of DarkSide-50.” In: *Phys. Rev. D* 107 (6 Mar. 2023), p. 063001. DOI: `10.1103/PhysRevD.107.063001`.

[99] G. Adhikari, E. Barbosa de Souza, N. Carlin, et al. “Three-year annual modulation search with COSINE-100.” In: *Phys. Rev. D* 106 (5 Sept. 2022), p. 052005. DOI: `10.1103/PhysRevD.106.052005`. URL: `https://link.aps.org/doi/10.1103/PhysRevD.106.052005`.

[100] J. Amaré, S. Cebrián, D. Cintas, et al. “Annual modulation results from three-year exposure of ANAIS-112.” In: *Phys. Rev. D* 103 (10 May 2021), p. 102005. DOI: `10.1103/PhysRevD.103.102005`. URL: `https://link.aps.org/doi/10.1103/PhysRevD.103.102005`.

[101] Angloher, G., Dafinei, I., Marco, N. Di, et al. “Simulation-based design study for the passive shielding of the COSINUS dark matter experiment.” In: *Eur. Phys. J. C* 82.3 (2022), p. 248. DOI: `10.1140/epjc/s10052-022-10184-5`. URL: `https://doi.org/10.1140/epjc/s10052-022-10184-5`.

[102] M. Antonello, I. J. Arnquist, E. Barberio, et al. “Characterization of SABRE crystal NaI-33 with direct underground counting.” In: *The European Physical Journal C* 81.4 (Apr. 2021), p. 299.

[103] Barberio, E., Baroncelli, T., Bignell, L. J., et al. “Simulation and background characterisation of the SABRE South experiment - SABRE South Collaboration.” In: *Eur. Phys. J. C* 83.9 (2023), p. 878. DOI: `10.1140/epjc/s10052-023-11817-z`. URL: `https://doi.org/10.1140/epjc/s10052-023-11817-z`.

[104] R. Agnese, A. J. Anderson, M. Asai, et al. "Search for Low-Mass Weakly Interacting Massive Particles with SuperCDMS." In: *Phys. Rev. Lett.* 112.24 (June 2014), p. 241302. doi: `10.1103/PhysRevLett.112.241302`. url: `http://link.aps.org/doi/10.1103/PhysRevLett.112.241302` (visited on 05/22/2015).

[105] E. Aprile, J. Aalbers, F. Agostini, et al. "Light Dark Matter Search with Ionization Signals in XENON1T." In: *Phys. Rev. Lett.* 123 (25 Dec. 2019), p. 251801. doi: `10.1103/PhysRevLett.123.251801`. url: `https://link.aps.org/doi/10.1103/PhysRevLett.123.251801`.

[106] H. Jiang, L. P. Jia, Q. Yue, et al. "Limits on Light Weakly Interacting Massive Particles from the First 102.8 kg × day Data of the CDEX-10 Experiment." In: *Phys. Rev. Lett.* 120.24 (June 2018), p. 241301. doi: `10.1103/PhysRevLett.120.241301`. url: `https://link.aps.org/doi/10.1103/PhysRevLett.120.241301` (visited on 04/29/2019).

[107] A. Aguilar-Arevalo, D. Amidei, D. Baxter, et al. "Results on Low-Mass Weakly Interacting Massive Particles from an 11 kg d Target Exposure of DAMIC at SNOLAB." In: *Phys. Rev. Lett.* 125 (24 Dec. 2020), p. 241803.

[108] Q. Arnaud, D. Asner, J. .-. Bard, et al. "First results from the NEWS-G direct dark matter search experiment at the LSM." In: *Astropart. Phys.* 97 (Jan. 2018), pp. 54–62. issn: 0927-6505. doi: `10.1016/j.astropartphys.2017.10.009`. url: `http://www.sciencedirect.com/science/article/pii/S0927650517301871` (visited on 03/29/2019).

[109] C. Amole, M. Ardid, I. J. Arnquist, et al. "Dark matter search results from the complete exposure of the PICO-60 $C_3F_8$ bubble chamber." In: *Phys. Rev. D* 100 (2 July 2019), p. 022001. doi: `10.1103/PhysRevD.100.022001`. url: `https://link.aps.org/doi/10.1103/PhysRevD.100.022001`.

[110] J. I. Collar. "Search for a nonrelativistic component in the spectrum of cosmic rays at Earth." In: *Phys. Rev. D* 98.2 (July 2018), p. 023005. doi: `10.1103/PhysRevD.98.023005`. url: `https://link.aps.org/doi/10.1103/PhysRevD.98.023005` (visited on 02/22/2019).

[111] G. Adhikari, E. B. de Souza, N. Carlin, et al. "Strong constraints from COSINE-100 on the DAMA dark matter results using the same sodium iodide target." In: *Sci. Adv.* 7.46 (2021), eabk2699. doi: `10.1126/sciadv.abk2699`. eprint: `https://www.science.org/doi/pdf/10.1126/sciadv.abk2699`. url: `https://www.science.org/doi/abs/10.1126/sciadv.abk2699`.

[112] R. Bernabei, P. Belli, F. Cappella, et al. "First results from DAMA/LIBRA and the combined results with DAMA/NaI." In: *Eur. Phys. J. C* 56 (2008), pp. 333–355. doi: `https://doi.org/10.1140/epjc/s10052-008-0662-y`.

[113] C. Savage, G. Gelmini, P. Gondolo, and K. Freese. “Compatibility of DAMA/LIBRA dark matter detection with other searches.” In: *J. Cosmol. Astropart. Phys.* 2009.04 (Apr. 2009), p. 010. DOI: `10.1088/1475-7516/2009/04/010`. URL: `https://dx.doi.org/10.1088/1475-7516/2009/04/010`.

[114] A. Gütlein, G. Angloher, A. Bento, et al. “Impact of Coherent Neutrino Nucleus Scattering on Direct Dark Matter Searches based on $CaWO_4$ Crystals.” In: *Astropart. Phys.* 69 (Sept. 2015), pp. 44–49. ISSN: 09276505. DOI: `10.1016/j.astropartphys.2015.03.010`. URL: `http://arxiv.org/abs/1408.2357` (visited on 05/24/2015).

[115] D. R. Fuchs. “New Analysis Methods for Enhanced Sensitivity to Light Dark Matter at CRESST-III and Studies of Discovery Potential for Next Generation Cryogenic Experiments.” en. PhD thesis. Technische Universität München, 2023, p. 232. URL: `https://mediatum.ub.tum.de/1709800`.

[116] C. A. J. O’Hare. “New Definition of the Neutrino Floor for Direct Dark Matter Searches.” In: *Phys. Rev. Lett.* 127 (25 Dec. 2021), p. 251802. DOI: `10.1103/PhysRevLett.127.251802`. URL: `https://link.aps.org/doi/10.1103/PhysRevLett.127.251802`.

[117] S. Derenzo, R. Essig, A. Massari, et al. “Direct detection of sub-GeV dark matter with scintillating targets.” In: *Phys. Rev. D* 96 (1 July 2017), p. 016026. DOI: `10.1103/PhysRevD.96.016026`. URL: `https://link.aps.org/doi/10.1103/PhysRevD.96.016026`.

[118] R. Essig, J. Mardon, and T. Volansky. “Direct detection of sub-GeV dark matter.” In: *Phys. Rev. D* 85 (7 Apr. 2012), p. 076007. DOI: `10.1103/PhysRevD.85.076007`. URL: `https://link.aps.org/doi/10.1103/PhysRevD.85.076007`.

[119] R. Catena, T. Emken, N. A. Spaldin, and W. Tarantino. “Atomic responses to general dark matter-electron interactions.” In: *Phys. Rev. Res.* 2 (3 Aug. 2020), p. 033195. DOI: `10.1103/PhysRevResearch.2.033195`. URL: `https://link.aps.org/doi/10.1103/PhysRevResearch.2.033195`.

[120] N. F. Bell, J. B. Dent, R. F. Lang, et al. “Observing the Migdal effect from nuclear recoils of neutral particles with liquid xenon and argon detectors.” In: *Phys. Rev. D* 105 (9 May 2022), p. 096015. DOI: `10.1103/PhysRevD.105.096015`. URL: `https://link.aps.org/doi/10.1103/PhysRevD.105.096015`.

[121] D. Adams, D. Baxter, H. Day, et al. “Measuring the Migdal effect in semiconductors for dark matter detection.” In: *Phys. Rev. D* 107 (4 Feb. 2023), p. L041303. DOI: `10.1103/PhysRevD.107.L041303`. URL: `https://link.aps.org/doi/10.1103/PhysRevD.107.L041303`.

[122] G. Angloher, M. Bruckmayer, C. Bucci, et al. “Limits on WIMP dark matter using sapphire cryogenic detectors.” In: *Astropart. Phys.* 18.1 (Aug. 2002), pp. 43–55. ISSN: 0927-6505. DOI: `10.1016/S0927-6505(02)00111-1`. URL: `http://www.sciencedirect.com/science/article/pii/S0927650502001111` (visited on 05/22/2015).

[123] G. Angloher, M. Bauer, I. Bavykina, et al. "Results from 730 kg days of the CRESST-II Dark Matter Search." In: *Eur. Phys. J. C* 72.4 (2012), pp. 1–22. DOI: `https://doi.org/10.1140/epjc/s10052-012-1971-8`.

[124] G. Bellini, J. Benziger, D. Bick, et al. "Cosmic-muon flux and annual modulation in Borexino at 3800 m water-equivalent depth." In: *J. Cosmol. Astropart. Phys.* 2012.05 (May 2012), p. 015. DOI: `10.1088/1475-7516/2012/05/015`. URL: `https://dx.doi.org/10.1088/1475-7516/2012/05/015`.

[125] A. C. Kinast. "Enhancing the Dark Matter Sensitivity of CRESST: Purification, Stress Reduction and 17O Enrichment of CaWO4 Target Crystals." en. PhD thesis. Technische Universität München, 2023, p. 254. URL: `https://mediatum.ub.tum.de/1726057`.

[126] V. B. Mikhailik, H. Kraus, D. Wahl, et al. "One- and two-photon excited luminescence and band-gap assignment in $CaWO_4$." In: *Phys. Rev. B* 69 (20 May 2004), p. 205110. DOI: `10.1103/PhysRevB.69.205110`. URL: `https://link.aps.org/doi/10.1103/PhysRevB.69.205110`.

[127] G. Angloher et al. "Commissioning run of the CRESST-II dark matter search." In: *Astropart. Phys.* 31.4 (2009), pp. 270–276. ISSN: 0927-6505. DOI: `https://doi.org/10.1016/j.astropartphys.2009.02.007`. URL: `https://www.sciencedirect.com/science/article/pii/S0927650509000358`.

[128] A. Abdelhameed, G. Angloher, P. Bauer, et al. "Geant4-based electromagnetic background model for the CRESST dark matter experiment." In: *Eur. Phys. J. C* 79 (2019), pp. 1–18. DOI: `https://doi.org/10.1140/epjc/s10052-019-7385-0`.

[129] A. Abdelhameed, G. Angloher, P. Bauer, et al. "Erratum to: Geant4-based electromagnetic background model for the CRESST dark matter experiment." In: *Eur. Phys. J. C* 79 (Dec. 2019), p. 987. DOI: `10.1140/epjc/s10052-019-7504-y`.

[130] G. Angloher, S. Banik, G. Benato, et al. *High-Dimensional Bayesian Likelihood Normalisation for CRESST's Background Model.* arXiv:2307.12991. 2023. arXiv: `2307.12991 [physics.ins-det]`.

[131] H. Kluck. "ELOISE - Reliable background simulation at sub-keV energies." In: *SciPost Phys. Proc.* (2023), p. 064. DOI: `10.21468/SciPostPhysProc.12.064`. URL: `https://scipost.org/10.21468/SciPostPhysProc.12.064`.

[132] C. Collaboration, G. Angloher, and S. B. et al. "A likelihood framework for cryogenic scintillating calorimeters used in the CRESST dark matter search." In: *Eur. Phys. J. C* 84 (2024), p. 922. URL: `https://doi.org/10.1140/epjc/s10052-024-13141-6`.

[133] S. Yellin. "Finding an upper limit in the presence of an unknown background." In: *Phys. Rev. D* 66 (3 Aug. 2002), p. 032005. DOI: `10.1103/PhysRevD.66.032005`. URL: `https://link.aps.org/doi/10.1103/PhysRevD.66.032005`.

[134] S. Yellin. "Extending the optimum interval method." In: (2007). DOI: `10.48550/ARXIV.0709.2701`. URL: `https://arxiv.org/abs/0709.2701`.

[135] R. Strauss, G. Angloher, A. Bento, et al. “Energy-dependent light quenching in $CaWO_4$ crystals at mK temperatures.” In: *Eur. Phys. J. C* 74 (2014), pp. 1–6. URL: `https://doi.org/10.1140/epjc/s10052-014-2957-5`.

[136] A. Erb and J.-C. Lanfranchi. “Growth of high-purity scintillating CaWO4 single crystals for the low-temperature direct dark matter search experiments CRESST-II and EURECA.” In: *Cryst. Eng. Comm.* 15 (12 2013), pp. 2301–2304. DOI: `10.1039/C2CE26554K`. URL: `http://dx.doi.org/10.1039/C2CE26554K`.

[137] R. Strauss, G. Angloher, A. Bento, et al. “Beta/gamma and alpha backgrounds in CRESST-II Phase 2.” In: *J. Cosmol. Astropart. Phys.* 2015.06 (June 2015), p. 030. DOI: `10.1088/1475-7516/2015/06/030`. URL: `https://dx.doi.org/10.1088/1475-7516/2015/06/030`.

[138] A. R. Münster. “High-Purity $CaWO_4$ Single Crystals for Direct Dark Matter Search with the CRESST Experiment.” en. PhD thesis. Technische Universität München, 2017, p. 235.

[139] A. Kinast, G. Angloher, S. Banik, et al. “Characterisation of low background $CaWO_4$ crystals for CRESST-III.” In: *SciPost Phys. Proc.* (2023), p. 031. DOI: `10.21468/SciPostPhysProc.12.031`. URL: `https://scipost.org/10.21468/SciPostPhysProc.12.031`.

[140] G. Angloher et al. “Testing spin-dependent dark matter interactions with lithium aluminate targets in CRESST-III.” In: *Phys. Rev. D* 106 (9 Nov. 2022), p. 092008. DOI: `10.1103/PhysRevD.106.092008`. URL: `https://link.aps.org/doi/10.1103/PhysRevD.106.092008`.

[141] G. Angloher, S. Banik, G. Benato, et al. “Detector Development for the CRESST Experiment.” In: *J. Low Temp. Phys.* (2024). DOI: `10.1007/s10909-024-03154-6`. URL: `https://link.aps.org/doi/10.1103/PhysRevD.66.032005`.

[142] A. Kinast, A. Erb, S. Schönert, et al. *$^{17}O$ enrichment of $CaWO_4$ crystals for spin-dependent DM search.* arXiv:2311.03161. 2023. arXiv: `2311.03161 [astro-ph.IM]`.

[143] Y. Fukuda, T. Hayakawa, E. Ichihara, et al. “Evidence for Oscillation of Atmospheric Neutrinos.” In: *Phys. Rev. Lett.* 81 (8 Aug. 1998), pp. 1562–1567. DOI: `10.1103/PhysRevLett.81.1562`. URL: `https://link.aps.org/doi/10.1103/PhysRevLett.81.1562`.

[144] Q. R. Ahmad, R. C. Allen, T. C. Andersen, et al. “Direct Evidence for Neutrino Flavor Transformation from Neutral-Current Interactions in the Sudbury Neutrino Observatory.” In: *Phys. Rev. Lett.* 89 (1 June 2002), p. 011301. DOI: `10.1103/PhysRevLett.89.011301`. URL: `https://link.aps.org/doi/10.1103/PhysRevLett.89.011301`.

[145] D. Z. Freedman. “Coherent effects of a weak neutral current.” In: *Phys. Rev. D* 9 (5 Mar. 1974), pp. 1389–1392. DOI: `10.1103/PhysRevD.9.1389`. URL: `https://link.aps.org/doi/10.1103/PhysRevD.9.1389`.

[146] P. J. Mohr, E. Tiesinga, D. B. Newell, and B. N. Taylor. *Codata Internationally Recommended 2022 Values of the Fundamental Physical Constants*. en. 2024-05-08 04:05:00 2024. URL: `https://tsapps.nist.gov/publication/get_pdf.cfm?pub_id=958002`.

[147] T. Ohlsson. "Status of non-standard neutrino interactions." en. In: *Rep Prog Phys* 76.4 (Mar. 2013), p. 044201. DOI: `10.1088/0034-4885/76/4/044201`.

[148] M. Cadeddu, C. Giunti, K. A. Kouzakov, et al. "Neutrino charge radii from COHERENT elastic neutrino-nucleus scattering." In: *Phys. Rev. D* 98 (11 Dec. 2018), p. 113010. DOI: `10.1103/PhysRevD.98.113010`. URL: `https://link.aps.org/doi/10.1103/PhysRevD.98.113010`.

[149] C. Giunti and A. Studenikin. "Neutrino electromagnetic interactions: A window to new physics." In: *Rev. Mod. Phys.* 87 (2 June 2015), pp. 531–591. DOI: `10.1103/RevModPhys.87.531`. URL: `https://link.aps.org/doi/10.1103/RevModPhys.87.531`.

[150] N. F. Bell, M. Gorchtein, M. J. Ramsey-Musolf, et al. "Model independent bounds on magnetic moments of Majorana neutrinos." In: *Physics Letters B* 642.4 (2006), pp. 377–383. ISSN: 0370-2693. DOI: `https://doi.org/10.1016/j.physletb.2006.09.055`. URL: `https://www.sciencedirect.com/science/article/pii/S0370269306012305`.

[151] Y. Farzan, M. Lindner, W. Rodejohann, and X.-J. Xu. "Probing neutrino coupling to a light scalar with coherent neutrino scattering." In: *Journal of High Energy Physics* 2018.5 (May 2018), p. 66. DOI: `https://doi.org/10.1007/JHEP05(2018)066`.

[152] D. A. Sierra, B. Dutta, S. Liao, and L. E. Strigari. "Coherent elastic neutrino-nucleus scattering in multi-ton scale dark matter experiments: classification of vector and scalar interactions new physics signals." In: *Journal of High Energy Physics* 2019.12 (Dec. 2019), p. 124. DOI: `https://doi.org/10.1007/JHEP12(2019)124`.

[153] J. Billard, J. Johnston, and B. J. Kavanagh. "Prospects for exploring New Physics in Coherent Elastic Neutrino-Nucleus Scattering." In: *Journal of Cosmology and Astroparticle Physics* 2018.11 (Nov. 2018), p. 016. DOI: `10.1088/1475-7516/2018/11/016`. URL: `https://dx.doi.org/10.1088/1475-7516/2018/11/016`.

[154] J. Billard, E. Figueroa-Feliciano, and L. Strigari. "Implication of neutrino backgrounds on the reach of next generation dark matter direct detection experiments." In: *Phys. Rev. D* 89 (2 Jan. 2014), p. 023524. DOI: `10.1103/PhysRevD.89.023524`. URL: `https://link.aps.org/doi/10.1103/PhysRevD.89.023524`.

[155] J. Monroe and P. Fisher. "Neutrino backgrounds to dark matter searches." In: *Phys. Rev. D* 76 (3 Aug. 2007), p. 033007. DOI: `10.1103/PhysRevD.76.033007`. URL: `https://link.aps.org/doi/10.1103/PhysRevD.76.033007`.

[156] L. E. Strigari. "Neutrino coherent scattering rates at direct dark matter detectors." In: *New Journal of Physics* 11.10 (Oct. 2009), p. 105011. DOI: `10.1088/1367-2630/11/10/105011`. URL: `https://dx.doi.org/10.1088/1367-2630/11/10/105011`.

[157] A. Gütlein, C. Ciemniak, F. von Feilitzsch, et al. "Solar and atmospheric neutrinos: Background sources for the direct dark matter searches." In: *Astroparticle Physics* 34.2 (2010), pp. 90–96. ISSN: 0927-6505. DOI: `https://doi.org/10.1016/j.astropartphys.2010.06.002`. URL: `https://www.sciencedirect.com/science/article/pii/S0927650510001143`.

[158] L. Michel. "Interaction between Four Half-Spin Particles and the Decay of the $\mu$-Meson." In: *Proceedings of the Physical Society. Section A* 63.5 (May 1950), p. 514. DOI: `10.1088/0370-1298/63/5/311`. URL: `https://dx.doi.org/10.1088/0370-1298/63/5/311`.

[159] K. Scholberg. "Prospects for measuring coherent neutrino-nucleus elastic scattering at a stopped-pion neutrino source." In: *Phys. Rev. D* 73 (3 Feb. 2006), p. 033005. DOI: `10.1103/PhysRevD.73.033005`. URL: `https://link.aps.org/doi/10.1103/PhysRevD.73.033005`.

[160] D. Akimov, J. B. Albert, P. An, et al. "Observation of coherent elastic neutrino-nucleus scattering." In: *Science* 357.6356 (2017), pp. 1123–1126. DOI: `10.1126/science.aao0990`. eprint: `https://www.science.org/doi/pdf/10.1126/science.aao0990`. URL: `https://www.science.org/doi/abs/10.1126/science.aao0990`.

[161] D. Akimov, P. An, C. Awe, et al. "Measurement of the Coherent Elastic Neutrino-Nucleus Scattering Cross Section on CsI by COHERENT." In: *Phys. Rev. Lett.* 129 (8 Aug. 2022), p. 081801. DOI: `10.1103/PhysRevLett.129.081801`. URL: `https://link.aps.org/doi/10.1103/PhysRevLett.129.081801`.

[162] D. Akimov, J. B. Albert, P. An, et al. "First Measurement of Coherent Elastic Neutrino-Nucleus Scattering on Argon." In: *Phys. Rev. Lett.* 126 (1 Jan. 2021), p. 012002. DOI: `10.1103/PhysRevLett.126.012002`. URL: `https://link.aps.org/doi/10.1103/PhysRevLett.126.012002`.

[163] S. Adamski, M. Ahn, P. S. Barbeau, et al. *First detection of coherent elastic neutrino-nucleus scattering on germanium*. 2024. arXiv: `2406.13806 [hep-ex]`. URL: `https://arxiv.org/abs/2406.13806`.

[164] W. Hampel, G. Heusser, J. Kiko, et al. "Final results of the 51Cr neutrino source experiments in GALLEX." In: *Physics Letters B* 420.1 (1998), pp. 114–126. ISSN: 0370-2693. DOI: `https://doi.org/10.1016/S0370-2693(97)01562-1`. URL: `https://www.sciencedirect.com/science/article/pii/S0370269397015621`.

[165] C. Bellenghi, D. Chiesa, L. Di Noto, et al. "Coherent elastic nuclear scattering of $^{51}$Cr neutrinos." In: *The European Physical Journal C* 79.9 (Aug. 2019), p. 727. DOI: `https://doi.org/10.1140/epjc/s10052-019-7240-3`.

[166] G. Bellini, D. Bick, G. Bonfini, et al. "SOX: Short distance neutrino Oscillations with BoreXino." In: *Journal of High Energy Physics* 2013.8 (Aug. 2013), p. 38. DOI: `https://doi.org/10.1007/JHEP08(2013)038`.

[167] V. I. Kopeikin. "Flux and spectrum of reactor antineutrinos." In: *Physics of Atomic Nuclei* 75.2 (Feb. 2012), pp. 143–152. ISSN: 1562-692X. DOI: `10.1134/S1063778812020123`. URL: `https://doi.org/10.1134/S1063778812020123`.

[168] J. Hakenmüller, C. Buck, K. Fülber, et al. "Neutron-induced background in the CONUS experiment." In: *The European Physical Journal C* 79.8 (Aug. 2019), p. 699. ISSN: 1434-6052. DOI: `10.1140/epjc/s10052-019-7160-2`. URL: `https://doi.org/10.1140/epjc/s10052-019-7160-2`.

[169] S. Karmakar, M. Singh, H. Wong, and V. Sharma. "Coherent neutrino-nucleus elastic scattering at reactor with TEXONO experiment." In: *XVIII International Conference on Topics in Astroparticle and Underground Physics*. 2024, p. 226. URL: `https://pos.sissa.it/441/226/pdf`.

[170] H. Bonet, A. Bonhomme, C. Buck, et al. "Constraints on Elastic Neutrino Nucleus Scattering in the Fully Coherent Regime from the CONUS Experiment." In: *Phys. Rev. Lett.* 126 (4 Jan. 2021), p. 041804. DOI: `10.1103/PhysRevLett.126.041804`. URL: `https://link.aps.org/doi/10.1103/PhysRevLett.126.041804`.

[171] N. Ackermann, S. Armbruster, H. Bonet, et al. *The CONUS+ experiment*. 2024. arXiv: `2407.11912 [hep-ex]`. URL: `https://arxiv.org/abs/2407.11912`.

[172] D. V. Ponomarev, A. D. Bystryakov, A. M. Konovalov, and A. V. Lubashevskiy. "Coherent Elastic Neutrino-Nucleus Scattering Search in the $\nu$GeN Experiment." In: *Physics of Particles and Nuclei Letters* 21.4 (Aug. 2024), pp. 680–682.

[173] A. Aguilar-Arevalo, X. Bertou, C. Bonifazi, et al. "Exploring low-energy neutrino physics with the Coherent Neutrino Nucleus Interaction Experiment." In: *Phys. Rev. D* 100 (9 Nov. 2019), p. 092005. DOI: `10.1103/PhysRevD.100.092005`. URL: `https://link.aps.org/doi/10.1103/PhysRevD.100.092005`.

[174] A. A. Aguilar-Arevalo, N. Avalos, X. Bertou, et al. *Searches for CE□NS and Physics beyond the Standard Model using Skipper-CCDs at CONNIE*. 2024. arXiv: `2403.15976 [hep-ex]`. URL: `https://arxiv.org/abs/2403.15976`.

[175] T. Salagnac, J. Billard, J. Colas, et al. "Optimization and Performance of the CryoCube Detector for the Future Ricochet Low-Energy Neutrino Experiment." In: *Journal of Low Temperature Physics* 211.5 (June 2023), pp. 398–406.

[176] C. Augier, G. Baulieu, V. Belov, et al. "Results from a prototype TES detector for the Ricochet experiment." In: *Nuclear Instruments and Methods in Physics Research Section A: Accelerators, Spectrometers, Detectors and Associated Equipment* 1057 (2023), p. 168765. ISSN: 0168-9002. DOI: `https://doi.org/10.1016/j.nima.2023.168765`. URL: `https://www.sciencedirect.com/science/article/pii/S0168900223007568`.

[177] V. Iyer, N. Mirabolfathi, G. Agnolet, et al. "Large mass single electron resolution detector for dark matter and neutrino elastic interaction searches." In: *Nuclear Instruments and Methods in Physics Research Section A: Accelerators, Spectrometers, Detectors and Associated Equipment* 1010 (2021), p. 165489. ISSN: 0168-9002. DOI: `https://doi.org/10.1016/j.nima.2021.165489`. URL: `https://www.sciencedirect.com/science/article/pii/S0168900221004745`.

[178] N. Mirabolfathi, H. R. Harris, R. Mahapatra, et al. "Toward single electron resolution phonon mediated ionization detectors." In: *Nuclear Instruments and Methods in Physics Research Section A: Accelerators, Spectrometers, Detectors and Associated Equipment* 855 (2017), pp. 88–91. ISSN: 0168-9002. DOI: `https://doi.org/10.1016/j.nima.2017.02.032`. URL: `https://www.sciencedirect.com/science/article/pii/S0168900217302127`.

[179] J. B. Dent, B. Dutta, D. Kim, et al. "New Directions for Axion Searches via Scattering at Reactor Neutrino Experiments." In: *Phys. Rev. Lett.* 124 (21 May 2020), p. 211804. DOI: `10.1103/PhysRevLett.124.211804`. URL: `https://link.aps.org/doi/10.1103/PhysRevLett.124.211804`.

[180] J. R. Klein, A. Machado, D. Schmitz, et al. *SNOWMASS Neutrino Frontier NF10 Topical Group Report: Neutrino Detectors*. 2022. arXiv: `2211.09669 [hep-ex]`. URL: `https://arxiv.org/abs/2211.09669`.

[181] R. Strauss, J. Rothe, G. Angloher, et al. "The $\nu$-cleus experiment: a gram-scale fiducial-volume cryogenic detector for the first detection of coherent neutrino–nucleus scattering." In: *The European Physical Journal C* 77.8 (2017), p. 506. DOI: `https://doi.org/10.1140/epjc/s10052-017-5068-2`.

[182] V. Wagner, R. Rogly, A. Erhart, et al. "Development of a compact muon veto for the Nucleus experiment." In: *Journal of Instrumentation* 17.05 (May 2022), T05020. DOI: `10.1088/1748-0221/17/05/T05020`. URL: `https://dx.doi.org/10.1088/1748-0221/17/05/T05020`.

[183] A. Erhart, V. Wagner, A. Wex, et al. "A plastic scintillation muon veto for sub-Kelvin temperatures." In: *The European Physical Journal C* 84.1 (Jan. 2024), p. 70.

[184] B. Mauri. *Development of a cryogenic veto system for the NUCLEUS CEvNS experiment*. June 2022. DOI: `10.5281/zenodo.6767397`. URL: `https://doi.org/10.5281/zenodo.6767397`.

[185] A. Wex. In preparation. PhD thesis. Technische Universität München.

[186] N. Schermer. *Exploring CEvNS from Nuclear Reactors with the NUCLEUS Experiment*. July 2022. DOI: `10.5281/zenodo.6805366`. URL: `https://doi.org/10.5281/zenodo.6805366`.

[187] J. Rothe, G. Angloher, F. Ardellier-Desages, et al. "NUCLEUS: Exploring coherent neutrino-nucleus scattering with cryogenic detectors." In: *J. Low Temp. Phys.* 199.1 (2020), pp. 433–440. DOI: `https://doi.org/10.1007/s10909-019-02283-7`.

[188] C. Goupy. In preparation. PhD thesis. Université Paris Saclay.

[189] L. Thulliez, D. Lhuillier, F. Cappella, et al. "Calibration of nuclear recoils at the 100 eV scale using neutron capture." In: *J. Instrum.* 16.07 (July 2021), P07032. DOI: `10.1088/1748-0221/16/07/P07032`. URL: `https://dx.doi.org/10.1088/1748-0221/16/07/P07032`.

[190] *EXCESS Workshop*. `https://indico.cern.ch/event/1013203/`. Accessed: 28.11.2023.

[191] *EXCESS2022 Workshop*. `https://indico.scc.kit.edu/event/2575/`. Accessed: 28.11.2023.

[192] *EXCESS22@IDM Workshop*. `https://indico.cern.ch/event/1117540/`. Accessed: 28.11.2023.

[193] *EXCESS23@TAUP Workshop*. `https://indico.cern.ch/event/1213348/overview`. Accessed: 28.11.2023.

[194] *EXCESS24 Workshop*. `https://agenda.infn.it/event/39007/`. Accessed: 17.10.2024.

[195] EXCESS workshop. *Data repository of the EXCESS workshop*. https://github.com/fewagner/excess. 2021. DOI: `https://github.com/fewagner/excess`.

[196] G. Agnolet et al. "Background studies for the MINER Coherent Neutrino Scattering reactor experiment." en. In: *Nucl. Instrum. Meth. A* 853 (2017), p. 53. ISSN: 0168-9002. DOI: `10.1016/j.nima.2017.02.024`. URL: `https://www.sciencedirect.com/science/article/pii/S0168900217302085` (visited on 09/20/2021).

[197] G. Angloher et al. "Results on MeV-scale dark matter from a gram-scale cryogenic calorimeter operated above ground." In: *Eur. Phys. J. C* 77.9 (2017), pp. 1–6. DOI: `10.1140/epjc/s10052-017-5223-9`.

[198] A. Aguilar-Arevalo et al. "Results on Low-Mass Weakly Interacting Massive Particles from an 11 kg d Target Exposure of DAMIC at SNOLAB." In: *Phys. Rev. Lett.* 125 (24 Dec. 2020), p. 241803. DOI: `10.1103/PhysRevLett.125.241803`. URL: `https://link.aps.org/doi/10.1103/PhysRevLett.125.241803`.

[199] L. Barak et al. "SENSEI: Direct-Detection Results on sub-GeV Dark Matter from a New Skipper CCD." In: *Phys. Rev. Lett.* 125 (17 Oct. 2020), p. 171802. DOI: `10.1103/PhysRevLett.125.171802`. URL: `https://link.aps.org/doi/10.1103/PhysRevLett.125.171802`.

[200] P. Abbamonte, D. Baxter, Y. Kahn, et al. "Revisiting the dark matter interpretation of excess rates in semiconductors." In: *Phys. Rev. D* 105 (12 June 2022), p. 123002. DOI: `10.1103/PhysRevD.105.123002`. URL: `https://link.aps.org/doi/10.1103/PhysRevD.105.123002`.

[201] N. Kurinsky, D. Baxter, Y. Kahn, and G. Krnjaic. "Dark matter interpretation of excesses in multiple direct detection experiments." In: *Phys. Rev. D* 102 (1 July 2020), p. 015017. DOI: `10.1103/PhysRevD.102.015017`. URL: `https://link.aps.org/doi/10.1103/PhysRevD.102.015017`.

[202] R. Harnik, R. Plestid, M. Pospelov, and H. Ramani. "Millicharged cosmic rays and low recoil detectors." In: *Phys. Rev. D* 103.7 (2021), p. 075029. DOI: `10.1103/PhysRevD.103.075029`. arXiv: `2010.11190 [hep-ph]`.

[203] S. Knapen, J. Kozaczuk, and T. Lin. "Migdal Effect in Semiconductors." In: *Phys. Rev. Lett.* 127.8 (2021), p. 081805. DOI: `10.1103/PhysRevLett.127.081805`. eprint: `2011.09496` (hep-ph).

[204] M. Heikinheimo, S. Sassi, K. Nordlund, et al. "Identification of the low-energy excess in dark matter searches with crystal defects." In: *Phys. Rev. D* 106 (8 Oct. 2022), p. 083009. DOI: `10.1103/PhysRevD.106.083009`. URL: `https://link.aps.org/doi/10.1103/PhysRevD.106.083009`.

[205] M. F. Albakry, I. Alkhatib, D. W. P. Amaral, et al. "Investigating the sources of low-energy events in a SuperCDMS-HVeV detector." In: *Phys. Rev. D* 105 (11 June 2022), p. 112006. DOI: `10.1103/PhysRevD.105.112006`. URL: `https://link.aps.org/doi/10.1103/PhysRevD.105.112006`.

[206] E. Queguiner. "Analysis of the data of the EDELWEISS-LT experiment searching for low-mass WIMP." PhD thesis. Université de Lyon, 2018.

[207] R. Anthony-Petersen, A. Biekert, R. Bunker, et al. "A stress-induced source of phonon bursts and quasiparticle poisoning." In: *Nature Communications* 15.1 (2024), p. 6444. DOI: `10.1038/s41467-024-50173-8`. URL: `https://doi.org/10.1038/s41467-024-50173-8`.

[208] H. Lattaud, E. Guy, J. Billard, et al. "Characterization of the Phonon Sensor of the CRYOSEL Detector with IR Photons." In: *J. Low Temp. Phys.* (2024). DOI: `10.1007/s10909-024-03096-z`. URL: `https://doi.org/10.1007/s10909-024-03096-z`.

[209] J. Åström, P. Di Stefano, F. Pröbst, et al. "Fracture processes observed with a cryogenic detector." In: *Physics Letters A* 356.4 (2006), pp. 262–266. ISSN: 0375-9601. DOI: `https://doi.org/10.1016/j.physleta.2006.03.059`. URL: `https://www.sciencedirect.com/science/article/pii/S0375960106005007`.

[210] D. Delicato, A. Ahmad, L. Bandiera, et al. "Low-energy spectrum of the BULLKID detector array operated on surface." In: *Eur. Phys. J C* 84.4 (2024), p. 353. DOI: `https://doi.org/10.1140/epjc/s10052-024-12714-9`.

[211] G. Angloher, S. Banik, G. Benato, et al. "DoubleTES detectors to investigate the CRESST low energy background: results from above-ground prototypes." In: *The European Physical Journal C* 84.10 (Oct. 2024), p. 1001. DOI: `https://doi.org/10.1140/epjc/s10052-024-13282-8`.

[212] R. Romani. "Observations of the LEE in a Two Channel SPICE Athermal Phonon Detector." EXCESS@TAUP Workshop. 2023. URL: `https://indi.to/w9kP6`.

[213] M. Murakami and T. Kuan. "Thermal strain in lead thin films V: Strain relaxation above room temperature." In: *Thin Solid Films* 66.3 (1980), pp. 381–394. ISSN: 0040-6090. DOI: `https://doi.org/10.1016/0040-6090(80)90391-0`. URL: `https://www.sciencedirect.com/science/article/pii/0040609080903910`.

[214] J. W. Hutchinson. "Stresses and failure modes in thin films and multilayers." In: 1996. URL: `https://api.semanticscholar.org/CorpusID:11726712`.

[215] E. Chason, M. Karlson, J. J. Colin, et al. "A kinetic model for stress generation in thin films grown from energetic vapor fluxes." In: *Journal of Applied Physics* 119.14 (Apr. 2016), p. 145307. ISSN: 0021-8979. DOI: `10.1063/1.4946039`. eprint: `https://pubs.aip.org/aip/jap/article-pdf/doi/10.1063/1.4946039/15180291/145307\_1\_online.pdf`. URL: `https://doi.org/10.1063/1.4946039`.

[216] N. Schermer. In preparation. PhD thesis. Technische Universität München.

[217] R. K. Romani. "Aluminum relaxation as the source of excess low energy events in low threshold calorimeters." In: *Journal of Applied Physics* 136.12 (Sept. 2024), p. 124502. ISSN: 0021-8979. DOI: `10.1063/5.0222654`. eprint: `https://pubs.aip.org/aip/jap/article-pdf/doi/10.1063/5.0222654/20176808/124502\_1\_5.0222654.pdf`. URL: `https://doi.org/10.1063/5.0222654`.

[218] J. Billard. "Searching for Dark Matter and New Physics in the Neutrino sector with Cryogenic detectors." PhD thesis. Université Claude Bernard Lyon 1, 2021. URL: `https://theses.hal.science/tel-03259707/document`.

[219] L. Peters. In preparation. PhD thesis. Technische Universität München.

[220] L. Cardani, N. Casali, I. Colantoni, et al. "Final results of CALDER: kinetic inductance light detectors to search for rare events." In: *The European Physical Journal C* 81.7 (July 2021), p. 636. DOI: `https://doi.org/10.1140/epjc/s10052-021-09454-5`.

[221] L. Cardani, N. Casali, A. Cruciani, et al. "Al/Ti/Al phonon-mediated KIDs for UV–vis light detection over large areas." In: *Superconductor Science and Technology* 31.7 (May 2018), p. 075002. DOI: `10.1088/1361-6668/aac1d4`. URL: `https://dx.doi.org/10.1088/1361-6668/aac1d4`.

[222] S. Sassi, M. Heikinheimo, K. Tuominen, et al. "Energy loss in low energy nuclear recoils in dark matter detector materials." In: *Phys. Rev. D* 106 (6 Sept. 2022), p. 063012. DOI: `10.1103/PhysRevD.106.063012`. URL: `https://link.aps.org/doi/10.1103/PhysRevD.106.063012`.

[223] J. Xu, P. Barbeau, and Z. Hong. "Detection and Calibration of Low-Energy Nuclear Recoils for Dark Matter and Neutrino Scattering Experiments." In: *Annu. Rev. Nucl. Sci.* 73.1 (2023), pp. 95–121. DOI: `10.1146/annurev-nucl-111722-025122`. eprint: `https://doi.org/10.1146/annurev-nucl-111722-025122`. URL: `https://doi.org/10.1146/annurev-nucl-111722-025122`.

[224] G. Angloher, S. Banik, G. Benato, et al. “Observation of a low energy nuclear recoil peak in the neutron calibration data of the CRESST-III experiment.” In: *Phys. Rev. D* 108 (2 July 2023), p. 022005. doi: 10.1103/PhysRevD.108.022005. url: https://link.aps.org/doi/10.1103/PhysRevD.108.022005.

[225] G. Soum-Sidikov, H. Abele, J. Burkhart, et al. “Study of collision and $\gamma$-cascade times following neutron-capture processes in cryogenic detectors.” In: *Phys. Rev. D* 108 (7 Oct. 2023), p. 072009. doi: 10.1103/PhysRevD.108.072009. url: https://link.aps.org/doi/10.1103/PhysRevD.108.072009.

[226] N. F. Iachellini. “Increasing the sensitivity to low mass dark matter in CRESST-III with a new DAQ and signal processing.” Feb. 2019. url: http://nbn-resolving.de/urn:nbn:de:bvb:19-237623.

[227] F. Reindl. “Exploring Light Dark Matter With CRESST-II Low-Threshold Detectors.” en. PhD thesis. Technische Universität München, 2016, p. 206. url: https://mediatum.ub.tum.de/1294132.

[228] M. Stahlberg. “Probing Low-Mass Dark Matter with CRESST-III Data Analysis and First Results.” PhD thesis. Technische Universität Wien, 2020. doi: 10.34726/hss.2021.45935. url: https://repositum.tuwien.at/handle/20.500.12708/16833.

[229] E. Gatti and P. F. Manfredi. “Processing the signals from solid-state detectors in elementary-particle physics.” In: *La Rivista del Nuovo Cimento (1978-1999)* 9 (1986), pp. 1–146. doi: https://doi.org/10.1007/BF02822156.

[230] M. Mancuso, A. Bento, N. F. Iachellini, et al. “A method to define the energy threshold depending on noise level for rare event searches.” In: *Nucl. Instrum. Methods.* 940 (2019), pp. 492–496. issn: 0168-9002. doi: https://doi.org/10.1016/j.nima.2019.06.030. url: https://www.sciencedirect.com/science/article/pii/S0168900219308708.

[231] F. Wagner. “Towards next-generation cryogenic dark matter searches with superconducting thermometers.” en. PhD thesis. Technische Universität Wien; Österreichische Akademie der Wissenschaften, 2023, p. 238. url: https://doi.org/10.34726/hss.2023.106550.

[232] A. R. Münster. “High-Purity CaWO<sub>4</sub> Single Crystals for Direct Dark Matter Search with the CRESST Experiment.” en. PhD thesis. Technische Universität München, 2017, p. 235. doi: https://nbn-resolving.de/urn/resolver.pl?urn:nbn:de:bvb:91-diss-20171117-1393806-1-5. url: https://mediatum.ub.tum.de/1393806.

[233] C. Strandhagen. “Low Energy Excess in CRESST.” EXCESS Workshop. 2021. url: https://indi.to/kQxKW.

[234] A. Gieb. “Study of the sub-keV background in cryogenic detectors.” en. Bachelor’s Thesis. Technische Universität München, 2021.

[235] A. Erb and J.-C. Lanfranchi. "Growth of high-purity scintillating CaWO4 single crystals for the low-temperature direct dark matter search experiments CRESST-II and EURECA." In: *Cryst. Eng. Comm.* 15 (12 2013), pp. 2301–2304. DOI: `10.1039/C2CE26554K`. URL: `http://dx.doi.org/10.1039/C2CE26554K`.

[236] P. M. M. Bauer. "Data Analysis for the CRESST Experiment: New Methods, improved Alpha Analysis, and Results on Light Dark Matter and Backgrounds." en. PhD thesis. Technische Universität München, 2020, p. 238. URL: `https://mediatum.ub.tum.de/1543574`.

[237] S. Gupta. "Sub-GeV Dark Matter Studies and Universal Bound States Exploration with CRESST-III." PhD thesis. Technische Universität Wien, 2024. URL: `https://doi.org/10.34726/hss.2024.112984`.

[238] *Update of X Ray and Gamma Ray Decay Data Standards for Detector Calibration and Other Applications*. Vienna: International Atomic Energy Agency, 2007. ISBN: 92-0-113606-4. URL: `https://www.iaea.org/publications/7551/update-of-x-ray-and-gamma-ray-decay-data-standards-for-detector-calibration-and-other-applications`.

[239] S. Kuckuk. In preparation. PhD thesis. Universität Tübingen.

[240] R. Strauss et al. "A prototype detector for the CRESST-III low-mass dark matter search." In: *Nucl. Instrum. Methods Phys.* 845 (2017). Proceedings of the Vienna Conference on Instrumentation 2016, pp. 414–417. ISSN: 0168-9002. DOI: `https://doi.org/10.1016/j.nima.2016.06.060`. URL: `https://www.sciencedirect.com/science/article/pii/S0168900216306039`.

[241] M. Wüstrich. "Improving Particle Discrimination and Achieving a $4\pi$-Veto Detector Concept for the CRESST Experiment." en. PhD thesis. Technische Universität München, 2020, p. 194.

[242] F. Pucci. "Results of doubleTES detectors." EXCESS23@TAUP Workshop. 2023. URL: `https://indi.to/cMmfR`.

[243] J. Rothe. "Above-ground operation of 0.5 g $Al_2O_3$ cryogenic detector prototypes for NUCLEUS." EXCESS Workshop. 2021. URL: `https://indi.to/vWg2h`.

[244] C. Mancini-Terracciano and M. Vignati. "Noise correlation and decorrelation in arrays of bolometric detectors." In: *Journal of Instrumentation* 7.06 (June 2012), P06013. DOI: `10.1088/1748-0221/7/06/P06013`. URL: `https://dx.doi.org/10.1088/1748-0221/7/06/P06013`.

[245] A. Langenkämper, X. Defay, N. Ferreiro Iachellini, et al. "A Cryogenic Detector Characterization Facility in the Shallow Underground Laboratory at the Technical University of Munich." In: *Journal of Low Temperature Physics* 193.5 (Dec. 2018), pp. 860–866.

[246] R. Underwood. "Dark Matter Searches with Germanium and Silicon Detectors in SuperCDMS and CUTE." PhD thesis. Queen's University, 2022. URL: `http://hdl.handle.net/1974/29957`.

[247] M. Cappelli, G. D. Castello, and M. Vignati. “Estimation of waveform deformation with the matched filter.” In: *Journal of Instrumentation* 19.06 (June 2024), P06034. DOI: `10.1088/1748-0221/19/06/P06034`. URL: `https://dx.doi.org/10.1088/1748-0221/19/06/P06034`.

[248] N. Schermer. In preparation. PhD thesis. Technische Universität München.

[249] G. Soum-Sidikov, J.-P. Crocombette, M.-C. Marinica, et al. *Calculation of crystal defects induced in $CaWO_4$ by 100 eV displacement cascades using a linear Machine Learning interatomic potential*. 2024. arXiv: `2407.00133 [physics.ins-det]`. URL: `https://arxiv.org/abs/2407.00133`.

[250] A. Erhart. In preparation. PhD thesis. Technische Universität München.

[251] A. Abdelhameed, G. Angloher, P. Bauer, et al. “Cryogenic characterization of a LiAlO2 crystal and new results on spin-dependent dark matter interactions with ordinary matter: CRESST Collaboration.” In: *The European Physical Journal C* 80 (2020), pp. 1–10. DOI: `10.1140/epjc/s10052-020-8329-4`. URL: `https://doi.org/10.1140/epjc/s10052-020-8329-4`.

[252] S. Dorer. In preparation. PhD thesis. Technische Universität Wien.

[253] H. Böck, M. Villa, and R. Bergmann. “Five decades of TRIGA reactors.” In: *25th Int. Conf. Nucl. Energy New Eur.* 2016, pp. 1–8.

[254] J. Lindhard, V. Nielsen, and M. Scharff. “Cross sections for ion-atom collisions in solids.” In: *Mat.-Fys. Medd. K. Dan. Vidensk. Selsk* 36.10 (1968).

[255] S. Agostinelli, J. Allison, K. a. Amako, et al. “GEANT4—a simulation toolkit.” In: *Nucl. Instrum. Meth.* 506.3 (2003), pp. 250–303. DOI: `10.1016/S0168-9002(03)01368-8`.

[256] J. Allison, K. Amako, J. Apostolakis, et al. “Geant4 developments and applications.” In: *IEEE Trans. Nucl. Sci.* 53.1 (2006), pp. 270–278. DOI: `10.1109/TNS.2006.869826`.

[257] J. Allison, K. Amako, J. Apostolakis, et al. “Recent developments in Geant4.” In: *Nucl. Instrum. Meth.* A835 (2016), pp. 186–225. DOI: `10.1016/j.nima.2016.06.125`.

[258] F. J. Kerr and D. Lynden-Bell. “Review of galactic constants.” In: *Mon. Notices Royal Astron. Soc.* 221.4 (Aug. 1986), pp. 1023–1038. ISSN: 0035-8711. DOI: `10.1093/mnras/221.4.1023`. URL: `https://doi.org/10.1093/mnras/221.4.1023`.

[259] D. Hooper and S. D. McDermott. “Robust constraints and novel gamma-ray signatures of dark matter that interacts strongly with nucleons.” In: *Phys. Rev. D* 97 (11 June 2018), p. 115006. DOI: `10.1103/PhysRevD.97.115006`. URL: `https://link.aps.org/doi/10.1103/PhysRevD.97.115006`.

[260] B. J. Kavanagh. *Verne: Earth-stopping effect for heavy dark matter*. Astrophysics Source Code Library, record ascl:1802.005. Feb. 2018. ascl: `1802.005`.

[261] B. J. Kavanagh. “Earth scattering of superheavy dark matter: Updated constraints from detectors old and new.” In: *Phys. Rev. D* 97 (12 June 2018), p. 123013. DOI: `10.1103/PhysRevD.97.123013`. URL: `https://link.aps.org/doi/10.1103/PhysRevD.97.123013`.

# Acknowledgments

In these last pages, I would like to express my heartfelt gratitude to all the people who have accompanied me on this incredible journey. These years have been anything but easy, filled with both personal and global challenges. Yet, I could always rely on the amazing people around me. That support has been my greatest privilege, and for that, I am profoundly grateful. To everyone who supported my work or lifted my spirits in difficult times, thank you.

First and foremost, to my supervisor Raimund Strauß – thank you for so much more than just the opportunity to conduct my PhD within the amazing Cryo group at TUM. Throughout my PhD, I knew I could always rely on your support, both professionally and personally. Your guidance made all the difference. THANK YOU!

To Stefan Schönert, thank you for welcoming me to the E15 Chair and for all your support throughout these years. It is an honor to be part of such a vibrant research environment.

To Jochen Schieck and Florian Reindl – thank you for helping me find my way to Munich. I wouldn't be here without you.

To the CRESST, NUCLEUS, and CRAB collaborations – thank you for providing a stimulating and supportive environment. The opportunities to work on pioneering dark matter and neutrino research, and the amazing discussions among experienced scientists and fellow PhD students, were invaluable. And of course, thank you for all the good times during collaboration meetings and beyond!

To my Cryo group colleagues – Angelina Kinast, Alexander Langenkämper, Tobias Ortmann, Luca Pattavina – thank you for welcoming me into the group from day one and for always sharing your knowledge. To later joined Johannes Rothe, Victoria Wagner, Alexander Wex, Andreas Erhart, Nicole Schermer, and Lilly Peters – thank you for being the most supportive colleagues I could have wished for, always ready to help and have fun together! To all the students who joined us over the years – especially Guià Resina, Katharina von Mirbach, and Àfrica González – your enthusiasm and support have meant so much. And to Mattia Atzori Corona – thank you for bringing sunshine into our group with your stories and vibrant personality during the time you spent in Munich.

To Johannes – thank you for your bright mind and for sharing so much of your knowledge about physics and cryogenic detectors with me. To Luca – thank you for your patience in explaining things and for all your funny stories. To Vici – thank you, not only for your support in countless ways but especially for reminding me that my opinions matter.

To the entire E15 Chair – thank you for all the fun parties, lively corridor conversations and coffee breaks. It was always a pleasure to come into the office because of the wonderful people around me!

I would like to thank the CRESST and NUCLEUS analysis groups: Martin Stahlberg – thank you for always being available to help with the CAT software, even at inconvenient hours. Giorgio Del Castello – thank you for being my anylsis partner during the CRAB analysis campaign and beyond, your enthusiasm and expertise are amaizing. Marco Vig-

nati – thank you for your feedback, insights from the frequency domain, and unwavering support. Thierry Lasserre – thank you for always approaching problems with a fresh and unbiased perspective.

To Franz Pröbst – thank you for sharing your unbelievably deep knowledge, which helped make so many things clearer! To Karoline Schäffner – thank you for inviting me to co-author the review on scintillating cryogenic dark matter searches; it was an incredible adventure that taught me so much. To Florian Reindl, Felix Wagner, and Alexander Fuß – thank you for co-initiating the EXCESS workshop, which turned out to be a true success (I believe!). I am truly grateful for this ongoing journey that has brought me together with so many amazing, enthusiastic people attempting to unravel the web of excess mysteries.

To Dominik Fuchs, Angelina Kinast, and Athoy Nilima – thank you for working on the CRESST LEE paper together, I think it turned out very well. To Johannes Rothe, Andreas Erhart, Alexander Wex, and Nicole Schermer – thank you for making the data collected at TUM a reality, laying the foundation for much of this work. I am also grateful for all your input and for your help in proofreading parts of this thesis. To Samir Banik and Valentyna Mokina – thank you for joining me in the hunt for the origin of the lines in the silicon spectrum. To Sarah Kuckuk – thank you for raising important issues and for engaging in all the LEE discussions.

To my bachelor's and master's supervisor at Moscow State University, Pavel Klimov – thank you for introducing me to the world of science, for believing in me, and for offering me so many opportunities. I cannot fully express my gratitude. To my former colleagues at SINP MSU, Sergej Sharakin and Mikhail Zotov – thank you for teaching me so much about cosmic rays, programming, and data analysis, and for always being supportive.

Shubham – thank you for your support during our night walk in Santo Stefano and for our unforgettable Rome adventure. Felix – thank you for showing me through your example what it means to be proactive, to take on big challenges, and for all the fun we had together!

To my "work friends" who are now simply just friends – Alex, Christoph, Moritz – thank you for all the nice conversations, funny jokes and your support!

To (Cr)Andi – thank you for our night walks through Schwabing and the deep conversations about life. Leaving parties just isn't the same anymore.

To (L)Andi – thank you for creating our horror group, for bringing light and laughter to my days, and for sharing all your stories. Your energy is infectious, and I'm so grateful for all the joy and fun moments we had together.

To Nici – thank you for being so warm and open. You are amazing and inspiring, and I have no idea how you manage to find the energy to do everything you do, at such a high level. Go girl, keep shining!

To my physicist friends – Natasha, Borya, Sereja, and Petya – thank you for maintaining our friendship over the years. Your support and inspiration mean everything to me. I miss you!

To my energy-sparkling Masha – thank you for never giving up on me, for all our wonderful nature trips, for the endless conversations, and for the crazy, amazing times

we had together.

To Konsi – without your unwavering support and unconditional love, I doubt this thesis would have ever been completed. I have learned so much from you – about physics, servers, kindness, healthy work-life balance, and meat factories in Germany. Thank you for being in my life, for giving me the chance to find a family in Germany by sharing your amazing Schweizer squad, and for making every moment more joyful. Let's keep having fun together!

В конце я хочу поблагодарить мою семью: мама и папа, спасибо, что всегда меня поддерживали, во всех моих начинаниях и разных ситуациях. Вы супер, и я вас очень люблю и очень скучаю!